NEW INSIGHTS INTO THE LIMITATIONS ON THE EFFICIENCY AND ACHIEVABLE GRADIENTS IN Nb_3Sn SRF CAVITIES

A Dissertation

Presented to the Faculty of the Graduate School

of Cornell University

in Partial Fulfillment of the Requirements for the Degree of

Doctor of Philosophy

by

Daniel Hall

December 2017

NEW INSIGHTS INTO THE LIMITATIONS ON THE EFFICIENCY AND ACHIEVABLE GRADIENTS IN NB_3SN SRF CAVITIES

Daniel Hall, Ph.D.

Cornell University 2017

The A15 superconductor Nb_3Sn has shown great promise to replace niobium as the material of choice for the construction of superconducting radio-frequency (SRF) accelerator cavities. It promises, at least on paper, greater efficiency and higher accelerating gradients, with the potential to enable the construction of smaller yet more powerful accelerators than can be constructed using niobium. Although the state-of-the-art performance of cavities coated with Nb_3Sn has shown great potential, the achievable limits in cavity quality factor Q_0 and accelerating gradient E_{acc} are still below that expected given theoretical limits. In this work we present and discuss results of experiments carried out to understand the current limitations on Q_0 and E_{acc}, and propose methods to improve these further. We will conclude with an outlook to the future, and the prospects that Nb_3Sn could enable.

BIOGRAPHICAL SKETCH

Daniel Hall is (or was) a half-Australian, half-British individual who spent most of his growing life living near Rome, Italy. He attended an international school near Rome, before reading Physics at the University of Manchester (with a year spent studying at UC Santa Barbara). Following completion of a Masters in High Energy Physics, he found that his in interest in particle physics was less because of the science itself and more because of a love of the machines involved, and so he enrolled at Cornell University for a PhD as part of the SRF accelerator group. He maintains an interest in vintage computing, ice skating, and ballroom dancing (this last because it allows him to tick the boxes of social interaction, physical activity, and musical engagement with one stroke).

I dedicate this work to my parents,

and to all those who have in some way taught me something.

ACKNOWLEDGEMENTS

At the end of any PhD research project, first dibs for thanks and praise goes to the advisor. Indeed, I could not have hoped for a better advisor than Prof. Matthias Liepe, whose untiring support and ever-helpful advice have allowed me to enjoy a degree of success through my graduate studies beyond that which I could have imagined when I begun. A PhD is not a one-man effort – indeed, in the field of SRF, the graduate students of a group such as ours must band together to overcome the many tough but interesting challenges that are commonplace in our field. In this endeavour, I could note have hoped for better colleagues (and friends) than past and present graduate students (in order of date joining the group) Yi Xie, Nicholas Valles, Sam Posen, Dan Gonnella, James Maniscalco, Peter Koufalis, Ryan Porter, and Thomas Oseroff. But a lab does not run on graduate students alone, and indeed we would be lost were it not for the efforts of all the personnel at Newman lab. I would like to acknowledge the unwavering support of James Sears, Greg Kulina, John Kaufman, Paul Bishop, Brendan Elmore, Brian Clasby, Holly Conklin, Terri Gruber, Neal Alexander, Randy Miller, Gregory Abbott, Shawn Clark, Fumio Furuta, Minqi Ge, Tim O'Connell, Katerina Malysheva, Monica Wesley, Eric Smith, Dwight Widger, Colby Shore, and Dan Sabol. The list goes on, but must be terminated for the sake of brevity: all others who should be there, your contribution is strongly implied and gratefully acknowledged. During my time at Cornell, I have been blessed with a string of fantastic students who have participated in my research, namely Ivaylo Madjarov, Chad Burton, Byeonghee Yu, Alexander Wikner, Adam Kline, Melissa Allen, and Katherine (Jixun) Ding. The ingenuity demonstrated by each of these individuals has made significant contributions to the field of SRF and to the work in this thesis. Finally, on a more

personal note, I would like to thank the following close relations: David Wise, for his always sage advice and engaging conversation; the members of the Cornell Ballroom team and club, for their friendship and the times spent dancing; Peter Klavins, for hours wiled away playing Minecraft; and to Jessica Lamb, for the companionship and occasional injection of Midwestern-flavoured common sense. At the end of all things, some mention of acknowledgement goes to the second Iran-Iraq war; had it not given my father a reason to flee Baghdad, he would not have run into my mother playing guitar in a bar in Jordan, and I would never have enjoyed the many years of love and support (or any years at all, for that matter) that have given me the best I could hope for in life. But that is another story.

TABLE OF CONTENTS

Biographical Sketch . . . iii
Dedication . . . iv
Acknowledgements . . . v
Table of Contents . . . vii
List of Tables . . . ix
List of Figures . . . x

1 Introduction **1**
1.1 Motivation . . . 2
1.2 An SRF primer . . . 4
1.2.1 Superconducting theory relevant to SRF . . . 4
1.2.2 Major parameters of SRF cavities . . . 10

2 Nb_3Sn for SRF cavities **16**
2.1 Advantages of Nb_3Sn cavities . . . 16
2.2 Material properties of Nb_3Sn . . . 19

3 Fabrication of Nb_3Sn cavities **24**
3.1 History of Nb_3Sn fabrication for SRF cavities . . . 24
3.2 The Cornell Nb_3Sn coating furnace . . . 36
3.3 Standard coating procedure . . . 43
3.4 Nature of the coated layer . . . 46

4 RF testing of SRF cavities **50**
4.1 The vertical test setup . . . 51
4.2 Measuring cavity quality factor . . . 59

5 Limitations on cavity efficiency **68**
5.1 Uniformity of the surface coating . . . 68
5.1.1 The pre-anodization process . . . 79
5.1.2 Studies on the impact of pre-anodization . . . 81
5.1.3 Pre-anodization of a single-cell cavity . . . 93
5.2 Losses from trapped magnetic flux . . . 99
5.2.1 Theoretical model of thermoelectric magnetic flux and flux losses . . . 110
5.3 Conclusions on the limitations on cavity efficiency . . . 118

6 Limitations on achievable gradient **121**
6.1 Constraints on the quench mechanism . . . 121
6.1.1 Ultimate limit: the superheating field . . . 122
6.1.2 HPP Klystron testing . . . 123
6.1.3 Global and local thermal runaway . . . 126
6.1.4 Surface roughness and post-coating chemistry . . . 128

6.2 Dynamics of the cavity quench 131
6.2.1 Temperature mapping experiment 132
6.2.2 Sudden heating before quench 137
6.2.3 Hard and soft quenches 142
6.2.4 Temperature "slip" phenomenon 146
6.2.5 Surface analysis of cavity cut-outs 149
6.2.6 Theoretical candidates for quench mechanisms 152
6.3 Conclusions on cavity quench mechanisms 156

7 Conclusion **158**
7.1 Considerations for the coating of niobium structures 158
7.1.1 Impact of trapped magnetic flux 159
7.1.2 Maximum achievable gradient 162
7.2 Outlook 164
7.2.1 Altering the electron mean free path 164
7.2.2 Current state-of-the-art and future projects 168

Bibliography **172**

LIST OF TABLES

1.1 Cavity types and their parameters that have been used in the Nb_3Sn program at Cornell. The CEBAF designed was used by the University of Wuppertal and continues to be used by Jefferson Lab. At Cornell, a single-cell TeSLA shape R&D cavity is designated LTE (e.g. LTE1-7). This table was originally published in [Pos14]. 13

LIST OF FIGURES

1.1 The BCS resistance of the superconductor niobium as a function of the normal conducting electron mean free path at a temperature of 2.0 K. The frequency of the applied RF field is 1.3 GHz. This curve was calculated using the BCS fitting code SRIMP [Hal70] using T_c = 9.2 K, $\Delta(T = 0)/k_bT_c$ = 1.96, λ_L = 39 nm, and ξ_0 = 38 nm. 7

1.2 Left, a diagram of magnetic flux lines trapped and quantised in a Type-II superconductor. Right, a measurement using SQUID magnetometry demonstrating the presence of a lattice of magnetic flux lines in the superconductor YBCO. Image from [WPW+15]. 9

1.3 (A) The electromagnetic fields in a single-cell cavity operating in the TM_{010} mode. The electric field oscillates back and forth along the beam axis. Correct timing of the passage of the beam will result in acceleration. (B) The same cavity mounted inside a cryomodule, inside which it is immersed in liquid helium. The cryomodule is equipped with an antenna that provides RF power for the cavity. (C) A collection of cavities at Cornell University. At the top is a 200 MHz CERN copper cavity whose inside is coated with niobium. Bottom left are a 1.3 GHz 9-cell ILC cavity and its 1-cell R&D counterpart. Bottom right is a 500 MHz B-cell cavity. 10

1.4 An example of the performance of a 1.3 GHz LTE-shape (see Table 1.1) cavity tested at Cornell. The Q vs E was taken at a bath temperature of 2.0 K. High field Q-slope can be seen beginning at 25 MV/m. A plot of the surface resistance against inverse temperate, obtained from a measurement of Q vs T, is shown fitted with SRIMP. Data courtesy of Peter Koufalis, Cornell University. 14

2.1 Left, the Coefficient of Performance (COP) for a cryoplant. This value indicates the amount of power that must be invested to remove 1 Watt of heating power from the cold region. Right, the power draw from grid for a cryoplant working on a 1.3 GHz TeSLA-style cavity (both niobium and Nb_3Sn-coated), normalised per cell and MV/m. The higher T_c of Nb_3Sn allows operation at 4.2 K, and the increase in cryoplant efficiency significantly reduces the power draw of the cavity. 18

2.2 Far left, the A15 crystal structure of Nb_3Sn. Centre and right, high resolution HAADF images of the Nb_3Sn crystal lattice from samples coated at Cornell University, with the crystal structure overlaid. The images were taken down the 100 and 111 axes. HAADF images courtesy of Paul Cueva, Muller Group, Cornell University 19
2.3 The thermal conductivity of Nb_3Sn against that of 300 RRR niobium. The considerably lower thermal conductivity of Nb_3Sn could result in issues with local or global thermal feedback and instability. Niobium data from[KB96], Nb_3Sn data from [CC64] . 20
2.4 The phase diagram of the niobium-tin system, as measured by Charlesworth et al. [CMM70]. Feschotte et al [FPB79] measured a similar phase diagram in 1979. The shaded area indicates the Nb_3Sn-only region. Of note, above 930°C the other phases of Nb-Sn do not occur. The pure Nb_3Sn region was re-drawn by Okamoto [Oka90] in 1990 (shown in blue), and then again by Toffolon [TSGS02] in 2002 (shown in red). This last measurement was confirmed by Okamoto [Oka03] in 2003 and by Li et al. [LDGL09] in 2009. This figure is adapted from the one originally published in [God06]. 22
2.5 Left, the superconducting transition temperature of Nb_3Sn as a function of the atomic-% tin. The data is fitted with a Boltzmann function. On the right, the normalised energy gap as a function of the atomic-% tin, indicating that as the crystal becomes tin-depleted the superconductor moves from a strongly-coupled BCS superconductor to a weak one. This figure is adapted from those shown in [God06], with references to [DJD+81, MZRB79]. . 23

3.1 Left, an example of some of the best results from the 10 GHz cavities used in the Siemens AG Nb_3Sn program. Values of Q were given only at zero field and the quench field. This figure was originally published in [Pos14] with data from [HMP+77, Hil76, HKP+81]. Right, the distribution of quench fields at 4.2 K seen in all Siemens TE-mode cavities. A Gaussian distribution is fitted. This figures is adapted from data in [HKP+81]. 25
3.2 The standard Cornell coating recipe at time of writing. The major steps are annotated, although the 24-hour degas stage is not shown. The different stages are described in the text. 27
3.3 A schematic of the Siemens AG coating furnace, showing the two configuration of the furnace, (A) and (B), corresponding to the indicated regions in the coating recipe shown in Figure 3.4. This figure is adapted from images shown in [dHHR+78]. 29

3.4 An example Siemens coating recipe. The two regions correspond to the two different furnace configurations, (A) and (B), shown in Figure 3.3. Although a 5-hour coating is shown, Siemens AG experiment with a number of different coating lengths. This figure is adapted from data given in [dHHR+78]. 30
3.5 Schematic of the furnace used for coating 1 GHz cavities coated at the University of Wuppertal. In contrast to the Siemens design, the cavity and source are kept in separate hot-zones. This image is reproduced from [PHK+88]. 32
3.6 An example of the coating recipe used at the University of Wuppertal. The separate hot-zone allowed the source to be operated at a temperature both above and below that of the cavity. This image is adapted from data found in [Pei83]. 33
3.7 Characteristic performance of 1.5 GHz Nb_3Sn-coated cavities produced at Wuppertal. The Q-slope see at medium fields and above is very characteristic for cavities of this era, and it was suspected that this behaviour was fundamental to Nb_3Sn. This figure is reproduced from [MKM96]. Note that the gradient given is the peak electric surface field – this can be converted to accelerating gradient or peak surface magnetic field using the constants given for CEBAF cavities in Table 1.1 (e.g. $E_{pk} = 20$ MV/m is equivalent to $E_{acc} = 11.4$ MV/m). 34
3.8 Simplified schematics summarising the operation of the major coating furnace designs to date. The Jefferson Laboratory furnace is an adaption of the Siemens design, and the Fermi National Laboratory furnace is a horizontal variant of the Cornell design, which is in itself adapted from the Wuppertal furnace. . . 35
3.9 A diagram showing the Cornell University coating insert, which is housed inside an ultra-high vacuum furnace (shown top right) located in the Newman laboratory cleanroom. The tin source is located at the bottom of the insert, surrounded by a secondary heater that allows the source to be held at a temperature above that of the cavity. The inside of the insert, shown bottom right, shows a single-cell TeSLA-style cavity placed inside the coating insert. This figure is adapted from material originally published in [Pos14]. 37
3.10 The control system for the Cornell coating furnace. Pumps and valves are operated from the central rack, which also hosts the power supply interlock. Once active, the furnace is controlled from the computer on the left. The furnace can be seen through the cleanroom door on the right. 40
3.11 Left, the vapour pressure of tin and tin chloride as a function of temperature. Right, the mean free path of tin as calculated from Equation (3.1). Vapour pressure data from [Pei83, MO87]. 41

3.12 Accuracy of the prediction for the amount of tin consumed during a coating from the evaporation calculation of Equation (3.2), as determined by the error relative to the measured change of the weight of the crucible after coating. The scatter indicates a typical accuracy of ±6%. 43
3.13 (A) An image of the surface of the Nb_3Sn layer as viewed in the scanning electron microscope. (B) The grains outlined using a graphical watershed method. (C) Distribution of grain surface areas from a number of images like that in (A). The average grain size for this coupon was found to be 1.32 μm^2. 47
3.14 Left, an STEM image of the cross-section of the Nb_3Sn layer. On the right the image has been false-coloured to identify the RF surface, and the Nb_3Sn layer, and the niobium substrate. The grain boundaries of the Nb_3Sn layer are highlighted. The protective platinum layer is introduced during the sample preparation for STEM and is not present during coating or RF testing. 48
3.15 EDX chemical analysis of a cross-section from a Nb_3Sn sample coated at Cornell. The difference signal of the tin and niobium indicates the presence of a tin-depleted Nb_3Sn phase within the layer. These images courtesy of Thomas Proslier, Argonne National Laboratory [BPG+15]. 49

4.1 The vertical test facility at Newman Laboratory on Cornell campus. The three test pits – the furthest one is covered by the block necessary for radiation shielding – house the cryostats in which the cavities are tested. The operator station can be seen at the control racks on the left side of the photograph. 51
4.2 Diagram of a vertical test insert used for cavity testing in the facility at Newman laboratory. The major components are annotated. The forward power cable for supplying the cavity with RF power is not shown. This figure originally published in [Kno97]. 53
4.3 The helium insertion device – or stinger – used on the vertical test inserts at Cornell for controlling the cooldown temperature rate and gradient during vertical testing. The cold helium gas is throttled using a Joule-Thompson valve and heated using a heater maze in the passage of the gas. The gas is then injected at the base of the cryostat. 55
4.4 Part of the cryoplant used at Newman laboratory for vertical testing. The dewar on the right is capable of supplying a maximum of 3000 L of liquid helium to the test pits. This helium is recovered – in gaseous form – by a compressor and stored in an outside tank. The warm gaseous helium is converted back into liquid by the liquefier on the left, which injects the product directly back into the main dewar. 56

4.5 The RF vertical testing setup for single-cavity testing. For simplicity, some attenuators have been omitted. The signal generator emits an RF signal that is amplified by a solid state amplifier or a klystron (not shown). Part of this amplified output is siphoned for measurement of P_f. The rest is transmitted to the cavity, and the reflected portion is diverted away from the amplifier by a circulator. Of this power, some is extracted for a measurement of P_r (which is P_c at steady-state lock). The remainder is dissipated in a load. The power transmitted through the cavity is split, with half going for a measurement of P_t, and the other half (after a 180 degree phase shift) being combined with the signal from the generator inside a mixer. The output from the mixer is used to modulate the output of the signal generator. Use of a phase shifter allows the phase-lock to be optimised to drive the cavity on resonance. 58

4.6 Examples of the behaviour of the returning coupler power P_c, relative to the forward power into the coupler when the RF is on (i.e. P_c/P_f). The value of P_f is constant. At $t = 0$, the RF is turned on and the P_c decreases until it reaches a steady state, where $P_c = P_r$. The value of P_r is indicated. At $t/\tau_L = 25$, the RF is turned off, and $P_f = 0$ (although P_c remains defined relative to P_f when the RF was on). The value of P_c the instant when the RF turned off is where $P_c = P_e$, and is also indicated. The value of P_c now decays according to τ_L. 62

4.7 A Q vs E of a Cornell Nb_3Sn cavity taken at 4.2 K. The points from a conventional Q vs E are shown. A Q vs E using the continuous method, derived from the highest-field conventional point, is shown in blue. 65

5.1 A comparison of the performance of the ERL1-5 (the first cavity coated at Cornell) against one of the more recent ones, LTE1-7. The coating procedure of LTE1-7 is seen in Figure 3.2, while the coating recipe for ERL1-5 can be seen in Figure 5.5. Whereas later cavities showed a lack of Q-slope, ERL1-5 demonstrated a Q-slope very similar to that seen in Wuppertal cavities (see Figure 3.7. 69

5.2 A temperature map (T-Map) of the Nb_3Sn cavity designation ERL1-5, operating at 10 MV/m. This map is a projection (onto a rectangular grid) of the outside surface of the cavity. Along the x-axis, the board number progresses about the cavity beam axis. Along the y-axis, going from resistor 0 to 17 moves from the lower iris to the upper iris (with the equator being along the x-axis at resistor 9). The T-Map showns extensive heating on the lower half of the T-Map, corresponding to heating on the entirety of the half-cell of the cavity that faced away from the tin source during coating. 70
5.3 EDS mix-map of a cut-out from a region of the ERL1-5 cavity that showed heating (sample designated M5). Green regions indicate regions where quantification gives 25 atomic percent Sn, red areas correspond to 6 atomic percent Sn. The lower atomic percent at these regions is due to the Nb_3Sn layer being too thin, and the SEM probe interacting with the niobium bulk below. 71
5.4 A cross section of Nb_3Sn cut from a fine grain niobium substrate sample, designation E3F. On the left is the STEM image, with the RF layer on top (a thin layer of platinum resides between the Nb_3Sn surface and the vacuum for protection during sample preparation) and the niobium substrate at the bottom. On the right is an EDS map of the region outlined in red, giving the atomic percent Sn at each region. The interface between the Nb_3Sn and Nb is seen to be tin depleted. This image is courtesy of Paul Cueva, Muller Group, Cornell University. 72
5.5 A comparison of the coating of ERL1-5 (left) and ERL1-4 (right). ERL1-5 was the first cavity coated at Cornell, and the ramp up to coating temperature was done with the tin source and the coating chamber at the same temperature, with the gradient between the source and the chamber being introduced upon arriving at the coating temperature. Later, in coatings of ERL1-4 and beyond, a temperature gradient was introduced between the tin source and the chamber before the ramp-up to coating temperature. 74
5.6 Two figures demonstrating the change in niobium to tin signal given by the X-ray probe at the tin film regions. The SEM region on the left is centred on a thin film region. As the SEM beam energy in the probe regions 1 and 2, shown, is changed, the ratio of the heights of the niobium $L_{\alpha-1}$ peak to the tin $L_{\alpha-1}$ peak is measured. This is plotted on the right. As the beam energy increases, it probes deeper into the bulk - at region 1, the Nb_3Sn layer is thin enough that the beam begins to probe the niobium bulk. At region 2, the Nb_3Sn layer is thick enough that this is not the case. 75

5.7 Top, an SEM image of a fine grain niobium sample coated with Nb_3Sn. The sample was hung in the furnace at the height of the cavity equator, and received the coating recipe given in Figure 3.2. Bottom left, the raw mixmap obtained from the X-ray data, with thick regions in green and thin regions in blue. Bottom right, the contrast has been enhanced using the method in Ref. [KHL16], with thin regions being highlighted in white. . . . 76
5.8 Examples of the different coverages seen in samples coated in the furnace. Regions in green are sufficiently thick - red regions are considered too thin. Figure a) is a large grain sample placed near the base of the furnace, showing (4.0 ± 0.7)% thin film coverage. Figure b) is a cut-out from ERL1-5 showing (65.7 ± 1.5)% coverage. Figure c) is a fine grain sample placed high up in the furnace, above the cavity equator height, and shows (30±2.0)% coverage. Figure d) is a fine grain sample located near the equator and coated alongside cavity ERL1-4, that shows less than 0.5% coverage by thin film regions - a zoomed-in inset locates a very small region that may still be thick enough for good performance. 77
5.9 A diagram summarising the coating behaviour of different samples depending on their preparation and their location in the furnace. The combination of a high local tin vapour pressure during the ramp-up (dependent on the position in the furnace) and the use of pre-anodisation results in the most uniform coverage. . . . 79
5.10 Left, the chemistry setup for anodising the interior of a niobium cavity. Right, a series of samples with different voltages of pre-anodisation, these being (from L to R): 0 (none), 5, 15, 30, and 60 volts. 80
5.11 Histograms of the ratio of Sn to total signal for the pixels from EDS maps (taken at a beam energy of 30 kV) of samples of different substrate RRR, both pre-anodised (blue) and not pre-anodised (red). In all non-anodised samples, regions of thin film were seen, as evidence by the presence of a tail on the left side of the Gaussian distribution at approximately 0.17. By comparison, pre-anodised samples do not show any evidence of thin film regions, regardless of the RRR. 82
5.12 A histogram, in a manner similar to Fig. 5.11, of the ratio of the tin signal to total signal for all pixels in an EDS map taken of sample, for four different samples. Each sample received a different level of anodisation before coating, corresponding to a difference in the oxide layer thickness (literature gives a value of 2.2 nm/V [JCC+91]). 83

5.13 Simplified diagram of the stop motion coating process. Each sample was taken through the same coating, but interrupted at a different point, as given by the labels (A) through (E). The complete coating cycle was that given in Figure 3.2. Exact temperatures at which the coating was interrupted are annotated and also given in the text. 84
5.14 SEM images of samples taken from steps (A) through (E) in the stop motion coating process, showing the difference in coating between a pre-anodised and non-anodised sample. The box on the left side of each image pair is a scale box for that pair, and is 2×2 µm in size. 86
5.15 Histograms of the pre-anodised (left) and non-anodised (right) EDS maps for the samples from the stop motion coating. Note that pure niobium does not result in an intensity ratio of Sn to the total of zero – this is due to background noise resulting in a false positive signal in each energy channel of the EDS detector. Therefore, a systematic error results in all values of the ratio being shifted to the right along the x-axis. 87
5.16 Schematic diagram of the Wuppertal 1 GHz coating furnace, from Reference [PHK+88]. The tube that passes between the hot-zones of the tin source and the coating chamber is suspected to have played a role in cooling the tin gas during the ramp-up stage and suppressing the beneficial effect of the ΔT during the ramp-up, resulting in the formation of a small number of thin film regions (in the manner of sample A1L in Figure 5.8), which resulted in the Q-slope seen [MKM96]. 92
5.17 Q vs E taken at a cavity bath temperature of 4.2 K for 1.3 GHz single-cell cavity LTE1-6, without and with pre-anodisation of the cavity surface prior to coating. An improvement of approximately 3 nΩ at 14 MV/m is seen. 94
5.18 The setup for the thermal simulation of Nb_3Sn on niobium, coated on both sides (in the style of a Cornell coating) [DHL17]. The three layers are simulated separately, and the power flow at each interface is matched in a iterative fashion until a complete, stable solution for the heat flow equation is found. This image courtesy of Jixun Ding, Cornell University [DHL17]. 97

5.19 Results of the simulation for the setup shown in Figure 5.18, for both 1.3 and 6 GHz cavities with different substrate RRR operating at a cavity bath temperature of 4.2 K. At 1.3 GHz, global thermal feedback is so small that substrate does not become an issue until the RRR reaches reactor grade. At 6 GHz, substrate purity is more of a concern. These simulations assume a niobium substrate wall thickness of 3 mm, a Nb_3Sn coating thickness (inside and outside) of 3 μm, and 8 mG of trapped flux. This image courtesy of Jixun Ding, Cornell University [DHL17]. 98
5.20 Experimental setup for flux trapping studies of cavity designated LTE1-7. A Helmholtz coil pair is mounted above and below the cavity, allowing application of a uniform magnetic field. This field is measured by two flux gates placed on the upper iris of the cavity, one point axially and the other azimuthal to the beampipe axis. Three temperature sensors allow measurement of temperature gradients along the cavity. The use of a heater at the helium input allows a development of a thermal gradient (or, the suppression of one) during the cooldown through T_c. 102
5.21 Temperature (red) and magnetic field (blue) measurements for a cooldown with an external magnetic field applied. The thermal gradient across the cavity during this time is approximately 200 mK/m. A field of approx. 60 mG (axial measurement) is applied before going through T_c, and maintained until the cryostat is filled with liquid helium at 4.2 K. The field is then turned off, and the remaining field is taken to be that which has been trapped – in this case, (32 ± 5) mG. 103
5.22 An example of a cooldown in a large thermal gradient through T_c. Due to multiplexing of the temperature measurement, only one sensor can be read at a time, and interpolation using fourth-order polynomial fit is used to extrapolation the full range of data. The Helmholtz coil is turned off during this time. 105
5.23 Spread of the Q vs T measurements for all the cooldowns of cavity LTE1-7, in different thermal gradients and applied magnetic fields. The impact of the trapped flux on residual resistance can be seen in the quality factor at low temperatures. 107
5.24 Plot of the surface resistance at 2.0 K – which is dominated by the residual resistance – of LTE1-7 for different values of thermal gradient (blue) and trapped magnetic flux (red). In both cases, a linear relationship with R_s is seen. The black diamond indicates the resistance seen at 2.0 K and 1 MV/m in a cavity following a normal slowcool, in which the thermal gradients and ambient field are minimised to the greatest extend possible (this point is not considered when making the linear fits shown). 108

5.25 Q vs E curves (obtained using the "continuous" method described in section 4.2) for all the cooldowns performed as part of the experiment on LTE1-7, separated by thermal gradient cooldowns and applied field cooldowns. For comparison, a curve taken following a normal slowcool (in which the thermal gradients and ambient fields are minimised to the maximum extent possible) is also shown. 109
5.26 Left, a plot of the sensitivity to trapped flux (red) and thermal gradient through T_c (blue) as a function of the applied RF magnetic field. On the right, the ratio of these two sensitivities has been fitted to a linear fit, as shown. The ratio is found to be constant with RF field within the confidence interval of the linear fit, which is shown as the dotted lines above and below the fit line. . 109
5.27 The sensitivity to trapped flux of Nb_3Sn cavity designation LTE1-7, as a function of the applied RF magnetic field. The data from the thermal gradient measurements has been rescaled to amount of trapped magnetic flux by (6.2 ± 0.3) mG/(K/m). 110
5.28 Circuit model of the thermocurrents generated by the bimetallic interface between Nb and Nb_3Sn in the presence of a thermal gradient along the length of the interface. The layer is modelled as a series of connected batteries, with a thermoelectric voltage from the Seebeck effect and an internal resistance that comes from the resistivity of the material and the cross-sectional area of the layer. 112
5.29 (A) A diagram visualising the weak pinning scenario. A vortex line, strongly pinned deep in the bulk, moves under the influence of the RF field, and is hindered in its motion by a sea of weak pinning centres that it must overcome. (B) The motion of the vortex during the first quarter of the RF period T, as it is displaced from the origin. (C) The motion of the vortex during the second and third quarter of the RF period. The impact of the pinning centres resists the motion of the vortex from being restored to its position at the origin. These figures courtesy of Danilo Liarte, Cornell University. 116
5.30 Contour plot giving contribution to residual resistance from trapped flux in a 1.3 GHz ILC cavity as a function of the peak applied RF magnetic field. Lines of equipotential give the specification required for operation at a Q of 1 and 2×10^{10} at 4.2 K bath temperature, assuming a BCS component at 4.2 K of 8 nΩ. . 119

6.1 Histogram of the quench fields observed in the majority of Nb_3Sn cavity tests performed at Cornell. 122

6.2 A comparison of HPP data from 120°-baked niobium and Nb_3Sn coated at Cornell. The CW (continuous) quench fields from standard Q vs E curves are also given. Niobium data from [Val13]. . 124
6.3 The quench field of the cavity in HPP testing against the time taken to quench. As the forward power from the Klystron is increased, the cavity fills quicker and quenches sooner. The faster filling allows for a better outrunning of thermal effects, but in Nb_3Sn even at 400 kW of forward power this is found to be insufficient to fully outrun them. 125
6.4 HPP test results from Campisi at SLAC and Hays and Hall at Cornell [Cam85, CF84, HP97]. The higher field achieved by Campisi can be attributed to the use of a higher forward power from the Klystron. 126
6.5 Q vs E of a Nb_3Sn cavity immediately post-coating and after a short outside BCP to remove the outside layer of Nb_3Sn. 128
6.6 Atomic force microscope scan of the surface of a sample of Nb_3Sn coated at Cornell. The surface roughness is of the order of 1 μm peak-to-peak over a 20×20 μm span. This image courtesy of James Maniscalco, SRF Group, Cornell University. 129
6.7 Q vs E of a Nb_3Sn cavity immediately post-coating and after 3 passes of 30 V oxipolish (anodisation in NaOH to 30 V, followed by an HF rinse), corresponding to the removal of approximately 50-100 nm of Nb_3Sn. 130
6.8 Photograph of the temperature mapping system (T-Map) assembled onto cavity LTE1-7. Board number progresses anticlockwise around the cavity (as viewed from above), while resistor number increases going from the lower iris to the upper iris. The orientation of the cavity is the same as it is in the coating furnace - i.e., the lower half-cell is the side facing away from the tin source during coating. 134
6.9 Quench map of LTE1-7, taken at a bath temperature of 2.0 K. The colorbar is a time integral of the heating at each sensor beginning immediately after quench. The longer the sensor stays hot, the greater the value. The quench origin is found to be at board 28, resistor 4, on the lower half of the cavity. 135

6.10 Left, an example of a "single-scan" measurement taken at the quench origin at a bath temperature of 2.0 K. After acquisition on a chosen sensor is triggered, the field in the cavity (red) is altered, while being measured using a pickup probe. Simultaneously, the temperature at the sensor (blue) is also acquired. In this trace, RF power was turned on at the 2 second mark and off at 30 seconds. The cavity did not quench during this trace. The temperature oscillations are due to the opening and closing of the cryostat pumping valve that maintains the bath temperature of 2.0 K. On the right, the value of the peak surface field (squared) is plotted against the ΔT at that time, with the blue line corresponding to the time the cavity is filling ($t = 2 - 30$ s in the left plot) and red to the time after the RF power is turned off. The linear shape indicates that the temperature rise is due to Ohmic heating. . . . 136
6.11 A singlescan trace from LTE1-7 taken at 2.0 K at the quench origin, during which the gradient in the cavity is taken very close to (but not allowed to exceed) the quench field of the cavity. At surface fields very close to the quench field, sudden jumps in temperature can be seen on top of the more conventional Ohmic heating. 138
6.12 A plot of the temperature difference of a sensor (in this case, the quench origin sensor) from the bath, ΔT, against the square of the peak surface magnetic field in the cavity. These example traces were taken at bath temperatures of 2.0 K (left) and 4.2 K (right). The jumps seen during the cavity fill (evident in Figure 6.11) are marked with arrows. At both 2.0 K and 4.2 K, a hysteresis effect is seen in the ΔT during the fill and ring-down portions of the trace. 139
6.13 Scatter plot of the jumps seen during the three cooldowns (2 at 2.0 K, 1 at 4.2 K). Each set of jumps has been normalised to the mean of the height of the first jump seen in that series. 140
6.14 Scatter plot of the jumps seen at 4.2 K before and after quench. All jumps have been rescaled such that the first jump has a mean height of 1. 141
6.15 Difference between a "soft" quench, in which the field in the cavity only just reaches the quench field, and only a small spike in temperature is seen at the quench origin at the moment of quench; and a "hard" quench, in which the field in the cavity rises fast enough to trigger a large temperature spike that takes the quench origin above the transition temperature of 18 K. . . . 143

6.16 Collection of temperature maps taken during the three cooldowns. Maps a), c) and e) were taken after 1 soft quench, in which the cavity was only just brought to the quench field. Maps b), d) and f) were taken after the many hard quenches necessary to construct a quench map such as that seen in Figure 6.9. 144
6.17 a) An example of the "slip" phenomenon, as seen in cavity LTE1-7 while operating at 2.0 K, in this case seen at the quench origin after many quenches. The time at which slip begins to occur is labelled the "slip field", and the temperature difference between the beginning and end of the slip is given to be the "slip ΔT". b) At 2.0 K, after quenching the cavity many times, a measurement of the slip ΔT against the peak surface magnetic field at which the slip occurs. 147
6.18 A example of the "single slip" and "double slip" features seen in traces taken at 4.2 K after many quenches of cavity LTE1-7. The second slip is always more subtle than the first. 147
6.19 a) The ΔT of the slip versus the peak magnetic surface field at which the slip occurs (for reference, see Fig. 6.17 a)) at 4.2 K before quench, after 1 soft quench, and after many hard quenches. b) Changing the fill time of the cavity, the time after RF on at which the slip occurs against the maximum surface magnetic field achieved in the trace. 148
6.20 Compositional backscatter (left) and chamber secondary electron (right) images of a feature found at the quench origin. A sharp ridge across which the Nb_3Sn layer bends to conform. The upper images are of a wide area - the yellow insets indicate the region in which the lower images were taken. The yellow double-headed arrow indicates the direction of the oscillating surface RF magnetic field. 151
6.21 Normalised power dissipated in a grain boundary as a function of normalised current through the grain boundary, modelled as an underdamped Josephson junction. The result is plotted as the peak normalised supercurrent through the grain boundary induced by the RF field $\beta = J_0/J_c$ (where $J = J_0 \sin(\omega t)$ is the supercurrent across the grain boundary induced by the surface RF field with angular frequency ω) against the power dissipated in the grain boundary (normalised to the power dissipated when the grain boundary is fully normal conducting). Figure reproduced from [SG17]. 153

6.22 Gibbs free energy per unit length of a vortex at a surface field of 80 mT in Nb_3Sn at a bath temperature of 4.2 K, for three different scenarios: no T_c suppression, a specific T_c suppression that removes the energy barrier entirely, and a constant T_c suppression of 3-5 K in which a second, smaller barrier appears to remain. This figure courtesy of Danilo B. Liarte and James P. Sethna, Cornell University. 156
6.23 Two examples of slightly tin-depleted grains seen at the RF surface in cross-section of samples coated at Cornell. Overlaid on the EDS map is a line EDS; due to the standardless quantification used, the absolute error of the measurement is large, but relative differences are precise to the level of the noise seen in the measurement. This image courtesy of Paul Cueva and David A. Muller, Cornell University. 157

7.1 Data from literature sources comparing the values of R^0_{fl} and R^1_{fl} for different niobium surfaces against that measured in Nb_3Sn. This data was collected from (A) [MCG+15] (B) [CG07] (C) [BCD+97]. 160
7.2 A Q vs E obtained at a bath temperature of 4.2 K from cavity LTE1-7 in the Newman vertical test setup. Equation 7.2 has been used to extrapolate the performance for a state-of-the-art cooldown. 162
7.3 A STEM HAADF image of a grain boundary in a Nb_3Sn cross-section. The image indicates a grain boundary thickness of less than 2 nm. Image courtesy of Paul Cueva, Muller Group, Cornell University. 164
7.4 A measurement of the residual Q-slope R^1_{fl} against the square of the normalised RF penetration depth. A fit of $A\lambda^2 + B$ has been superposed on the image. This image was adapted from [BCC+99], with the penetration depth $\lambda^2_{\text{rel}} = 1 + (\pi/2)(\xi_0/l)$. 166
7.5 The best performance observed in three different 1.3 GHz single-cell cavities that have seen use in the Cornell University Nb_3Sn programme, operating at a bath temperature of 4.2 K. The Q-specification for LCLS-II is shown, adjusted to take into account the improved efficiency of the cryoplant at 4.2 K. 169
7.6 A size comparison of a 1.5 GHz 6-cell and a 3 GHz 9-cell cavity. An 8.6 GHz single-cell can be seen perched on the beampipe of the 1.5 GHz 6-cell. A doubling of the frequency results in a significantly smaller cavity in all dimensions. 170

7.7 An example of what a cryocooler-equipped module would look like. Using a cryocooler power from a compressor unit, a single-cell or small multi-cell Nb_3Sn cavity powered by a solid state amplifier (not shown) can be operated at 4.2 K. Some example specifications for such a machine are shown in the table on the right. 171

CHAPTER 1

INTRODUCTION

The A15 superconductor Nb_3Sn has generated significant interest as a potential next-generation superconductor for use in superconducting radio-frequency (SRF) cavities. This work presents research carried out with the intent of understanding the physics underlying the current limitations on efficiency and accelerating gradient currently seen in state-of-the-art Nb_3Sn cavities. The work is laid out as follows, numbered by Chapter:

1. We will begin by motivating research into SRF technology, and provide a brief primer on the physics of SRF technology,
2. The advantages of applying Nb_3Sn to SRF technology will be presented, and its relevant properties will be discussed,
3. A history of Nb_3Sn in the field of SRF will be given, alongside a description of the vapour diffusion method; this will be followed by a detailed description of the fabrication apparatus and method used at Cornell University,
4. We will describe the method used to test SRF cavities made from niobium and Nb_3Sn,
5. Studies on the current limitations on Nb_3Sn cavity efficiency are presented, and results are given,
6. Studies on the latest understanding of the limitations on Nb_3Sn cavity gradient are presented and results given,
7. Finally, conclusions regarding the nature of these limitations are discussed, and suggestions are given for the next direction to take in the re-

search and development of Nb_3Sn as a next-generation material for use in SRF cavities.

1.1 Motivation

Particle accelerators have played an often quiet but always crucial role in the progress of human civilization since the development of the Crookes tube in the latter half of the 19th century. They have served to probe the nature of the atom, cure cancer, and display endless re-runs of Baywatch to audiences around the world[1]. From the early electrostatic accelerators, the contributions of great minds such as Rolf Wideroe, Gustav Ising, Max Steenbeck, and Ernest Lawrence, led to a myriad of machines whose raison detre is to accelerate a beam of charged particles for a variety of applications. These include cyclotrons, used for the production of medical tracer isotopes; electron microscopes, used for imaging material features down to the level of individual atoms; and cathode-ray tubes, used throughout the 20th century for the generation of images in television sets and computer monitors.

The discovery of superconductivity in 1911 by Heike Kamerlingh Onnes was the enabler of one such type of machine: the superconducting radio-frequency accelerator cavity. To date, they remain unmatched in the beam current that they are capable of delivering while still ensuring the phenomenal beam quality demanded of many modern applications. In the large hadron collider (LHC), superconducting cavities are used to sustain the high intensity proton beams whose collisions resulted in the observation of the Higgs boson. At the Cornell

[1]The contribution of the latter to the improvement of humankind is debatable

High Energy Synchrotron Source (CHESS), 500 MHz superconducting cavities are used to store the beam that is used to generate high energy X-rays for probing the nature of a variety of materials. Contemporary and future high brightness light sources such as the European X-ray Free Electron Laser (XFEL) and the upgraded LINAC Coherent Light Source (LCSL-II) rely on 1.3 GHz cavities to provide the bright beam necessary to generate the X-rays demanded by the latest generation of material science techniques.

A primary cost driver in implementing SRF technology is the operation and demands upon the cryogenic plant that is required to keep the cavities superconducting. For almost 50 years[TW68], virtually all production cavities have been fabricated from niobium (either bulk, with the entire cavity being niobium, or clad, with niobium affixed to a substrate such as copper). With a superconducting transition temperature of 9.2 K, niobium cavities are operated in the range of 2.0-4.2 K, depending on the frequency of the cavity, which demands that the cavity be immersed in liquid helium and which will be in the superfluid state when operating below 2.17 K. As a non-renewable resource, the price of liquid helium is (at time of writing) $\approx$ 10 US dollars per litre. Furthermore, cryogenic systems for liquid helium - particularly those required for operation below the atmospheric temperature of 4.2 K - are complex, and require specialized operators and numerous man-hours of maintenance. The addition of a helium re-liquefaction system, a must for any large-scale machine, adds further complexity to the system.

As science and industry demand more power and greater accessibility (and therefore a greater number of) to SRF machines, it is critical that costs can be reduced to allow supply to meet demand. Currently, the cost of building and

operating these machines render them prohibitively expensive to all but institutions benefiting from significant government funding. Improving the efficiency of SRF cavities is one of the primary means of reducing both the operating cost and the size of these facilities. It is this that motivates research into Nb_3Sn as a next-generation, higher efficiency superconductor to replace niobium as the current standard.

1.2 An SRF primer

1.2.1 Superconducting theory relevant to SRF

For the benefit of those unacquainted with superconductivity as it applies to RF accelerators, we will now summarise the basics necessary to understand the results given later in this work. This summary will largely be based on the works of Padamsee, Hays, and Knobloch[PKH98], and Tinkham[Tin12]. Those already familiar with the physics of SRF can move to the next chapter with impunity.

Bardeen-Cooper-Schrieffer (BCS) theory describes the family of "conventional" superconductors, to which both niobium and Nb_3Sn belong (the theory does not describe high temperature superconductivity, such as cuprates). When a superconductor is cooled beneath it's superconducting transition temperature T_c, the electrons begin to interact with each other via an electron-phonon interaction and condense to form Cooper pairs, a composite, Boson-like entity with integer spin. In this state, the electrons can travel through the lattice unimpeded, resulting in the phenomenon of zero DC electric resistance. Upon transitioning into the superconducting state, the generation of supercurrents – currents

of Cooper pair electrons – result in the cancellation and expulsion of magnetic field from inside the bulk of the superconductor. External fields can still penetrate, but their magnitude quickly decays in an exponential fashion, as dictated by the penetration depth λ of the superconductor, such that

$$H(x) = H_0 e^{-x/\lambda} \,, \tag{1.1}$$

where H_0 is the surface magnetic field and x is the depth into the superconductor.

Although superconductors offer no resistance to the passage of DC currents, the finite inertia of the Cooper pairs results in a non-zero resistance when under the influence of AC fields, as they are unable to completely screen the remaining normal conducting electrons from the oscillating electromagnetic field. The movement of these normal conducting electrons results in a small yet finite resistance, on the order of nΩs at RF. This surface resistance R_s is often quoted as having two parts as a function of the temperature T and applied magnetic field H, these being

$$R_s = R_{\mathrm{BCS}}(T, H) + R_{\mathrm{Residual}}(H) \,, \tag{1.2}$$

where the first term represents the temperature-dependent contribution explained by BCS theory, and the second term that which remains once the first term is subtracted. The latter can originate from a number of sources. Although classical BCS theory is only strictly valid at $H = 0$, recent extensions have been made to extrapolate BCS out to non-zero field[Gur14, XRK13]. A simplified formulation of the BCS component in the dirty limit is [PKH98]

$$R_{\mathrm{BCS}} = A\frac{f^2}{T}\exp\left[-\frac{\Delta}{k_b T}\right], \tag{1.3}$$

where A is a fitting constant, f is the frequency of the applied field, and T is the temperature. The term Δ is the superconducting energy gap, being the energy required per electron to break a superconducting pair (i.e. 2Δ breaks a pair), and is often quoted normalised by $k_b T_c$. A perfectly ideal BCS superconductor is expected to have $\Delta(T = 0)/k_b T_c = 1.75$, [Tin12] although real superconductors will have values larger (strongly-coupled) and lower (weakly-coupled) than this.

The surface resistance described by Equation (1.3) does not explicitly take into account impurities in the superconductor. A superconductor free of impurities and imperfections that can scatter Cooper pairs is considered "clean". In this scenario, the coherence length ξ of a Cooper pair (roughly equivalent to its size) is given by[Tin12]

$$\xi_0 \sim \frac{\hbar v_f}{k T_c}, \tag{1.4}$$

which is referred to as the "intrinsic" or "characteristic" coherence length (v_f is the Fermi velocity). For a clean superconductor, the penetration depth in Equation (1.1) is given by London theory to be

$$\lambda_L = \sqrt{\frac{mc^2}{4\pi n e^2}}, \tag{1.5}$$

where m is the electron mass and n is the density of normal conducting electrons.

When impurities are introduced, the mean free path of the normal conducting electrons l is reduced, and the superconductor is said to be "dirty". This

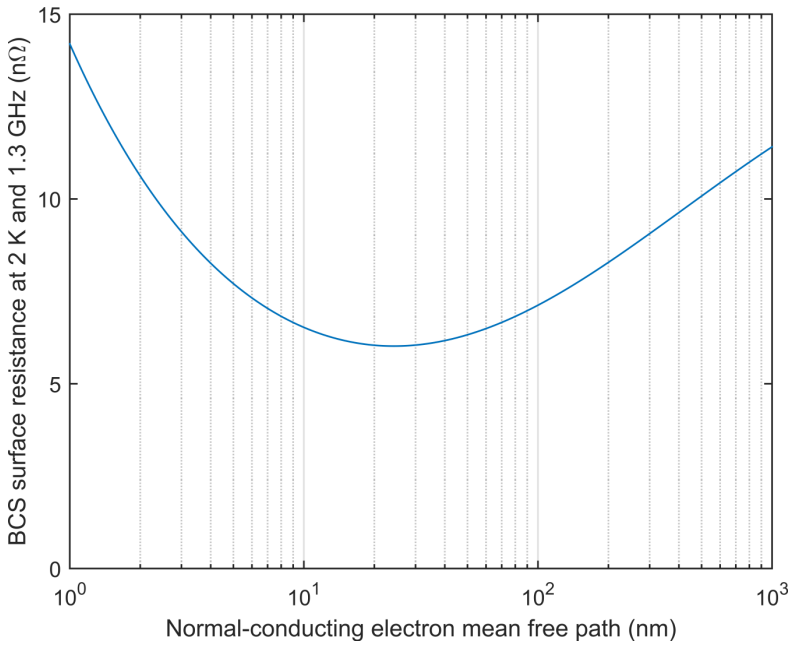

Figure 1.1: The BCS resistance of the superconductor niobium as a function of the normal conducting electron mean free path at a temperature of 2.0 K. The frequency of the applied RF field is 1.3 GHz. This curve was calculated using the BCS fitting code SRIMP [Hal70] using T_c = 9.2 K, $\Delta(T = 0)/k_b T_c = 1.96$, $\lambda_L = 39$ nm, and $\xi_0 = 38$ nm.

results in significant changes to the various superconducting parameters. Equation (1.3) is too simplified to explicitly include the impact of a change in the value of l – however, a success of the full BCS theory is the description of the change in R_s as a function of l, which is demonstrated (using the BCS-fitting code SRIMP [Hal70]) in Figure 1.1. Changing l also results in changes to the coherence length and penetration depth. Using a version Ginzburg-Landau theory updated by Lev Gor'kov using BCS theory, one can obtain the Ginzburg-Landau penetration depth and coherence length [Tin12, OMFB79]

$$\lambda(T = 0)_{GL} = \lambda_L \sqrt{1 + \frac{\lambda_0}{l}}\,, \tag{1.6}$$

and

$$\xi(T=0)_{GL} = 0.739\left[\xi_0^{-2} + \frac{0.882}{\xi_0 l}\right]^{-\frac{1}{2}} . \tag{1.7}$$

The ratio of the penetration depth and coherence length of a superconductor form one of its primary characteristics,

$$\kappa_{GL} = \frac{\lambda_{GL}}{\xi_{GL}} , \tag{1.8}$$

referred to as the Ginzburg-Landau parameter [GL09]. This parameter is used to separate the two types of conventional superconductors, Type-I and Type-II. Type-I superconductors are defined as having $\kappa < 1/\sqrt{2}$, and are characterised by a thermodynamic critical field

$$H_c = \frac{\phi_0}{2\sqrt{2}\pi\mu_0\lambda\xi} , \tag{1.9}$$

where ϕ_0 is the flux quantum. When the surface magnetic field exceeds this value, becomes energetically favourable for magnetic flux to exist inside the superconductor (n.b. this does not necessarily imply that the flux *enters* at this field – this technicality will be explained by the superheating field). Entry of the magnetic flux into superconductor results in the superconducting state being lost. In contrast, Type-II superconductors with $\kappa > 1/\sqrt{2}$ possess two critical fields, $H_{c1} < H_c < H_{c2}$. Above H_{c1}, it is again energetically favourable for magnetic flux to exist inside the bulk, but in quantised vortices of magnitude ϕ_0 that form a flux lattice as seen in Figure 1.2. Therefore, the superconducting state can be maintained alongside the presence of magnetic flux, in contrast to Type-I superconductors. Once in, flux can continue to be accommodated while still

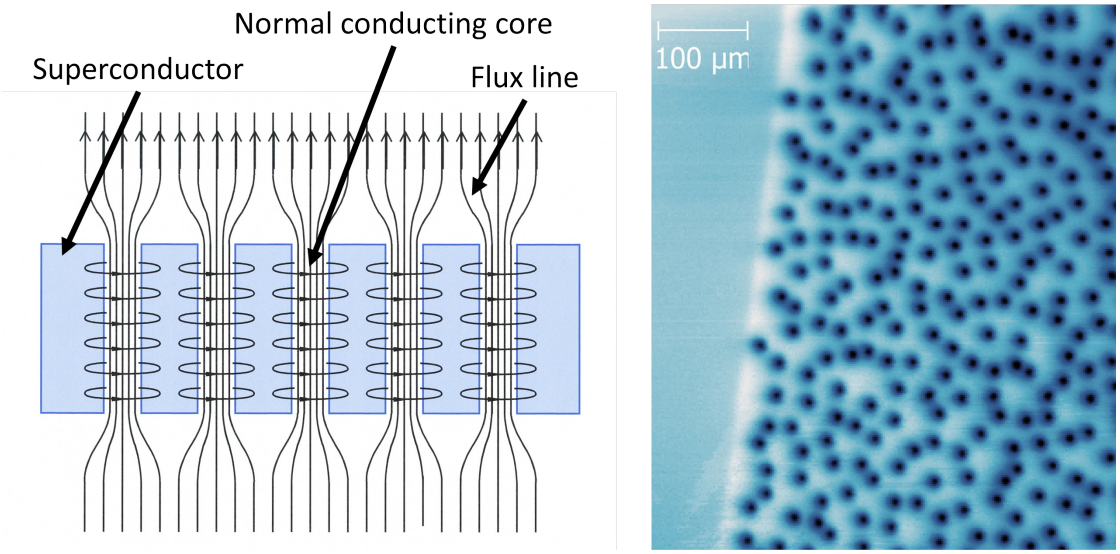

Figure 1.2: Left, a diagram of magnetic flux lines trapped and quantised in a Type-II superconductor. Right, a measurement using SQUID magnetometry demonstrating the presence of a lattice of magnetic flux lines in the superconductor YBCO. Image from [WPW+15].

allowing the superconducting state to be sustained until the upper critical field H_{c2}, at which point all superconductivity in the bulk is quashed.

As mentioned, it becomes favourable for magnetic flux to exist inside the superconductor at fields above H_c (for Type-I) and H_{c1} (for Type-II). However, the nucleation of a magnetic vortex at the surface of the superconductor incurs an energy cost, which results in a superheating effect [MSJ67, Cha95, VL11]. The result is a surface energy barrier that the flux must overcome in order to enter. Therefore, flux does not enter until a field $H_c < H < H_{sh}$ for Type-I and $H_{c1} < H < H_{sh}$ for Type-II, where H_{sh} is the superheating field. The superheating field represents the theoretical ultimate limit for flux entry into a superconductor (i.e. the largest possible surface barrier), although the realistic flux entry field can be lowered by a number of effects (such as demagnetisation from surface geometry).

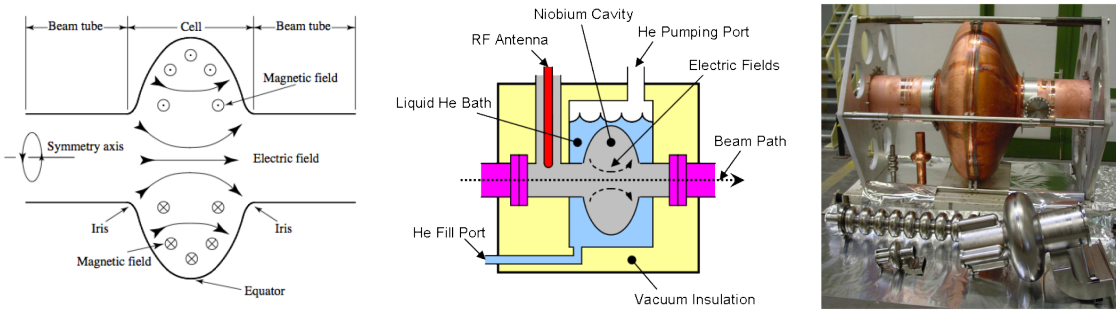

Figure 1.3: (A) The electromagnetic fields in a single-cell cavity operating in the TM_{010} mode. The electric field oscillates back and forth along the beam axis. Correct timing of the passage of the beam will result in acceleration. (B) The same cavity mounted inside a cryomodule, inside which it is immersed in liquid helium. The cryomodule is equipped with an antenna that provides RF power for the cavity. (C) A collection of cavities at Cornell University. At the top is a 200 MHz CERN copper cavity whose inside is coated with niobium. Bottom left are a 1.3 GHz 9-cell ILC cavity and its 1-cell R&D counterpart. Bottom right is a 500 MHz B-cell cavity.

1.2.2 Major parameters of SRF cavities

An SRF cavity is an electromagnetic cavity, most commonly operated in the fundamental TM_{010} mode, with openings at either end and whose walls are made of a superconducting material. A diagram of a cavity is shown in Figure 1.3. The field in the cavity is sustained from an input coupler located in one of the beampipes attached to the ends of the cavity. The majority of SRF cavities have a resonant frequency f_0 ranging from a hundred MHz to a few GHz, with the region around 1 GHz being most popular for electron accelerators. Given a uniform surface resistance R_s, the power dissipated in the cavity is given by

$$P_{\text{diss}} = \frac{1}{2} R_s \int_S |\mathbf{H}|^2 \, dS \ , \tag{1.10}$$

where the integral is taken of the magnitude of the magnitude of the magnetic field over the surface of the cavity. The energy stored in the cavity is given by

$$U = \frac{\mu_0}{2} \int_V |\mathbf{H}|^2 \, dV \, , \tag{1.11}$$

where the integral is taken over the interior volume of the cavity. One of the two major characteristic parameters is the intrinsic quality factor Q_0 of the cavity, which is a dimensionless parameter that quantifies the rate of energy loss (dissipated power) in the walls of the cavity to the energy stored in the cavity, and is given by

$$Q_0 = \frac{\omega_0 U}{P_{\text{diss}}} \, , \tag{1.12}$$

where $\omega_0 = 2\pi f_0$. Equations (1.10) and (1.11) allow us to write

$$Q_0 = \frac{\omega_0 \mu_0}{R_s} \frac{\int_V |\mathbf{H}|^2 \, dV}{\int_S |\mathbf{H}|^2 \, dS} \, , \tag{1.13}$$

which can be condensed into $Q_0 = G \cdot R_s$ by defining the "geometry factor"

$$G = \omega_0 \mu_0 \frac{\int_V |\mathbf{H}|^2 \, dV}{\int_S |\mathbf{H}|^2 \, dS} \, , \tag{1.14}$$

which is a function of the geometry of the cavity and can be calculated for a given shape using electromagnetic codes such as Omega3P or CLANS.

When a charged particle of charge q passes through the cavity at the appropriate time during the cycle, it is accelerated. For the chosen phase (most

commonly, the optimum), the particle is subjected to a potential V_{acc} during its passage through the cavity and gains kinetic energy qV_{acc}. The second major characteristic parameter for a cavity is accelerating gradient, defined as

$$E_{\text{acc}} = \frac{V_{\text{acc}}}{L} , \tag{1.15}$$

where L is the length of the cavity. The potential V_{acc} can be related to the dissipated power using the relation

$$P_{\text{diss}} = \frac{V_{\text{acc}}^2}{\frac{R_a}{Q_0} Q_0} , \tag{1.16}$$

where R_a is the shunt impedance of the cavity and R_a/Q_0 is a geometry-dependent constant[2] that can be obtained from electromagnetic simulations of the cavity structure. These simulations are also used to obtain

- $\left[E_{\text{pk}}/E_{\text{acc}}\right]$, the ratio of the peak surface electric field to the accelerating gradient,
- $\left[E_{\text{pk}}/\sqrt{U}\right]$, the ratio of the peak surface electric field to the root of the stored energy in the cavity, and
- $\left[B_{\text{pk}}/E_{\text{pk}}\right]$, the ratio of the peak surface magnetic field to the peak surface electric field.

The parameters for the single-cell cavities that have been used during the Nb_3Sn programme at Cornell, as well as those for a single-cell CEBAF cavity (which have been used in the Nb_3Sn programmes at other institutions), are given in Table 1.1.

[2] In this work, the accelerator definition for $R_a/Q_0 = |V|^2/(\omega U)$ is used

	TeSLA (LTE)	Cornell ERL	CEBAF
f [GHz]	1.3	1.3	1.5
E_{pk}/E_{acc}	1.88	1.76	1.81
B_{pk}/E_{acc} [mT/MVm^{-1}]	4.28	4.08	4.4
G [Ω]	278	272	255
R_a/Q_0 [Ω]	105	116	102
$E_{pk}/\sqrt{U}$ [MVm^{-1}/$\sqrt{\text{J}}$]	15.1	14.7	17.6
Reference	[HMS92, Edw95]	[VLF+14]	[KAK+85, Kno97]

Table 1.1: Cavity types and their parameters that have been used in the Nb_3Sn program at Cornell. The CEBAF designed was used by the University of Wuppertal and continues to be used by Jefferson Lab. At Cornell, a single-cell TeSLA shape R&D cavity is designated LTE (e.g. LTE1-7). This table was originally published in [Pos14].

The most common characterisation of a superconducting cavity consists of measuring the quality factor Q_0 as a function of the accelerating gradient E_{acc} and bath temperature T – these are referred to as a Q vs E and Q vs T measurement. The former is used to quantify the power cost of operating a cavity at the desired gradient, and the latter is used to determine the magnitude of the two components of resistance given in Equation (1.2). An example of both of these for a conventional niobium cavity is shown in Figure 1.4. The Q is often seen to be a function of the accelerating gradient, and significant changes in Q with E are referred to as Q-slope. The suppression of negative Q-slope out to high fields has been the subject of research into niobium for many decades, and recent advances [GRS+13, GKL16, GEF+14] have even enabled the introduction of a positive Q-slope (or "anti-Q-slope").

The Q vs T in Figure 1.4 is overlaid with a BCS fit done using the SRIMP fitting code, which as been used to extract the energy gap (normalised to k_bT_c) and residual resistance R_0. A separate measurement of the cavity frequency with temperature near T_c, not shown here, is used to extract the mean free path l. This is done by measuring the frequency as $T \to T_c$, which begins to decrease

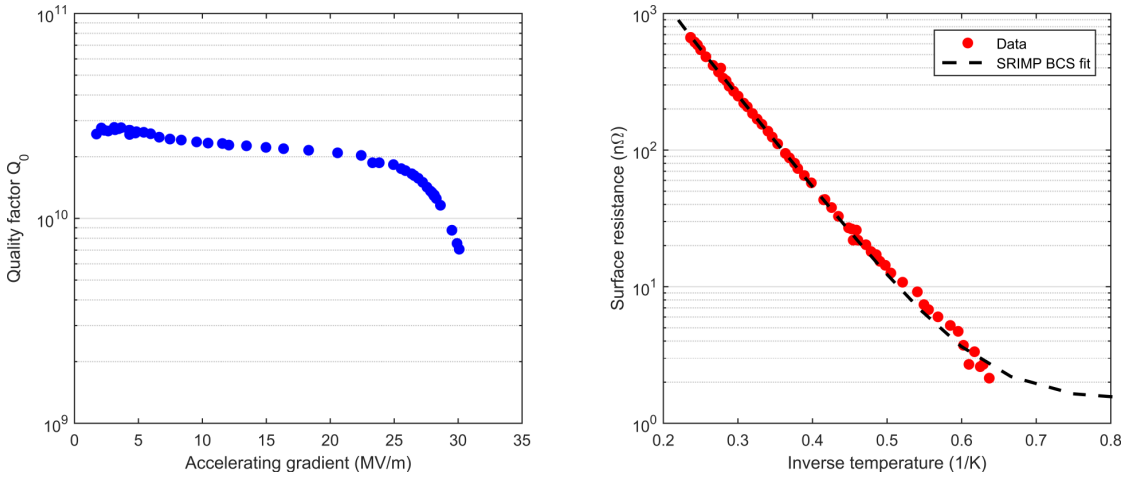

Figure 1.4: An example of the performance of a 1.3 GHz LTE-shape (see Table 1.1) cavity tested at Cornell. The Q vs E was taken at a bath temperature of 2.0 K. High field Q-slope can be seen beginning at 25 MV/m. A plot of the surface resistance against inverse temperate, obtained from a measurement of Q vs T, is shown fitted with SRIMP. Data courtesy of Peter Koufalis, Cornell University.

in a well-defined manner [Cio04, Val13]. This occurs because the penetration depth λ increases as $T \to T_c$, effectively making the cavity larger. Use of SRIMP allows the change in λ with T to be determined, from which (given an input of ξ_0 and λ_L) the mean free path l is extracted.

It can be seen in Figure 1.4 that the curve ends at a field of 30 MV/m. A number of phenomena can result in the cavity being unable to sustain the presence of the electromagnetic field within it, at which point the superconducting state is lost and the cavity is said to have "quenched". This is a third characteristic (related to the accelerating gradient) referred to as the "quench field", which is the ultimate gradient achievable in that cavity.

The vast majority of research performed on conventional niobium cavities has focussed on increasing Q while pushing the quench field to even higher values of E_{acc}. A higher Q reduces the demand on the cryogenic plant, reducing

its size and cost. A higher operating gradient reduces the length of the machine required to achieve the desired beam energy, reducing the size of the machine. Pushing these two ever higher is crucial to the future development of SRF accelerators. Although niobium has made considerable advances over the last few decades and enabled the construction of a number of extraordinary machines, at the time of writing its ultimate limits imposed by our understanding of superconducting theory are close to being achieved. The time has therefore come to invest substantially in the development of a next-generation replacement for niobium.

CHAPTER 2

NB_3SN FOR SRF CAVITIES

In this chapter we will quantify the potential improvement that the use of Nb_3Sn offers over the current convention of niobium, and briefly compare it to other comparable superconductors, some of which are also being considered for use in SRF cavities. Following this, we will summarise the material properties of Nb_3Sn as they relate to their use in SRF, which will justify the choice of fabrication method described in the next chapter.

2.1 Advantages of Nb_3Sn cavities

At the time of writing, the theoretical maximum performance of niobium is close to being achieved, in terms of both the cavity quality factor and the accelerating gradient (although not necessarily both at the same time). The improvement of techniques such as vertical electro-polishing and the introduction of methods such as impurity doping have brought about the most recent improvements and Qs of 4×10^{10} at 2.0 K and 16 MV/m [MDF+17]. However, these more recent advances in quality factor are measured in factors of 2-4, as opposed to the factors of 8-10 seen in the earlier work on niobium. Likewise, the superheating field of niobium of $\approx$ 200 mT [Val13], corresponding to a gradient of approximately 45 MV/m in an ILC cavity, places are hard limit on the maximum achievable gradient; one which has since been achieved in R&D cavities[GPSS05].

Nb_3Sn is part of a family of compound superconductors that represent the potential next step for SRF technology. These compound superconductors offer the prospect of higher transition temperatures and superheating fields, at

the expense of being more complicated to produce than a bare niobium cavity. Two other prospective candidates are niobium nitride (NbN), which is used for single-photon detection in the infra-red spectrum [STS73, KBH$^+$07, CCJ$^+$08], and magnesium diboride (MgB_2), whose transition temperature of 37 K[WPJ01] is the highest amongst the conventional superconductors. Other A15 phases of niobium also exist, including niobium-germanium (Nb_3Ge) [DR84, Dor03, PS08] and niobium-aluminum (Nb_3Al)[KTO05], although so far interest in the application of these two for SRF has been minimal.

Of these, Nb_3Sn offers the best compromise regarding ease of fabrication and improvement over conventional niobium. It has a higher transition temperature than NbN, and a more amenable phase diagram for fabrication. Unlike MgB2, it is an isotropic superconductor, and does not suffer from the high sensitivity to water of the latter[Tsu02], meaning that common post-processing methods such as a high pressure water rinse can be used to clean Nb_3Sn cavities. The transition temperature of 18 K is double that of niobium, allowing operation at twice the standard operating temperature of 2.0 K for 1.3 GHz cavities while maintaining the same quality factor which is convenient, since the temperature of atmospheric liquid helium is 4.2 K. The superheating field is likewise twice that of niobium, which would suggest that the ultimate limit for a Nb_3Sn ILC cavity would be raised to approximately 90 MV/m.

The prospect of moving the operation of 1.3 GHz cavities to an operating temperature of 4.2-4.5 K is particularly exciting when the improvement of cryomodule wall-power efficiency is considered. When considering the coefficient of performance (COP) for a refrigerator operating at these low temperatures, there is a significant decrease in the power cost per power extracted (measured

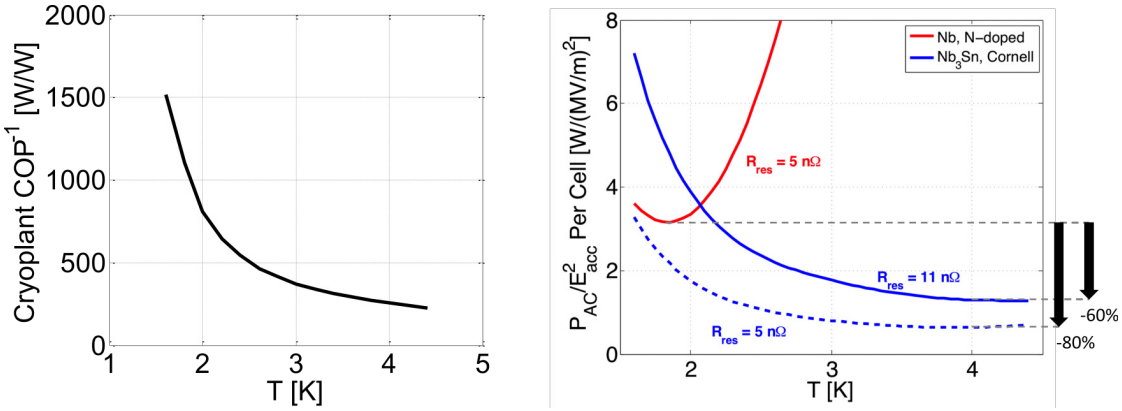

Figure 2.1: Left, the Coefficient of Performance (COP) for a cryoplant. This value indicates the amount of power that must be invested to remove 1 Watt of heating power from the cold region. Right, the power draw from grid for a cryoplant working on a 1.3 GHz TeSLA-style cavity (both niobium and Nb_3Sn-coated), normalised per cell and MV/m. The higher T_c of Nb_3Sn allows operation at 4.2 K, and the increase in cryoplant efficiency significantly reduces the power draw of the cavity.

in watts per watt) when moving from 2.0 K to 4.2 K. If we compare Nb_3Sn against niobium for a 1.3 GHz ILC-style cavity operating at 16 MV/m, and assume equal amounts of residual resistance, then Nb_3Sn offers an improvement in the wall-power efficiency of approximately 80%. This is shown in Figure 2.1.

Operation in atmospheric liquid helium offers a number of other advantages. Firstly, it reduces the complexity of the cryoplant, removing the need for the cold compressors. Secondly, operation at atmospheric pressure substantially reduces the risk of leaks causing helium contamination. This reduces the cost of maintenance of such a system, a reduction gained in addition to the decreased power expenditure.

Another exciting prospect for Nb_3Sn is low-field operation at 5 K, using a standard cryocooler. Although this would negate a significant amount of the gain in efficiency from the Nb_3Sn (due to the very low efficiency of the cry-

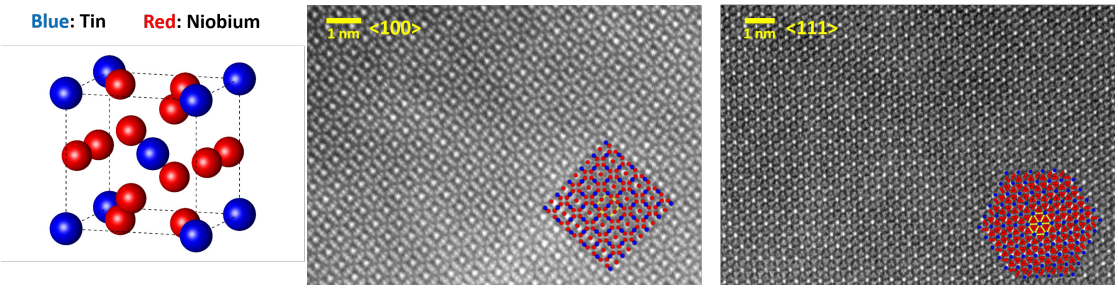

Figure 2.2: Far left, the A15 crystal structure of Nb_3Sn. Centre and right, high resolution HAADF images of the Nb_3Sn crystal lattice from samples coated at Cornell University, with the crystal structure overlaid. The images were taken down the 100 and 111 axes. HAADF images courtesy of Paul Cueva, Muller Group, Cornell University

ocooler), it would significantly reduce the footprint of the cryogenic system. Coupled with a solid-state amplifier and a small RF electron gun, this could result in the first "miniature" SRF accelerator that could provide continuous MeV electron beams for small-scale and industrial applications. Applications envisioned for such a device include the generation of high intensity X-rays for high-throughput water sterilization, extreme UV lithography, electron-beam processing of polymers including airplane runway tarmac, and medical isotope production.

2.2 Material properties of Nb_3Sn

Nb_3Sn is an intermetallic alloy of niobium and tin with an A15 structure, as shown in Figure 2.2. It has already received significant attention from the superconducting magnet community[Xu17], and the reader is encouraged to refer to the exceptional review paper on the various properties of Nb_3Sn written by A. Godeke[God06]. Here we will summarise the properties of Nb_3Sn that most pertain to its use in SRF cavities.

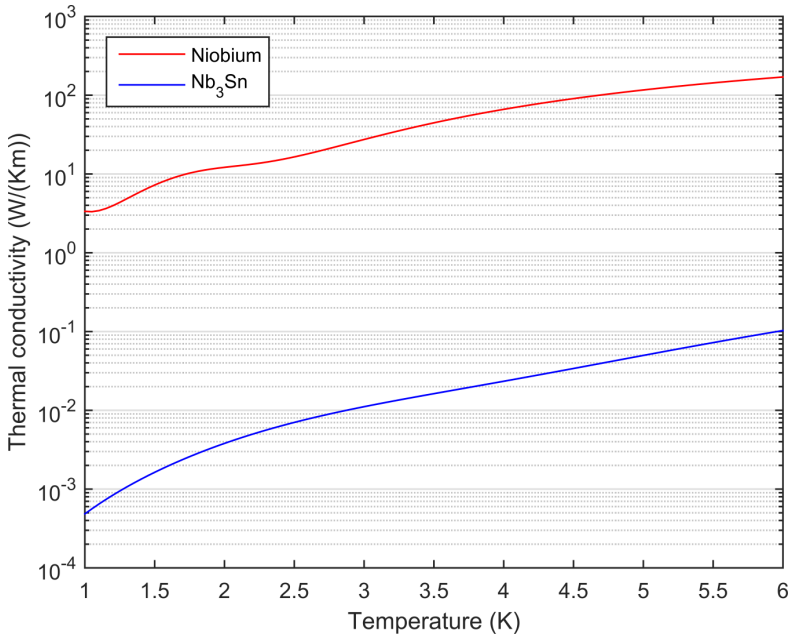

Figure 2.3: The thermal conductivity of Nb_3Sn against that of 300 RRR niobium. The considerably lower thermal conductivity of Nb_3Sn could result in issues with local or global thermal feedback and instability. Niobium data from[KB96], Nb_3Sn data from [CC64]

Mechanically, Nb_3Sn is brittle and a poor thermal conductor. Previous experiments have shown that bending of Nb_3Sn films results in cracking[Hil80]. Prior to annealing, cracks where seen to follow grain boundaries, while samples that had been annealed where found to crack along the interior of grain faces. Compared to niobium, the thermal conductivity of Nb_3Sn is approximately three orders of magnitude lower, as seen in Figure 2.3. To mitigate these issues, all fabrication methods to date focus upon creating a film of Nb_3Sn on a pre-fabricated structure with significantly higher thermal conductivity that is comparatively easier to work with, such as niobium or copper. Given the penetration depth of Nb_3Sn, a layer 2-3 microns thick is sufficient to act as a bulk superconductor for the purposes of the RF field, while still maintaining good thermal contact to the substrate and therefore the helium bath.

The phase diagram of the niobium tin system, as measured by Charlesworth et al [CMM70], is shown in Figure 2.4. The niobium-tin system allows for two other intermetallic alloys to exist beyond Nb_3Sn, namely Nb6Sn5 and NbSn2. These two, while superconducting, have transition temperatures of 2.07 K and 2.68 K, respectively [Cha66]; their presence is therefore highly undesirable when attempting to fabricate Nb_3Sn. Fortunately, above temperatures of approximately 930°C, Nb_3Sn remains as the only thermodynamically favourable alloy phase.

As can be seen in Figure 2.4, Nb_3Sn is the only species expected to be present when the atomic concentration of tin lies between 17 and 25 percent. In the phase, Nb_3Sn whose atomic-% is less than 25% is referred to as "tin-depleted, with the current understanding being that some tin sites are replaced by niobium. As the atomic concentration of tin decreases, so too do both the superconducting transition temperature and the energy gap, as can be seen in Figure 2.5. As a result of this, tin-depleted Nb_3Sn has a significantly higher BCS resistance. In the interest of ensuring the highest possible cavity performance, it is therefore necessary to ensure that only stoichiometric Nb_3Sn is produced. The Nb_3Sn-only region of the phase diagram has been re-drawn two times since the measurement by Charlesworth et al: once in 1990 by Okamoto [Oka90] and again in 2002 by Toffolon [TSGS02]. This last measurement has been repeated by Okamoto in 2003 [Oka03] and Li et al. [LDGL09] in 2009. These updates are shown in Figure 2.4. However, the measurements of material parameters from Godeke [God06] rely on the original diagram by Charlesworth, and by extension so does the majority of past and contemporary literature on Nb_3Sn cavities. Although the implications of these updates are the subject of on-going research, no results have been published at time of writing. Therefore, this work will rely

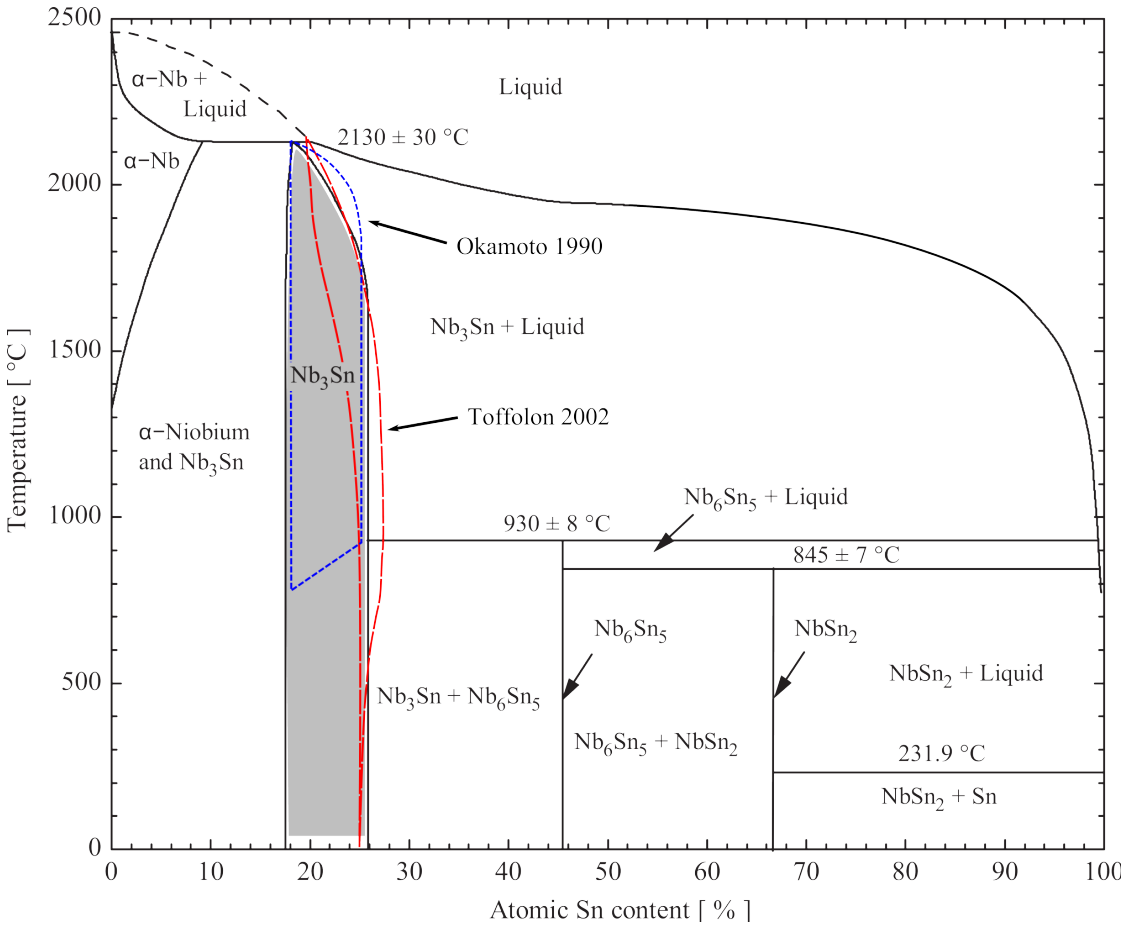

Figure 2.4: The phase diagram of the niobium-tin system, as measured by Charlesworth et al. [CMM70]. Feschotte et al [FPB79] measured a similar phase diagram in 1979. The shaded area indicates the Nb_3Sn-only region. Of note, above 930°C the other phases of Nb-Sn do not occur. The pure Nb_3Sn region was re-drawn by Okamoto [Oka90] in 1990 (shown in blue), and then again by Toffolon [TSGS02] in 2002 (shown in red). This last measurement was confirmed by Okamoto [Oka03] in 2003 and by Li et al. [LDGL09] in 2009. This figure is adapted from the one originally published in [God06].

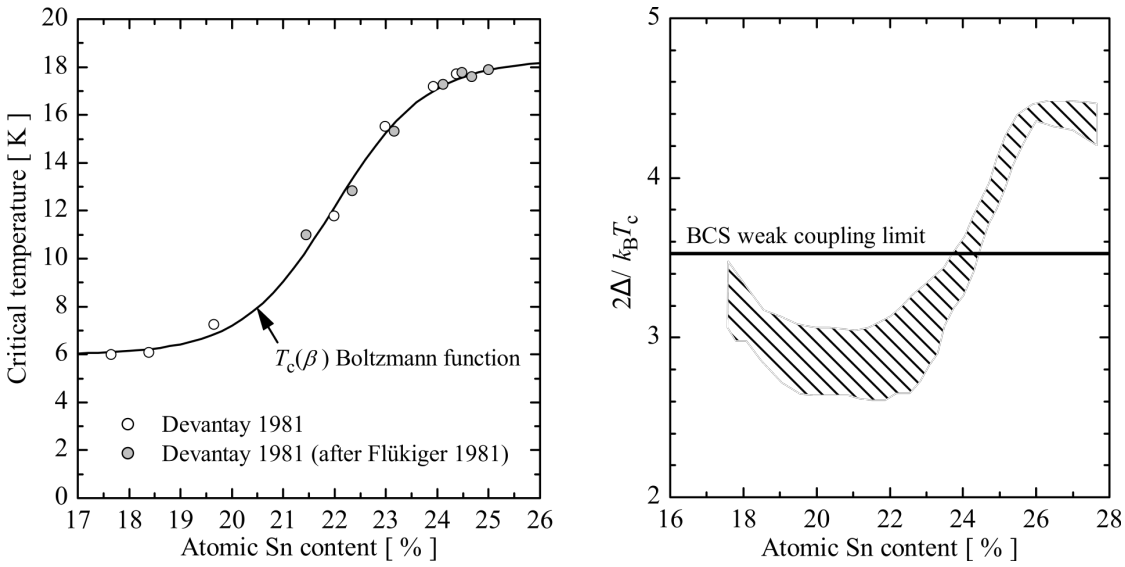

Figure 2.5: Left, the superconducting transition temperature of Nb_3Sn as a function of the atomic-% tin. The data is fitted with a Boltzmann function. On the right, the normalised energy gap as a function of the atomic-% tin, indicating that as the crystal becomes tin-depleted the superconductor moves from a strongly-coupled BCS superconductor to a weak one. This figure is adapted from those shown in [God06], with references to [DJD+81, MZRB79].

on the original diagram by Charlesworth.

CHAPTER 3

FABRICATION OF NB_3SN CAVITIES

In this chapter we will cover a history of the fabrication of Nb_3Sn as it pertains to SRF cavities, and illustrate some of the results from previous programs. Following this we will go into more detail regarding the workings of the coating furnace used at Cornell University, and describe the standard coating process used throughout this work. This chapter will end with a description of the Nb_3Sn layer post-coating, before it is sent for testing.

3.1 History of Nb_3Sn fabrication for SRF cavities

The superconductivity of Nb_3Sn was discovered in 1954 [MGGC54], a decade before the first demonstration of electron acceleration in a lead SRF cavity at Stanford University [SWPF65]. The first published attempts at adapting Nb_3Sn for use in SRF cavities began at Siemens AG in Erlangen, Germany, during the 1970s [HMP+75]. They performed some of the groundbreaking work on Nb_3Sn, producing 10 GHz TE and TM-mode cavities using the vapour diffusion method of Saur and Wurm [SW62]. Their X-band TE cavities, although not applicable to electron acceleration, have demonstrated the highest CW surface fields to date obtained in an Nb_3Sn cavity, up to 106 mT. Siemens performed more than 50 coatings of such TE cavities, allowing the collection of statistics regarding quality factor and quench field. An example of the performance of a few select cavities is shown in Figure 3.1. The quench field of the cavities was found to be normally distributed about a peak surface field of 60 mT, as also shown in Figure 3.1.

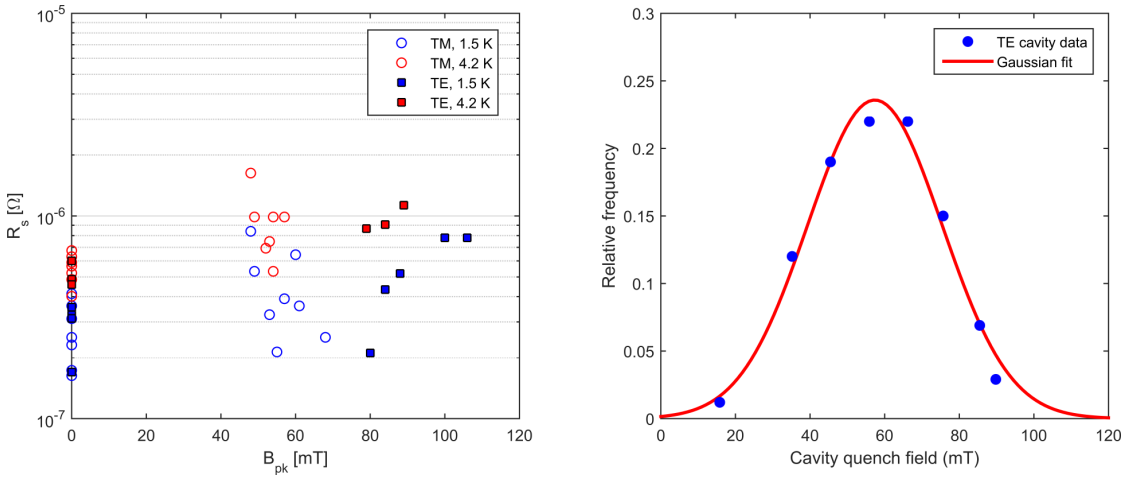

Figure 3.1: Left, an example of some of the best results from the 10 GHz cavities used in the Siemens AG Nb_3Sn program. Values of Q were given only at zero field and the quench field. This figure was originally published in [Pos14] with data from [HMP+77, Hil76, HKP+81]. Right, the distribution of quench fields at 4.2 K seen in all Siemens TE-mode cavities. A Gaussian distribution is fitted. This figures is adapted from data in [HKP+81].

The fabrication of Nb_3Sn cavities using the vapour diffusion method involves evaporating tin to form a vapour, and exposing a niobium substrate to this gas. The niobium substrate is heated to a temperature high enough such that, upon deposition and diffusion of the tin into the niobium, it will react to form Nb_3Sn. This method mitigates a number of potential issues: firstly, it allows the structure to be fabricated entirely from niobium, a material whose properties regarding machining, welding, etc. are already well known, reserving the coating to the final step. Fabrication of cavities directly from Nb_3Sn, in the manner of niobium, would be impossible due to the brittle nature of former. Secondly, the layer is only a few microns thick, which is a bulk coating from the perspective of the RF field (approximately 20-30 times the superconducting penetration depth), but is thin enough to suppress issues of global thermal instability related to the considerably lower thermal conductivity of Nb_3Sn [DHL17].

There are a number of steps common to all past and present applications of the vapour diffusion technique. The process is carried out in a specially adapted ultra-high vacuum (UHV) furnace that contains a reaction chamber, within which are situated the niobium part to be coated and a crucible filled with high purity tin. If one is being used, a nucleation agent (commonly $SnCl_2$ or SnF_2) is placed in a crucible near the tin source. Nucleation may also be aided by electrolytically growing the niobium oxide layer prior to coating, a process referred to as pre-anodisation [Hil80]. Depending on the design of the furnace, the reaction chamber may be part of a vacuum system separate from that of the furnace proper, and the option may be available to pump (or not) on the reaction chamber during the coating proper.

The temperature profile of any given coating consists of five separate stages common to all coatings to date, with some extra options depending on furnace design. An example of a temperature profile used at Cornell University is shown in Figure 3.2, with the different stages marked. These are, in order:

1. A degas stage. The furnace is taken to a temperature between 100°C and 200°C and held at this temperature, commonly for a period of 24-48 hours. During this time the active pumping on the reaction chamber removes residual moisture and any species that may outgas from the chamber or niobium part. Once the degas process is complete, the operator may decide to seal the reaction chamber from active pumping.
2. A nucleation stage. The furnace is taken to an intermediate temperature, during which time nucleation sites (small droplets of tin) are formed on the surface of the niobium part. This can be achieved using pre-anodisation, the introduction of a temperature gradient between the cavity

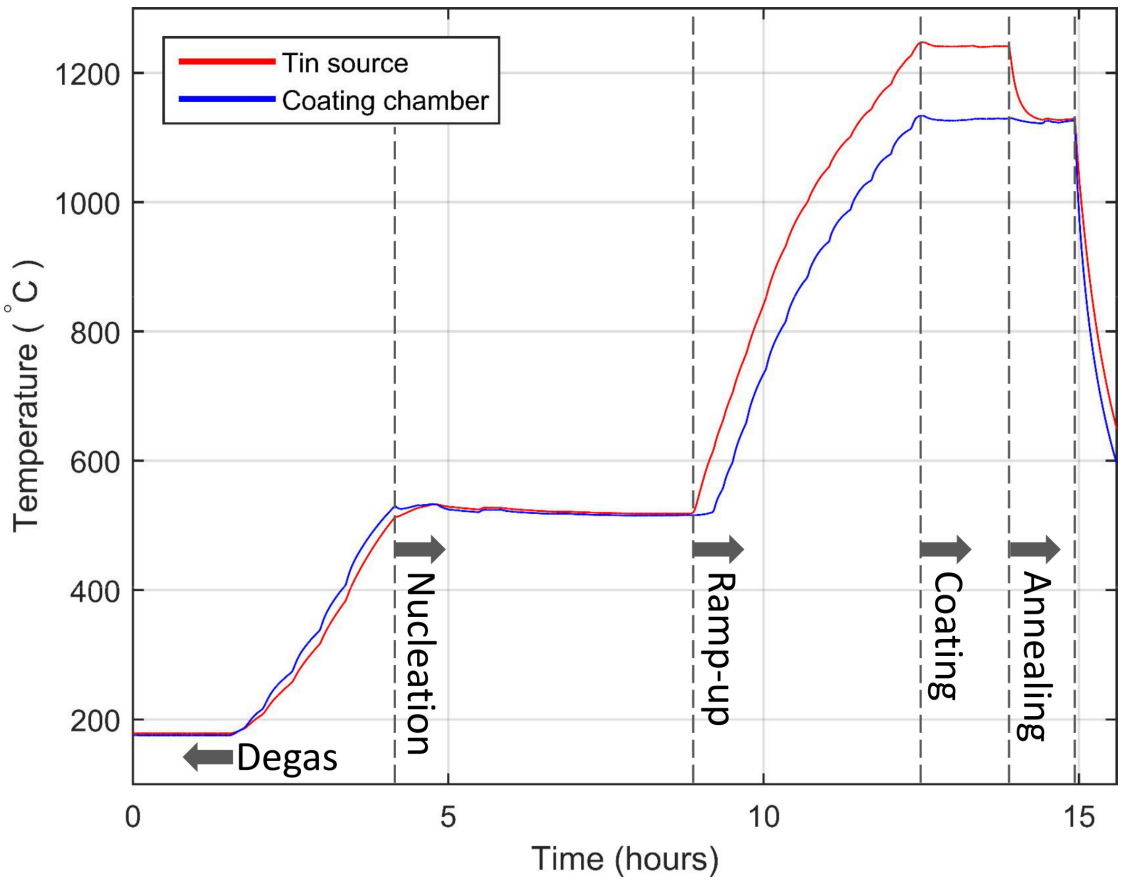

Figure 3.2: The standard Cornell coating recipe at time of writing. The major steps are annotated, although the 24-hour degas stage is not shown. The different stages are described in the text.

and the tin source (as performed at Siemens AG [dHHR+78]), and/or the use of a nucleation agent such as SnF_2 or $SnCl_2$. The use of a nucleation agent offers an advantage over the use of pre-anodisation in that it does not reduce the RRR of the substrate from the oxide migrating into the bulk during coating. The temperature may be held at this intermediate stage for quite some time, to allow the nucleation to develop fully over the entire area to be coated.

3. A ramp-up to the coating temperature. During this stage, if one is present, the secondary hot-zone surrounding the tin source can be activated, creating a temperature gradient between tin source and the reaction chamber.

The secondary heater may be activated at the beginning, during, or at the end of the ramp-up.

4. The coating stage. The cavity is held at a temperature above 950°C, at which point the low-T_c phases of Nb-Sn (Nb6Sn5 and NbSn2) are thermodynamically unfavourable. If a tin source heater is present, the temperature gradient between source and reaction chamber is maintained constant for the duration of this step. It is at this stage that the majority of the Nb_3Sn layer growth occurs.

5. An annealing stage. If a separate source heater is not present, this step is often considered part of the coating stage. If a source temperature gradient is being used, the secondary heater is turned off to allow the source to cool to the same temperature or below that of the reaction chamber (depending on the furnace design). This significantly reduces the input of new tin vapour into the reaction, giving the remaining tin time to react. During this step the cavity is maintained at a temperature above 950°C. Once complete, the furnace is turned off and allowed to cool naturally by radiation and conduction until furnace is cool enough to be let up to atmospheric pressure and opened.

Not all of these stages may be used in every coating for instance, in furnace designs that do not use a secondary hot-zone for the source, stages 4 and 5 will be combined into one coating stage (unless an annealing stage is carried out at a lower chamber temperature). However, almost every coating to date can be classified in terms of the parameters for these five stages.

At Siemens AG, coating of 10 GHz niobium cavities was carried out inside a quartz reaction chamber, in which a crucible containing high purity tin

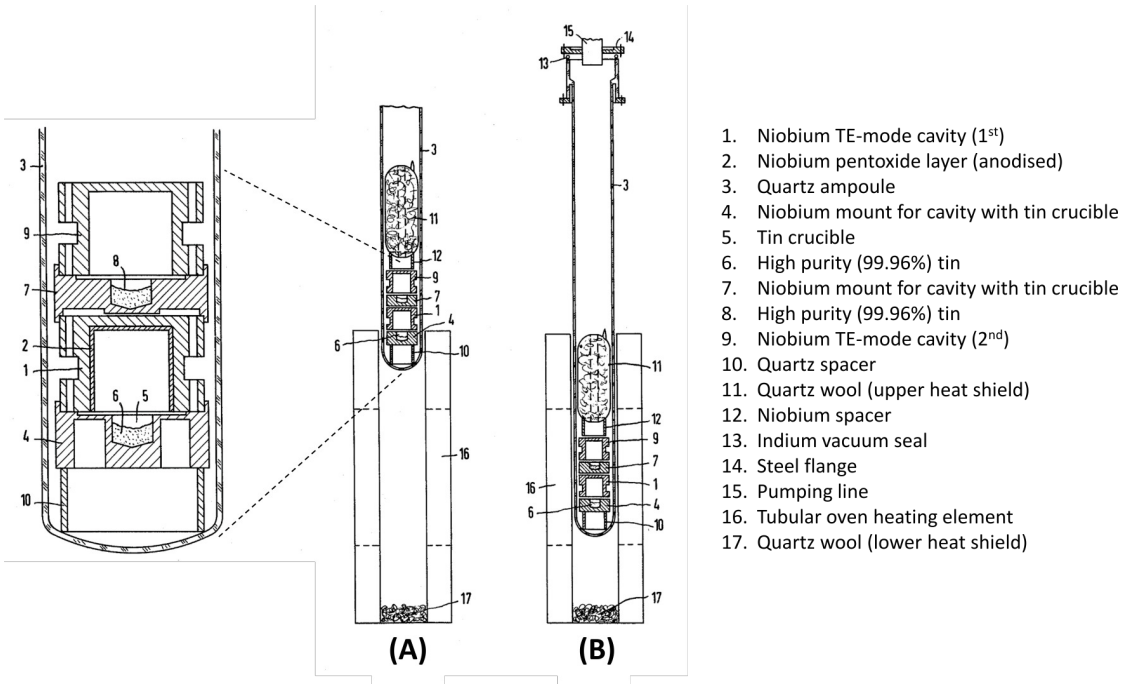

Figure 3.3: A schematic of the Siemens AG coating furnace, showing the two configuration of the furnace, (A) and (B), corresponding to the indicated regions in the coating recipe shown in Figure 3.4. This figure is adapted from images shown in [dHHR+78].

and the niobium part to be coated were placed. However, first results demonstrated that at the high temperatures involved the quartz was contaminating the Nb_3Sn[HMP+75], and the coating method was altered. All subsequent coatings were performed with the cavity serving as the reaction chamber, with only niobium surfaces. A diagram of the Siemens coating apparatus is shown in Figure 3.3.

Coating at Siemens was carried out at a reaction temperature of 1050°C [dHHR+78]. Early coatings were plagued by regions of niobium that appeared essentially uncoated [Hil80]; the suspicion was that uneven nucleation was preventing uniform coverage of the Nb_3Sn layer. This issue was resolved through the use of (separately or combined):

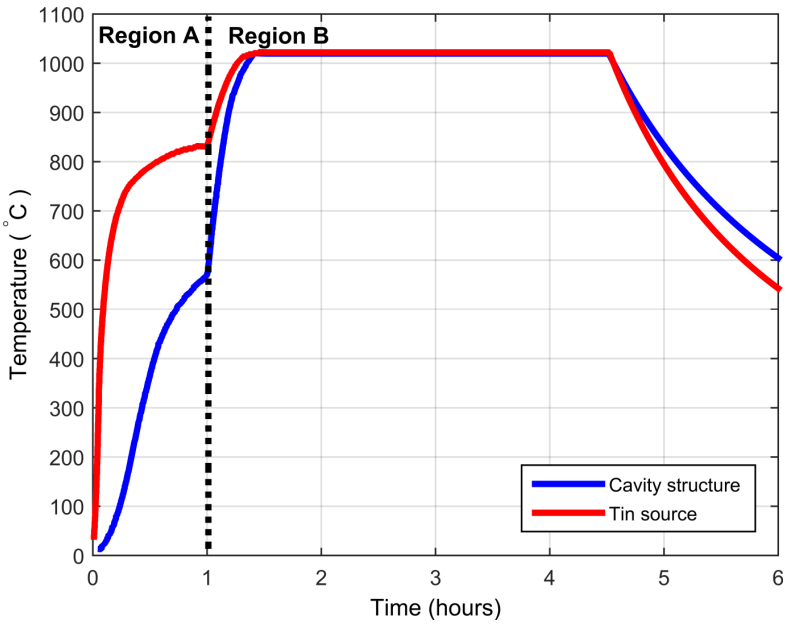

Figure 3.4: An example Siemens coating recipe. The two regions correspond to the two different furnace configurations, (A) and (B), shown in Figure 3.3. Although a 5-hour coating is shown, Siemens AG experiment with a number of different coating lengths. This figure is adapted from data given in [dHHR+78].

- A temperature gradient between the tin source and the cavity during the initial temperature ramp-up, as given in the temperature profile shown in Figure 3.4,
- Growing the oxide layer of the niobium substrate prior to coating using electrolytic anodization, and
- The use of a nucleation agent such as $SnCl_2$ or SnF_2 to cover the niobium substrate with tin nucleation sites prior to reaching coating temperature.

Following these changes, the performance demonstrated in Figures 3.1 was obtained.

Following shortly after the beginning of the Siemens research program, similar programs began at Kernforschungszentrum Karlsruhe (KfK) and the Uni-

versity of Wuppertal [HGM+84]. The latter included collaboration with Thomas Jefferson National Laboratory [BKM+97], and resulted in the production of the first Nb_3Sn 1.5 GHz multi-cell cavities. With the transition to larger cavities, a major change that was made was the introduction of a second hot-zone surrounding the tin source. This allowed the temperature gradient between the source and the reaction chamber to be altered in a more controlled manner than was previously possible with the smaller Siemens furnace design. A schematic of the Wuppertal 1 GHz coating furnace is shown in Figure 3.5, showing the location of the separate hot-zone containing the tin source.

In a manner similar to the Siemens coatings, Wuppertal introduced a temperature gradient during the ramp-up to temperature, as seen in an example of their coating profile shown in Figure 3.6. However, this temperature gradient was maintained during the coating, in order to ensure an adequate supply of tin for the larger cavity. The tin source was powered down before the cavity, allowing the unreacted tin to diffuse before turning the furnace off and allowing the cavity to cool by radiation.

The cavities coated at Wuppertal were considerably larger than those coated at Siemens AG, including 1.5 GHz cavities of the CEBAF [KAK+85] design. These cavities achieved exceptional quality factors of above 10^{10} at fields of 2-5 MV/m [MKM96] however, at higher fields they saw the onset of a drastic Q-slope that brought the quality factor down to below $Q = 10^9$ at 15 MV/m. An example of this performance is shown in Figure 3.7. At the time, this Q-slope was feared to be fundamental to Nb_3Sn coated cavities, as the field at which the slope onset corresponded to the expected range of the lower critical field H_{c1} of Nb_3Sn. This created the suspicion that the Q-slope was being caused by

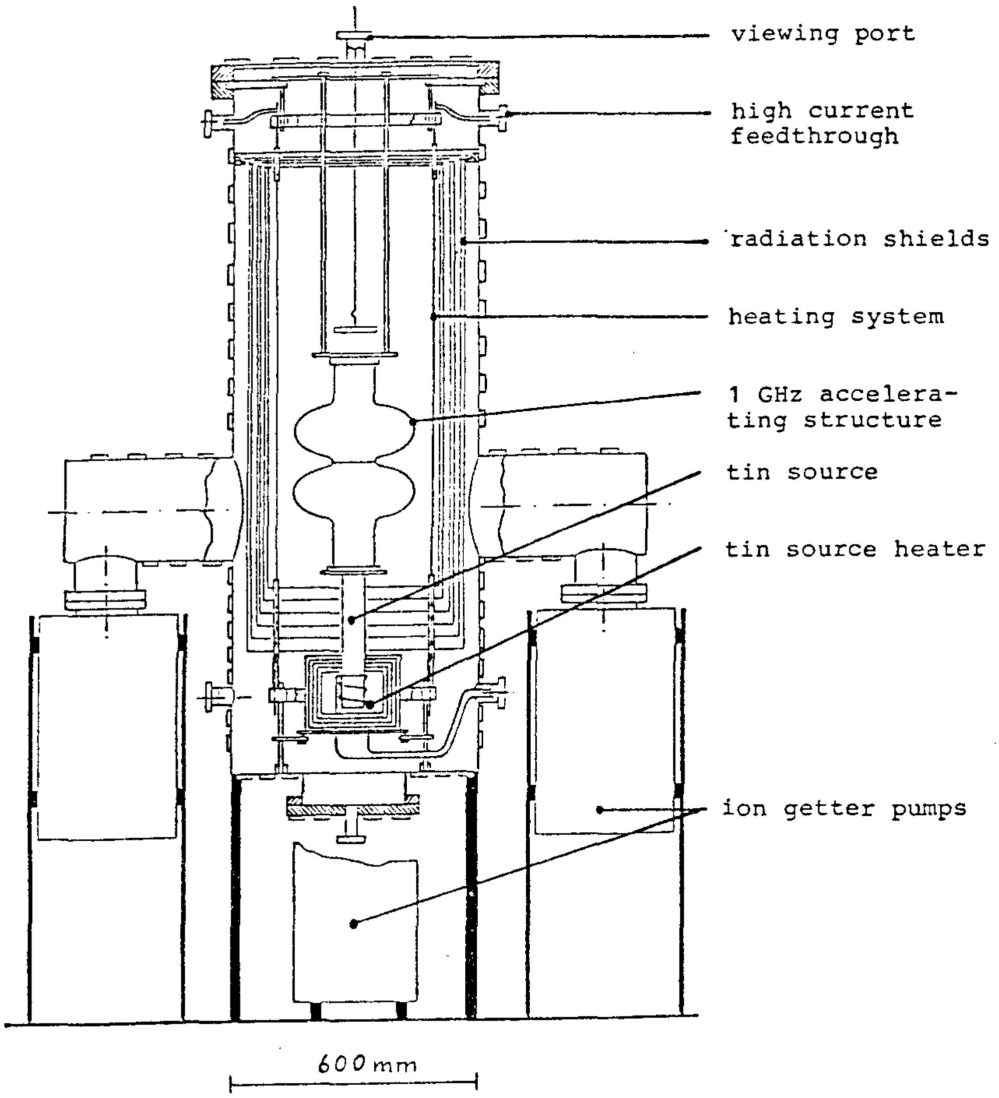

Figure 3.5: Schematic of the furnace used for coating 1 GHz cavities coated at the University of Wuppertal. In contrast to the Siemens design, the cavity and source are kept in separate hot-zones. This image is reproduced from [PHK+88].

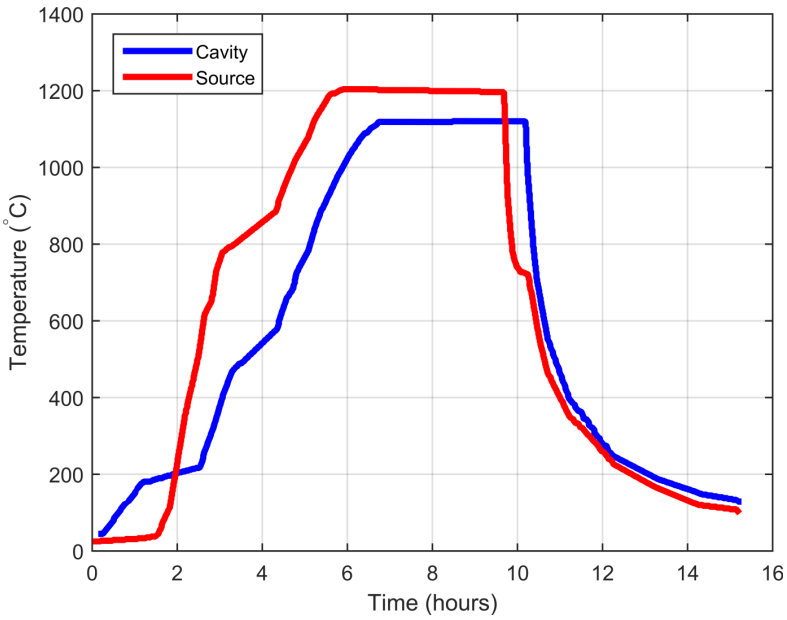

Figure 3.6: An example of the coating recipe used at the University of Wuppertal. The separate hot-zone allowed the source to be operated at a temperature both above and below that of the cavity. This image is adapted from data found in [Pei83].

magnetic vortices entering above this field and causing increased losses.

Studies on SRF cavities were also carried out from the 1970s through to the 1990s at CERN, SLAC, and at Cornell University [AMC86, ABHT83, Sti78]. By the turn of 2000, however, the majority of the programs including the major players of Siemens AG and the University of Wuppertal had either ended or were winding down, no longer producing new cavity coatings. Development of Nb_3Sn cavities using the vapour diffusion method was put on hold during first decade of the new millennium, until in 2009 a new program was started at Cornell University [PLX11, PL11]. This program was based on a coating furnace whose design was adapted from that used at the University of Wuppertal, and whose operation will be described in detail in the next section. The 1.3 GHz single-cell cavities produced on this program did not show Q-slope previously seen at Wuppertal, abating the fear that H_{c1} was a fundamental limitation for

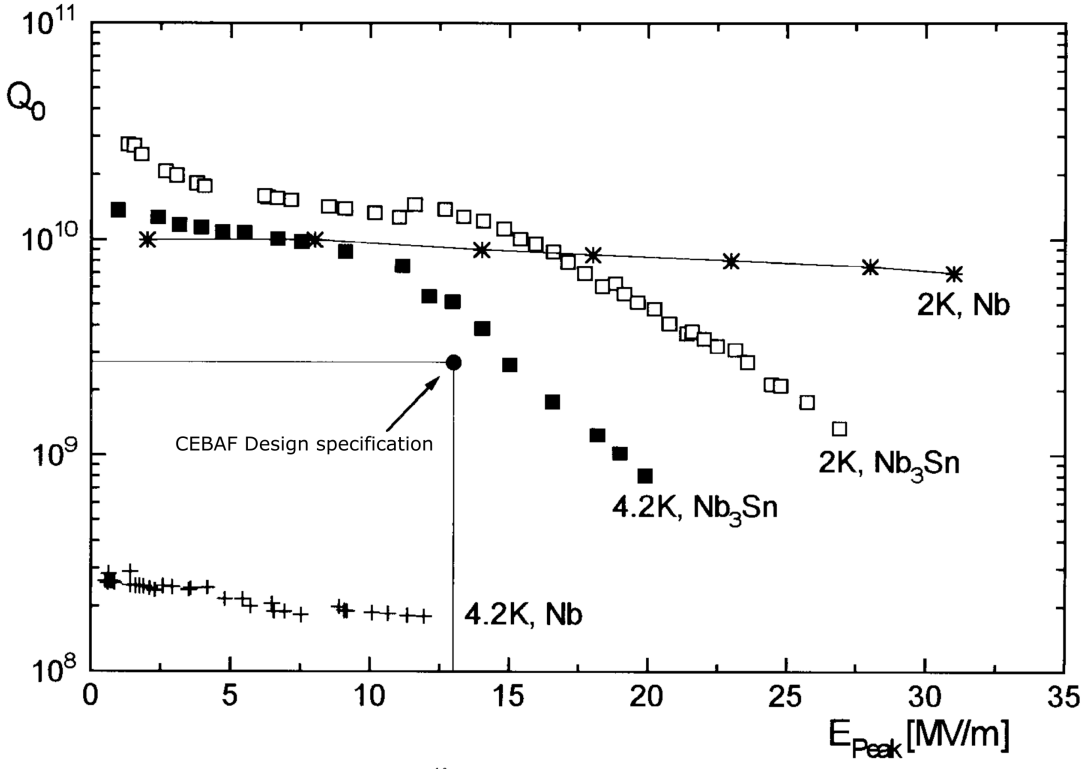

Figure 3.7: Characteristic performance of 1.5 GHz Nb_3Sn-coated cavities produced at Wuppertal. The Q-slope see at medium fields and above is very characteristic for cavities of this era, and it was suspected that this behaviour was fundamental to Nb_3Sn. This figure is reproduced from [MKM96]. Note that the gradient given is the peak electric surface field – this can be converted to accelerating gradient or peak surface magnetic field using the constants given for CEBAF cavities in Table 1.1 (e.g. $E_{pk} = 20$ MV/m is equivalent to $E_{acc} = 11.4$ MV/m).

Type-II superconductors [BKM+97]. This result generated a resurgence in interest for Nb_3Sn as an alternative to niobium. In 2011, a program began to coat cavities with Nb_3Sn at Thomas Jefferson National Laboratory [EKR+15] using an adaption of the Siemens process. More recently, this furnace has been upgraded to coat 5-cell CEBAF cavities complete with endgroups. In 2014, a program was started at Fermi National Accelerator Laboratory to adapt a furnace for the coating of 1.3 GHz 9-cell TeSLA cavities [PMRT15]. As of 2017, this program has completed commissioning of the furnace, which is an adaption of the Cor-

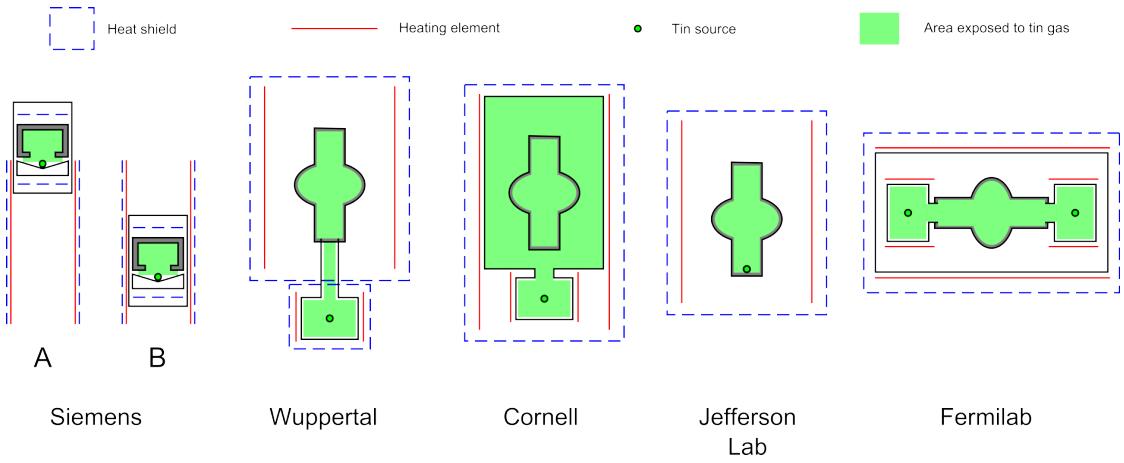

Figure 3.8: Simplified schematics summarising the operation of the major coating furnace designs to date. The Jefferson Laboratory furnace is an adaption of the Siemens design, and the Fermi National Laboratory furnace is a horizontal variant of the Cornell design, which is in itself adapted from the Wuppertal furnace.

nell design, and has successfully coated 1.3 GHz single-cells. A diagram that summarises the furnace designs used up to the present day is shown in Figure 3.8.

Other programs to produce Nb_3Sn coatings using methods besides vapour diffusion have also made continuing process throughout the last decade, although they have received comparatively less attention and investment. These include methods such as chemical vapour deposition (CVD), liquid tin dipping, multilayer sputtering, mechanical plating, electron beam coevaporation, bronze processing, and electrodeposition [RSI+16, BBR+16, Kri12, Mit10, DRR+09, RDS+09, DKR+06, CRZ+06, Ham75, Hak88, HHO74]. These alternative methods could potentially provide a number of advantages over the vapour diffusion process, including reduction in material costs (using a substrate of copper), and potentially more control over layer stoichiometry. However, they are also more complex, and can suffer from the formation of undesirable phases, coating non-uniformity, high surface roughness, and very small grain sizes

(which have been associated with weak link grain boundary effects [PCH+99]). At time of writing, none of these methods have achieved cavity quality factors or gradients close to those of cavities produced by the vapour diffusion method. However, progress continues to be made in all areas of Nb_3Sn production, and nowhere is it written that vapour diffusion is the ultimate method of producing Nb_3Sn cavities.

3.2 The Cornell Nb_3Sn coating furnace

The Cornell Nb_3Sn coating furnace is an adaption of the Wuppertal design seen in Figure 3.5. However, instead of having the tin source as a separate hot-zone connected by a tube, the source hot-zone lies within the primary hot-zone [PHLX12, Pos14]. This means that the source is comparatively closer to the cavity; however, it does mean that the source cannot be cooler than the cavity. It is located in the cleanroom facility at Newman Laboratory on Cornell's campus.

A diagram of the coating furnace is shown in Figure 3.9. The furnace itself was originally designed as a baking furnace for degassing and purification of niobium cavities and assembled in-house at Cornell in the 1980s. A cylindrical chamber is mounted inside the furnace, within which cavities are placed vertically (as opposed to more recent furnace designs in which they lie on their side). The original baking insert was removed, and replaced with a specially designed coating insert.

The coating insert is a niobium cylinder, with a niobium base at one end, and a steel flange at the other for connection to the main furnace. The niobium to steel transition is done using a copper braze located a few centimetres from the

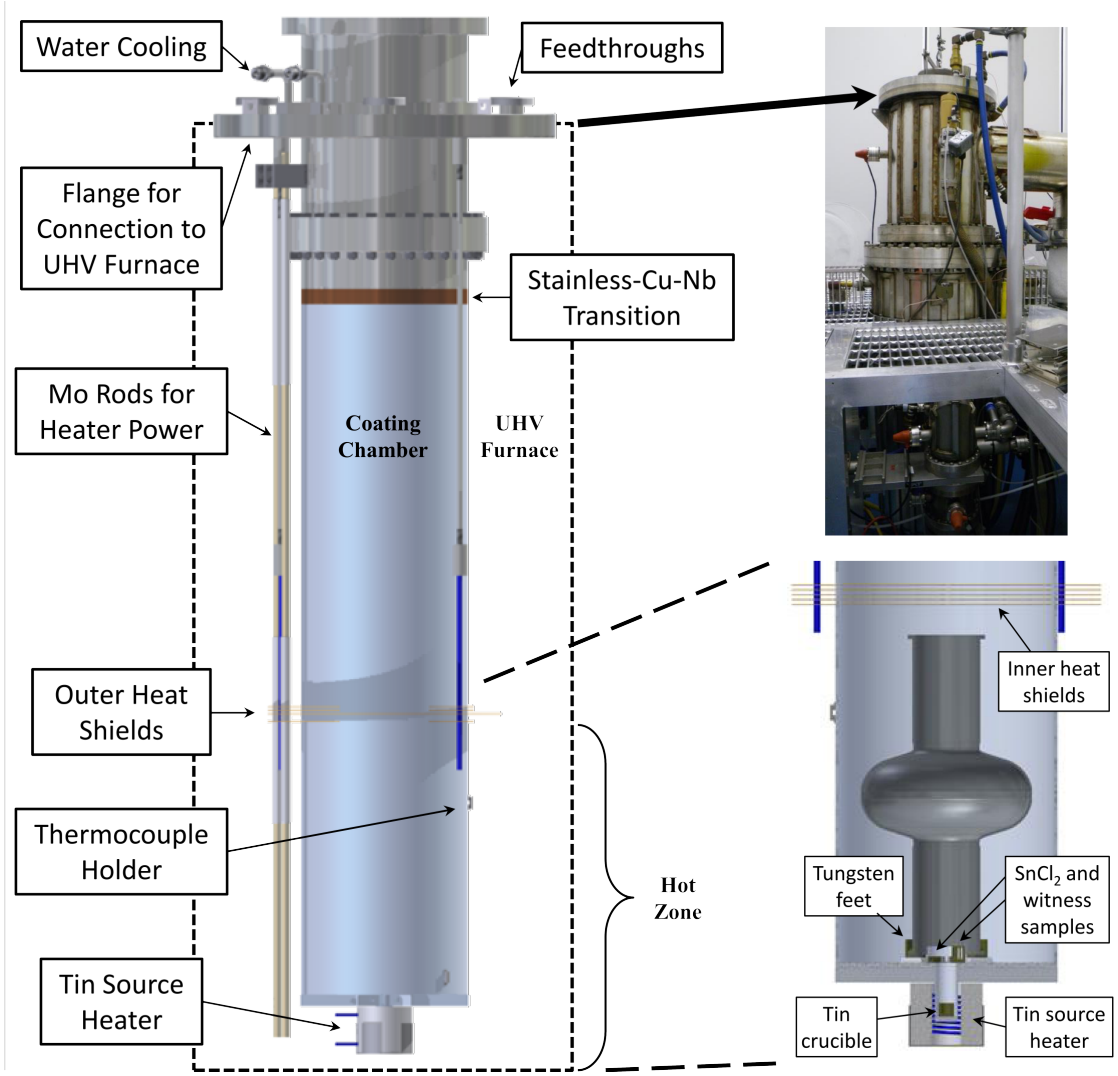

Figure 3.9: A diagram showing the Cornell University coating insert, which is housed inside an ultra-high vacuum furnace (shown top right) located in the Newman laboratory cleanroom. The tin source is located at the bottom of the insert, surrounded by a secondary heater that allows the source to be held at a temperature above that of the cavity. The inside of the insert, shown bottom right, shows a single-cell TeSLA-style cavity placed inside the coating insert. This figure is adapted from material originally published in [Pos14].

steel flange. Once in place, the steel flange serves as the opening to the furnace, into which cavities and samples can be lowered. A steel plate with a vacuum connection is bolted on top to seal the chamber. This vacuum connection links the chamber and furnace vacuum spaces, and can be closed using a manual valve on the top of the furnace. This allows the chamber to be completely sealed during coating.

In the centre of the base of the niobium cylinder is a small alcove, which sticks out below the length of the cylinder, as seen in Figure 3.9. Inside this alcove, lowered from the top of the furnace, is placed the tungsten crucible filled with tin that will act as the tin source. Surrounding this alcove from the outside of the cylinder is the secondary heater, whose power connections run up the outside of the insert and through a vacuum feedthrough on the upper flange. The secondary heater is encased in a white ceramic heat shield, inside of which are located the C-type thermocouples for measuring the source temperature. The connections for these also run outside the insert and up through a vacuum feedthrough on the top of the furnace.

On the outside of the insert, at the height of the equator of a single-cell 1.3 GHz cavity when placed in the furnace insert, are placed two more C-type thermocouples. These act as a temperature measurement for the furnace chamber and its contents. These thermocouple connections follow those from the source up through a feedthrough at the top of the furnace. From here, extension cables carry these four wires (2 for the chamber, 2 for the source) from inside the cleanroom to a data acquisition box located near the furnace control computer. Each thermocouple is measured using an isolated channel - this is necessary as accidental grounding of the thermocouples can result in significant DC bias

relative to each other.

Power for the primary heater is delivered from a high power DC power supply originally intended for welding. The power supply provides a direct measurement of the voltage provided by the power supply, which is proportional to a 0-10 volt control input, and a voltage measurement of a shunt resistor provides a measurement of the current through the main furnace heating filaments. These measurements also provide information regarding dissipated power and filament resistance, useful for monitoring any ageing or issues with the furnace filaments. The secondary heater for the tin source is powered from a constant-current silicon control rectifier (SCR) power supply, which sends a chopped 60 Hz AC drive to the heater. The RMS current is proportional to a 0-10 volt signal provided by the control system. The RMS voltage is measured directly across the connections to the secondary heater at the top of the furnace, and use of a current transformer provides a measurement of the RMS current through the secondary heater. From this, the dissipated power and heater coil resistance are extrapolated.

Measurements of the pressure in the furnace filament zone are provided by hot filament ion (HFIG) gauges. A separate measurement of the pressure in the coating chamber is provided by a cold cathode (CCG) gauge, which is sealed off from the chamber alongside the vacuum pumps during the coating to avoid contamination from the nucleation agent or tin vapour. Therefore, the pressure during the coating is unknown. The furnace is pumped on using a combination of a turbo-molecular pump (backed by a roughing pump) and a cryo-pump, with cold pressures post-degas being in the low 10^{-8} Torr. During degas, the pressure in the chamber can go as high as the low 10^{-5} Torr region, and degas is

Figure 3.10: The control system for the Cornell coating furnace. Pumps and valves are operated from the central rack, which also hosts the power supply interlock. Once active, the furnace is controlled from the computer on the left. The furnace can be seen through the cleanroom door on the right.

considered complete when pressures at 180°C fall into the low 10^{-6} range.

The majority of the furnace systems are monitored and managed from a combination of a control rack and a PC located just outside the cleanroom. A photo of this system is shown in Figure 3.10. A MatLab control program monitors the major parameters of the furnace and allows for operation via a remote login. A recent addition to the furnace monitoring program is a dead reckoning system for deducing the amount of tin remaining in the crucible during coating. The vapour pressure of tin and tin chloride are known from literature [Pei83, MO87], and the mean free path can be calculated using [Loe04]

$$l = \frac{k_b T}{\sqrt{(2)}\pi d^2 p}\,, \tag{3.1}$$

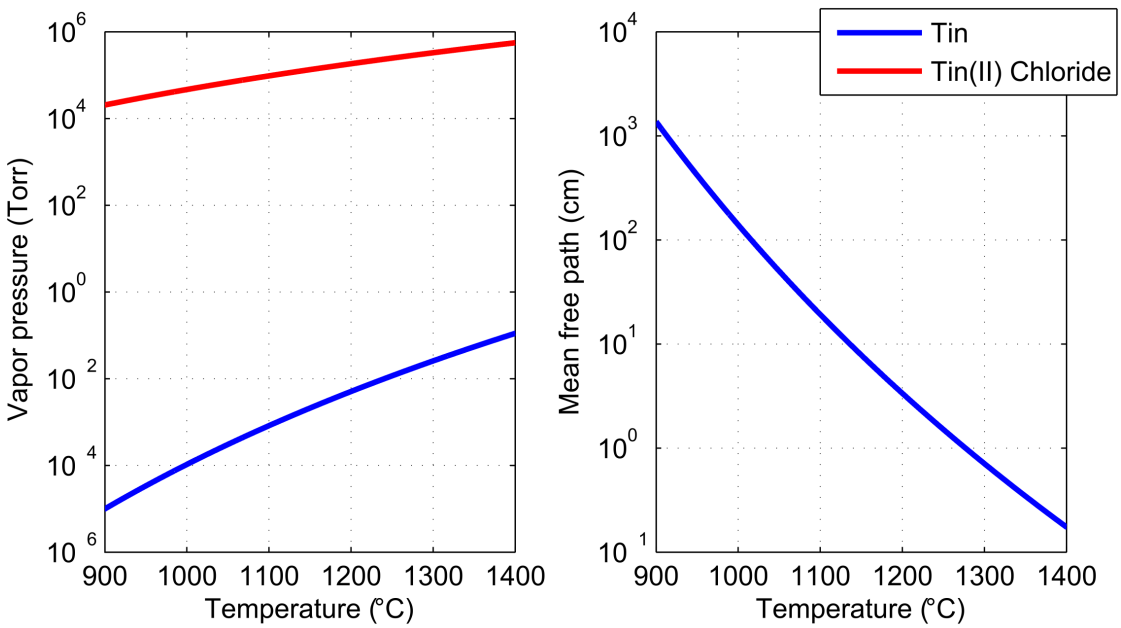

Figure 3.11: Left, the vapour pressure of tin and tin chloride as a function of temperature. Right, the mean free path of tin as calculated from Equation (3.1). Vapour pressure data from [Pei83, MO87].

where T is the temperature of the gas, d the Van Der Waal's diameter of the atom (450 pm in the case of tin), and p the vapor pressure of the gas. The vapour pressure and mean free path of tin and tin chloride are shown in Figure 3.11. Given this, we can surmise that for a 1.3 GHz single-cell cavity with an iris diameter of approximately 7 cm, a tin vapour temperature of above 1150°C is necessary to ensure a uniform coating. Knowing the temperature of the tin source, we can use the Langmuir formula for evaporation to deduce the evaporation rate [Meu58],

$$\frac{dM}{dt} = Ap\sqrt{\frac{m}{2\pi k_b T}}, \tag{3.2}$$

where M is the mass of tin in the crucible, A is the area of the mouth of the tin source, and m is the mass of a tin molecule. Since the temperature of the source

is known at all times during the coating, and the initial amount of tin is measured prior to coating, the amount of tin remaining can be deduced from this evaporation rate. The extrapolated final amount can be compared to the measured final amount post coating. To test the accuracy of the evaporation rate, the data from 23 coatings (specifically chosen from all coatings for being the ones in which tin remained in the crucible after coating) was used to generate an estimate for the amount of tin consumed during the coating. This gives an extrapolated change in mass of the crucible, δm_{extrap}. This was compared to the measured change in mass of the crucible from measurements before and after coating, giving a measured value δm_{meas}. The relative accuracy of the extrapolation, $\sigma = \delta m_{\text{meas}}/\delta m_{\text{extrap}} - 1$, is plotted for the 23 coatings in Figure 3.12. The average accuracy of the extrapolated amount of tin consumed was found to be ±6% compared to the actual change in the weight of the crucible during coating.

The furnace insert can accommodate a variety of items for coating. The hot-zone of the furnace extends up approximately half the height of the furnace, with separate heat shields being lowered into the reaction chamber (as seen in Figure 3.9) to complete the hot-zone enclosure. The hot-zone is large enough to accommodate a 1.3 GHz single-cell ILC-style cavity, which sits on three tungsten feet arranged in a circular fashion around the base of the furnace (these are necessary to prevent the cavity flange from welding to the chamber). Samples can either be hung from the heat shields using niobium wire, or placed in tungsten sample holders and seated near the tin source. Up to two samples can be seated near the source, alongside the tungsten boat containing the $SnCl_2$ nucleation agent. Samples and other items weighing up to 1 kg can be hung from the heatshields, and past coatings have included items such as elliptical samples for muon spin rotation measurements [JAA+17], optical coupling cavities [YSBS15],

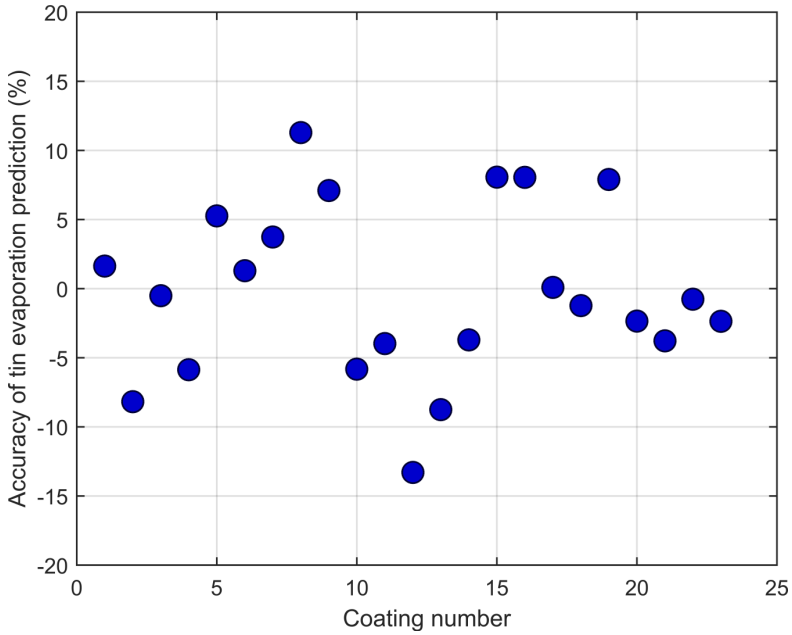

Figure 3.12: Accuracy of the prediction for the amount of tin consumed during a coating from the evaporation calculation of Equation (3.2), as determined by the error relative to the measured change of the weight of the crucible after coating. The scatter indicates a typical accuracy of ±6%.

and scanning tunneling microscopy tips.

3.3 Standard coating procedure

The standard coating procedure, at time of writing, consists of 5 hours of nucleation, 1.5 hours of coating, and 1 hour of annealing. This differs from the coating used previously in [Pos14], and uses a larger temperature gradient between the tin source and cavity during coating (ΔT = 130°C as opposed to 100°C). The standard coating cycle described in this section is the product of a study of the impact the recipe parameters on the performance of the cavity [HGK+15, HLM16]. The results of this study showed that the best performance was obtained for a coating in which the ΔT was as high as could be

safely achieved in the furnace, and an amount of tin between 1.4 and 1.8 g was consumed. A comparatively short annealing period of 1 hour was chosen, in light of the observation that cavities that were subject to 6 hours or more of annealing (or an elevated chamber temperature during the annealing period) demonstrated a higher residual resistance than cavities that had only received 0.5-1 hour of annealing. The full coating cycle takes one week, when all the procedures are considered (loading, pump-down, coating, let-up, and unloading).

Following the previous coating, the cavity is let up to atmosphere using ultra-high purity nitrogen gas. The let up is done slowly over the course of 12 hours using a mass flow controller (MFC) introducing nitrogen at a rate of 10 SCCM. This is done to suppress turbulence in the piping that might introduce particles and contaminants into the furnace chamber.

Once the furnace is at positive pressure, the letup is stopped and the vacuum connection between the reaction chamber and furnace filament space is closed. This keeps the furnace space at slight positive pressure while the reaction chamber is opened to air, and prevents moisture from entering the system. The lid of the furnace is removed to expose the reaction chamber, and the heat shields are removed. Samples, which hang from the heat shields, are removed at the same time. If a cavity was being coated, it is removed using a hook system with niobium cables. Following this, the source sample holders, $SnCl_2$ boat, and tin crucible are removed, in that order.

With the furnace now empty, new tin is now introduced. A standard coating uses approximately 1.5-1.7 grams of tin. The empty weight of the tin crucible is known to be 60.022 g - if tin remains from the previous coating, additional tin is added to ensure that the weight of the crucible is 2.0-2.2 g above the empty

weight, to ensure a sufficient supply of tin. In the event of a non-standard coating, an appropriate amount of tin is added to ensure that sufficient tin is available without excessive amounts remaining at the end of coating. A scale in the furnace chamber is used to measure the weight of the crucible both pre and post coating. Once ready, the crucible with tin is lowered into the alcove at the base of the reaction chamber.

If called for, source sample coupons (up to 2 of them) are now added to their holders and lowered into the furnace to their seating areas next to the source. Tin chloride is added to the tin chloride boat - the standard amount being 0.22 g - and lowered to its seating area next to the source. If a cavity is being coated, it is lowered into the furnace and seated onto the three tungsten feet on the floor of the reaction chamber, centred around the source which now looks up through the centre of the cavity. Samples, by contrast, are hung from the heat shields using niobium wire and lowered into the furnace with the heat shields. Once the heat shields are in place, the reaction chamber is sealed and the vacuum connection between the reaction chamber and the furnace space is opened.

The furnace is slowly pumped down to roughing vacuum through an MFC at 10 SCCM. Once at roughing vacuum, a turbo-molecular pump is used to lower the reaction chamber pressure to approximately 10^{-6} Torr. Once at this pressure, a cryopump is used in combination with the turbo-molecular pump to lower the pressure further to 10^{-7} Torr. The entire pumping process takes 24-48 hours, depending on the amount of moisture introduced into the reaction chamber.

Now at vacuum, the furnace water cooling systems are engaged and the furnace is turned on. The degas stage begins, raising the temperature of the reac-

tion chamber to 180°C. This is held for 24-48 hours. Once complete, the reaction chamber is sealed and the coating process is begun. The temperature profile for the standard coating procedure is shown in Figure 3.2. Unless otherwise stated, this is the coating procedure that all samples and cavities introduced in later chapters were subjected to. Following 5 hours of nucleation, a temperature gradient of >150°C is introduced between the source and the chamber. The furnace is ramped up to a temperature of 1120°C and 1250°C on the reaction chamber and tin source, respectively. This state is held for 1.5 hours, at which point the tin source heater is turned off and the tin source is allowed to cool to the temperature of the furnace. From the moment of turning the source heater off, the furnace is kept on at the same temperature for 1 hour before the power to the furnace is cut and the chamber is allowed to cool naturally. Once the reaction chamber falls below 40°C, the furnace letup can begin and the cycle ends. The furnace is opened, the coated parts are removed, and the new cycle begins.

Once coated, samples and cavities are ready for use. Standard procedure for samples is to clean them with methanol using a lint-free rag before being sent for analysis, whilst cavities are subjected to a standard high-pressure rinse before being assembled onto a cavity test assembly. The subsequent testing of these Nb_3Sn SRF cavities is the subject of the next chapter.

3.4 Nature of the coated layer

The layer formed by the standard process is approximately 2-3 μm thick with a mean grain size of approximately 1 μm. A scanning electron microscope (SEM) image of the surface of the coated layer is shown in Figure 3.13 alongside the

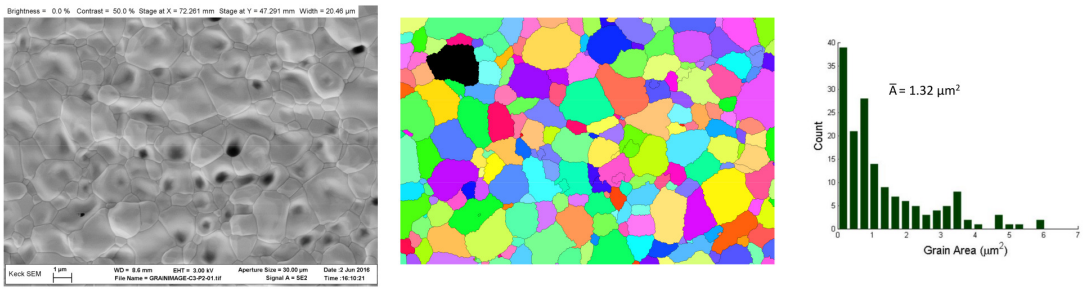

Figure 3.13: (A) An image of the surface of the Nb_3Sn layer as viewed in the scanning electron microscope. (B) The grains outlined using a graphical watershed method. (C) Distribution of grain surface areas from a number of images like that in (A). The average grain size for this coupon was found to be 1.32 µm^2.

distribution of grain sizes. A cross-section image of the layer is shown in Figure 3.14, showing the columnar nature of grains.

In the current range of reaction temperatures of 1000-1200°C, the growth mechanism is understood to be dominated by grain boundary diffusion [Hil80]. Once the initial Nb_3Sn layer is formed, tin migrates through the grain boundaries to the Nb_3Sn-niobium interface to form tin-depleted Nb_3Sn. This tin-depleted phase is brought to stoichiometry by the introduction of more tin from the boundaries. As the layer grows, the grains increase in size, which decreases the surface density of grain boundaries. In turn, this slows the growth rate of the layer, as grain boundaries are required to carry tin from the surface to the interface. Wuppertal measured the growth rate to be [PHK+88]

$$d(t) = d_0 t^{0.38\pm0.04}\,, \tag{3.3}$$

where $d_0 = (1.3 \pm 0.1)$ µm and t is the time in hours.

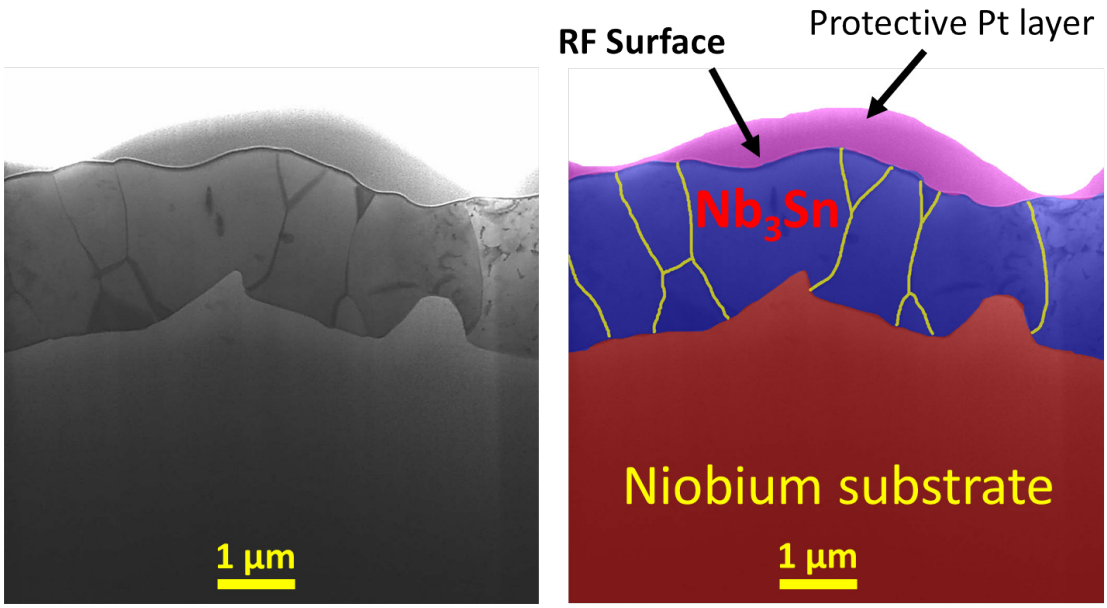

Figure 3.14: Left, an STEM image of the cross-section of the Nb_3Sn layer. On the right the image has been false-coloured to identify the RF surface, and the Nb_3Sn layer, and the niobium substrate. The grain boundaries of the Nb_3Sn layer are highlighted. The protective platinum layer is introduced during the sample preparation for STEM and is not present during coating or RF testing.

Tin-depletion has been observed in chemical analysis of cross-sections using energy dispersive x-ray spectroscopy (EDS), as seen in the image taken at Argonne National Lab shown in Figure 3.15 [BPG+15]. Tin-depletion is seen both at the Nb_3Sn-niobium interface and, at regions in the layer, a few penetration depths away from the RF layer. The mechanism by which these tin-depleted regions form and sustain themselves is not yet fully understood, although their impact upon cavity performance is currently believed to be minimal provided that no surface material removal is performed. Indeed, the best performance observed in 1.3 GHz cavities to date has been achieved using the surface as received immediately post-coating, with only a water-based cleaning regime requited. Unless otherwise specified, all cavities results given in this work have received no post-coating processing to alter the layer.

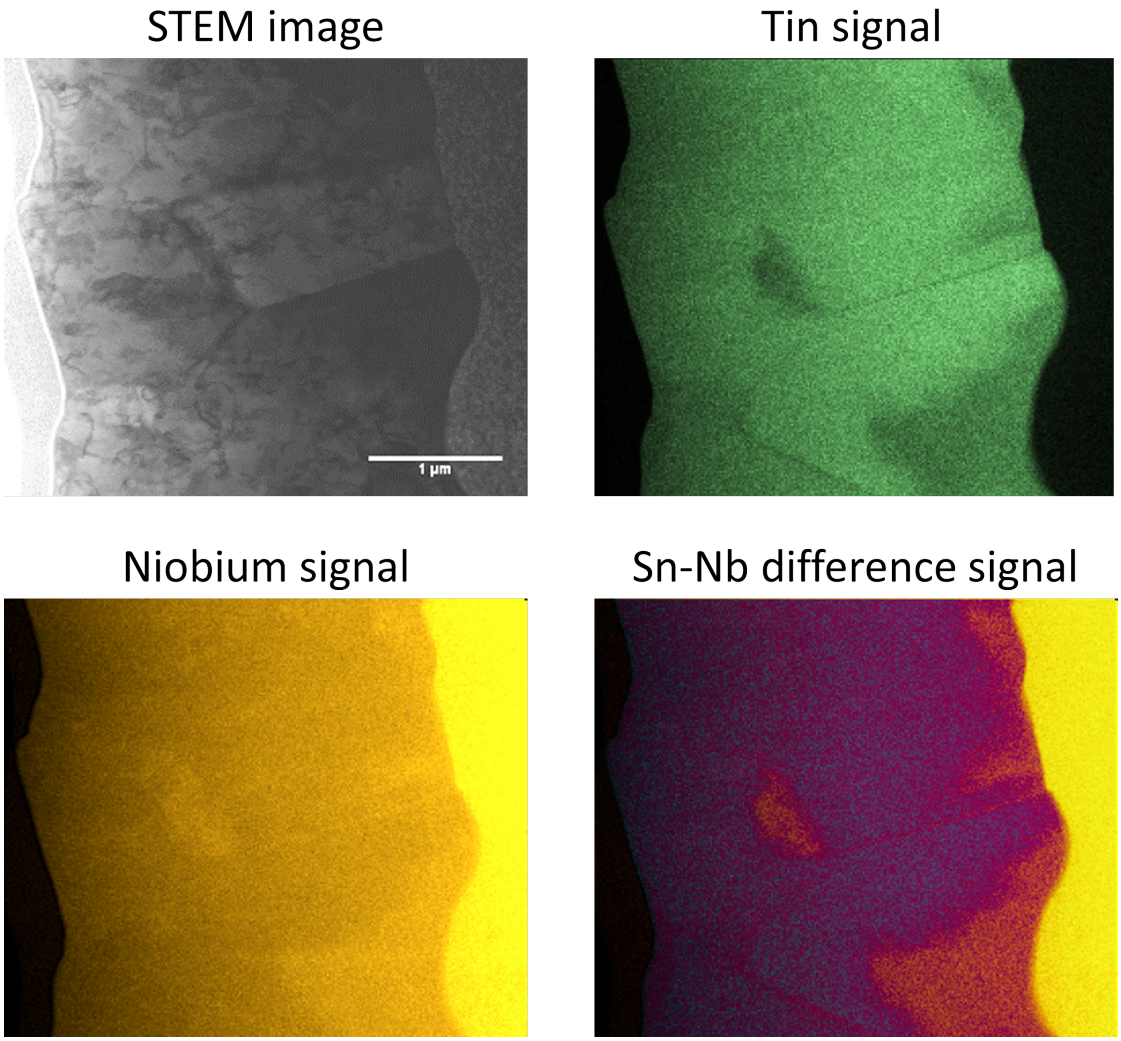

Figure 3.15: EDX chemical analysis of a cross-section from a Nb_3Sn sample coated at Cornell. The difference signal of the tin and niobium indicates the presence of a tin-depleted Nb_3Sn phase within the layer. These images courtesy of Thomas Proslier, Argonne National Laboratory [BPG+15].

CHAPTER 4

RF TESTING OF SRF CAVITIES

An SRF cavity can undergo two kinds of tests: a vertical test, in which the cavity is tested bare, without any of the paraphernalia necessary for beam acceleration; and a horizontal test, in which the cavity is assembled into a cryomodule with all or almost all the necessary components for beam acceleration. Due to the expense involved, a horizontal test is usually reserved for multi-cell cavities that form the tail-end of a research program that is looking to move into production. However, all cavities will undertake at least one, if not many more, vertical tests during their lifetime.

The vertical test facility at Cornell University is located in the basement of Newman Laboratory on central campus. The test area consists of three test pits, shown in the photo in Figure 4.1. These three pits accommodate helium cryostats of different sizes, allowing a variety of cavity shapes and sizes to be tested. The most common measurement carried out is a measurement of the cavity quality factor with accelerating gradient (Q vs E) and temperature (Q vs T). The system is extremely flexible however, and a number of other measurements can be carried out including measurements of cavity frequency with temperature (f vs T), high pulsed power (HPP) measurements of critical breakdown fields, temperature mapping (T-Mapping) of local heating on the cavity surface, and more. A few of these more specific methods will be described later when they are used in experiments carried out on Nb_3Sn cavities. In this chapter we will describe the most common elements of a cavity vertical test and how

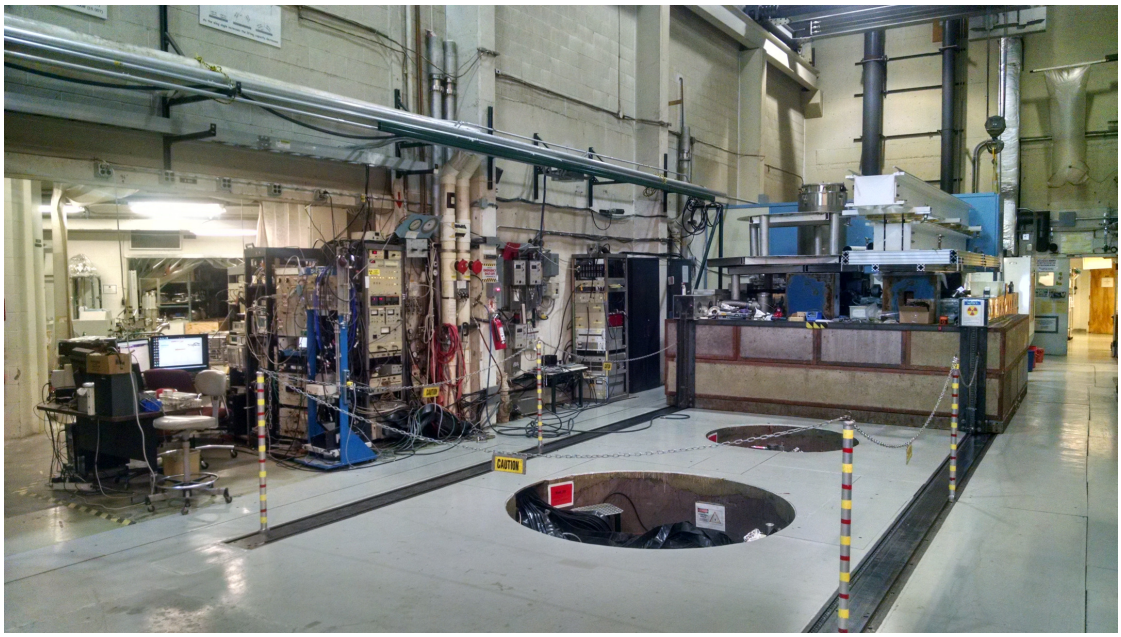

Figure 4.1: The vertical test facility at Newman Laboratory on Cornell campus. The three test pits – the furthest one is covered by the block necessary for radiation shielding – house the cryostats in which the cavities are tested. The operator station can be seen at the control racks on the left side of the photograph.

they are carried out.

4.1 The vertical test setup

In preparation for a cavity test, an SRF cavity is subjected to a number of pre-processing methods, which can include chemical polishing [PDK+93, TRK+06, DSMS71, TCRK08], impurity doping [GKL16], and Nb_3Sn coating. The final step is common to all cavity preparations, and consists of subjecting the cavity to a high-pressure rinse with DI water [KL95] in a cleanroom environment. Once this cleaning is complete, the cavity is dried and is ready to be assembled onto the testing apparatus.

In a vertical test, a cavity is mounted on a test insert, as shown in Figure 4.2.

The top end of the cavity is sealed with a plate in whose centre is located a small RF pickup probe. The other end is connected to the main flange on the insert, through which the main RF power coupler protrudes. At the base of the coupler is located a vacuum port that travels through the piping inside one of the two support struts up to the top plate of the insert. This piping splits to an ion pump and a vacuum port that can be connected to a pumping line.

In order to avoid undesirable effects such as field emission and thermal quenches due to surface contamination, cavities must be assembled in a cleanroom. At Cornell, assembly of the cavity onto the insert is done in a class 10 (ISO 4) cleanroom area immediately following the cavity high pressure rinse. The ends of the cavity are sealed using indium flanges. All vacuum spaces that are connected to the cavity space are kept as clean as possible to lower the possibility that they contaminate the cavity surface during transport and operation.

SRF cavities must operate with their interior at vacuum, to allow free passage of the electron beam and to avoid generation of a plasma from the gas inside the cavity. Even in the absence of beam, in order to sustain the high electric gradients experienced during a vertical test the cavity must be held at a vacuum of approximately 10^{-8} Torr or less. The initial pump-down of the cavity is done by connecting a pumping line to the top of the insert, which pumps down the cavity space slowly through the use of a mass flow controller. Once at vacuum, the cavity vacuum is maintained during transport to the test facility using the ion pump located on the top of the insert.

Once sealed and pumped down, the assembled test insert is removed from the cleanroom and relocated to the test area. This is comprised of three test pits, as seen in Figure 4.1, inside which are three cryostats of different sizes. Before

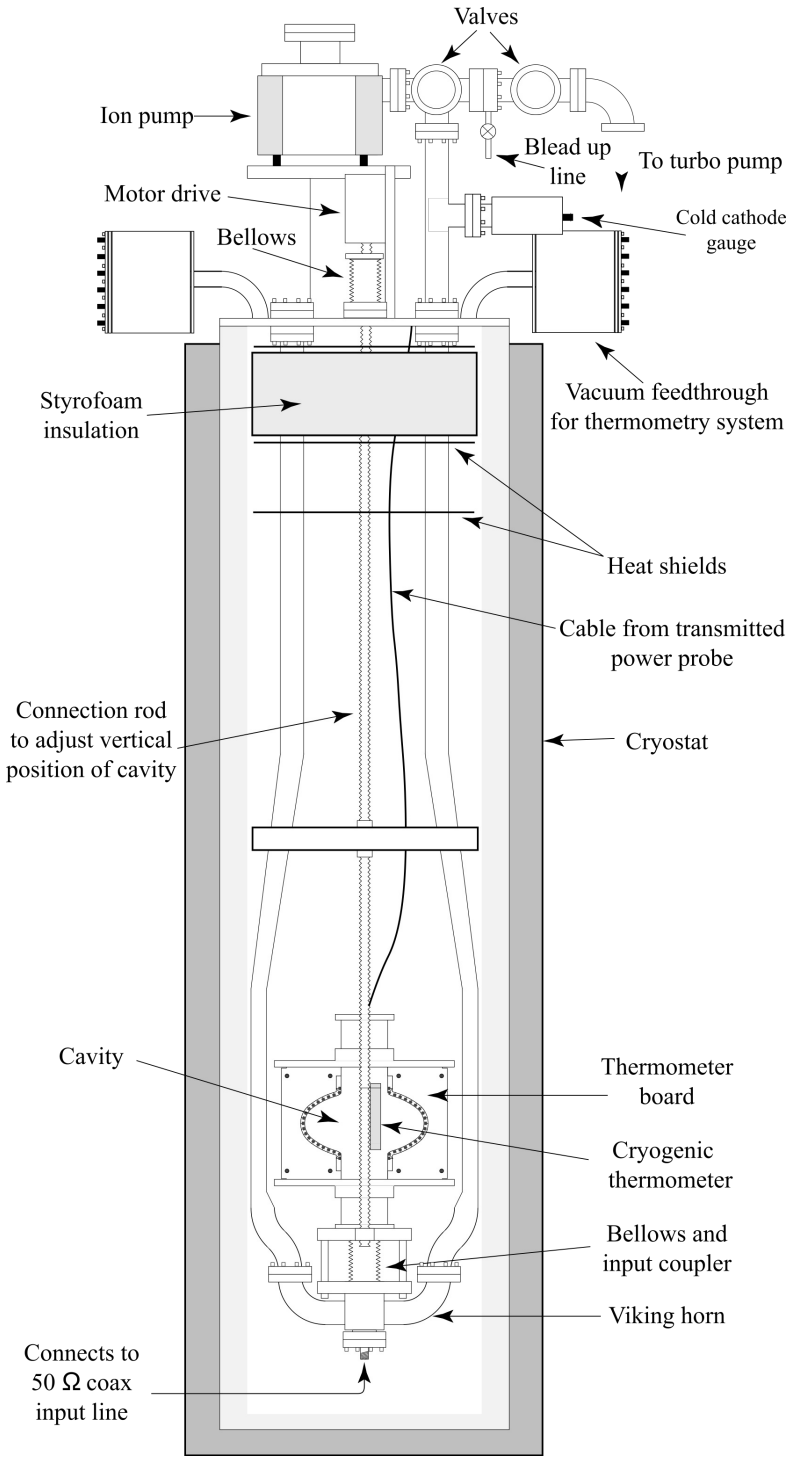

Figure 4.2: Diagram of a vertical test insert used for cavity testing in the facility at Newman laboratory. The major components are annotated. The forward power cable for supplying the cavity with RF power is not shown. This figure originally published in [Kno97].

insertion, a number of instruments are added to the insert. To begin, RF cables for the forward and transmitted power are attached to the base of the coupler and the pickup probe on the top plate of the cavity, respectively. This is followed by a helium level stick to measure the level of the liquid helium in the cryostat, and cryogenic temperature sensors on the cavity (or at other chosen locations) to determine cavity temperature. A helium delivery pipe referred to as a stinger is mounted such that liquid helium is carried from the delivery line at the top of the insert to the base of the cryostat. This completes the basic assembly, although a myriad of other items can be added for specific experiments, such as magnetic flux gates for the measurement of magnetic fields, and a temperature mapping system for measurements of local cavity heating during operation. These specialized items are described in more detail in the later sections in which they are used.

The helium delivery stinger for Nb_3Sn cavities is equipped with a special heating system for careful control of the temperature gradient during the transition through T_c. A photo of this system is shown in Figure 4.3. By controlling the input rate of helium using valves of the helium delivery system, and the temperature of the inserted helium using the heater located inside the stinger, the temperature gradient across the cavity and the cooldown rate can be precisely controlled. As will be explained in more detail in chapter 5, this is necessary to control the generation of thermoelectric currents that appear in the presence of temperature gradients due to the bimetallic interface that exists between the Nb_3Sn layer and the niobium substrate.

Once all the necessary equipment is mounted, the insert is lowered into the cryostat. The top plate seals against the top of the cryostat so that the interior

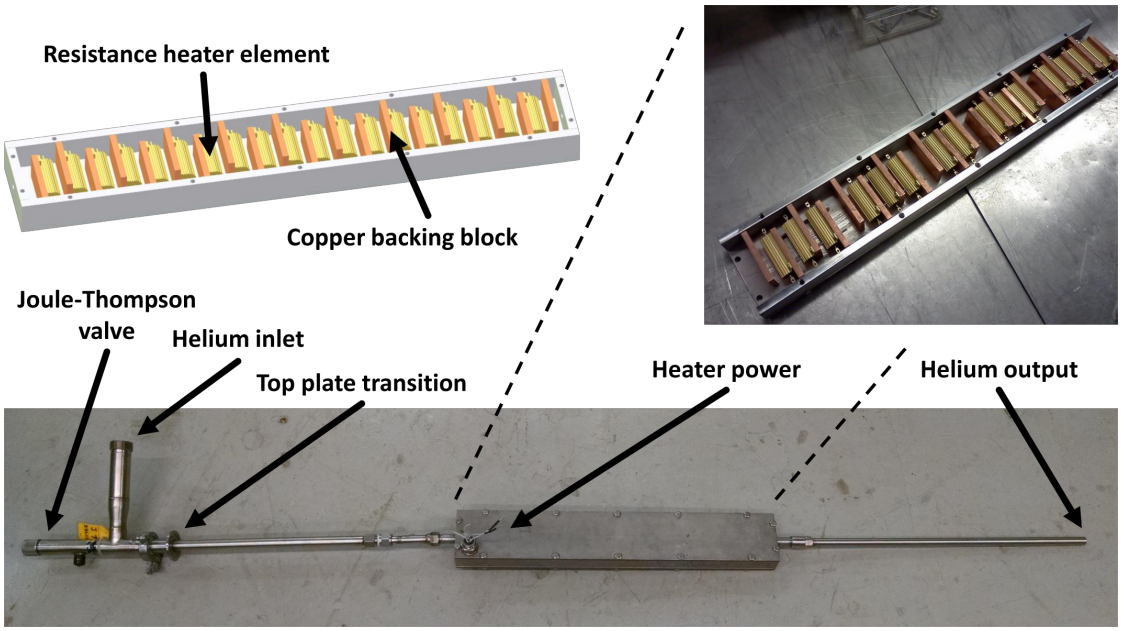

Figure 4.3: The helium insertion device – or stinger – used on the vertical test inserts at Cornell for controlling the cooldown temperature rate and gradient during vertical testing. The cold helium gas is throttled using a Joule-Thompson valve and heated using a heater maze in the passage of the gas. The gas is then injected at the base of the cryostat.

can be pumped down to vacuum. This is necessary prior the introduction of the liquid helium to prevent the air from freezing onto the insert and contaminating the helium recovery system. Liquid helium is introduced from a 3000 L dewar that is refilled by a helium liquefier. This system is shown in Figure 4.4. Gas generated from the boiling of liquid helium is siphoned off by a piping connection at the top of the insert that feeds the helium to a recovery system, where a compressor stores the gas in large outside storage tanks. These tanks feed the liquefier and allow $\approx$ 70 percent of the liquid helium to be recycled, saving approximately half a million US dollars per year.

Once at cryogenic temperatures and superconducting, the cavity can be operated. This is done through the use of the RF system illustrated in Figure 4.5.

Figure 4.4: Part of the cryoplant used at Newman laboratory for vertical testing. The dewar on the right is capable of supplying a maximum of 3000 L of liquid helium to the test pits. This helium is recovered – in gaseous form – by a compressor and stored in an outside tank. The warm gaseous helium is converted back into liquid by the liquefier on the left, which injects the product directly back into the main dewar.

A signal generator is used to generate the 1.3 GHz drive signal, which is attenuated by the desired amount before being sent to the amplifier system. Once amplified, a small amount of the forward power is siphoned off by a directional coupler, where it is measured by a power meter. This provides (via knowledge of attenuation from the directional coupler) the value of the forward power P_f. The majority of the power is sent along the main RF power cable to the coupler where, provided the signal is on the cavity resonance, it is injected into the cavity. Unless the coupler and cavity are impedance matched, the reflected power returns along the power cable where it is prevented from returning to the amplifier output by a circulator. This circulator diverts the power to another directional coupler, where part is extracted for measurement by a second power meter. This is used to measure the returning from the power coupler, P_c. The

remaining power is directed into a load, in which it is dissipated.

A small fraction of the power in the cavity is extracted by the pickup probe in the top plate of the cavity. This signal is split by a 3 dB splitter, with half of it being sent to a third power meter. This provides a measurement of the power transmitted through the cavity, P_t. The other half, which the splitter has shifted by 180°, is amplifier and then combined with the output signal from signal generator inside an RF mixer (as the radio-frequency and local oscillator inputs, respectively), whose intermediate frequency (IF) output is fed back into the external input of the signal generator to form a phase-lock loop (PLL). This is necessary to ensure that the frequency generated by the signal generator remains equal to the natural resonant frequency of the cavity. This can shift under the influence of mechanical oscillations from nearby equipment, such as vacuum pumps. Due to the high quality factor of the cavity, a deformation of 3 nm in a single-cell TeSLA cavity will result in a frequency shift of 1 Hz. For a cavity with a quality factor of 2×10^{10}, and therefore a bandwidth of $f/Q = 0.065$ Hz, this would result in a loss of the resonance drive if not corrected. The PLL ensures that the signal generator remains locked at the cavity resonant frequency. A difference in the path length between the local oscillator (forward power from signal generator) and the radio-frequency (transmitted power from the cavity) results in a phase offset, which is corrected through the use of a phase shifter. This allows the locked phase to be positioned at the centre of the resonance curve, which is referred to as "optimising" the cavity phase.

Operation of this RF system allows both for the control of the accelerating gradient in the cavity (provided the cavity can sustain this field), and measurement of the intrinsic quality factor Q_0 of the cavity at this field and bath tem-

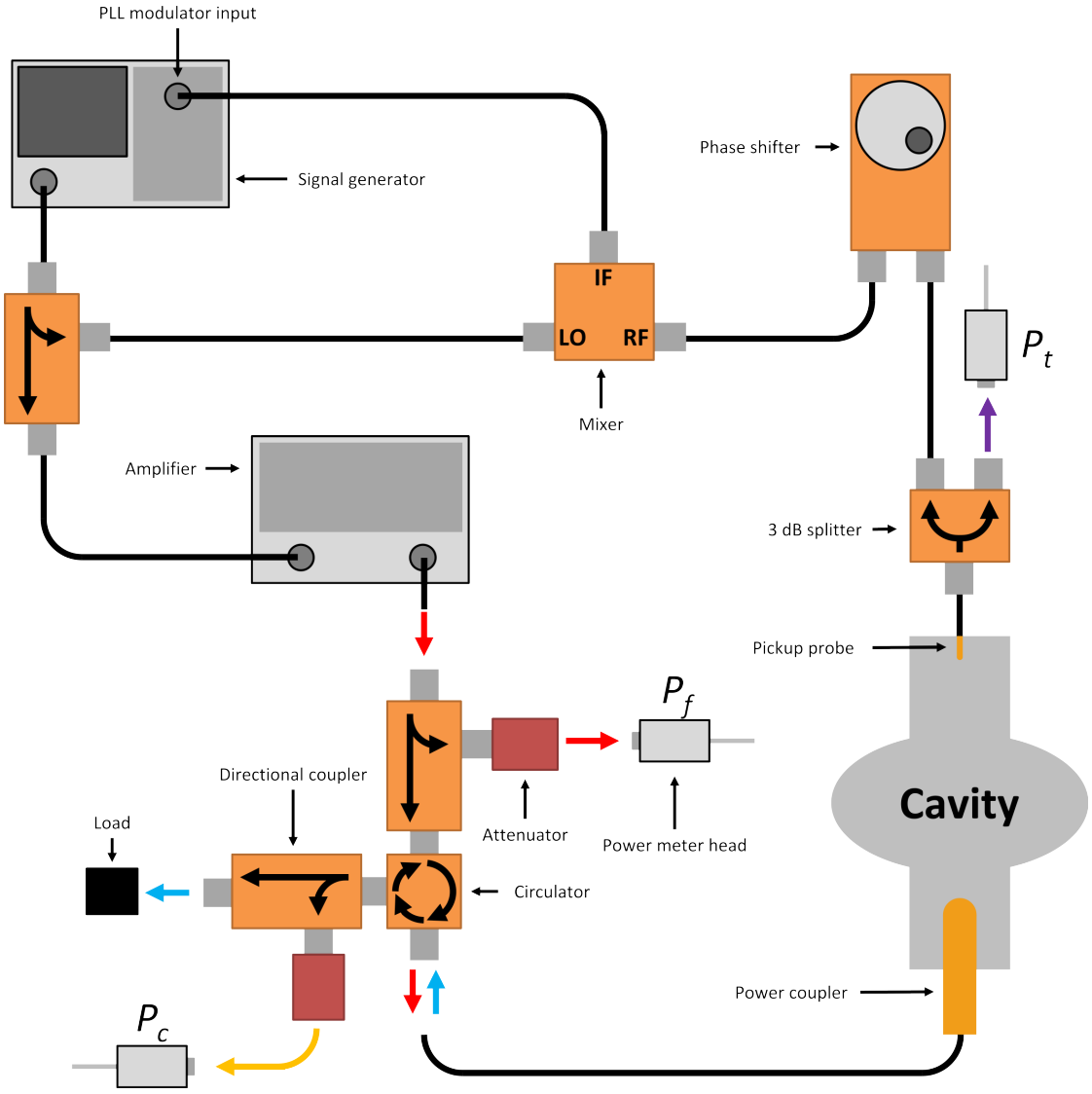

Figure 4.5: The RF vertical testing setup for single-cavity testing. For simplicity, some attenuators have been omitted. The signal generator emits an RF signal that is amplified by a solid state amplifier or a klystron (not shown). Part of this amplified output is siphoned for measurement of P_f. The rest is transmitted to the cavity, and the reflected portion is diverted away from the amplifier by a circulator. Of this power, some is extracted for a measurement of P_r (which is P_c at steady-state lock). The remainder is dissipated in a load. The power transmitted through the cavity is split, with half going for a measurement of P_t, and the other half (after a 180 degree phase shift) being combined with the signal from the generator inside a mixer. The output from the mixer is used to modulate the output of the signal generator. Use of a phase shifter allows the phase-lock to be optimised to drive the cavity on resonance.

perature. The method for measuring these parameters, and by extension the surface magnetic field to which the superconductor is being subjected and its RF surface resistance, are described in the next section.

4.2 Measuring cavity quality factor

Measuring cavity Q at Cornell is achieved using a decay method. With the RF on, and the cavity locked at its resonant frequency $\omega_0 = 2\pi f_0$, the cavity is filled to an energy U that is, in the steady state, held constant by the balance between the forward power from into the cavity at the coupler P_f and the power dissipated in the cavity P_d. Once in this steady state, the RF drive is turned off and the energy in the cavity is allowed to decay. The various powers (P_f, P_r, P_e, P_c, and so on) are measuring using the power meters indicated in Figure 4.5, and knowledge of the cable attenuations (using known calibrations) allow for the extrapolation of the power flow at the appropriate location in the RF system.

The presence of the RF power coupler creates a coupled oscillator system between the antenna and the cavity. This results in the complete system having a loaded quality factor Q_L that can be broken into three components, one pertaining to the cavity and the other two symbolising the losses from the power coupler and transmitted power probe:

$$\frac{1}{Q_L} = \frac{1}{Q_e} + \frac{1}{Q_0} + \frac{1}{Q_t}\,, \tag{4.1}$$

where Q_e and Q_t are the Q for the power coupler and pickup probe, respectively. The coupling of the transmitted probe is purposely designed to be small, such

that $Q_t \gg Q_0$ and therefore the contribution of $1/Q_t$ can be ignored in the calculation of Q_L. This leaves the task of determining Q_e to determine Q_0 from behaviour of the Q_L.

The coupling of the power coupler to the cavity is given by

$$\beta = \frac{Q_0}{Q_e} , \tag{4.2}$$

which, when $\beta = 1$, signifies that the antenna is impedance matched to the cavity and that therefore $P_f = P_d$. For all other values of β, a portion of P_f will be reflected back toward the load during operation at steady state. This power is referred to as the steady-state reflected power or P_r (a specific case of the power from the coupler P_c). The relationship between P_f and P_d is given by [PKH98]

$$P_d = \frac{4\beta}{(1+\beta)^2} P_f . \tag{4.3}$$

When the power is turned off, the energy in the cavity begins to decay in the manner describe by

$$\frac{dU}{dt} = -\frac{U(t)}{\tau_L(t)} , \tag{4.4}$$

where $\tau_L = Q_L/\omega_0$ is the characteristic decay time of the loaded system. The solution to this is the exponential decay

$$U(t) = U_0 e^{-t/\tau_L} , \tag{4.5}$$

where U_0 is the energy in the cavity just before the power is turned off. Equation (4.4) indicates that, after turning the RF off, the cavity will emit power from the coupler – just as the coupler can introduce power, it can also siphon it out. Depending on the coupling β, the value of P_c will jump to a new value the instant after the power is turned off (unless $\beta = 1/3$). This can be seen in Figure 4.6, where the value of P_c as a function of time is shown as the RF is turned on and then off again after reaching steady state. The value of P_c the instant after the RF is turned off is referred to as the peak emitted power, P_e. The values of P_e and the steady state reflected power P_r are noted in Figure 4.6. A particular case is that in which the cavity is impedance matched to the coupler, in which case $\beta = 1$, $P_r = 0$, and $P_e = P_f = P_d$, where P_f is the forward into the coupler when RF is on.

From the measurements of P_f and P_r (immediately prior to RF off) and P_e immediately after RF off, there are two methods of calculating β, these being

$$\beta_e = \frac{1}{2\sqrt{\frac{P_f}{P_e} - 1}} \tag{4.6}$$

and

$$\beta_r = \frac{1 + \alpha\sqrt{\frac{P_r}{P_f}}}{1 - \alpha\sqrt{\frac{P_r}{P_f}}}\,, \tag{4.7}$$

where

$$\alpha = 2\left(\left[P_f < P_e?\right] - 0.5\right)\,, \tag{4.8}$$

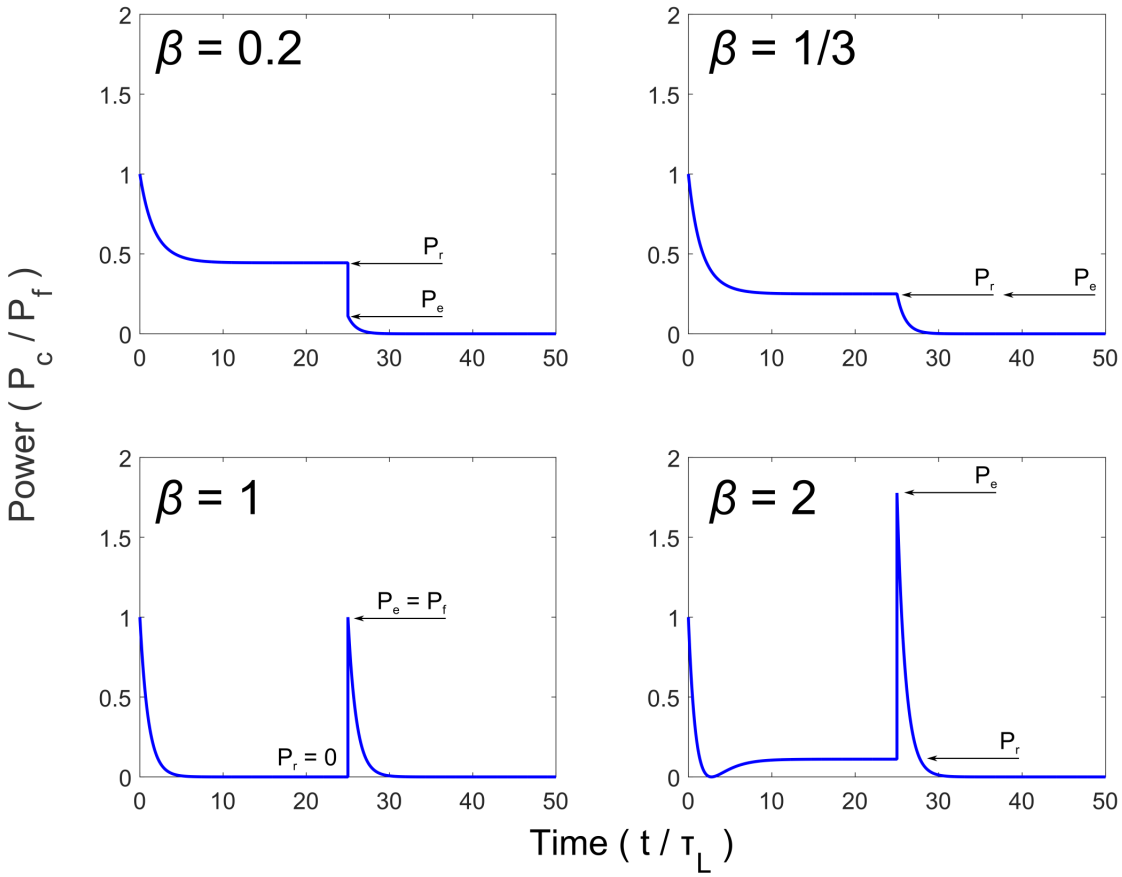

Figure 4.6: Examples of the behaviour of the returning coupler power P_c, relative to the forward power into the coupler when the RF is on (i.e. P_c/P_f). The value of P_f is constant. At $t = 0$, the RF is turned on and the P_c decreases until it reaches a steady state, where $P_c = P_r$. The value of P_r is indicated. At $t/\tau_L = 25$, the RF is turned off, and $P_f = 0$ (although P_c remains defined relative to P_f when the RF was on). The value of P_c the instant when the RF turned off is where $P_c = P_e$, and is also indicated. The value of P_c now decays according to τ_L.

and the term $\left[P_f < P_e?\right] = 1$ when $P_f < P_e$ and 0 otherwise. In measurement, the agreement between these two is used to determine the precision of the measurement, and β is taken to be the average of the two.

Assuming that the Q of the cavity does not change much during the initial part of the decay, then τ_L can be determined by taking the logarithm of P_c after the RF is turned off and performing a linear fit to the beginning of the decay.

With τ_L and β now known, the quality factor of the cavity at the time the power was turned off is given by

$$Q_0 = 2\pi f_0 \tau_L (1 + \beta) \,, \tag{4.9}$$

and the energy in the cavity is given by

$$U_0 = \frac{Q_0 P_d}{2\pi f_0} \,, \tag{4.10}$$

where the dissipated power P_d is given by Equation 4.3.

The accelerating gradient E_{acc} is calculated from U_0 using the parameters $\left[E_{\mathrm{pk}}/\sqrt{U}\right]$ and $\left[E_{\mathrm{pk}}/E_{\mathrm{acc}}\right]$, which are obtained from simulations of the cavity shapes. In a similar fashion, the average surface resistance $R_s = G/Q_0$ and peak surface magnetic field B_{pk} are obtained from the simulation constants G (the geometry factor) and $\left[B_{\mathrm{pk}}/E_{\mathrm{pk}}\right]$.

In the event of strong Q-slope being present, the assumption that the Q does not change during the initial stage of the decay (from which τ_L is extracted) no longer holds, and this will result in an inaccurate measurement of Q_0. This issue can be resolved through use of the transmitted power probe, which measures the transmitted power P_t. However, in contrast to the forward/reflected portion of the system, the attenuation in the transmitted power cable and the coupling of the transmitted power probe to the cavity are usually not known. It is therefore necessary that at least one measurement be made using the method describe above before the following method can be utilised. This calibration decay measurement is done in a portion of the Q vs E curve is sufficiently flat,

usually towards the lower end of the curve.

Once a conventional point has been measured, calibration constants for the transmitted power are obtained from this n^{th} point,

$$\Lambda = \frac{U_n}{P_{t,n}} \tag{4.11}$$

and

$$\Gamma = \frac{E_{\mathrm{pk},n}}{\sqrt{P_{t,n}}} \, . \tag{4.12}$$

For any subsequent point, the Q_0 and E_{acc} can be determined from P_t using

$$E_{\mathrm{acc}} = \Gamma \sqrt{P_t} \left[E_{\mathrm{pk}} / E_{\mathrm{acc}} \right]^{-1} \tag{4.13}$$

and

$$Q_0 = \frac{2\pi f_0 \Lambda P_t}{P_d} \, . \tag{4.14}$$

Use of the transmitted power allows for accurate measurement of Q_0 in spite of the presence of strong Q-slope.

By performing these measurements multiple times at different values of forward power from the amplifier (and by extension, energy in the cavity), a Q vs E curve is created at a given cavity bath temperature. An example is given in Figure 4.7. However, generating a dense Q vs E curve can be time consuming, and

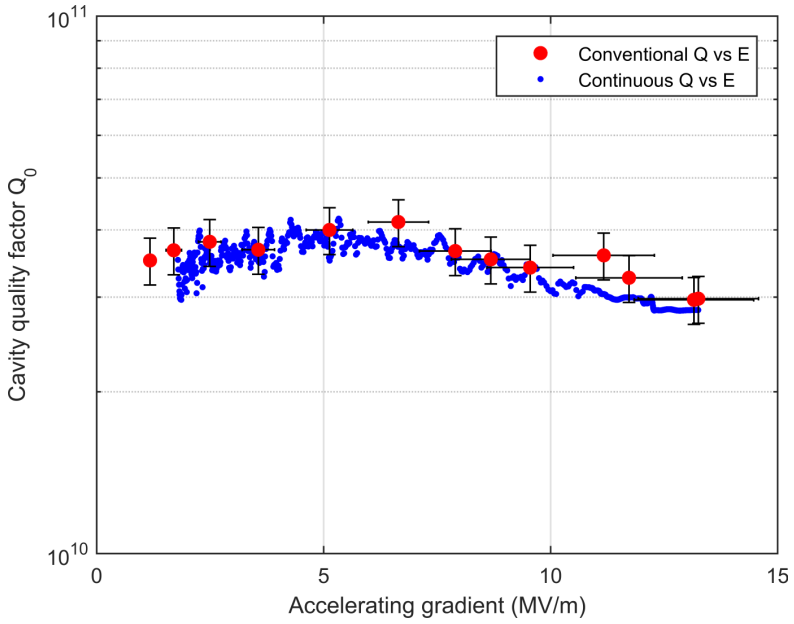

Figure 4.7: A Q vs E of a Cornell Nb_3Sn cavity taken at 4.2 K. The points from a conventional Q vs E are shown. A Q vs E using the continuous method, derived from the highest-field conventional point, is shown in blue.

the boiling of helium in the cavity naturally places a time limit on cavity measurements. A new method implemented for the experiments presented later is a "continuous" Q vs E measurement, in which the remainder of the decay of P_c after the RF is turned off, rather than being discarded, is used to extrapolate Q and E as the field in the cavity decays.

In the continuous method, a standard decay measurement is taken, which gives a measurement of β and Q_0 at the instant the forward power was turned off. From this, it is possible to determine Q_e,

$$Q_e = \frac{Q_0}{\beta}, \tag{4.15}$$

which will remain constant through the decay (as opposed to β, which will vary with Q_0). By taking the derivative of the logarithm of the decay of P_c, τ_L as a

function of time is obtained, i.e.

$$\tau_L(t) = \frac{d}{dt} \ln P_c(t) \,, \tag{4.16}$$

where $t = 0$ is the time at which the RF is turned off, such that $P_c(t) = P_e$.

From this we can obtain τ_0 through knowledge of Q_e,

$$\tau_0(t) = \left(\frac{1}{\tau_L(t)} - \frac{2\pi f_0}{Q_e} \right)^{-1} \,, \tag{4.17}$$

from which in turn we obtain

$$Q_0(t) = 2\pi f_0 \tau_0(t) \,. \tag{4.18}$$

The gradient in the cavity is obtained using

$$E_{\mathrm{acc}}(t) = \sqrt{\frac{P_r(t) Q_e}{2\pi f_0}} \,. \tag{4.19}$$

By equating times in the vectors of $Q_0(t)$ and $E(t)$, the full Q vs E curve can be obtained.

An example of a continuous Q vs E curve is shown overlaid on a conventionally obtained one in Figure 4.7. The continuous curve was obtained from the decay of the last conventional point. Alternatively, multiple overlaid continuous Q vs E curves (obtained from each conventional point) can be stitched together for even greater precision. The resolution of the continuous curve is limited by the number of time points that can be stored in the power meter (in

the system used at Cornell, two power meters are daisy-chained to double this number).

This method is useful when trying to compare the resistance at a given RF gradient from two different curves. A Q vs E curve collected in the conventional manner by using one decay point per field requires a considerable number of points to reduce the impact of interpolating between points. Comparatively, the high resolution of the continuous Q vs E curve allows the Q at a desired E to be extracted accurately while only needing a few measurement points to actually be taken. This is taken advantage of to compare the many Q vs E curves used to generate figures such as Figure 5.27. Although each curve only consisted of 5-10 decay points, the continuous method allows the Q vs E data between these points to be filled in accurately. It is also useful in ensuring that the data in a Q vs T curve is representative of a constant field – all the points are taken at a field slightly greater than the intended field, and then the Q at the desired field is extracted for all the points in the Q vs T curve.

CHAPTER 5

LIMITATIONS ON CAVITY EFFICIENCY

Arguably the biggest appeal of Nb_3Sn as an alternative to niobium is its greatly reduced BCS resistance at equivalent operating temperatures, which would unlock, amongst other things, operation of 1.3 GHz cavities at 4.2 K and the use of liquid-He-free cryomodules equipped with cryo-coolers. However, achieving these high quality factors requires success in a number of different battles. Two of, to date, most crucial factors affecting the Q are discussed here: the uniformity of the surface coating, and losses from trapped magnetic flux.

5.1 Uniformity of the surface coating

The first cavity coated with Nb_3Sn at Cornell University, designated ERL1-5, demonstrated very poor performance [PMR+15, Pos14], with a high residual resistance and a Q-slope similar to that seen in the Wuppertal and JLab cavities. This performance stands in stark contrast to later cavities coated at Cornell. The performance of ERL1-5 is compared to one of the most recent cavities, LTE1-7, in Figure 5.1; the latter shows an absence of the slope seen in ERL1-5. The lower Q of ERL1-5 corresponds to a power dissipation in the cavity, due to a higher surface resistance. To investigate this, a temperature mapping system was used to measure the local heating on the surface of the cavity during operation. By operating the cavity at a fixed field and using an array of thermometers mounted on the outside of the cavity, regions of increased power dissipation (and therefore higher surface resistance) could be identified. An example of a temperature map (T-Map) for ERL1-5 is shown in Figure 5.2.

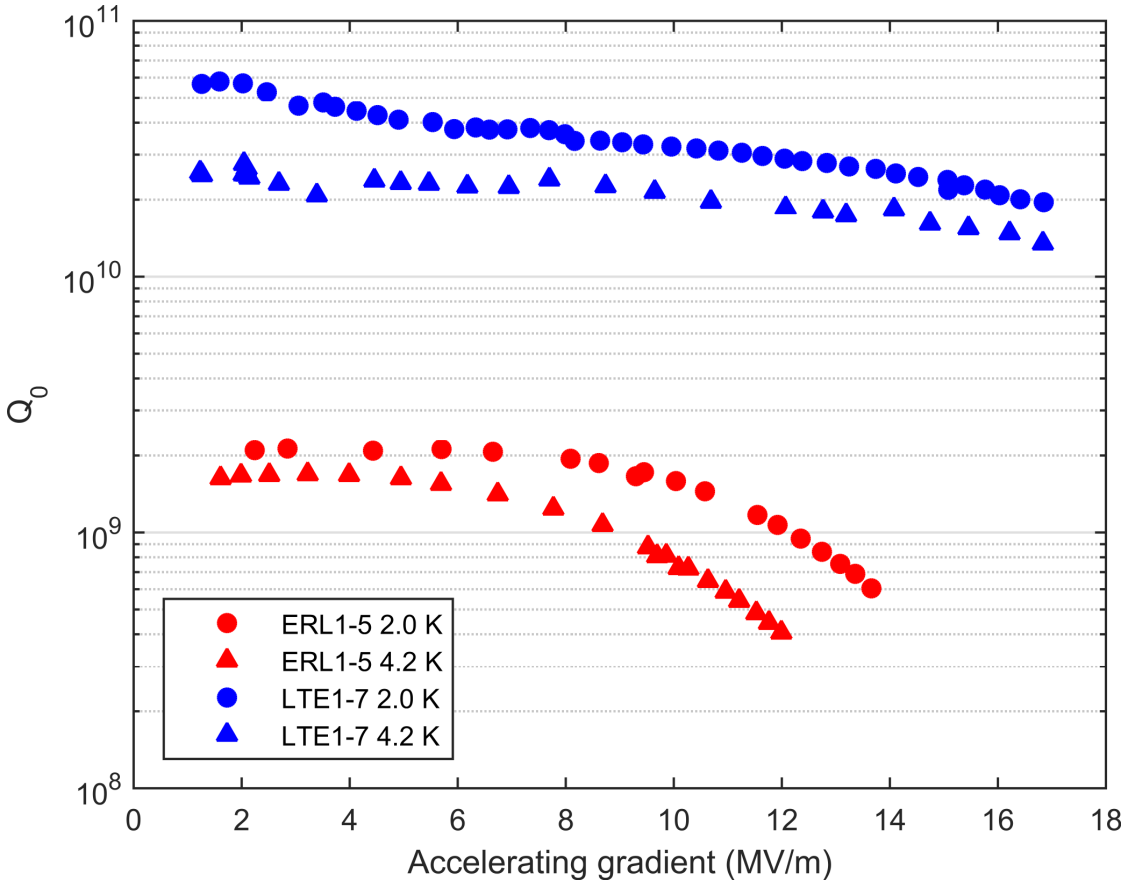

Figure 5.1: A comparison of the performance of the ERL1-5 (the first cavity coated at Cornell) against one of the more recent ones, LTE1-7. The coating procedure of LTE1-7 is seen in Figure 3.2, while the coating recipe for ERL1-5 can be seen in Figure 5.5. Whereas later cavities showed a lack of Q-slope, ERL1-5 demonstrated a Q-slope very similar to that seen in Wuppertal cavities (see Figure 3.7.

The T-Map of ERL1-5 shows that there was significantly higher power dissipated in the lower half-cell of the cavity, which served to reduce the Q of the cavity. In collaboration with Fermi National Accelerator laboratory, coupons were cut from the cavity at regions that showed severe, medium, and no heating (designated H, M and C samples, respectively), with the latter coming entirely from the half-cell that showed no heating. The intention was to investigate these samples to discern why the lower half-cell showed increased surface resistance compared to its upper counterpart. Surface analysis of these coupons

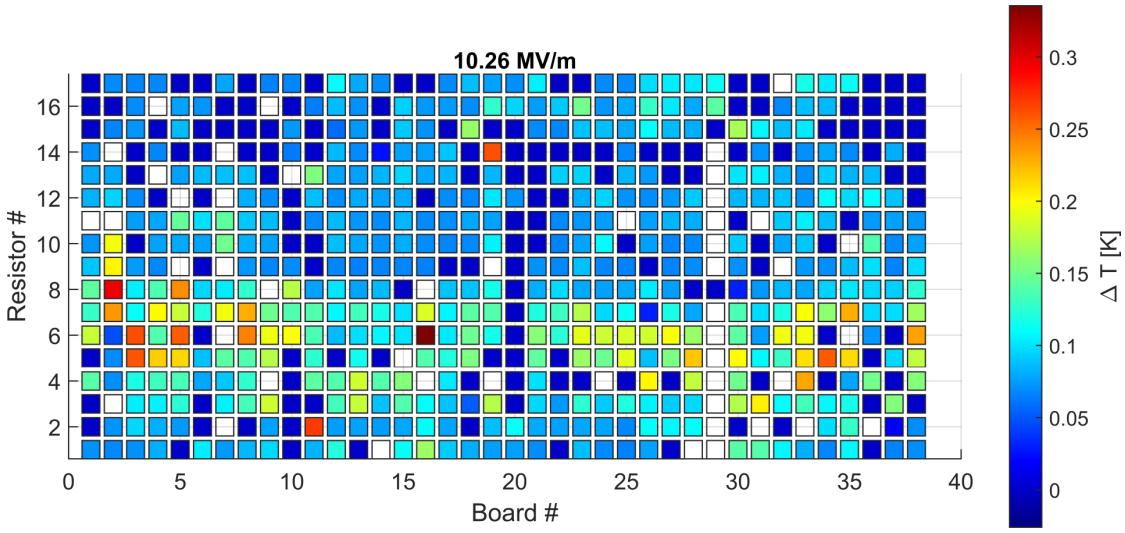

Figure 5.2: A temperature map (T-Map) of the Nb_3Sn cavity designation ERL1-5, operating at 10 MV/m. This map is a projection (onto a rectangular grid) of the outside surface of the cavity. Along the x-axis, the board number progresses about the cavity beam axis. Along the y-axis, going from resistor 0 to 17 moves from the lower iris to the upper iris (with the equator being along the x-axis at resistor 9). The T-Map showns extensive heating on the lower half of the T-Map, corresponding to heating on the entirety of the half-cell of the cavity that faced away from the tin source during coating.

using scanning electron microscopy and EDS mapping showed, when probed with a 30 kV SEM beam, regions of significant tin-depletion/niobium excess [PMR+15]. An example of such a map, taken from sample M5 is shown in Figure 5.3, showing the extent of these regions. Chemical quantification of these regions, albeit performed by standardless methods, gave atomic tin percentages of 10-12%, far lower than allowed by the Nb_3Sn-only region seen in the phase diagram (Figure 2.4).

Cross-section lamellae obtained from these regions of tin-depletion using FIB milling and imaging with transmission electron microscopy revealed that these regions were in fact covered with a coating of Nb_3Sn far too thin to screen the substrate from the probing of the 30 kV beam, which probes to a depth of

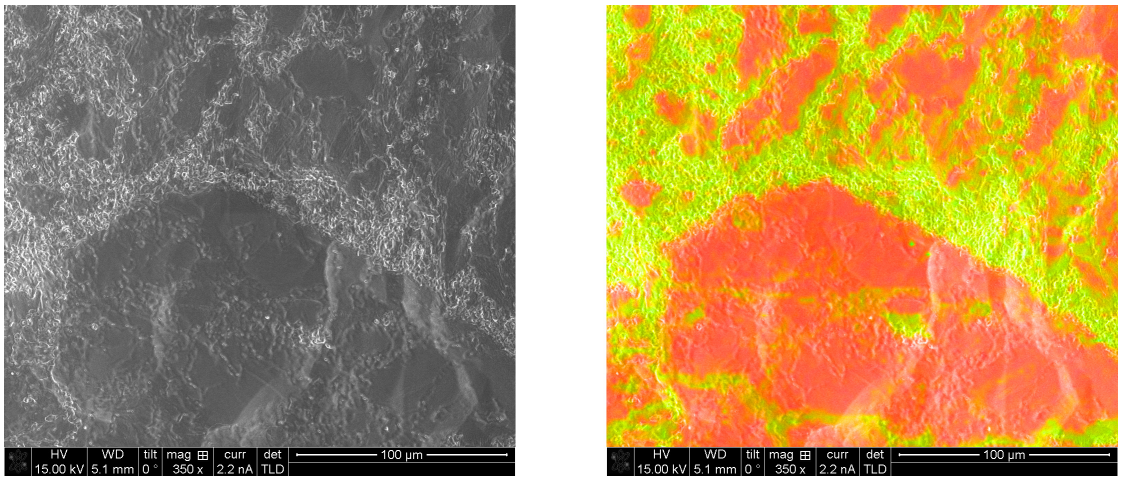

Figure 5.3: EDS mix-map of a cut-out from a region of the ERL1-5 cavity that showed heating (sample designated M5). Green regions indicate regions where quantification gives 25 atomic percent Sn, red areas correspond to 6 atomic percent Sn. The lower atomic percent at these regions is due to the Nb_3Sn layer being too thin, and the SEM probe interacting with the niobium bulk below.

$\approx$ 1 µm. These regions were found to be between 500 and 50 nm thick. An example of such a region is shown in the STEM image shown in Figure 5.4. These regions are also far too thin to screen the substrate from the RF layer, since the thickness is on the order of the penetration depth of the RF field, which will result in an impact on the performance of the cavity. In cut-outs from cold regions of the cavity, no such thin film regions were found, confirming that these regions are the causes of the increased losses that led to the half-cell heating and poor performance of ERL1-5.

It is interesting to note that the grain structure of these thin film regions is very different to that seen in the rest of the coating. Whereas the grain size of normal regions is composed of grain approximately 1 µm wide, these thin film regions consists of almost entirely one single large grain, many µm wide. Correspondingly, the density of grain boundaries in these regions is significantly lower than that seen in normal regions, which would explain why they are so

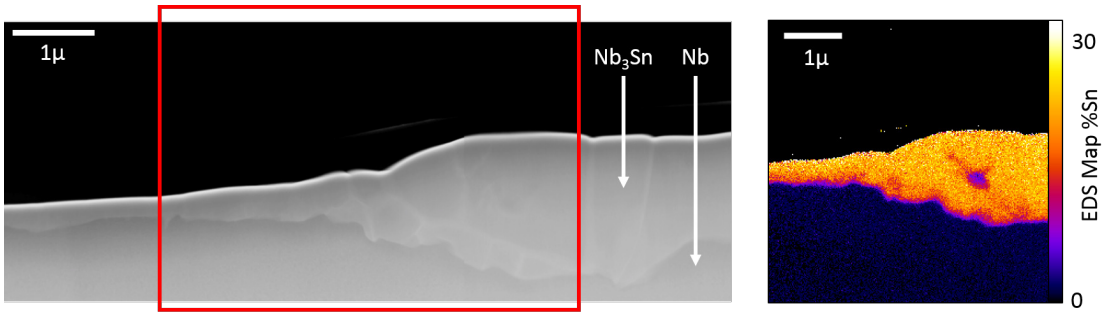

Figure 5.4: A cross section of Nb_3Sn cut from a fine grain niobium substrate sample, designation E3F. On the left is the STEM image, with the RF layer on top (a thin layer of platinum resides between the Nb_3Sn surface and the vacuum for protection during sample preparation) and the niobium substrate at the bottom. On the right is an EDS map of the region outlined in red, giving the atomic percent Sn at each region. The interface between the Nb_3Sn and Nb is seen to be tin depleted. This image is courtesy of Paul Cueva, Muller Group, Cornell University.

thin: as the layer growth is dominated by tin transport through grain boundaries, a region deficient in them will grow slower (relying on the much slower bulk diffusion) than a region with a higher density of them. The difference in the density of grain boundaries creates the difference in texture seen in the SEM image in Figure 5.3 (left).

EDS chemical mapping of these thin film regions reveals that most of the layer is actually of similar stoichiometry to the surrounding thicker regions. However, the interface between the Nb_3Sn layer and the niobium substrate is depleted, as often seen in even the thicker regions (see the EDS map in Figure 5.4). In the thicker regions, this tin-depletion is out of reach of the RF field; by comparison, in these regions of thin film the tin-depleted interface is well within the influence of the RF field. The presence of lossy phases of Nb_3Sn will result in significant losses even at low temperatures, where the niobium substrate will have significantly lower SRF resistance. This would explain the poor

performance seen even at 2.0 K in ERL1-5.

For the second cavity coated at Cornell, ERL1-4, a temperature gradient between the tin source and the coating chamber of approximately 100°C was introduced before beginning the ramp up to coating temperature from the nucleation stage. The difference between the two coating recipes is illustrated in Figure 5.5. The performance of this cavity was a substantial improvement over ERL1-5, free of the Q-slope seen in previously coated Nb_3Sn cavities [Pos14, PL13, LP13]. However, it is not a given to attribute the improvement in performance to the introduction of this temperature gradient during the ramp-up, as the University of Wuppertal recipe also used a temperature gradient during ramp-up [Pei83] (as seen in Figure 3.6), and these cavities were seen to have Q-slope. Although the original suspicion was that the addition of an extended annealing stage was the solution to the Q-slope, this was contradicted by the result that a later coating of ERL1-4 with the shortest annealing time to date produced the best result.

More recent studies on sample coupons coated at Cornell using a temperature gradient between the source and chamber (using the recipe seen in Figure 3.2) still revealed the presence of thin film regions in these samples, but with less area coverage than the H and M sample coupons taken from ERL1-5. EDS analysis confirmed that these regions were thin in a similar fashion to those seen in ERL1-5; by varying the voltage of the SEM beam from 30 kV down to 12 kV, the ratio of the tin to niobium signal varied from that of average low tin concentration of 10-12 atomic-% to almost stoichiometric. This measurement is demonstrated in Figure 5.6. By applying this result to EDS mapping, in which the ratio of tin to niobium is collected at each pixel of the map image, taking a map at 30 kV resulted in thin film regions being easily revealed over areas 0.5 to

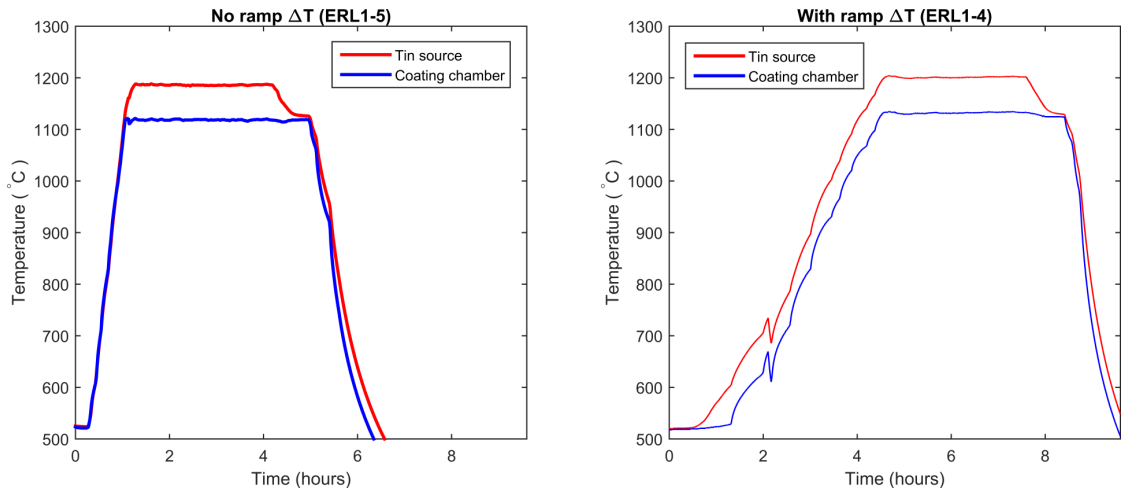

Figure 5.5: A comparison of the coating of ERL1-5 (left) and ERL1-4 (right). ERL1-5 was the first cavity coated at Cornell, and the ramp up to coating temperature was done with the tin source and the coating chamber at the same temperature, with the gradient between the source and the chamber being introduced upon arriving at the coating temperature. Later, in coatings of ERL1-4 and beyond, a temperature gradient was introduced between the tin source and the chamber before the ramp-up to coating temperature.

1 mm wide. An example of such a map is given in Figure 5.7. The contrast can be further enhanced using a filtering method [KHL16] to further enhance the contrast and allow quantification of the percentage of area of the map covered by these thin film regions. An example of such an enhanced map is shown in Figure 5.7. It was noted that the coverage and distribution of the thin film regions in these later samples is different to those seen in the cut-outs from ERL1-5; whereas ERL1-5 showed extensive coverage (up to 60% of the surface area) by thin film regions, samples such as that seen in Figure 5.7 show far less coverage ($\approx$ 7%) that covers the surface in a scattered, distributed fashion.

Analysis of a number of different samples coated with Nb_3Sn revealed a few different trends. First amongst these is that substrates of large grain niobium demonstrate a greater propensity for the formation of thin film regions than

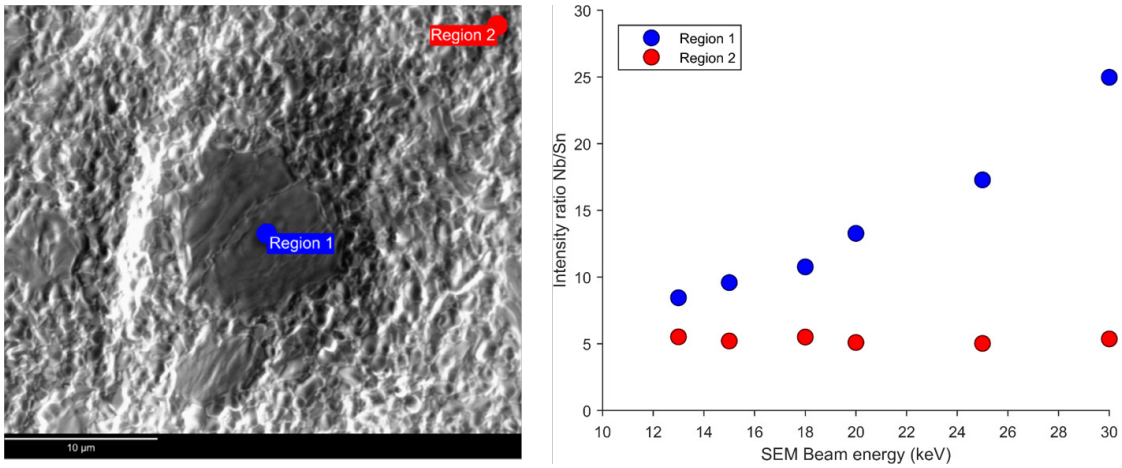

Figure 5.6: Two figures demonstrating the change in niobium to tin signal given by the X-ray probe at the tin film regions. The SEM region on the left is centred on a thin film region. As the SEM beam energy in the probe regions 1 and 2, shown, is changed, the ratio of the heights of the niobium $L_{\alpha-1}$ peak to the tin $L_{\alpha-1}$ peak is measured. This is plotted on the right. As the beam energy increases, it probes deeper into the bulk - at region 1, the Nb_3Sn layer is thin enough that the beam begins to probe the niobium bulk. At region 2, the Nb_3Sn layer is thick enough that this is not the case.

fine grain substrates coated in an equivalent manner. A coating of a large grain sample, A1L, showed (4.0 ± 0.7)% thin film coverage, as seen in Figure 5.8 a). This sample was coated while mounted in a sample holder located near the tin source, using a coating recipe that made use of the ΔT during the ramp-up (as seen in Figure 3.2). By contrast, sample ERL14-01, a fine grain sample placed in the same location in the furnace and subject to a similar coating recipe, demonstrated less than 1% coverage by thin film regions – at the limits of detection by the EDS mapping method.

The second trend is that identical substrates showed different degrees of coverage by thin film regions depending on their location in the furnace. As already mentioned, fine grain sample ERL14-01 coated near the source (where tin vapour pressure is higher) demonstrated a coverage less than the limits of

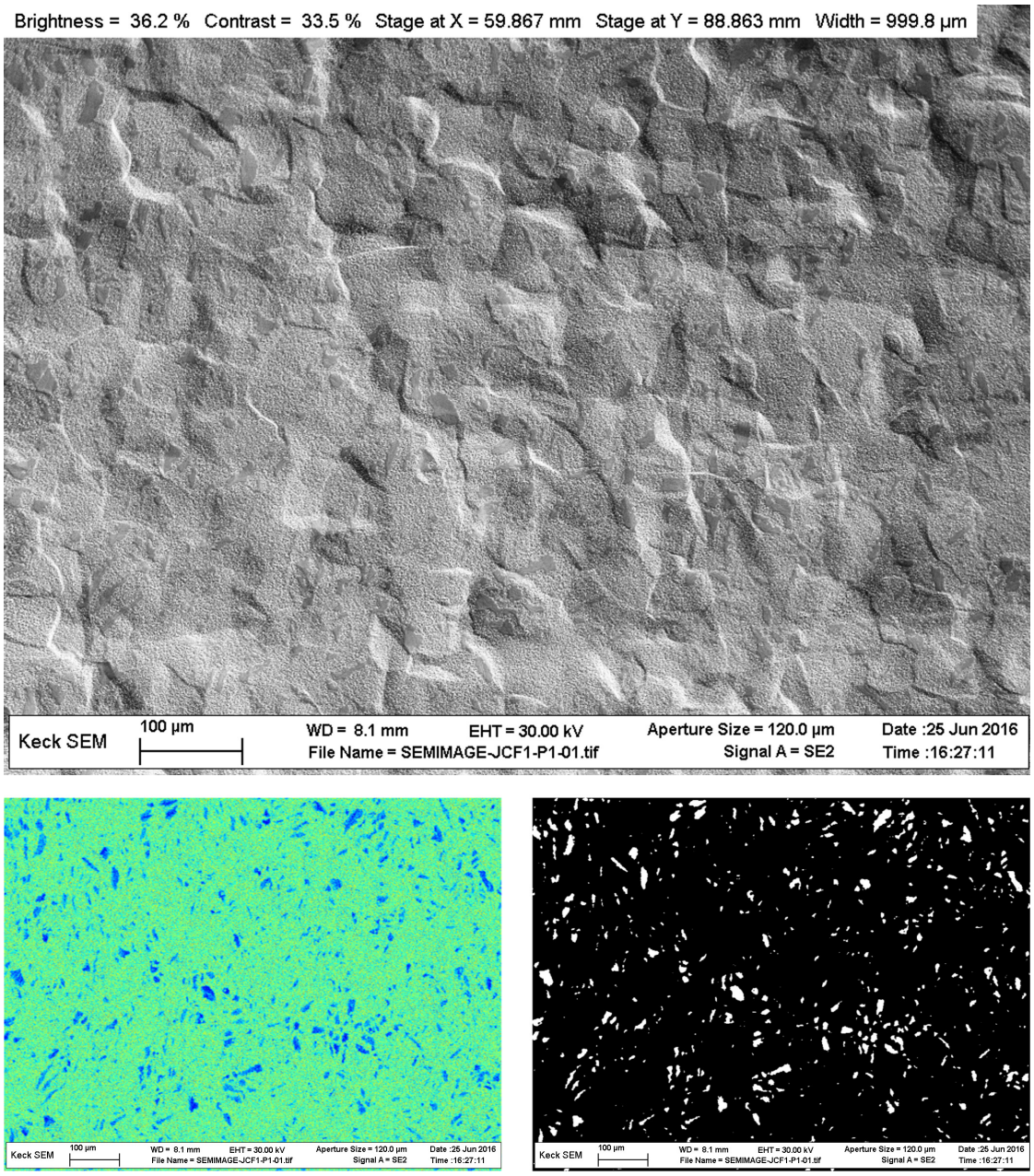

Figure 5.7: Top, an SEM image of a fine grain niobium sample coated with Nb_3Sn. The sample was hung in the furnace at the height of the cavity equator, and received the coating recipe given in Figure 3.2. Bottom left, the raw mixmap obtained from the X-ray data, with thick regions in green and thin regions in blue. Bottom right, the contrast has been enhanced using the method in Ref. [KHL16], with thin regions being highlighted in white.

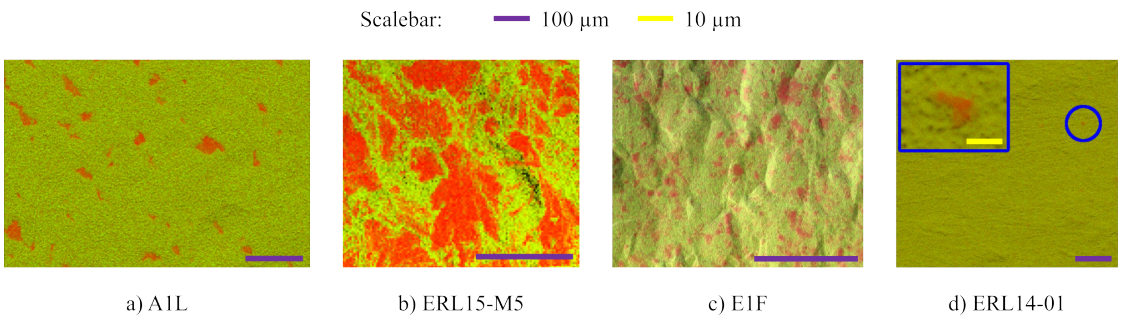

Figure 5.8: Examples of the different coverages seen in samples coated in the furnace. Regions in green are sufficiently thick - red regions are considered too thin. Figure a) is a large grain sample placed near the base of the furnace, showing (4.0 ± 0.7)% thin film coverage. Figure b) is a cut-out from ERL1-5 showing (65.7 ± 1.5)% coverage. Figure c) is a fine grain sample placed high up in the furnace, above the cavity equator height, and shows (30 ± 2.0)% coverage. Figure d) is a fine grain sample located near the equator and coated alongside cavity ERL1-4, that shows less than 0.5% coverage by thin film regions - a zoomed-in inset locates a very small region that may still be thick enough for good performance.

detection. By contrast, an identical fine grain sample E1F coated with the same recipe but hanging in the furnace at above the height of the cavity equator (although with no cavity actually being there) showed a much higher coverage of (30 ± 2.0)%, as seen in Figure 5.8 c). However, this is still not as high as the coverage seen in the cut-out from the fine-grain cavity ERL1-5, seen in Figure 5.8 b) – although this coating did not benefit from the ΔT during ramp-up as samples A1L, E1F, and ERL14-01 did.

The third and final trend seen is that if the oxide layer of the substrate is grown to a thickness of $\approx$ 60 nm prior to coating and then coated with a recipe with a ΔT during the ramp-up, the sample shows no coverage by thin film regions (down to detectable limits) regardless of substrate grain size or location in the furnace. This technique of electrolytic anodisation, referred to as pre-anodisation, was previously used at Siemens AG to improve the surface uni-

formity of their Nb_3Sn [HUS80, Hil80, KHPU81], but was later abandoned in favor of the use of nucleation agent [DMP+89] as the samples coated using only nucleation agent with no anodisation were deemed to be of satisfactory surface uniformity, and there were fears that the migration of the oxygen into the substrate would ruin the RRR of the substrate and degrade the performance of the cavity. However, considering that samples A1L and E1F still demonstrated detectable amounts of thin film region coverage in spite of the use of a ΔT during ramp-up and the use of $SnCl_2$ as a nucleation agent point to an additional benefit to be gained from the re-introduction of pre-anodisation. The exact impact of pre-anodisation is shown in the next section.

In light of these results, the following can be summarized:

- Samples coated in the reaction chamber, at the cavity equator level, exhibited thin film regions regardless of grain size, even in the presence of a gradient between source and chamber during the ramp to coating temperature
- Fine grain samples coated near the source did not exhibit thin film regions, but samples coated onto large or single grain niobium did
- Growing the oxide layer of the substrate before coating resulted in a uniform coverage free of thin film regions in both fine and small grain samples, regardless of location inside the furnace chamber

These results are further summarized in Figure 5.9. Following in the footsteps of these earlier results, we will now detail results from more systematic measurements performed to explain the coating behaviour.

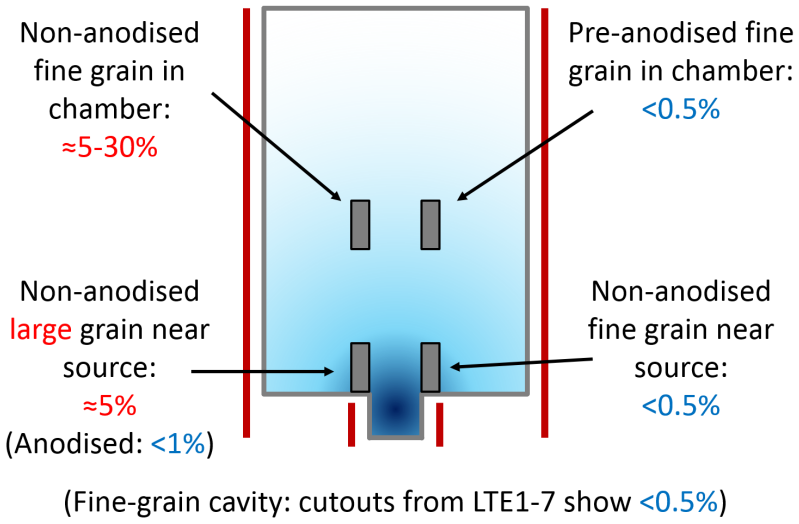

Figure 5.9: A diagram summarising the coating behaviour of different samples depending on their preparation and their location in the furnace. The combination of a high local tin vapour pressure during the ramp-up (dependent on the position in the furnace) and the use of pre-anodisation results in the most uniform coverage.

5.1.1 The pre-anodization process

Before continuing, a brief description of the electrolytic anodization process used at Cornell to grow the oxide layer on niobium will be given. We begin with the niobium samples, which are given an ultrasonic rinse in methanol and left to dry on a lint-free rag. They are then hung from a niobium wire in a bath of sodium hydroxide solution, 10% w/w, and surrounded by an electrode of high purity tin wire. A DC, current-controlled power supply was used, with the positive terminal attached to the niobium wire and the negative terminal attached to the tin wire electrode. The voltage on the power supply was set to the desired voltage - most often, 30 V - and the current was limited to a value corresponding to current density on the sample of approximately 10 mA/cm^2. The power supply was turned on, and the voltage was allowed to increase at a rate that kept the current density at the desired limit. Once at the target volt-

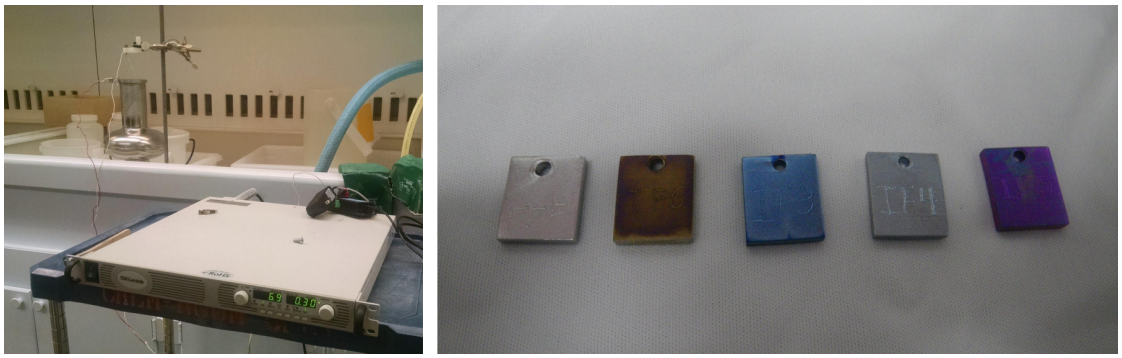

Figure 5.10: Left, the chemistry setup for anodising the interior of a niobium cavity. Right, a series of samples with different voltages of pre-anodisation, these being (from L to R): 0 (none), 5, 15, 30, and 60 volts.

age, the power supply was held there for 1 minute before being turned off, after which the samples were removed from the NaOH solution, rinsed in water, and given an ultrasonic bath in methanol. They were then dried on a lint-free rag and moved to the cleanroom for coating. Photographs of the anodization setup and the difference between an anodized and non-anodized sample are shown in Figure 5.10.

For cavities, the anodization process was slightly different. Due to the larger surface area and the limitations on the size of the anode, it was discovered that limiting the current during the early stages of the anodization resulted in the voltage locking around 3-5 V. This was overcome by briefly going to a higher current density, at which point the voltage limitation would be overcome and the voltage would begin to rise. The current density limitation was then reduced back to the desired level, whereupon the voltage would slowly and steadily increase to the set level. Once there, to ensure a uniform coating, the voltage was held for 5 minutes (as opposed to 1 for the samples). The cavity was then rinsed with DI water and given an ultrasonic in DI, before being moved to the cleanroom for a high pressure rinse (HPR) with ultra-pure DI water before coating.

The anodization voltage was chosen based on the desired oxide thickness. Literature on electrolytic anodization states that the relationship between ultimate voltage setting and oxide thickness is linear, with a relationship of approximately 2.2 nm/V [JCC+91]. The current density of 10 mA/cm^2 was chosen based on results in the literature [ONSA04] that this current density resulted in a uniform oxide layer. The anodisation was performed in an solution of 10% w/w NaOH in DI water.

5.1.2 Studies on the impact of pre-anodization

The first study performed to investigate the formation of these thin film regions on samples focused on the impact of substrate RRR. Four pairs of samples of different substrate RRR reactor grade (<50), 90, 320, and 500 were prepared, with one of each pair being anodized before going to 30 V, corresponding to an oxide thickness of approximately 70 nm. The four samples were coated together, hanging at the cavity equator level, using the coating recipe seen in Figure 3.2. The four samples were analyzed using EDS mapping to determine the coverage by thin film regions.

A new analysis method was developed for these samples, in which the map was separated into its individual pixels, each pixel being a ratio of the tin signal to the niobium signal at that pixel. A histogram of these ratios was then taken, and normalized by the sum of the frequencies. For a sample free of thin film regions, in which the coverage is uniformly coated with stoichiometric Nb_3Sn, the distribution will appear as a Gaussian distribution. The presence of thin film regions will result in an excess of signal in the low tin-to-niobium ratios,

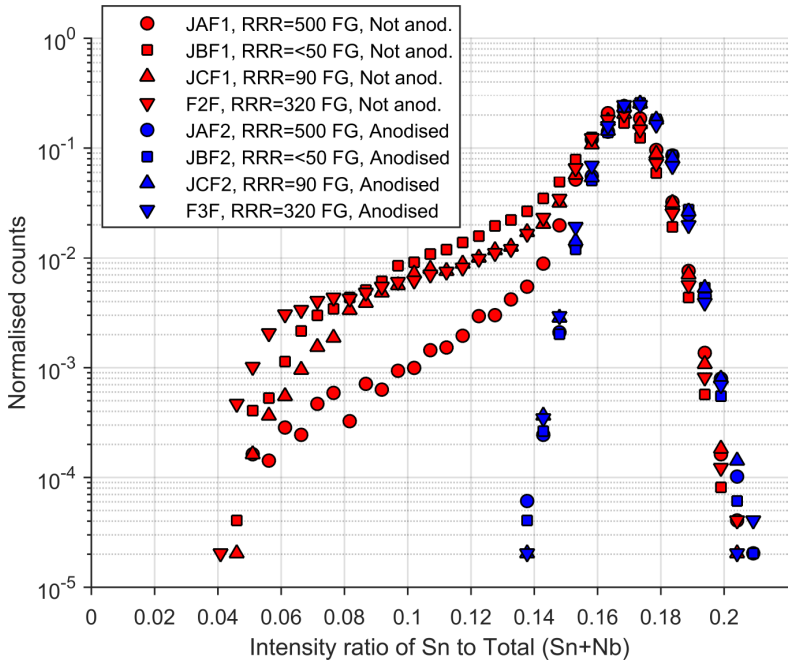

Figure 5.11: Histograms of the ratio of Sn to total signal for the pixels from EDS maps (taken at a beam energy of 30 kV) of samples of different substrate RRR, both pre-anodised (blue) and not pre-anodised (red). In all non-anodised samples, regions of thin film were seen, as evidence by the presence of a tail on the left side of the Gaussian distribution at approximately 0.17. By comparison, pre-anodised samples do not show any evidence of thin film regions, regardless of the RRR.

and create a "tail" on the left side of the Gaussian. This analysis was performed on all 8 samples, and the results can be seen in Figure 5.11.

The results show that in all the fine grain samples that were not anodized, thin film regions were detected. The measurement suggests a weak correlation between RRR and thin film surface coverage, although this is not certain. However, in all pre-anodized samples no thin film regions could be detected within the limits of the measurement. This result indicates that regardless of any correlation between substrate and the penchant for the formation of thin film regions, the action of the oxide layer overrides this correlation.

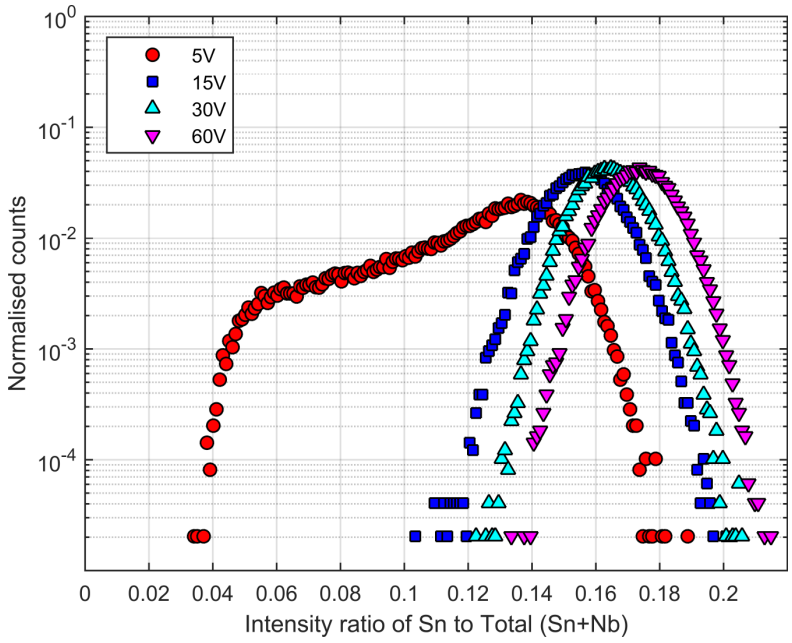

Figure 5.12: A histogram, in a manner similar to Fig. 5.11, of the ratio of the tin signal to total signal for all pixels in an EDS map taken of sample, for four different samples. Each sample received a different level of anodisation before coating, corresponding to a difference in the oxide layer thickness (literature gives a value of 2.2 nm/V [JCC+91]).

The second study focused on the thickness of the oxide layer before coating. Four samples, taken from the same 320 RRR fine grain substrate used for one of the sample pairs in the previous study, were prepared and anodized to different voltages: 5, 15, 30 and 60 volts, corresponding to an oxide thickness of 11, 33, 66, and 132 nm respectively. Following this, the samples were coated hanging in the furnace at the cavity equator level using the same recipe used in the variable-RRR study. After coating, the samples were analyzed using EDS mapping, and the maps plotted in the histogram seen in Figure 5.12.

Of these four samples, only that anodized to a voltage of 5 volts exhibited thin film regions. To the limits of the EDS measurement, there was no difference in surface chemistry or uniformity between the samples of 15, 30 and 60 volt oxide thickness. This suggests that the action of the oxide can saturate, and that

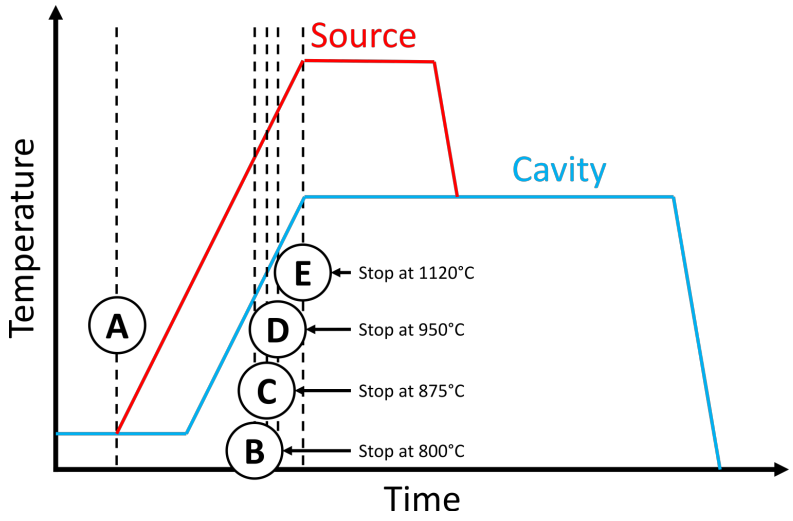

Figure 5.13: Simplified diagram of the stop motion coating process. Each sample was taken through the same coating, but interrupted at a different point, as given by the labels (A) through (E). The complete coating cycle was that given in Figure 3.2. Exact temperatures at which the coating was interrupted are annotated and also given in the text.

past a certain point the thickness of the oxide layer has no further effect.

At this point, it was determined that the next stage would be to make a "stop-motion" movie of the coating process, in which a sample pair (one anodized, one not) would be taken to a pre-set point in the coating process, at which point the power to the furnace would be cut and the samples removed upon complete cooling. This process was repeated, using different sample pairs all taken from the same RRR 320 niobium stock, for a number of different stages in the coating, as illustrated in the diagram seen in Figure 5.13. Each sample was then taken to the scanning electron microscope for imaging and EDS analysis.

Each sample pair, corresponding to a frame, is identified as follows:

(A) Nucleation only; This coating was taken to the end of the 5 hour nucleation stage before halting

(B) To 800°C; Following nucleation and the establishment of a 150°C ΔT between the source and the chamber, this coating was stopped when the chamber reached 800°C during the ramp.

(C) To 875°C; As for the previous pair, only upon reaching 875°C in the chamber.

(D) To 950°C; As for the previous pair, only upon reaching 950°C in the chamber.

(E) To end of ramp; The coating process was halted upon reaching the coating temperatures and officially beginning the coating stage.

For each pair of samples, images of the surface were taken, followed by an EDS map for the purposes of generating a histogram in the fashion of Figures 5.11 and 5.12. The images, arranged in their order in the coating process, are shown in Figure 5.14; the histograms for the non-anodized and pre-anodized samples are shown in Figures 5.15 a) and b), respectively.

Differences between the pre-anodised (PA) and not pre-anodised (NPA) samples are immediately clear even before coating, as seen in the first image in the series shown in Figure 5.14. The PA sample shows a more mottled surface, indicating that the oxide layer grown during the anodisation process is amorphous in nature. By comparison, the NPA sample appears smooth, with no visible oxide layer, and the odd surface contaminant (likely introduced during sample handling).

At the end of the nucleation stage, the difference is even more stark: the tin nucleation sites on the PA sample, while a similar distance apart from each other to the NPA sample, are much larger. The EDS histogram (seen in Fig-

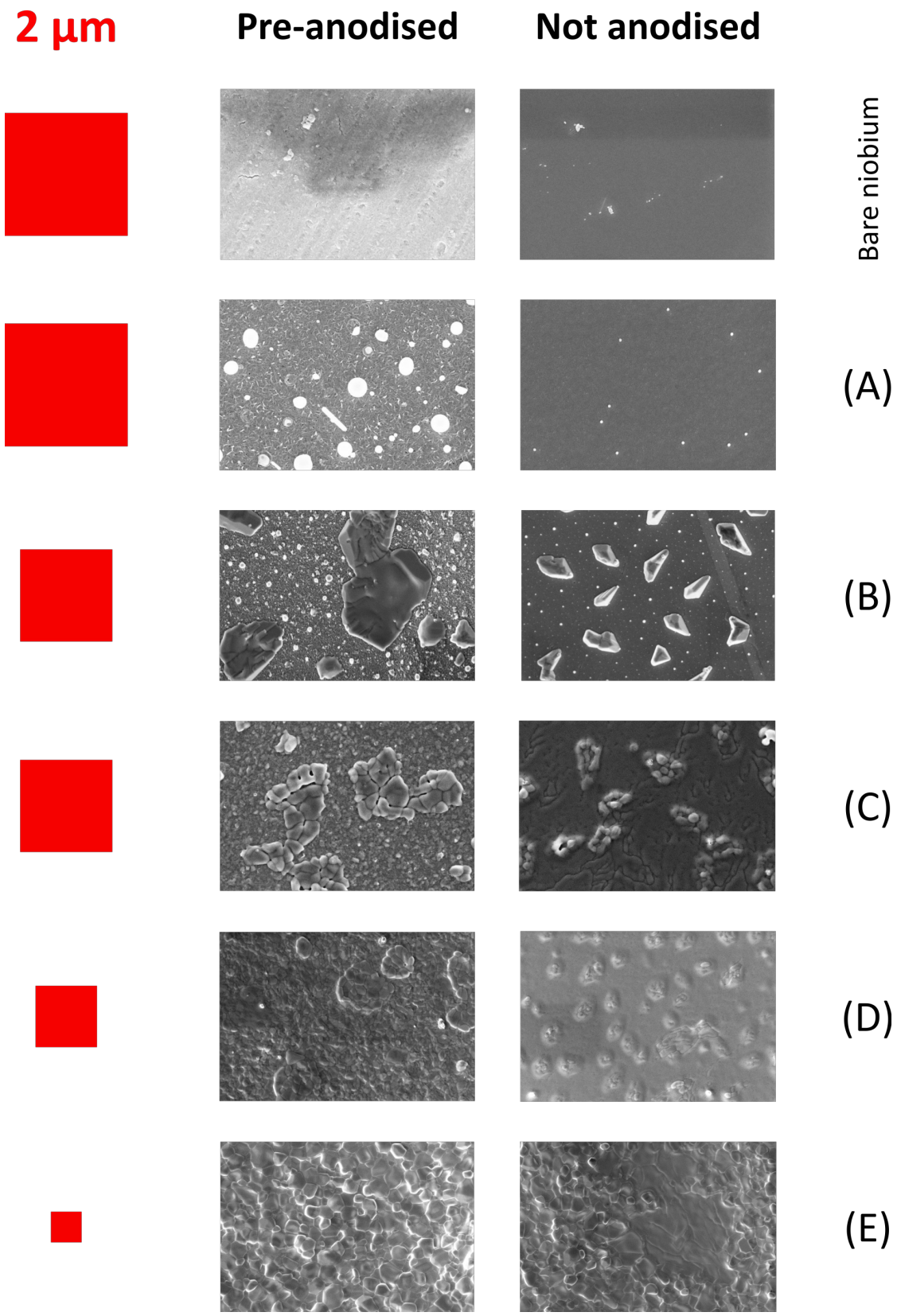

Figure 5.14: SEM images of samples taken from steps (A) through (E) in the stop motion coating process, showing the difference in coating between a pre-anodised and non-anodised sample. The box on the left side of each image pair is a scale box for that pair, and is 2×2 µm in size.

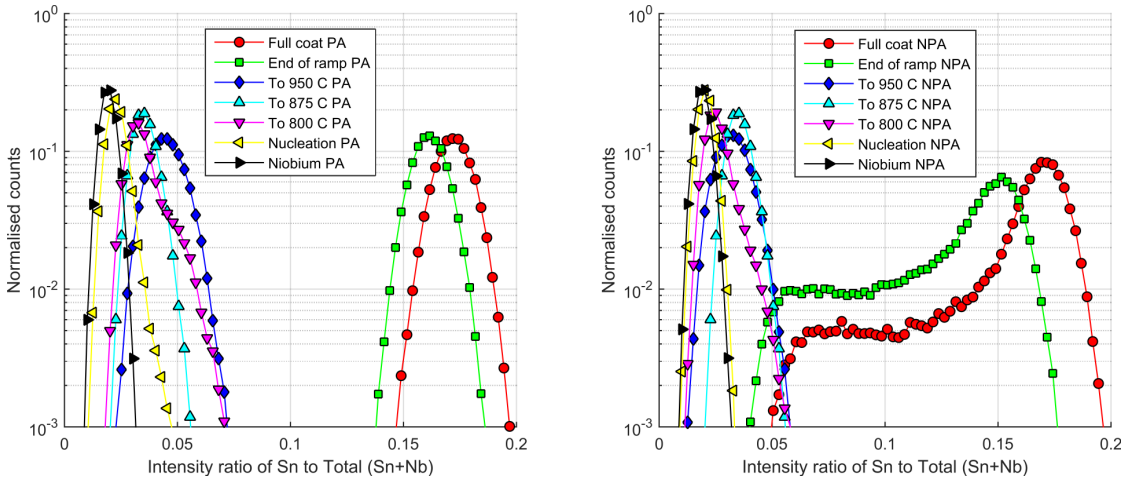

Figure 5.15: Histograms of the pre-anodised (left) and non-anodised (right) EDS maps for the samples from the stop motion coating. Note that pure niobium does not result in an intensity ratio of Sn to the total of zero – this is due to background noise resulting in a false positive signal in each energy channel of the EDS detector. Therefore, a systematic error results in all values of the ratio being shifted to the right along the x-axis.

ure 5.15) confirms that considerably more tin was drawn from the $SnCl_2$ vapor during the nucleation stage for the PA sample when compared to the NPA one. Surprisingly, the PA sample was a light dust brown when removed, indicating that a significant portion of the artificially grown oxide layer had survived the 5 hour nucleation stage at 500°C.

Moving to the 800°C sample, we see that small regions of Nb_3Sn have appeared on the surface. In the PA sample, these regions appear as large "blobs", appearing to be almost a single grain. By contrast, in the NPA sample, these Nb_3Sn regions appear as small triangular crystals, that appear to point in preferential directions (likely due to some epitaxy with the substrate). In both cases, in between these regions of Nb_3Sn we see that the nucleation sites continue to survive, although they still appear larger in the PA sample. The amorphous, mottled surface between the nucleation sites of the PA sample also indicates

that even by 800°C traces of the oxide layer survive.

At the 875°C mark, we see that in the PA sample the large Nb_3Sn blobs have broken up into smaller crystals, and in between them smaller crystals have begun to appear on the surface. A few nucleation sites are still visible on the surface between these features. In the NPA sample, the small triangular Nb_3Sn crystal have also broken up, but the area between them (now completely devoid of nucleation sites) appears matte and uniform, with a low density of grain boundaries compared to the PA sample. This surface appears very similar to that seen in the thin film regions, as seen in the SEM image shown in Figure 5.6.

Reaching 950°C point, the PA sample shows a uniform coverage by small grains of Nb_3Sn, although the outline of the blobs is still visible in the topography. At this stage, only a few trace nucleation sites remain, but at this stage the high density of grain boundaries across the surface will ensure that the layer grows in a uniform fashion free of thin film regions. In the NPA sample, the triangular crystals have been fully absorbed into the surface, as the thin film of Nb_3Sn between them has grown to the same height. However, annealing has led to the density of grain boundaries in these regions to decrease even further, which will eventually stunt the growth of the layer. Although regions of high grain boundary density exist at "blisters" on the surface where the triangular crystal were once located, and these regions will grow to cover the space between them, a significant amount of surface will remain devoid of growth-assisting grain boundaries.

The impact of this difference is visible even by the time the "coating" temperature of 1120°C is reached, in stage D). By this point, the regions that benefited from a high grain boundary density have grown to a thickness of just approx-

imately 1 μm, but whereas the PA sample shows know detectable trace of thin film regions, the NPA sample shows region where the coating has remained thin due to a low density of grain boundaries. These go on to act as the Q-slope inducing thin-film regions that plagued cavities such as ERL1-5.

Turning to the associated EDS map histograms seen in Figure 5.15, a similar picture is painted. In the nucleation of the coating, the PA samples have drawn more tin from the $SnCl_2$ gas, which agrees with the observation seen in Figure 5.14 of the larger nucleation sites. At 800, 875, and 950°C the EDS histograms do not reveal a difference as stark as the SEM images, but by the end of the ramp at 1120°C the characteristic left-hand tail indicative of the presence of thin-film regions is clearly visible in the NPA histogram. This tail persists all the way to the end of the coating and annealing stage. In contrast, this tail is absent from the PA samples, both at the beginning of the coating stage (at the end of the ramp) and at the end of the full coating.

The conclusion drawn from this experiment is two-fold: firstly, that the oxide layer acts as a catalyst to draw more tin from the $SnCl_2$ vapour, and also as a barrier that slows the uptake of the nucleation sites into the bulk. The outcome of this is that a higher density of small grains forms across the surface once Nb_3Sn begins to form during the ramp-up, and by extension a higher density of grain boundaries. With such a uniform density of grain boundaries, the layer grows free of thin film regions.

The natural oxide layer in fine grain niobium is sufficient to draw a significant amount of tin from the nucleation agent gas, but is not thick enough to prevent their uptake into the bulk before 875°C. Large grain niobium suffers more since the natural oxide layer is even thinner to begin with [SSW+06]. However,

the use of a ΔT between the source and the chamber can alleviate this issue somehwat as it increases the vapour pressure of the tin during the ramp-up at any given time. Once a high enough tin vapour pressure is established, the growth process is handed over from the nucleation agent to the source vapour. As the ΔT increases, this handover happens sooner, and the nucleation sites do not need to survive as long, sustained by the nucleation agent alone.

Although fine grain samples located near the source benefit from a very high vapour pressure, the gas that reaches the samples hanging in the furnace has expanded into a larger volume and is therefore lower in pressure. Therefore, the handover happens at different times for samples located at the source and hanging in the furnace chamber, and this explains the difference in coverage by thin film regions between sample ERL14-01 and E1F. In cavities, which act to contain the volume of the source gas, the vapour pressure remains as high as that seen by samples near the source, which explains why samples cut from cavities do not show thin film regions like those from fine grain samples hanging in the furnace.

Growing the oxide layer relaxes the need for a high tin vapour pressure sooner during ramp-up (and by extension a higher ΔT), as it increases both the amount of tin transferred during the nucleation stage (with which to fuel the growing layer) and the length of time for which they survive. While a high ΔT allows the hand-over to happen sooner, a thicker oxide layer allows it to happen later and still succeed. So long as the hand-over happens before the nucleation sites are extinguished, the formation of thin film regions is suppressed.

It is therefore this hand-over process from nucleation to coating where the layer is most at risk from the formation of thin film regions. The larger the

area/volume to be coated, the higher the action of the source vapor pressure alone will be sufficient, and the action of an artificially grown oxide layer can serve to guarantee the uniformity of larger structures. For structures such as 650 MHz 5-cell PIP-II cavities, it is likely that both a temperature gradient during ramp and pre-anodization of the substrate will be necessary to prevent the formation of thin film regions and the resulting Q-slope.

This raises the question as to why the Wuppertal cavities, which were coated using a separate tin source hot-zone, demonstrated Q-slope as seen in Figure 3.7 in spite of having a temperature gradient between source and chamber during ramp-up. We propose that the design of the furnace, reproduced in Figure 5.16, may lend to an explanation: the tin source and the reaction chamber are in completely separate hot-zones, separated by a (presumably niobium) tube of some length. It is likely that this tube had a cooling action on the tin vapor, reducing the vapor pressure during ramp-up and mitigating what assistance might have been given by the action of the temperature gradient during ramp-up. The literature published by the University of Wuppertal does not indicate that the oxide layer of the cavities was grown before coating, and that instead the action of the nucleation agent onto the native oxide layer was used.

The presence of thin film regions in the cavities coated at the University of Wuppertal is suggested by two results: in one [PHK+88], a measurement of quality factor against temperature for a 1 GHz cavity coated at Wuppertal exhibits a drop in surface resistance at around 9.2 and 6 K, which would suggest that the RF field was interacting with the Nb_3Sn-niobium interface, as would happen in the presence of thin-film regions. Secondly, a temperature map measurement performed at Jefferson lab [BKM+97] demonstrates heating

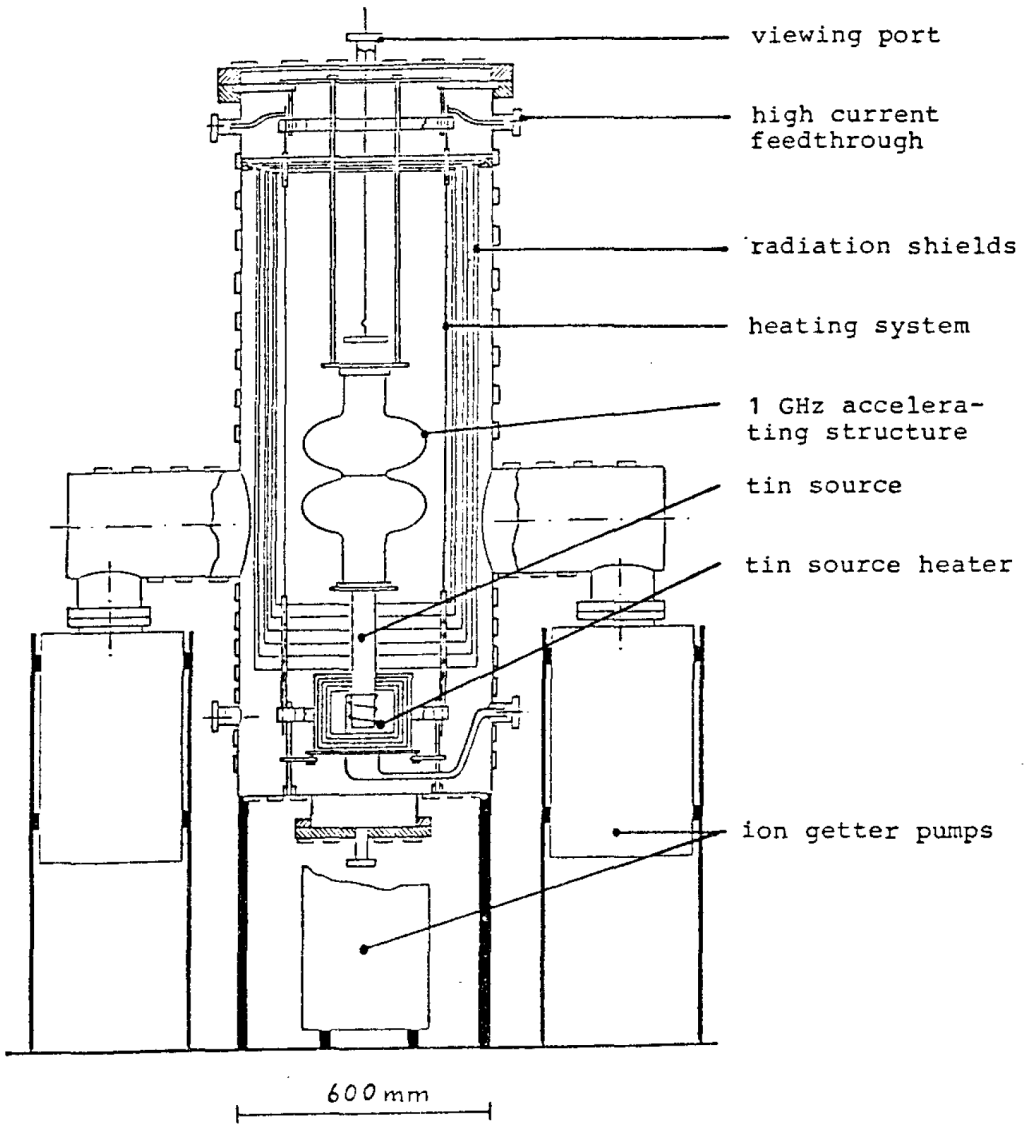

Figure 5.16: Schematic diagram of the Wuppertal 1 GHz coating furnace, from Reference [PHK+88]. The tube that passes between the hot-zones of the tin source and the coating chamber is suspected to have played a role in cooling the tin gas during the ramp-up stage and suppressing the beneficial effect of the ΔT during the ramp-up, resulting in the formation of a small number of thin film regions (in the manner of sample A1L in Figure 5.8), which resulted in the Q-slope seen [MKM96].

at the equator. The equator weld of a cavity usually exhibits larger niobium grains due to the action of the weld seam, and since (as discussed earlier) non-anodised large grain niobium exhibits greater propensity for the formation of thin-film regions, this is where the thin-film growth would most likely occur.

Although the coverage by thin-film regions in the Wuppertal cavities must be less than that seen in ERL1-5, it is likely still enough to cause heating and the resultant Q-slope. Samples that exhibit thin-film area coverages of 5-10% appear perfectly uniform to the human eye, and their presence is difficult to detect in the SEM without specific EDS mapping or knowledge of what these regions look like. Thin film regions have also been found in samples coated at Jefferson lab [PEK+17], which would explain why these cavities suffer from a Q-slope similar to that seen in the Wuppertal cavities. In the case of the Jefferson lab cavities, the lack of a secondary hot-zone for the tin source prevents the use of a temperature gradient, but pre-anodization may be sufficient (particularly if only coating a single-cell) to prevent the formation of thin film regions.

5.1.3 Pre-anodization of a single-cell cavity

Following the discovery that anodisation suppresses the formation of thin film regions, the procedure was applied to a cavity. The chosen cavity was LTE1-6, which had demonstrated good performance comparable to that seen in LTE1-7 (as shown in Figure 5.1). The performance of the cavity after having received a coating like that shown in Figure 3.2 is shown in Figure 5.17. Following this test the Nb_3Sn layer was stripped, and the niobium surface was anodised to a voltage of 30 V (an oxide thickness of 66 nm). The cavity was then re-coated with

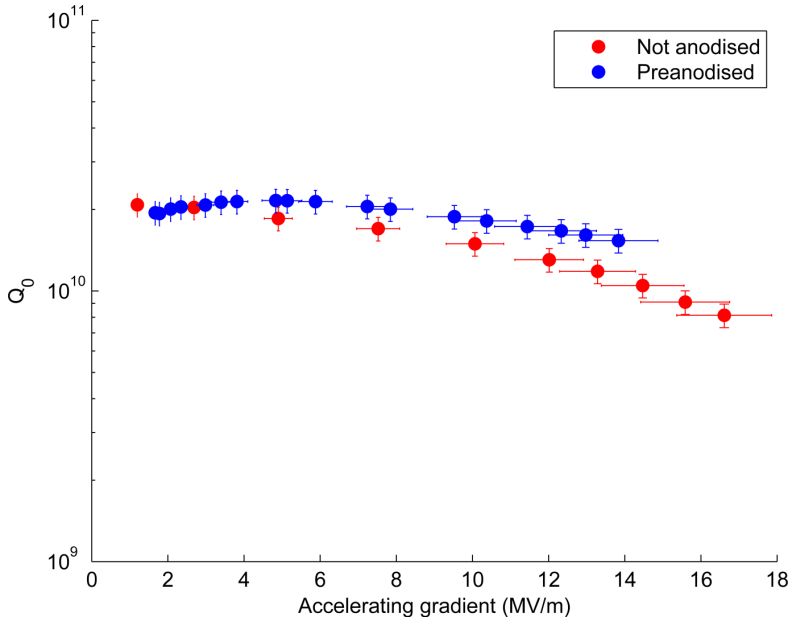

Figure 5.17: Q vs E taken at a cavity bath temperature of 4.2 K for 1.3 GHz single-cell cavity LTE1-6, without and with pre-anodisation of the cavity surface prior to coating. An improvement of approximately 3 nΩ at 14 MV/m is seen.

the recipe seen in Figure 3.2. The new performance is also shown in Figure 5.17.

As can be seen, the low-field Q is unchanged, but the medium field Q has improved. This can be explained by a further suppression of Q-slope inducing thin film regions. Although cut-outs from a cavity coated without the use of pre-anodisation (similar to the first coating of LTE1-6) did not reveal the presence of thin film regions using the EDS map method shown in Figure 5.7, this method is only sensitive down to a thin film coverage of 1%. It is therefore still possible for thin film regions to be present in quantities lower than this, inducing a mild Q-slope (although not nearly as severe as that seen in Wuppertal cavities). Although the change is not easily detectable by surface analysis methods, it is implied that the use of pre-anodisation further suppressed the formation of thin film regions and further improved the medium-field Q. In contrast, the quench field was measured to be lower after pre-anodisation; however, the change in

the quench field (although detectable) is not statistically significant given the distribution of quench fields seen in Nb_3Sn cavities (seen in Figure 6.1), and it is therefore unclear whether it was the pre-anodisation caused a lowering of the quench field.

One fear when pre-anodizing a cavity is that the oxygen will migrate into the niobium substrate during coating and reduce the RRR, and so with it the thermal conductivity $\kappa = 0.25\ \mathrm{W/(m{\cdot}K)} \cdot \mathrm{RRR}$ [PKH98]. From Ref. [PKH98], the definition of RRR is

$$\mathrm{RRR} = \frac{\rho_{300\,\mathrm{K}}}{\rho_{4.2\,\mathrm{K}}}\,, \tag{5.1}$$

where $\rho_{300\,\mathrm{K}}$ and $\rho_{4.2\,\mathrm{K}}$ are the normal conducting electrical resistivity of niobium at 300 K and 4.2 K, respectively. At 300 K, the impurity levels we are dealing with do little to affect the resistivity, which is $1.52 \times 10^{-7}\ \Omega\mathrm{m}$, with a niobium density of $8570\ \mathrm{kg/m^3}$ and a molar mass of $0.0929\ \mathrm{kg/mol}$ [Hay14]. If an oxide layer is grown in a pre-anodisation to 30 V, this corresponds to an oxide of a thickness of approximately 70 nm. Assuming a uniform Nb_2O_5 layer with a density of $4600\ \mathrm{kg/m^3}$ and a molar mass of $0.2658\ \mathrm{kg/mol}$ [Hay14], complete absorption of the oxide layer into the bulk (assuming a 3 mm wall thickness) will result in an increase in the atomic concentration of oxygen of approximately 22 ppm.

The change in electrical resistivity due to an increase in the concentration of impurities is given by [Sch81, KM00]

$$\Delta\rho = \alpha\,\Delta c\,, \tag{5.2}$$

where α is an empirically-measured constant that is different for each species of impurity (N, O, C, etc.), and $\Delta\ c$ is the change in impurity content, in this case 22 ppm or 2.2×10^{-3} atomic percent. For oxygen, $\alpha = 4.5 \times 10^{-8}$ Ωm/(at-%) [KM00]. The new RRR can then be determined relative to the pre-coating RRR by

$$\frac{\mathrm{RRR_{new}}}{\mathrm{RRR_{old}}} = \left(\frac{\rho_{300\,\mathrm{K}} + \Delta\rho}{\rho_{4.2\,\mathrm{K}} + \Delta\rho}\right)\left(\frac{\rho_{4.2\,\mathrm{K}}}{\rho_{300\,\mathrm{K}}}\right), \tag{5.3}$$

which, for an initial RRR of 320, gives a post-coating RRR of 260. After 5 coatings with 30 V pre-anodisations, the RRR has fallen to 150. Although this niobium bulk RRR would be unacceptable for operation at 2.0 K, as the thermal conductivity is too low, at the operating temperature of 4.2 K for Nb_3Sn cavities the thermal conductivity is largely unchanged from high RRR niobium – in fact, it is an order of magnitude higher [KB96]. Therefore, this reduction in RRR is of little consequence until the value falls below 40.

To model this, a thermal simulation was run with a 3 micron layer of Nb_3Sn coated atop a 3 mm substrate of Nb_3Sn [DHL17]. Since the Cornell furnace also coats the outside of the cavity, a further 3 microns of Nb_3Sn was added to the other side of the niobium substrate. The system being modelled is illustrated in Figure 5.18. Using a thermal feedback simulation that takes into account the non-linear nature of BCS surface resistance and thermal conductivity with temperature, the system was modelled as a function of surface field for different values of the substrate RRR and for the thickness of the two Nb_3Sn layers. The model was simulated at both 1.3 and 6 GHz. The resulting Q vs E curves are given in Figure 5.19.

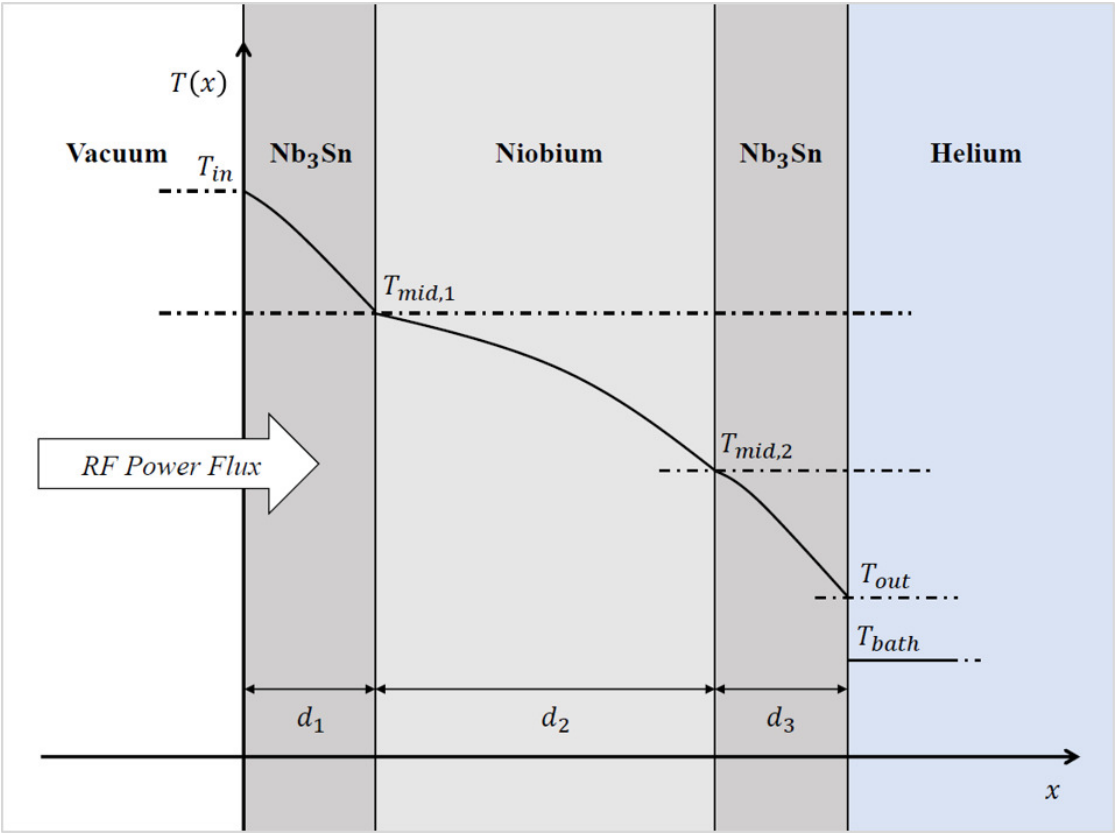

Figure 5.18: The setup for the thermal simulation of Nb_3Sn on niobium, coated on both sides (in the style of a Cornell coating) [DHL17]. The three layers are simulated separately, and the power flow at each interface is matched in a iterative fashion until a complete, stable solution for the heat flow equation is found. This image courtesy of Jixun Ding, Cornell University [DHL17].

The model shows that at 1.3 GHz and 4.2 K, there is no serious impact down to even reactor-grade RRR on cavity performance up to fields of 45 MV/m by global thermal feedback, a result that agrees with the result from LTE1-6, which saw no reduction (on the contrary, an improvement) in performance. However, at 6 GHz, where the BCS resistance of Nb_3Sn is higher, thermal feedback does result in a reduction in cavity performance. However, 6 GHz structures are much smaller than 1.3 GHz ones, and the reduction in volume means that the action of a source/chamber gradient alone will more than likely be enough without needing to pre-anodize the structure.

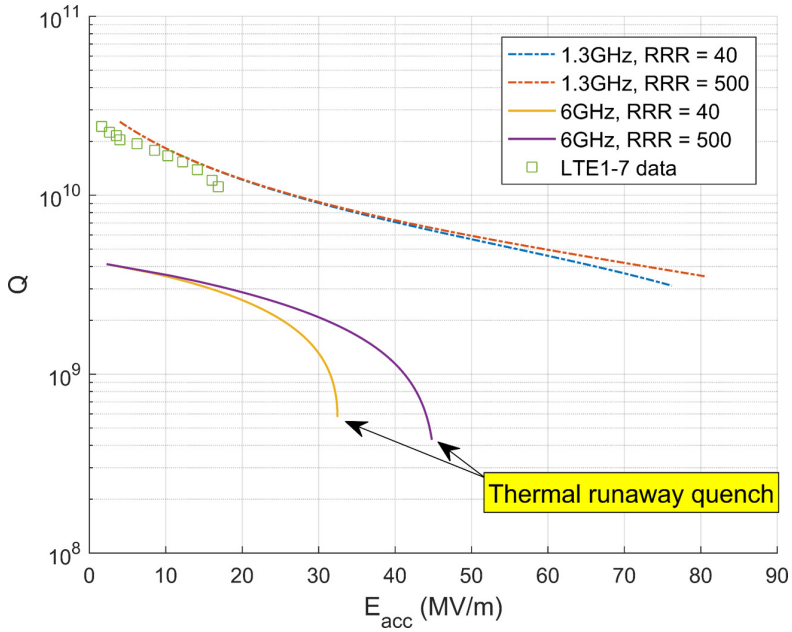

Figure 5.19: Results of the simulation for the setup shown in Figure 5.18, for both 1.3 and 6 GHz cavities with different substrate RRR operating at a cavity bath temperature of 4.2 K. At 1.3 GHz, global thermal feedback is so small that substrate does not become an issue until the RRR reaches reactor grade. At 6 GHz, substrate purity is more of a concern. These simulations assume a niobium substrate wall thickness of 3 mm, a Nb_3Sn coating thickness (inside and outside) of 3 μm, and 8 mG of trapped flux. This image courtesy of Jixun Ding, Cornell University [DHL17].

To conclude the first part of this chapter, we can summarize the following regarding the uniformity of the Nb_3Sn layer: that thin film regions arise due to a failure in the hand-over process from nucleation to coating, and that this formation can be suppressed through the use of a temperature gradient between the tin source and the reaction chamber and the growth of the niobium substrate oxide layer prior to coating. In the case of smaller structures, such as 1.3 GHz single-cells or 6 GHz multi-cells, where the source is sufficiently close to the RF surface, the use of pre-anodization is likely unnecessary and, in the case of high frequency structures, possibly unwanted as the reduction in substrate RRR would lead to thermal feedback. However, for larger structures such as 1.3 GHz

9-cells or 650 MHz 5-cells, where the coating volume is much larger, the action of the source/chamber temperature gradient alone will most likely be insufficient to guarantee a successful hand-over, and pre-anodization will be necessary. At these lower frequencies, and at the expected 4.2 K operation, the reduction in the substrate RRR is not expected to impact the cavity performance, and even if it were so, a slight decrease in performance would be infinitely preferred over the Q-slope seen in previous Nb_3Sn cavities.

5.2 Losses from trapped magnetic flux

Once the surface uniformity of an Nb_3Sn cavity has been achieved, ensuring the excellent performance expected of Nb_3Sn requires careful control of a number of operational parameters. Arguably chief amongst these is minimizing the amount of magnetic field that is trapped in the cavity walls after the transition through the critical temperature.

The negative impact of trapped magnetic flux on the performance of superconducting cavities has been well known for some time [Hal90, BCD+97, PKH98]. As the cavity transitions through the critical temperature, the action of the Meissner effect works to expel ambient magnetic fields from inside the superconductor. However, during the transition, some of the flux may become pinned on so-called pinning sites, remaining trapped as a normal conducting core inside the superconductor.

The losses from trapped flux are linearly proportional to the amount of flux trapped in the cavity. This can be explained by the fact that vortices in a superconductor are trapped in units of the flux quantum ϕ_0. Since the contribution to

the resistance from each vortex is (on average) equal, then the total contribution is proportional to the number of vortices trapped. A simplified model, in which the losses from each vortex originate from losses in the normal conducting core, gives a contribution to the resistance from trapped flux described by

$$R_s = \frac{H_{\text{trapped}} \pi \xi_0^2 \mu_0 R_n}{\Phi_0} , \tag{5.4}$$

where R_s is the surface resistance contribution from trapped flux, H_{trapped} is the amount of trapped flux, ξ is the superconductor coherence length, and R_n is the normal state resistance of the material [PKH98]. However, this model overestimates the contribution from the normal conducting core; instead, more recent theories by Gurevich [Gur14, GC13] and Checchin et al. [CGM+15] describe the loss in terms of viscous drag experienced by the vortex as the influence of the RF field causes it to oscillate back and forth.

In bulk niobium cavities, when ignoring thermoelectric currents generated by the cryomodule, trapped flux largely originates from ambient magnetic fields, such as the earths magnetic field or that from magnetized components near the cavity. In niobium cavities coated with Nb_3Sn, the bimetallic interface between the niobium and Nb_3Sn acts as a thermocouple, generating a thermoelectric current in the presence of a thermal gradient along the interface. These thermoelectric currents in turn generate a magnetic field that will inevitably become trapped in the cavity, resulting in a decrease in the efficiency of the cavity in the same manner as if it had been cooled in a large ambient magnetic field.

In order to quantify the losses from trapped flux in Nb_3Sn due to ambient magnetic fields and thermoelectric currents, we performed an experiment to

investigate this phenomenon in a single-cell cavity. The cavity used was the 1.3 GHz TeSLA shape single-cell designated LTE1-7, which was coated with the recipe seen in Figure 3.2. The experimental setup is illustrated in the diagram seen in Figure 5.20. The Helmholtz coils mounted on the cavity allowed for the generation of a uniform magnetic field that permeates the cavity cell, pointing in the direction along the cavity beampipe. This magnetic field simulates the presence of an increasingly strong ambient magnetic field, in excess of that already present in the cryostat (which is magnetically shielded to suppress the presence of the earths magnetic field). By cooling slowly and ensuring as uniform a thermal gradient as possible across the cavity during the transition through the critical temperature, the magnetic field generated by the Helmholtz coil will be trapped and the magnetic field generated by thermoelectric currents will be suppressed, allowing for the quantification of the impact of ambient magnetic fields. In contrast to this, cooling quickly while using the heater mounted at the base of the cryostat, with the Helmholtz coil turned off, allows for the generation of a large thermal gradient along the length of the cavity (up to 6-8 K/m), trapping a large amount of thermoelectrically generated magnetic field while suppressing the presence of the ambient magnetic field thanks to the shielding in the cryostat.

During an ambient field cooldown, a DC power supply is used to generate a current through the coils, which are 30 cm in diameter and placed 15 cm above and below the equator level of the cavity. A single-axis flux gate magnetometer, located on the upper iris of the cavity pointing along the direction of the beampipe (as shown in Figure 5.20), is used to measure the strength of the field applied by the coil. A second flux gate, also located on the upper iris but pointing in an azimuthal direction, is used to quantify (to first order) the ambient and

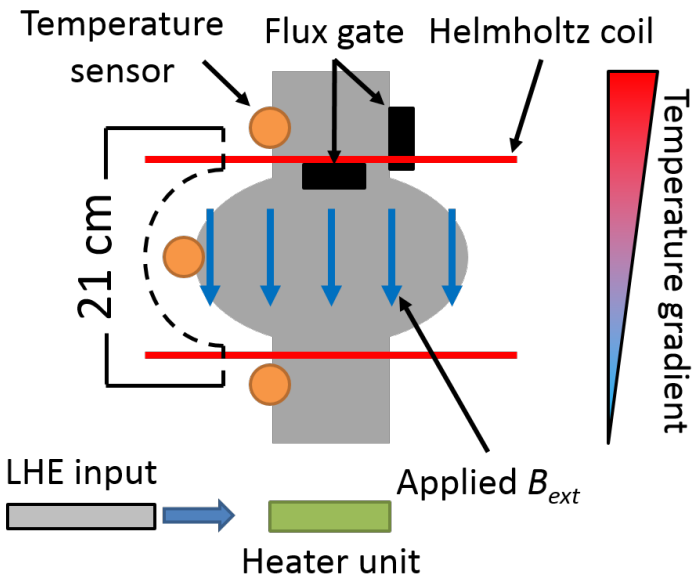

Figure 5.20: Experimental setup for flux trapping studies of cavity designated LTE1-7. A Helmholtz coil pair is mounted above and below the cavity, allowing application of a uniform magnetic field. This field is measured by two flux gates placed on the upper iris of the cavity, one point axially and the other azimuthal to the beampipe axis. Three temperature sensors allow measurement of temperature gradients along the cavity. The use of a heater at the helium input allows a development of a thermal gradient (or, the suppression of one) during the cooldown through T_c.

generated magnetic field that is not in the direction of the beampipe axis.

Upon establishment of the desired magnetic field, the cavity is cooled slowly through the transition temperature, at a rate of approximately 10 min/K and with a gradient of 200 mK/m. This rate is maintained down to a temperature of 6 Kelvin, whereupon the helium valve controlling the flow is opened to its maximum and liquid is allowed to enter the cryostat. Upon reaching 4.2 K, but before much liquid has entered the cryostat, the applied magnetic field is turned off, and the field reading remaining on the axial flux gate is used to determine the amount of flux that was trapped in the cavity. Due to the fact that the trapping in the cavity is not 100% effective, this amount will be less than

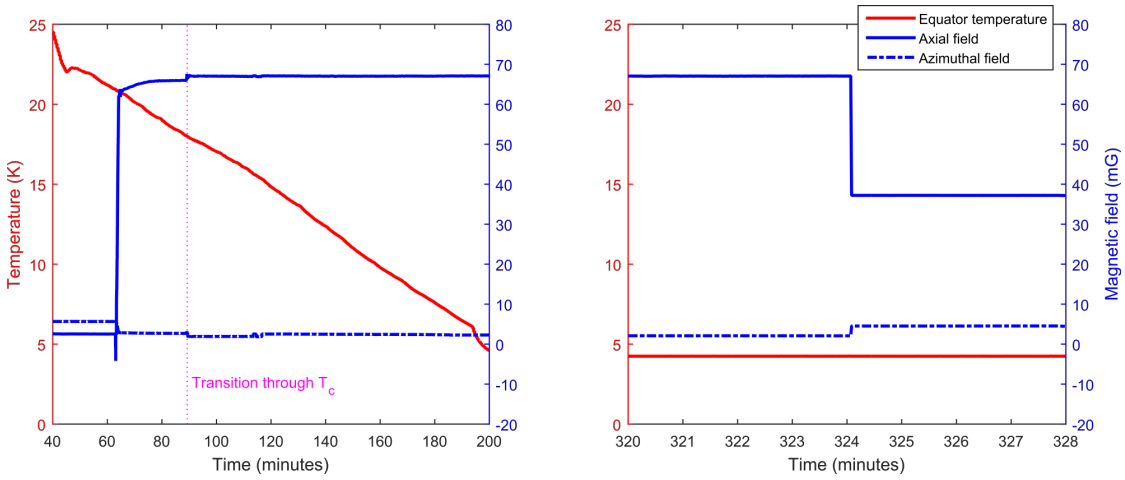

Figure 5.21: Temperature (red) and magnetic field (blue) measurements for a cooldown with an external magnetic field applied. The thermal gradient across the cavity during this time is approximately 200 mK/m. A field of approx. 60 mG (axial measurement) is applied before going through T_c, and maintained until the cryostat is filled with liquid helium at 4.2 K. The field is then turned off, and the remaining field is taken to be that which has been trapped – in this case, (32 ± 5) mG.

the field applied. An example of this measurement is shown in Figure 5.21. The measurement of the trapped flux from the magnetic field is considered the relevant parameter for this type of cooldown.

For a thermal cooldown, the Helmholtz coils are kept unplugged to prevent the generation of any current in them. Helium is introduced into the cryostat, cooling the cavity down to a temperature of approximately 30 K, at which the cryostat is equilibrated and briefly held. The heater at the base cavity is turned on, dissipating between 20 and 150 W of heat. The helium valve is then opened fully, allowing the cold gas to be introduced as quickly as possible. The gas striking the heater is heated and rises very quickly, while the cold gas cools the base of the cryostat and insert. This results in a temperature gradient forming, with the top of the cavity being many Kelvin warmer than the base. This gradient is measured using three Cernox cryogenic temperature sensors, which are

mounted on the irises and equator of the cavity, as seen in Figure 5.20. From this gradient value and knowledge of the geometry of the cavity, we calculate the temperature gradient along the cavity in Kelvin per metre. The transition through T_c begins when the lower iris goes through 18 K and ends when the upper iris does the same, as indicated by the "start" and "stop" annotations in Figure 5.22. The difference in temperature between the sensors at the upper and lower iris is measured at these two times, giving ΔT_1 and ΔT_2. The average of these is taken, and divided by the distance between the two sensors. Note that this distance is not the shortest distance in space, but instead the travel distance from sensor to sensor along the niobium wall, taking into account the curvature of the cavity. This was measured to be 21 cm for the experimental setup shown in Figure 5.20. From this, the thermal gradient $\Delta T/\Delta L$ during the superconducting transition is obtained.

as demonstrated in the example shown in Figure 5.22. This value is considered the relevant parameter for the gradient cooldowns.

By performing a number of cooldowns of these two different types we can demonstrate the equivalence of these two flux trapping mechanisms in their reduction of the cavity efficiency. Beyond this, we will also investigate the dependence of the losses from trapped flux as a function of the strength of the RF field in the cavity.

The cavity chosen for this experiment, designated LTE1-7, had already demonstrated good performance in previous cavity tests, being free of Q-slope and capable of fields up to 16-17 MV/m. In total, 10 cooldowns were performed, with 6 being of the gradient type, 3 of the ambient type, and 1 being "normal", with the ambient field and thermal gradients suppressed as much as possible.

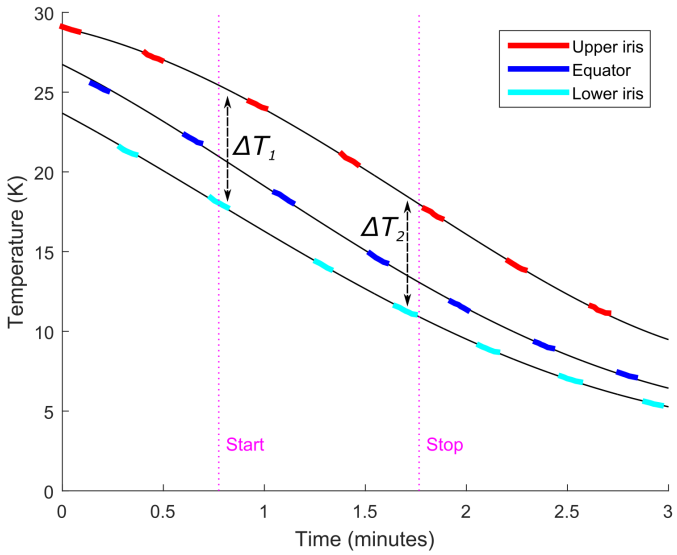

Figure 5.22: An example of a cooldown in a large thermal gradient through T_c. Due to multiplexing of the temperature measurement, only one sensor can be read at a time, and interpolation using fourth-order polynomial fit is used to extrapolation the full range of data. The Helmholtz coil is turned off during this time.

For each cooldown, the following data was collected: quality factor of the cavity from 12 K down to 1.6 K at a gradient of 1 MV/m; quality factor with RF field at 4.2 K up to 12-14 MV/m; quality factor with field RF field at 2.0 K up to 12-14 MV/m. The limit of 14 MV/m was chosen to avoid any chance of quenching the cavity (and in doing so, changing the amount and distribution of trapped flux in the cavity), particularly during the cooldowns where a large amount of magnetic field had been trapped and the quality factor of the cavity had been significantly reduced.

The spread of the quality factor with temperature for all the different cooldowns is shown in Figure 5.23, demonstrating the spread in the low-temperature quality factor with different amounts of trapped flux. For each of these cooldowns, the Q vs E plot taken at 2.0 K is assumed to be almost entirely dominated by residual resistance - a reasonable assumption, considering

that the contribution from the BCS resistance at these temperatures is approximately 0.2 pΩ. Therefore, these curves can be taken to be a measurement of the residual resistance against the accelerating gradient[1]. Separating the ambient and gradient cooldowns, and plotting the surface resistance at 2.0 K and 1 MV/m as a function of the cooldown parameter (trapped ambient field for the ambient cooldowns, thermal gradient for the gradient cooldowns), we can see the change in residual resistance as a function of the cooldown parameter. The outcome of this measurement is shown plotted in Figure 5.24.

As observed in niobium [GKL16], the residual resistance increases linearly with the amount of trapped magnetic flux. This linear dependence is also seen in the relationship between the surface resistance and the thermal gradient through the transition temperature. By performing a linear fit, we determine the sensitivity to trapped flux, i.e. the amount of surface resistance gained per unit of cooldown parameter, either the ambient field trapped from the Helmholtz coil or the thermal gradient through the transition temperature. At 1 MV/m of applied RF field, corresponding to a peak magnetic field of (4.2 ± 0.6) mT, the sensitivity is found to be (0.5 ± 0.2) nΩ/mG from the ambient cooldowns and (3.3 ± 0.5) nΩ/(K/m) from the gradient cooldowns.

It is of critical importance that the numbers are specified for a RF field value of 1 MV/m. This is because the sensitivity to trapped flux is a function of RF field. Upon comparison of the Q vs E at 2.0 K for the two types of cooldowns, we can see in Figure 5.25 that the surface resistance at 2.0 K (at which temperature the residual resistance dominates) increases with the peak applied mag-

[1]Although the Q vs T measurements were performed down to a temperature of 1.6 K, the cryostat is unable to sustain this temperature at higher gradients. Although curves taken at 1.6 K would have even less BCS contribution, the 2.0 K curves are more practical in terms of data taking and are already sufficiently representative of the residual resistance of the cavity

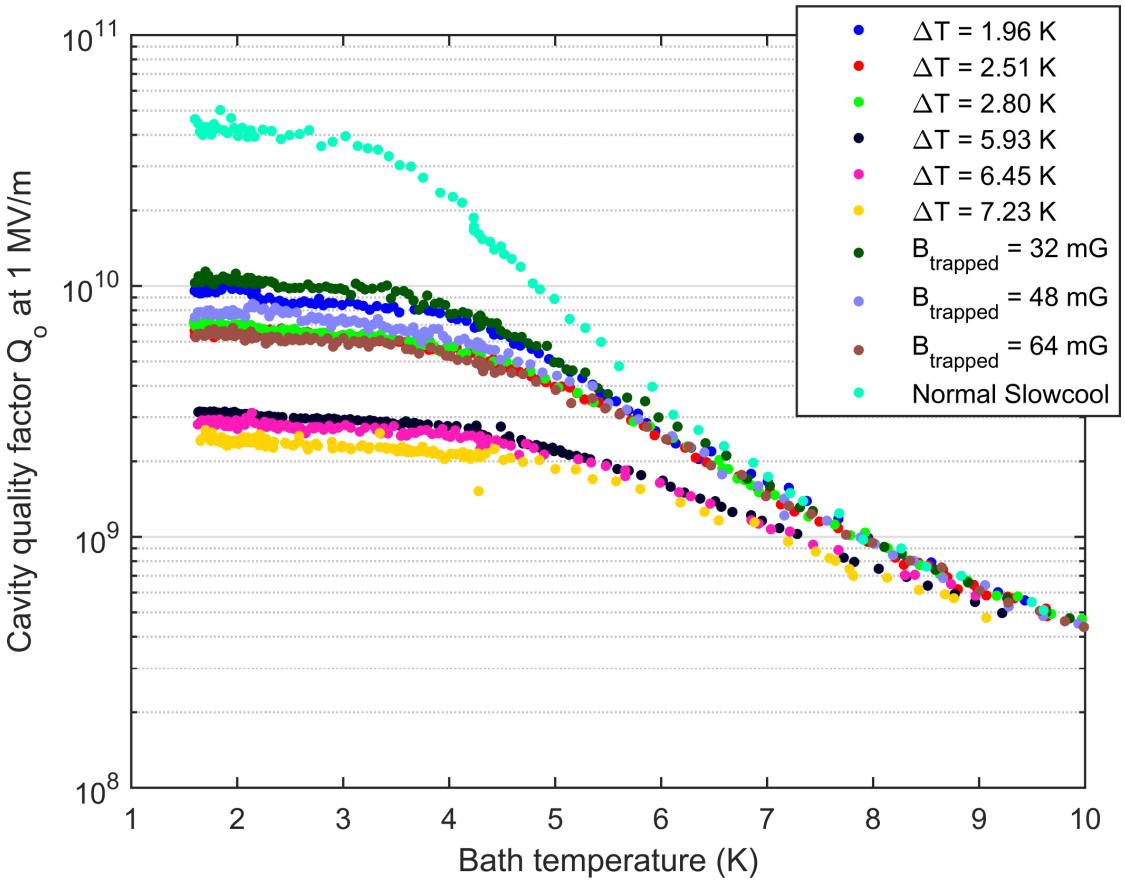

Figure 5.23: Spread of the Q vs T measurements for all the cooldowns of cavity LTE1-7, in different thermal gradients and applied magnetic fields. The impact of the trapped flux on residual resistance can be seen in the quality factor at low temperatures.

netic field, in a seemingly linear fashion. By comparing these slopes and taking a measurement of the sensitivity to trapped flux at different values of the RF field, we find that the sensitivity to trapped flux is increasing with RF field. The same can be found for the gradient cooldowns, with the sensitivity to gradient. The values of sensitivity to trapped flux and thermal gradient as a function of RF field are shown in Figure 5.26 (left).

Fitting for a linear increase in sensitivity for both ambient and gradient cooldowns, we can take the ratio of the two sensitivities as a function of field, shown plotted in Figure 5.26 (right). By taking a linear fit, we find the slope

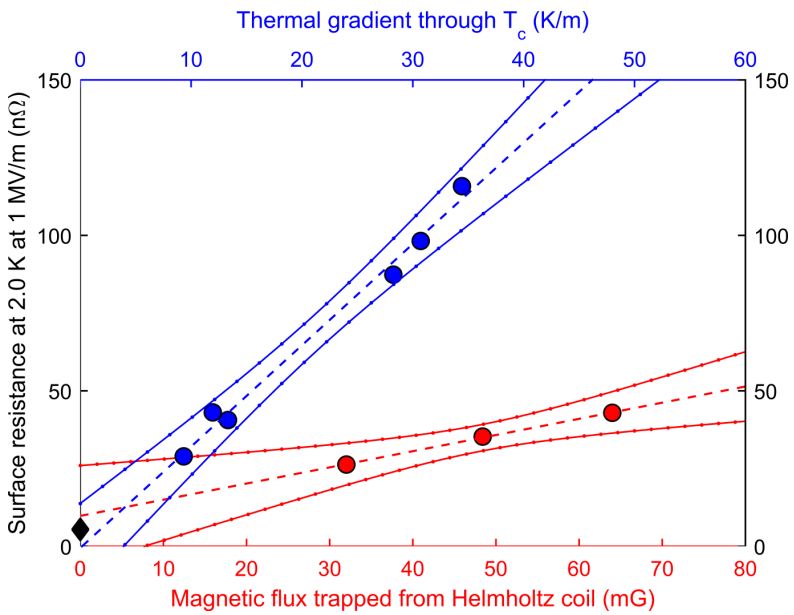

Figure 5.24: Plot of the surface resistance at 2.0 K – which is dominated by the residual resistance – of LTE1-7 for different values of thermal gradient (blue) and trapped magnetic flux (red). In both cases, a linear relationship with R_s is seen. The black diamond indicates the resistance seen at 2.0 K and 1 MV/m in a cavity following a normal slowcool, in which the thermal gradients and ambient field are minimised to the greatest extend possible (this point is not considered when making the linear fits shown).

to be zero within measurement error. Using the offset of the linear fit, this allows us to define a relationship between the ambient field trapped and the thermal gradient, i.e. the amount of flux trapped per unit of thermal gradient through the transition temperature. From this, we calculate this value to be (6.2 ± 0.3) mG/(K/m). Use of this value allows us to rescale the data from the gradient cooldowns and cast the parameter as an amount of trapped magnetic flux, in the fashion of the ambient cooldowns. From this we plot the sensitivity to trapped magnetic flux as a function of RF field for both the ambient and gradient cooldowns, as seen in Figure 5.27. A linear fit to this plot gives a flux-dependent contribution to the surface resistance of

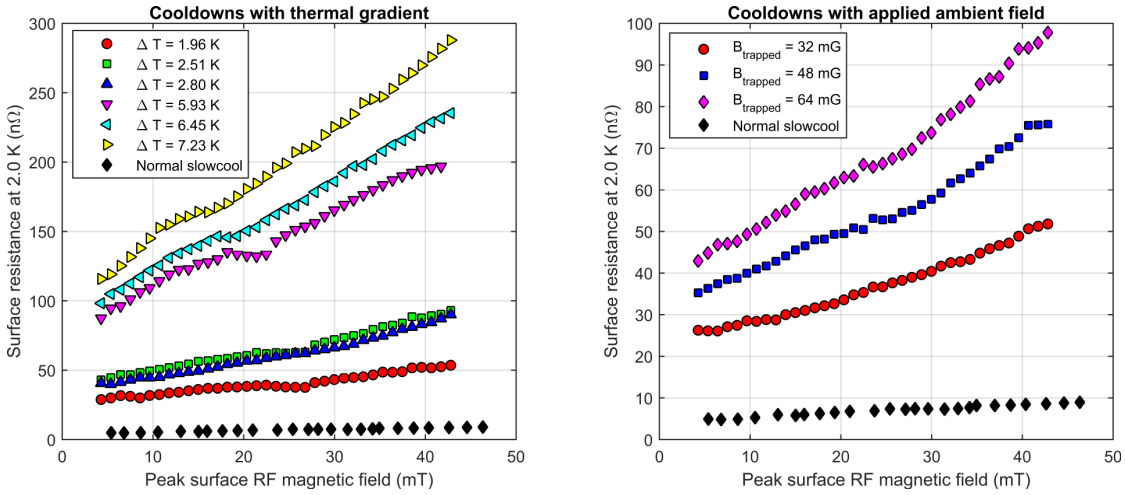

Figure 5.25: Q vs E curves (obtained using the "continuous" method described in section 4.2) for all the cooldowns performed as part of the experiment on LTE1-7, separated by thermal gradient cooldowns and applied field cooldowns. For comparison, a curve taken following a normal slowcool (in which the thermal gradients and ambient fields are minimised to the maximum extent possible) is also shown.

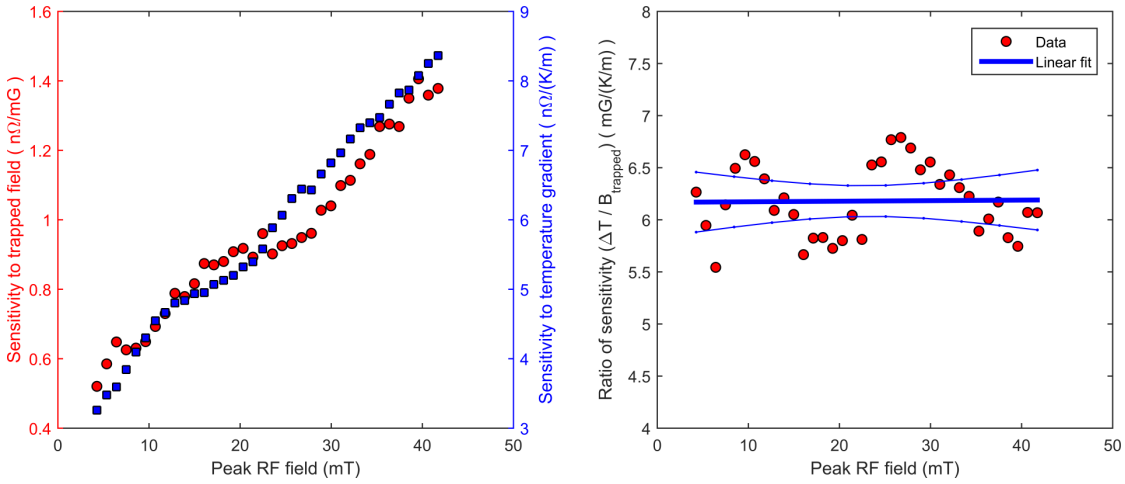

Figure 5.26: Left, a plot of the sensitivity to trapped flux (red) and thermal gradient through T_c (blue) as a function of the applied RF magnetic field. On the right, the ratio of these two sensitivities has been fitted to a linear fit, as shown. The ratio is found to be constant with RF field within the confidence interval of the linear fit, which is shown as the dotted lines above and below the fit line.

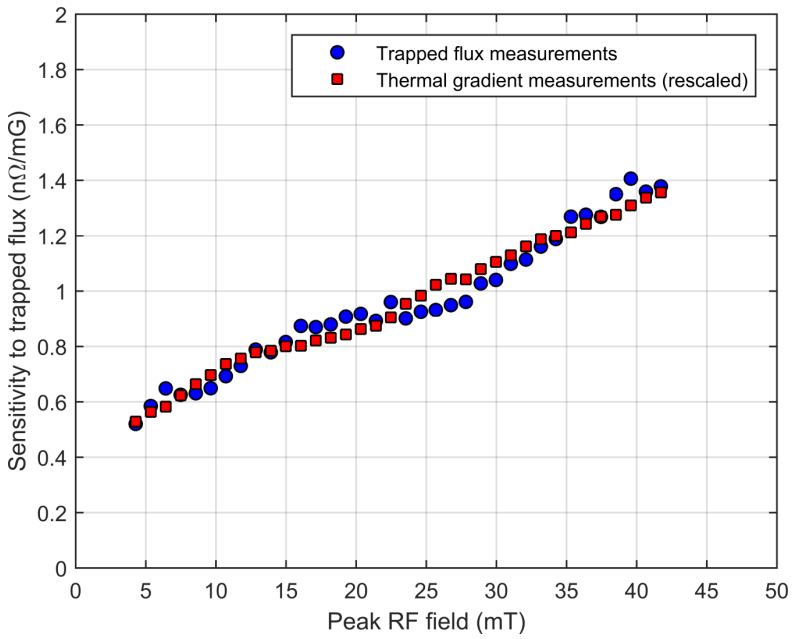

Figure 5.27: The sensitivity to trapped flux of Nb_3Sn cavity designation LTE1-7, as a function of the applied RF magnetic field. The data from the thermal gradient measurements has been rescaled to amount of trapped magnetic flux by (6.2 ± 0.3) mG/(K/m).

$$\frac{\mathrm{d}R}{\mathrm{d}B_{\text{trapped}}} = R^0_{fl} + R^1_{fl} B_{rf} \,, \tag{5.5}$$

where B_{rf} is the peak RF field in the cavity and the constants R^0_{fl} = (0.47 ± 0.02) nΩ/mG/ and R^1_{fl} = (21 ± 1) pΩ/mG/mT.

5.2.1 Theoretical model of thermoelectric magnetic flux and flux losses

The generation of magnetic fields causing an increase in the residual resistance of an Nb_3Sn cavity in the presence of a thermal gradient can be described theoretically using the Seebeck effect between a chain of thermocouples that repre-

sents the planar interface between the two metals. The Seebeck effect is a conversion of heat directly into a potential difference (referred to as a thermoelectric voltage), such that the voltage generated in a material along the direction of the thermal gradient is

$$V = \int S(T)\, dT \ , \tag{5.6}$$

where $S(T)$ is the Seebeck coefficient. The Seebeck coefficient is a function of temperature, but in the event that the thermal gradient is small then S can be approximated as being constant, such that $V = S\,\Delta T$. In a single material, the establishment of a temperature gradient will result in a thermoelectric voltage, but no current (provided ΔT is constant in time). However, a junction between two metals with dissimilar values of S (as in, for example, a thermocouple temperature sensor) will result in the establishment of a continuous thermoelectric current even with no time variation in ΔT.

We consider a substrate of niobium (material a) coated with a layer of Nb_3Sn (material b). Along the length of the coating, we break the system down into a concatenated series of length Δx with a thermal gradient along it of ΔT. We model each material as a battery with an internal resistance, with the voltage of each battery being provided by the Seebeck effect as $S_{a,b}\Delta T$, and shorted to each other and the top and bottom. This model is shown in Figure 5.28.

We can use the superposition principle to model each one of these sections, labelled N, $N+1$, and so on, separately. Since the short at the end of each section prevents the currents $I_a^{N+1,N-1}$, $I_b^{N+1,N-1}$ from contributing to the currents in sections travelled by I_a^N and I_b^N, it follows that $I_a^N = I_b^N$. We can therefore write

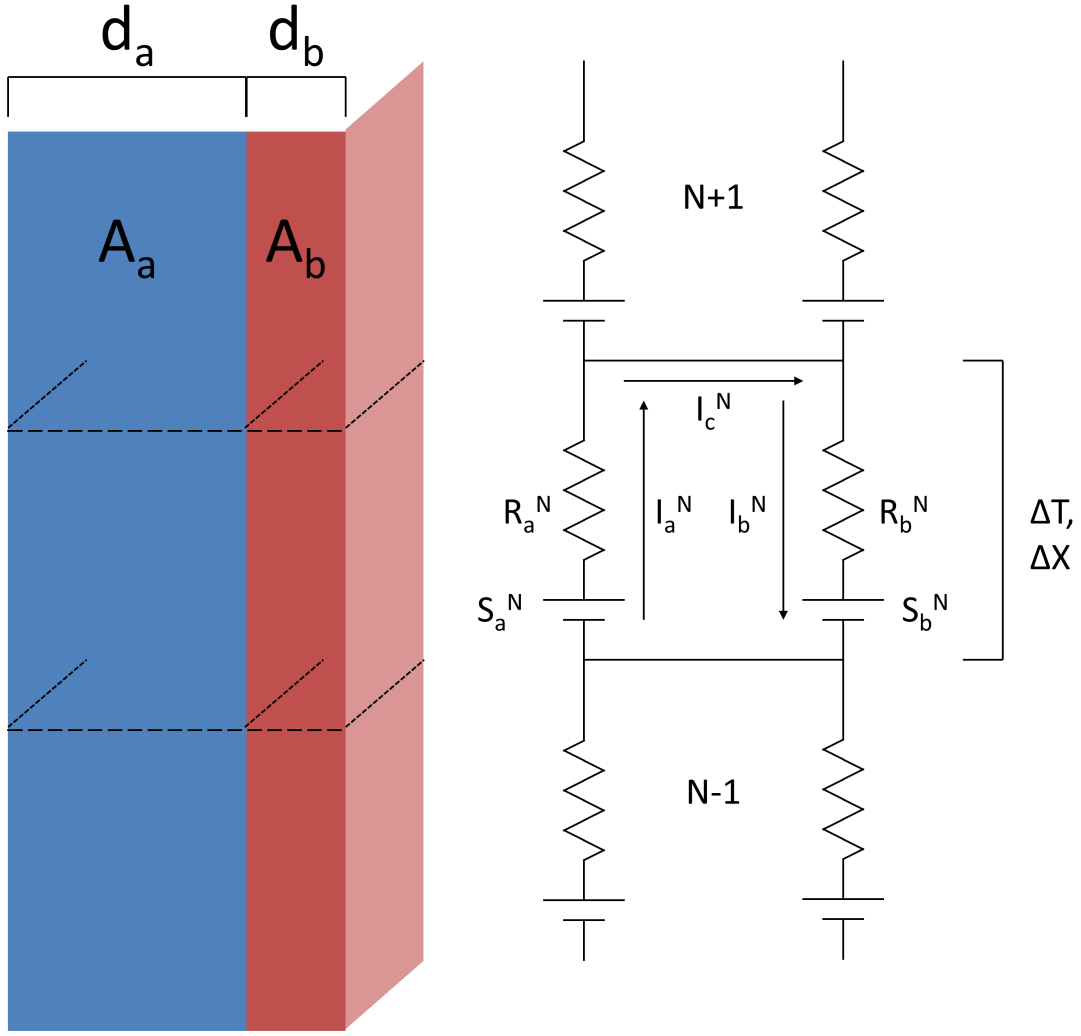

Figure 5.28: Circuit model of the thermocurrents generated by the bimetallic interface between Nb and Nb_3Sn in the presence of a thermal gradient along the length of the interface. The layer is modelled as a series of connected batteries, with a thermoelectric voltage from the Seebeck effect and an internal resistance that comes from the resistivity of the material and the cross-sectional area of the layer.

that

$$S_a^N \Delta T - I_a^N R_a^N = S_b^N \Delta T + I_b^N R_b^N \,, \tag{5.7}$$

and rewrite the resistance of the layers $R_{a,b}$ in the terms of their bulk resistivity $\rho_{a,b}$, such that

$$S_a^N \Delta T - I_a^N \frac{\rho_a^N}{A_a} \Delta x = S_b^N \Delta T + I_b^N \frac{\rho_b^N}{A_b} \Delta x \,, \tag{5.8}$$

where $A_{a,b}$ is the cross-section area of the substrate (a) and thin film (b), and Δx is an infinitesimal distance in the direction of the thermal gradient (as seen in Figure 5.28). This can be simplified to read

$$\left(S_a^N - S_b^N\right) \frac{\Delta T}{\Delta x} = I^N \left(\frac{\rho_a^N}{A_a} + \frac{\rho_b^N}{A_b}\right) . \tag{5.9}$$

We assume that the flux is trapped very shortly after the Nb_3Sn goes superconducting (and that therefore $\rho_b = 0$ and $S_b = 0$), which allows us to condense this to (taking $\Delta T, \Delta x \to dT, dx$)

$$S_a(x,T) \frac{dT}{dx} = I(x) \frac{\rho_a(x,T)}{A_a} \,. \tag{5.10}$$

Using Ampere's law, we can draw an Amperian loop to run around the equator of the cavity at a distance from the centre of the cavity to the interface of the niobium to the Nb_3Sn. Taking the current enclosed within this loop I, we determine the magnetic field at the interface to be,

$$B = \frac{\mu_0 I}{2\pi R_c}\,, \tag{5.11}$$

where R_c is the diameter of the cavity. Taking the values of $S_a = 1.0$ μV K^{-1} [Cra14] and $\rho_a = 6 \times 10^{-10}$ Ωm at $T = 18$ K [WW57], $d_a = 3$ mm, $A_a = 2 \times 10^{-3}$ m^2 (assuming a cavity diameter of ≈ 20 cm), gives a sensitivity to thermal gradient of 63 mG/(K/m). This is higher than the observed value; however, this sensitivity assumes that the trapped flux exposed to the RF field is equal to that generated at the interface. In reality, it will be lower, as the field generated by the thermocurrent at the RF surface must be zero (since taking an Amperian loop around the RF surface must give an enclosed current of $I = 0$). If we assume that the current distribution of I is uniform throughout the Nb_3Sn layer, then the thermocurrent-generated field B will increase linearly from zero at the RF surface to a maximum at the interface. If we estimate that only the magnetic field trapped approximately 2λ from the RF surface contributes to the sensitivity to thermal gradient, then the calculated sensitivity decreases by a factor of $2\lambda/d_b$, where $d_b = 3$μm is the thickness of the Nb_3Sn layer. For $\lambda = 140$ nm, this gives a calculated sensitivity to thermal gradient of $(0.28/3) \times 63 = 5.9$ mG/(K/m), which is in agreement with the measured result of (6.2 ± 0.3) mG/(K/m).

The linear dependence of the sensitivity to trapped flux on the RF field is more complex to describe. The linear dependence has been known for some time[BCD+01], but has to date only be described by empirical models. To understand the effect in Nb_3Sn and by extension, what parameters to vary in an effort to suppress it it is necessary to have a more detailed model that takes into account material parameters. A model of weak flux pinning, proposed by theorists Danilo Liarte and James Sethna, shows promise in describing the effect,

and the gist of the theory is described here, as well as its analytical result.

The observance of a non-constant sensitivity to trapped flux indicates the presence of non-ohmic losses, not described by Equation 1.10. The motion $\mathbf{u}$ of a vortex line whose magnetic flux $\mathbf{Œ}$ is subject to a current density $\mathbf{J}$ can be described using the Bardeen-Stephen equation of motion [BS65],

$$M\ddot{\mathbf{u}} = -\eta \frac{d\mathbf{u}}{dt} - \frac{\delta F_{\mathrm{e}}}{\delta \mathbf{u}} + \mathbf{J} \times \mathbf{Œ} - a\, n_{\mathrm{S}}\, e \frac{d\mathbf{u}}{dt} \times \mathbf{Œ} + \mathbf{f}_{\mathrm{p}}, \ , \tag{5.12}$$

where M is an effective mass, η is a viscosity constant, F_e is the elastic free energy, a is a constant, n_{S} is the density of superconducting electrons, e is the electron charge, and $\mathbf{f}_{\mathrm{p}}$ is a pinning force. The first term on the right hand side describes the viscous damping from the resistance that the superconductor presents to the motion of the vortex. The second term is an elastic line tension that represents dissipation due to reshaping of the vortex. The third and fourth terms represent the Lorentz and Magnus forces, respectively, from the electric current and the motion of the vortex. The final term is more general, and represents the impact of pinning sites.

As the vortex oscillates under the influence of the RF field, it dissipates energy due to the action of these different terms. For a non-constant sensitivity to occur, the motion of the vortex must possess a degree of hysteresis, which cannot be the result of the first four terms. To explain this, Liarte and Sethna generate a pinning term that models the impact of a collective sea of weak pinning centres [LAH+17]. As the vortex line moves, it must overcome the pinning from each site as it moves past. This model is visualised in Figure 5.29 (A).

The theory can be solved numerically, but an analytical solution demonstrat-

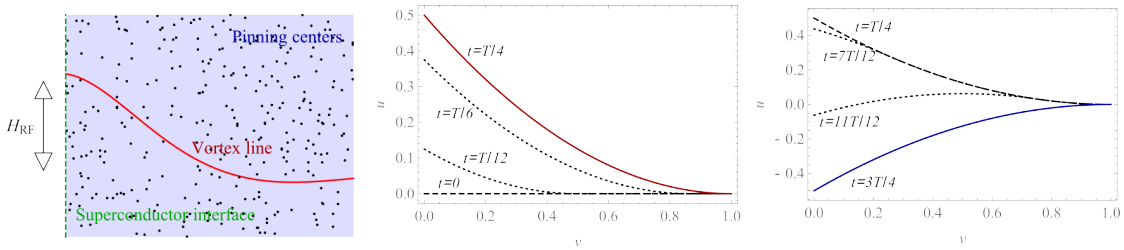

(A) (B) (C)

Figure 5.29: (A) A diagram visualising the weak pinning scenario. A vortex line, strongly pinned deep in the bulk, moves under the influence of the RF field, and is hindered in its motion by a sea of weak pinning centres that it must overcome. (B) The motion of the vortex during the first quarter of the RF period T, as it is displaced from the origin. (C) The motion of the vortex during the second and third quarter of the RF period. The impact of the pinning centres resists the motion of the vortex from being restored to its position at the origin. These figures courtesy of Danilo Liarte, Cornell University.

ing the linear dependence of the sensitivity on the applied RF field can be obtained. Ignoring the mass term (the LHS of Equation 5.12), and the viscous and Magnus terms, the vortex motion is described by

$$\epsilon_0 \frac{d^2y}{dz^2} = f_{\text{pin}} - f_L, \tag{5.13}$$

where $f_L = (\phi_0 H_{rf}/4\pi\lambda)e^{-z/\lambda} \sin \omega t$ is the Lorentz force (per unit length), and $\epsilon_0 = (\phi_0/4\pi\lambda)^2$ is the vortex line tension. The motion of the vortex described by Equation 5.13 follows that shown Figure 5.29 (B) and (C)[2]. As the RF field increases from zero, the vortex begins to be displaced. Although the RF field only penetrates to a depth λ, the impact of the elastic tension of the vortex carries this motion much deeper than λ. As the RF field reaches it maximum at the end of the first quarter of the RF period, the vortex reaches its maximum displacement,

[2]This picture is somewhat unrealistic as the vortex lines trapped from ambient fields and thermal currents are expected to be parallel, not perpendicular to the surface; however, the behaviour described by the analytical result is unchanged

as seen at $T/4$ is Figure 5.29 (B).

At this stage, the RF field begins to decrease. However, the elastic tension of the vortex does not restore the vortex to its original position as the influence of the weak pinning sites prevent this from occurring. As the RF field inverts, it beings to pull the vortex back to its original position and beyond to its new (opposite) maximum displacement. The same weak pinning sites that opposed the initial motion of the vortex to its first maximum now oppose its restoration, resulting in a "two-parabola" shape developing, as seen at $t = 7T/12$ and $t = 11T/12$. It is this process that generates the hysteresis that results in the non-linear sensitivity to trapped flux.

The full derivation will be published by Liarte and Sethna, but the result of solving Equation 5.13 is that the sensitivity to trapped flux is described by

$$\frac{R_0}{B_{\text{trapped}}} = AB_{rf} \ , \tag{5.14}$$

where

$$A = \frac{4}{3}\frac{f\lambda^2\mu_0}{{B_c}^2\xi}\left(\frac{j_o}{j_c}\right)^{3/2} \ , \tag{5.15}$$

where B_c is the thermodynamic critical field. The terms j_o and j_c are the de-pairing current (at which point the Cooper pairs are broken) and de-pinning current (at which point the flux line is de-pinned), respectively. Using Ginzburg-Landau theory, the former can be written as

$$j_o = \frac{4}{3\sqrt{6}\mu_0}\frac{B_c}{\lambda} \,. \tag{5.16}$$

By substituting Equation 5.16 into Equation 5.15, and substituting $B_c = \mu_0 H_c$ using Equation 1.9, we obtain the result that

$$A \propto \frac{f\lambda^2}{j_c} \,. \tag{5.17}$$

This suggest that increasing the mean free path, which according to Equation 1.6 will decrease the value of λ, will result in a decrease in the slope in the sensitivity.

Fitting Equation 5.14 to the curve in Figure 5.27 would result in a nonsensical value of j_c, as the analytical result neglects the impact of the viscous term. However, the analytical solution does demonstrate that the collective weak pinning model can describe the linear sensitivity to trapped flux seen in Nb_3Sn.

5.3 Conclusions on the limitations on cavity efficiency

The first step in ensuring a high-Q Nb_3Sn cavity is the uniform coverage of a sufficiently thick layer free of the thin film regions as seen on the left side of the STEM image in Figure 5.4. These thin film regions are suppressed by aiding the action of the nucleation agent – $SnCl_2$ or SnF_2 – through the use of a high tin vapour pressure during the ramp-up to coating temperatures (through the use of a ΔT during the ramp-up) and the pre-anodisation of the niobium substrate, growing the niobium pentoxide layer to a thickness of 40-70 nm prior to coating.

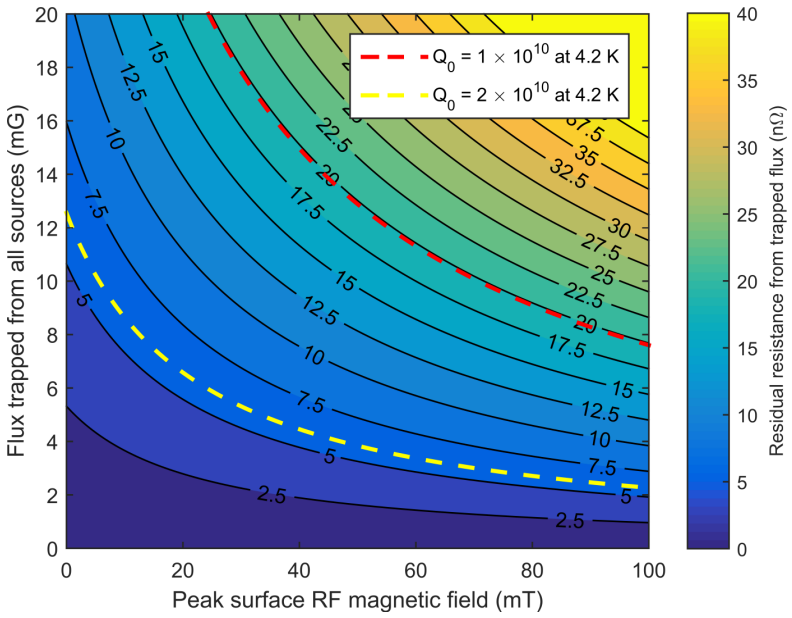

Figure 5.30: Contour plot giving contribution to residual resistance from trapped flux in a 1.3 GHz ILC cavity as a function of the peak applied RF magnetic field. Lines of equipotential give the specification required for operation at a Q of 1 and 2×10^{10} at 4.2 K bath temperature, assuming a BCS component at 4.2 K of 8 nΩ.

Following a successful coating, achieving the highest quality factors requires minimising the amount of trapped flux from both ambient sources and thermoelectric currents generated from thermal gradients during cooldown. The impact of trapped magnetic flux becomes more pronounced at higher RF fields; for example, from the values measured on cavity LTE1-7, a cooldown in 1 mG ambient field (assuming full trapping) and a gradient of 100 mK/m will result in 2.0 nΩ of residual resistance from trapped flux at 5 MV/m, which increases to 3.9 nΩ at 15 MV/m. Shown in Figure 5.30 is a contour plot giving the residual resistance contribution from trapped flux (from all sources) as a function of the peak applied RF magnetic field in an ILC cavity, with, superimposed, lines indicating the specifications required for a quality factor of 1 and 2×10^{10} at a bath temperature of 4.2 K.

Future work on high efficiency in Nb_3Sn shows two promising avenues of research. The first of these is the successful application of post-coating chemistry to decrease surface roughness. To date, no successful post-coating chemistry on 1.3-1.5 GHz cavities has been found (Siemens successfully applied oxipolishing to 10 GHz cavities, but this improvement has not been replicated yet). However, a reduction in the surface roughness would result in a decrease in the field enhancement, and lower the perceived sensitivity to trapped flux with RF magnetic field. This would result in a higher Q at medium-high RF fields.

The second avenue is the application of methods to alter the mean free path or the depinning current (j_c in Equation 5.17) of the material. Increasing the depinning current could be done by introducing stronger pinning sites, while increasing the mean free path ("cleaning" the superconductor) would result in a shorter penetration depth λ. Such changes would reduce the effect of Q-slope in the contribution from the residual resistance, potentially removing this Q-slope entirely. Although the mechanism for altering j_c is not yet clear, the impact of changing λ was observed in 1.5 GHz cavities of niobium sputtered onto copper [BCD+97]. The recent discovery of nitrogen doping [GRS+13] has shown that the mean free path can be lowered in a controlled manner – however, as the mean free path of Nb_3Sn is already quite short, a method will need to be found to increase it. Such a technique could unlock the ability to control the sensitivity to trapped flux of Nb_3Sn, and also increase the coherence length of the material, rendering it less susceptible to defects and potentially increasing the quench field. This is the subject of the next chapter.

CHAPTER 6

LIMITATIONS ON ACHIEVABLE GRADIENT

As important as achieving a high quality factor is, it is for naught if the gradient specification of the machine cannot be met. At time of writing, the gradient demanded for the continuous (CW) light source LCLS-II is 16 MV/m [BCC+15]; in the European XFEL, which operates in a pulsed mode, the gradient specification is 23.6 MV/m [Wei09]. The International Linear Collider has an even higher specification, at 35 MV/m in pulsed mode [BBF+13]. All of these machines would benefit significantly from the greatly improved efficiency offered by Nb_3Sn, but for this to happen the cavity must first demonstrate that it can reliably achieve these gradient demands.

6.1 Constraints on the quench mechanism

A number of measurements, both past and present, as well as the implications of a number of well-understood physical mechanisms, allow us to place a number of constraints on the nature of the quench mechanism without direct measurement. These results guided the choice of the experiment detailed in the second half of this chapter.

It is interesting to note that in all the coatings done at Cornell, the quench field of the cavities varies by only about ±20%, even in spite of some changes to the coating procedure. This can be seen in the histogram in Figure 6.1. This result agrees with a similar observation made on 10 GHz cavities at Siemens AG [HKP+81]. This would seem to suggest a reproducible feature that may be endemic to the method of vapour diffusion for the fabrication of Nb_3Sn, and

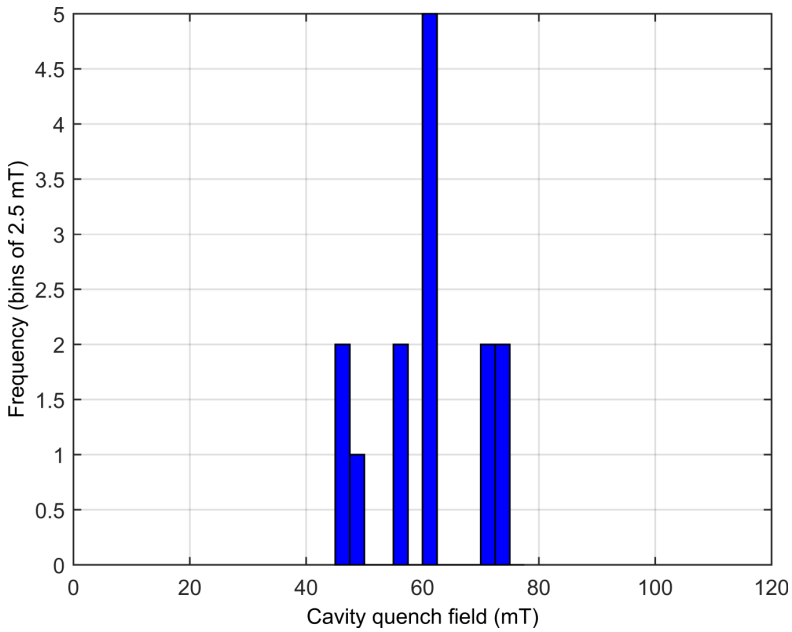

Figure 6.1: Histogram of the quench fields observed in the majority of Nb_3Sn cavity tests performed at Cornell.

that the cause of quench in the cavities coated at Cornell could be the same as that for cavities coated at the University of Wuppertal and at Siemens AG, in spite of the absence of the characteristic Q-slope seen in the former.

6.1.1 Ultimate limit: the superheating field

The superheating field [MSJ67, Cha95, TCS11, VL11] is largely understood to be the ultimate limitation in gradient for a superconducting cavity. The superheating field arises from the fact that although it is energetically favourable for a flux line to exist in the bulk of the superconductor, the energy cost of nucleating a vortex results in an energy barrier at the surface. This raises the field of first flux entry for strongly Type-II materials from the lower critical field H_{c1} [Hei99],

$$\mu_0 H_{c1} = \frac{\phi_0}{4\pi\lambda^2} (\ln\kappa + 0.5) \ , \tag{6.1}$$

to the superheating field H_{sh} [TCS11],

$$\mu_0 H_{sh} = \frac{\phi_0}{2\sqrt{2}\pi\lambda\xi} \left(\frac{\sqrt{20}}{6} + \frac{0.5448}{\sqrt{\kappa}} \right) . \tag{6.2}$$

For the Nb_3Sn coating of cavity LTE1-7, with a penetration depth of λ = (140 ± 20) nm and a coherence length of ξ = (3.4 ± 0.4) nm, equations 6.1 and 6.2 give $\mu_0 H_{c1}$ = (35 ± 8) mT and $\mu_0 H_{sh}$ = (404 ± 9) mT. In an ILC single-cell cavity, these fields correspond to an accelerating gradient of 8 and 95 MV/m, respectively.

Although the superheating field represents the ultimate limit to the entry of flux, defects with a size on the order of the coherence length ξ can serve as vortex nucleation sites, resulting in a suppression of the energy barrier. A local suppression of the critical temperature T_c will also result in a lowering of the energy barrier, allowing vortices to penetrate at these regions of effectively reduced H_{sh}. This latter scenario is a particular risk for Nb_3Sn, since a reduction in the atomic-% tin will result in a reduction in T_c (as described in Figure 2.5).

6.1.2 HPP Klystron testing

The use of high-pulsed-power (HPP) testing is useful in exploring the ultimate limits of a superconductor. A special cavity insert with very strong coupling ($Q_{ext} \approx 10^6, \beta \approx 10^4$) is powered from a high power pulsed klystron, which sends 1 MW pulses into the cavity to rapidly fill it with power. At these high values of

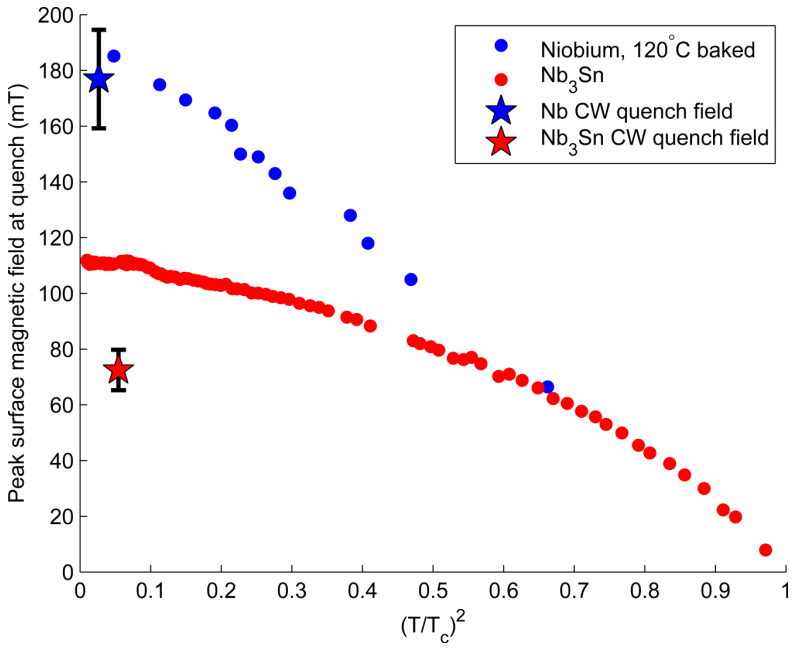

Figure 6.2: A comparison of HPP data from 120°-baked niobium and Nb_3Sn coated at Cornell. The CW (continuous) quench fields from standard Q vs E curves are also given. Niobium data from [Val13].

β, the fill time is very short (order 10s of μs), allowing the cavity to outrun local thermal limitations. This method has been successfully used to experimentally determine the superheating field of niobium at 1.3 GHz [VL11, Val13], and has been previously used on Nb_3Sn [Cam85, CF84, HP97, PVL15].

The data from a klystron test for niobium is compared to a recent one on Nb_3Sn in Figure 6.2. Data from klystron tests is plotted as the peak surface magnetic field at which the cavity quenches against the square of the temperature – this is because the superheating field is expected to approximately follow a temperature dependence of [VL11]

$$H_{sh}(T) = H_{sh}(T=0)\left[1-\left(\frac{T}{T_c}\right)^2\right], \tag{6.3}$$

which is seen to be the case in niobium. However, in Nb_3Sn the quench field

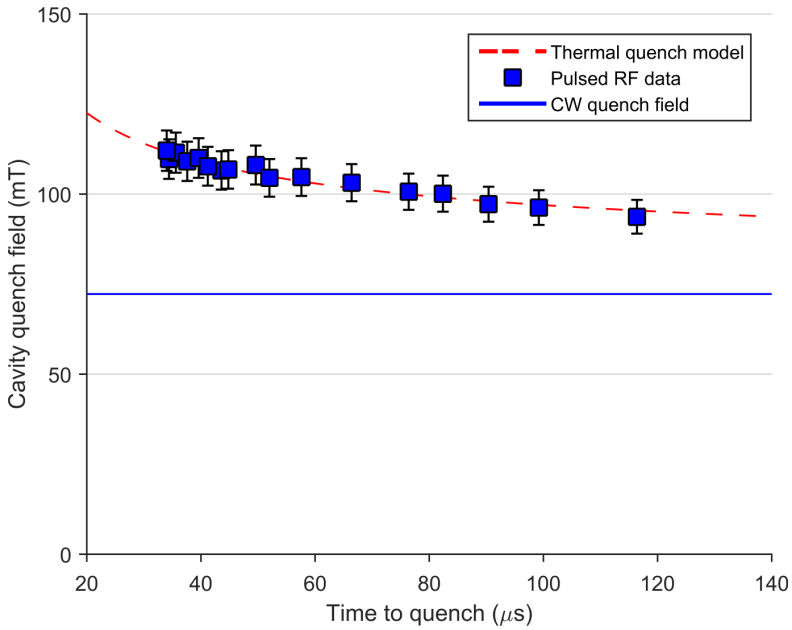

Figure 6.3: The quench field of the cavity in HPP testing against the time taken to quench. As the forward power from the Klystron is increased, the cavity fills quicker and quenches sooner. The faster filling allows for a better outrunning of thermal effects, but in Nb_3Sn even at 400 kW of forward power this is found to be insufficient to fully outrun them.

follows a curve towards a low-temperature value considerably lower than the expected H_{sh}, although higher than both H_{c1} and the quench field observed in CW testing. This result suggests that the klystron is still not providing enough power to outrun strong, localised defects. This is further emphasised by the result that increasing the power output of the klystron increases the low temperature quench field, as seen in Figure 6.3. Notably, the work of Campisi at SLAC [Cam85, CF84] achieved somewhat higher pulsed fields than the work from Cornell [HP97, PVL15] – this could be attributed to the use of a higher power klystron (36 MW, 2.856 GHz at SLAC versus 1 MW, 1.3 GHz at Cornell), allowing for even faster filling times. However, even this result does not give the same behaviour seen in niobium, as evidenced by Figure 6.4.

The conclusion that can be drawn from HPP testing is that Nb_3Sn cavities

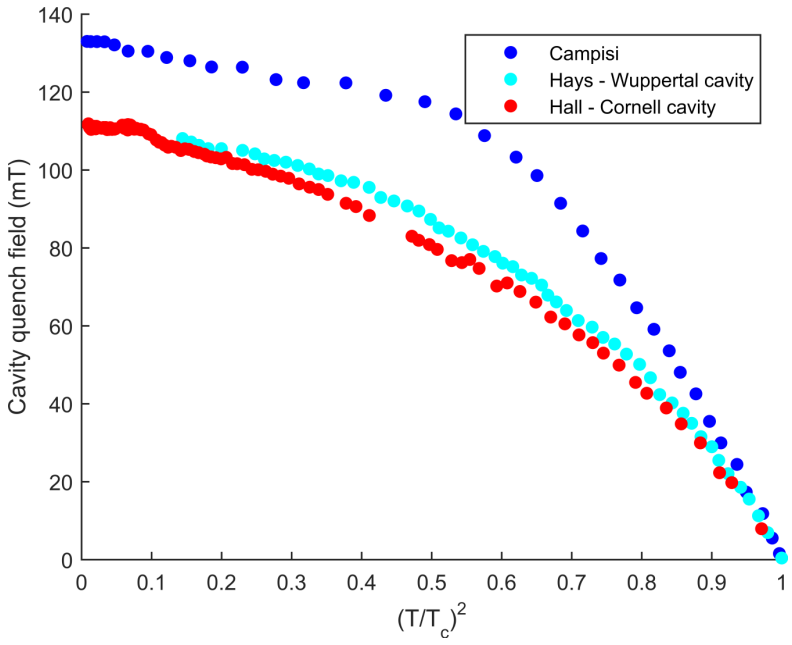

Figure 6.4: HPP test results from Campisi at SLAC and Hays and Hall at Cornell [Cam85, CF84, HP97]. The higher field achieved by Campisi can be attributed to the use of a higher forward power from the Klystron.

are limited by a localised – as opposed to global – defect. The data is unable to discern, however, the exact nature of this defect; it could be a region of increased BCS resistance resulting in local thermal runaway, or a region where magnetic flux is breaking in before H_{sh} and drastically increasing the losses at this defect. The end result is the same: increased local heating results in the area being driven above T_c, which then results in a loss of superconductivity and a severe reduction in the Q_0 of the cavity.

6.1.3 Global and local thermal runaway

The question now becomes: how do we differentiate between a defect in which flux enters first, resulting in heating, and one in which local thermal feedback results in the temperature being driven high enough for flux to enter? Global

thermal runaway is not expected to be a limitation in 1 GHz Nb_3Sn cavities – a result shown in the previous chapter, in Figure 5.19 – although at 6 GHz global thermal runaway can occur at fields below H_{sh}.

An experiment was carried out to verify whether the removal of the outside layer of Nb_3Sn, which serves no role in the RF performance, still played a role in causing global thermal feedback due to the lower thermal conductivity of Nb_3Sn. This was done by filling a Nb_3Sn cavity with DI water and sealing both ends before immersing the cavity in BCP, to remove the outside layer of Nb_3Sn without altering the inside layer. The performance of the cavity, before and after the outside chemistry, is shown in Figure 6.5. The Q of the cavity decreased slightly, although no Q-slope was introduced, possibly suggesting an imperfect seal on the cavity ends. However, the quench field remained unchanged, at $\approx$ 16 MV/m, indicating that the outside layer of Nb_3Sn has little impact on global thermal feedback at these medium fields – which would be in agreement with the simulations for different RRR of the substrate given in Figure 5.19.

However, local thermal runaway can occur at much lower fields. A region of tin-depleted Nb_3Sn, with a T_c of 6 K, could be a significant source of dissipated power if it were exposed to the RF field. Tin-depleted regions have indeed been seen in the cross-sections of samples, such as shown in Figure 3.15 – if these were to be found at the surface, they would result in significant thermal feedback at a localised region. Such heating would not be evident in a Q vs E diagram, as the presence of the region is small enough that it's effect is only felt when driven normal conducting, resulting in cavity quench.

Heating from defects has previously been studied [RKM+92]. Results of simulations on RRR=300 niobium indicate that normal conducting defects larger

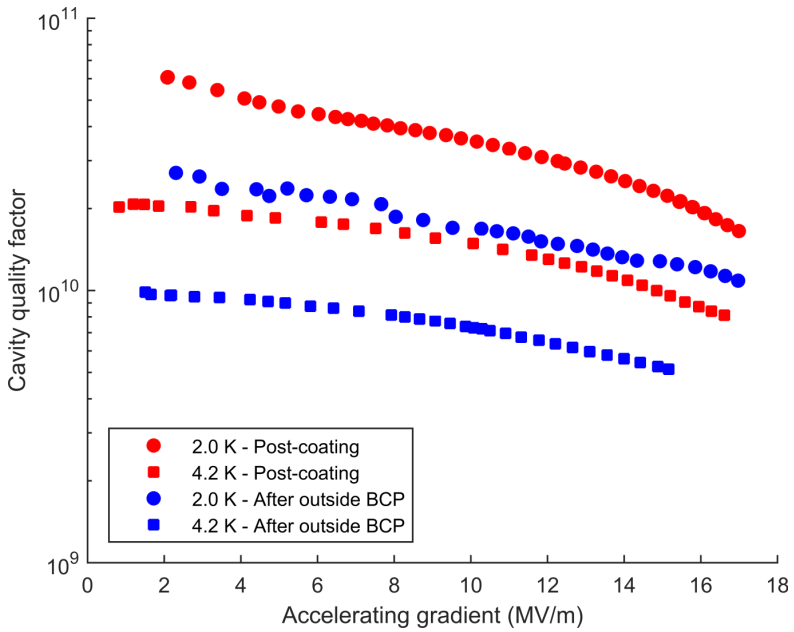

Figure 6.5: Q vs E of a Nb_3Sn cavity immediately post-coating and after a short outside BCP to remove the outside layer of Nb_3Sn.

than 30 microns in size will result in a quench field of 19 MV/m or below. In Nb_3Sn, in spite of the improved BCS resistance, the far lower thermal conductivity could result in a significant reduction in the size of a defect necessary to limit the quench field to 16 MV/m or below, by an order of magnitude or more.

6.1.4 Surface roughness and post-coating chemistry

To add to the difficulty of identifying the source of quench, the surface roughness of Nb_3Sn immediately post-coating has been found to be significant. In particular, the short scale roughness is quite high, with a roughness on the order of ± 1 μm peak-to-peak over a span of 20×20 μm, as indicated by the atomic force microscope scan shown in Figure 6.6. Such roughness can cause field enhancement, with simulations indicating that a region such as the scan shown in Figure 6.6 would result in a peak enhancement factor of 1.8 [PHLM17]. On a

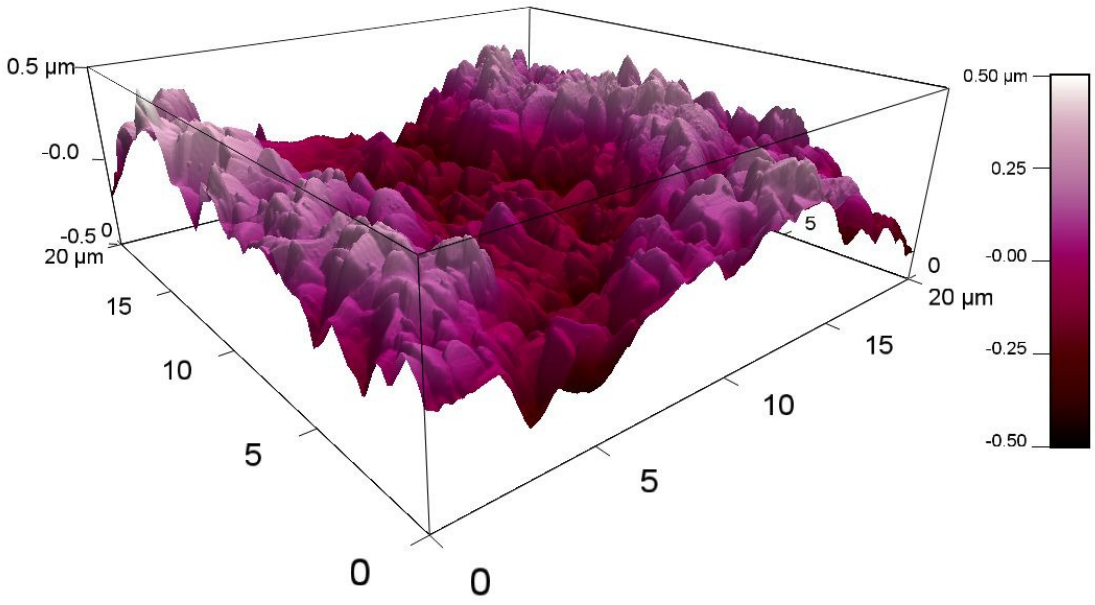

Figure 6.6: Atomic force microscope scan of the surface of a sample of Nb_3Sn coated at Cornell. The surface roughness is of the order of 1 µm peak-to-peak over a 20×20 µm span. This image courtesy of James Maniscalco, SRF Group, Cornell University.

global scale, field enhancement would result in an effective "lowering" of the superheating field as measured by klystron tests, as the effective surface field would be higher than given by the calibration from cavity shape simulations. Significant local field enhancement from a sharp edge or ridge could also turn an otherwise harmless region into a "defect" as the local field is driven close to the field of flux entry.

Surface roughness in niobium is suppressed using centrifugal barrel polishing (CBP) [HSY+01, CSB+11] and, more extensively, chemical techniques such as buffered chemical polishing (BCP) [PDK+93, TRK+06] and electro-polishing (EP) [DSMS71, TCRK08]. At the time of writing, EP cavities have demonstrated the best performance. However, these techniques often remove material at a rate of 0.5-1 micron per minute, and with the average Nb_3Sn coating being 2-3 mi-

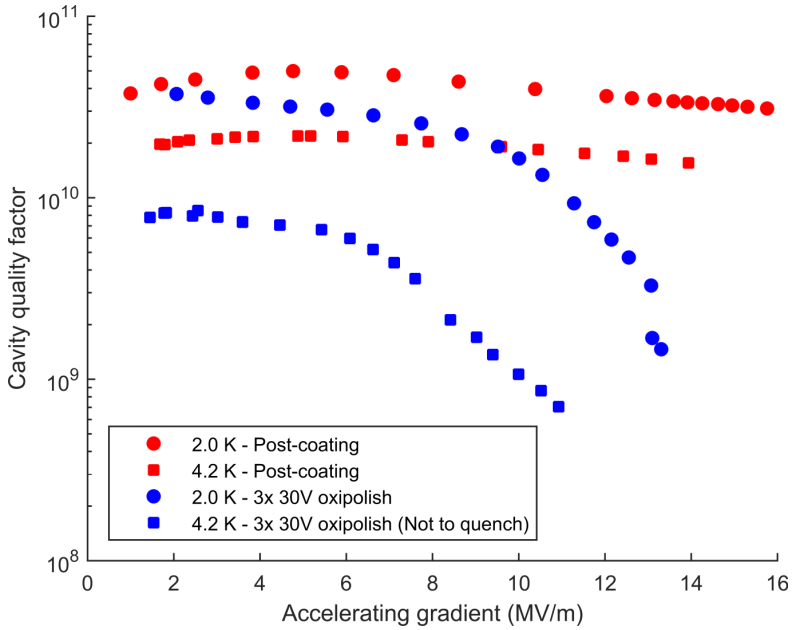

Figure 6.7: Q vs E of a Nb_3Sn cavity immediately post-coating and after 3 passes of 30 V oxipolish (anodisation in NaOH to 30 V, followed by an HF rinse), corresponding to the removal of approximately 50-100 nm of Nb_3Sn.

crons thick, this would result in the layer being stripped inside of 5 minutes. A more rarely used technique, oxipolishing [Die78] has been successfully used in the production of 10 GHz Nb_3Sn cavities at Siemens AG [Hil76], but attempts to reproduce the technique recently in 1.3 GHz Nb_3Sn cavities have resulted in the introduction of Q-slope without any improvement in low field Q or quench field. An example of a Q vs E of a single-cell cavity, designation LTE1-6, before and after oxi-polishing is seen in Figure 6.7. As can be seen, the oxi-polishing resulted in the introduction of Q-slope not unlike that seen at the University of Wuppertal and a reduction of the quench field.

However, contemporary experiments on Nb_3Sn samples have demonstrated that oxipolishing can successfully reduce the surface roughness [PFH+17]. These studies are continuing with a view to investigating the cause behind the introduction of the Q-slope following the chemistry. It is possible that if thin

film regions (such as the one seen in Figure 5.4) are present in the cavity, even 50-100 nm of removal will result in the tin-depleted interface being further exposed to the RF field. The tin-depleted interface is expected to have a T_c of 6 K, and their exposure will lead to both a higher BCS resistance and the introduction of Q-slope. This situation could explain the Q vs E curve seen in Figure 6.7, where the 2.0 K Q at low field (where residual resistance dominates) is the same before and after the oxipolish, but at 4.2 K the Q after oxi-polish is over a factor of 2 worse than before chemistry. In addition to the thin film regions, the removal of the surface layer could also expose tin-depleted regions deeper in the bulk of the normal thick regions, such as the one seen in Figure 3.15. It is also possible that the chemical process removes tin and niobium at different rates, resulting in a tin-depleted surface layer, although this has yet to be confirmed by cross-section X-ray analysis or secondary ion mass spectrometry.

6.2 Dynamics of the cavity quench

From what can be discerned from previous measurements, it appears reasonable to conclude that the origin of the quench in current Nb_3Sn cavities is a surface defect of order 10 μm or less in diameter (this given previous simulations done with niobium [RKM+92] and the poorer thermal conductivity of Nb_3Sn). The repeatability of the quench fields would suggest that this defect is very common, and that the quench is instigated by what happens to be the worst in the field of available candidates, possibly aided by local field enhancement. Such a small defect would be impossible to find by standard cavity optical inspection methods [GFG+16]. However, the surface heating from such a point defect could be expected to spread to a radius equal to the thickness of the niobium

wall, approximately 3 mm. This brings the heating within range of the Cornell temperature mapping system [Kno97]. Careful studies of heating close to quench would allow us to determine whether the quench is instigated by a thermal runaway phenomenon (such as thermal feedback at a high BCS resistance region) or early flux entry, such as at grain boundaries or regions of suppressed T_c.

In light of this, the single-cell 1.3 GHz TeSLA-style cavity LTE1-7 was coated with Nb_3Sn using the recipe shown in Figure 3.2 and tested using the temperature mapping system, whose operation is described in detail in the next section. The performance of this coating of LTE1-7 has been shown previously in Figure 5.1. The objective of the exercise was simple: first, to locate the origin of the quench, and then, to use the temperature mapping system to investigate the local heating at this location before, during, and after quench, with the hope that the heating pattern would reveal the nature of the cavity quench. Following the experiment, the quench origin was cut from the cavity for surface analysis. The results of this experiment are the focus of the remainder of this chapter.

6.2.1 Temperature mapping experiment

The primary measurement apparatus used in this experiment was a cavity temperature mapping system, or T-map. The system, shown mounted onto a cavity in Figure 6.8, is comprised of 38 boards that surround the cavity at equally spaced intervals. Each board is equipped with 17 temperature sensors mounted on spring-loaded supports that press against the outer surface of the cavity. Thermal paste is applied to the sensor to improve thermal contact between the

sensor and the outer cavity surface. Each sensor is a 100 Ω Allen-Bradley carbon resistor, which is possessed of a large temperature coefficient at cryogenic temperatures and as such allows measurements of temperature changes of approximately 0.2 mK at 2.0 K and 1 mK at 4.2 K. This is sensitive enough to be able to detect local heating on the inner surface of the cavity, even if this heating is small enough to allow the cavity to continue operating unhindered.

The system can be used in 3 scenarios. The first, a standard T-Map, relies on keeping the cavity operating at a constant gradient while the sensors are carefully read off one by one, to ensure high temperature precision. The result is a map of local temperature differences from the bath at each resistor. The second mode, dubbed a quench map, is used for identifying the origin of the quench limitation. In this mode, each of the 24 data acquisition modules that read the T-Map is triggered, in sequence, while operating in a high-speed, low precision mode. As each module is triggered, a few seconds of data are obtained during which the cavity is allowed to quench. After quenching the cavity a minimum of 24 times, quench map is completed. The resulting map shows the integral with time (beginning immediately after quench) of the temperature at each active sensor – sensors that remained hotter for longer contribute more strongly to the signal. The third mode, dubbed single-scan mode, is a compromise of the previous two modes. A single sensor, operating in a high-speed, high-precision mode, is triggered to acquire up to one minute of data, during which the cavity can be operated as necessary. This allows precision measurements of heating at the specified location as a function of the field in the cavity.

An example of a temperature map, showing heating at a location on the lower-half cell of the cavity, is shown in Figure 6.16 b). This heating was caused

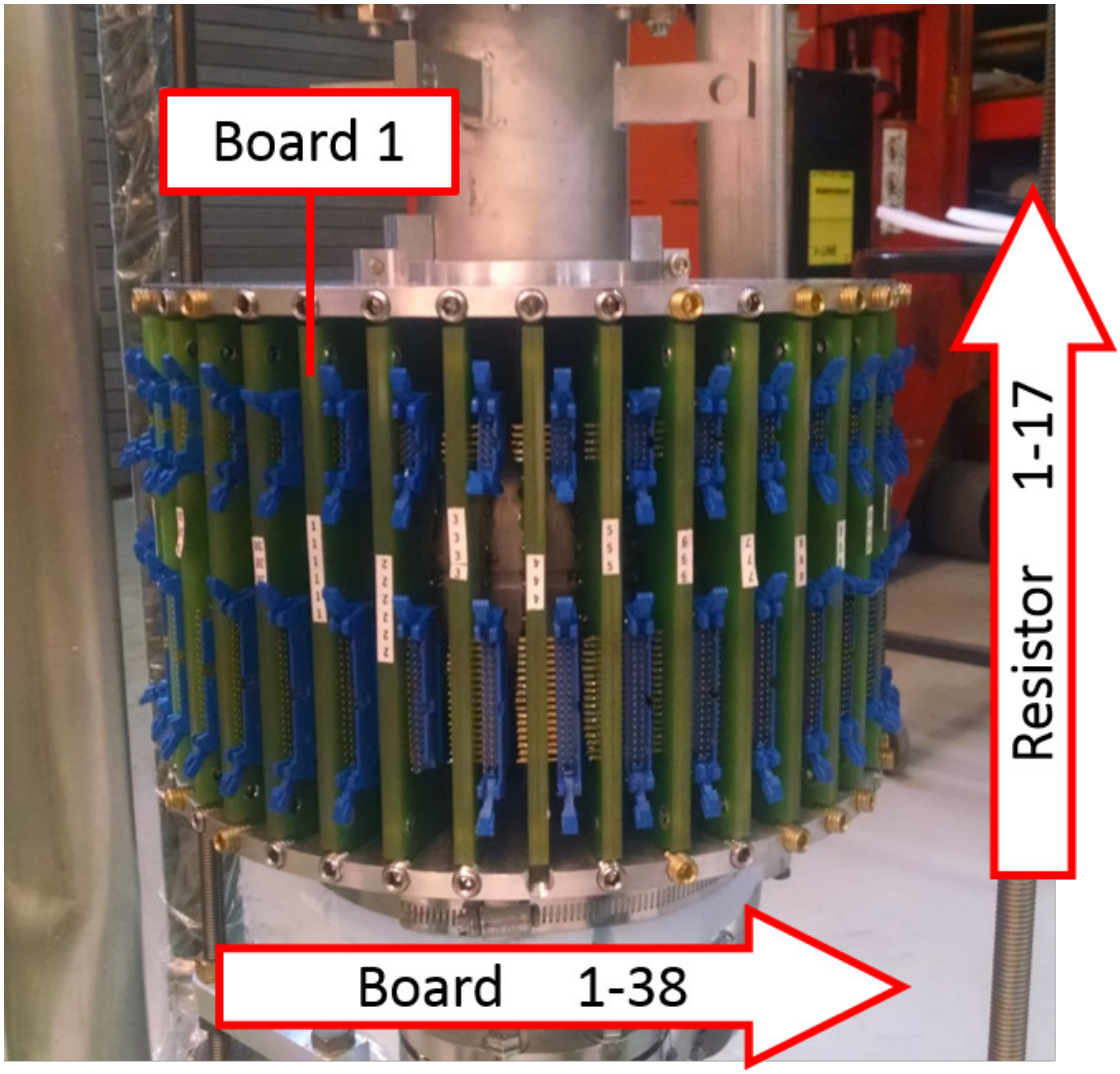

Figure 6.8: Photograph of the temperature mapping system (T-Map) assembled onto cavity LTE1-7. Board number progresses anti-clockwise around the cavity (as viewed from above), while resistor number increases going from the lower iris to the upper iris. The orientation of the cavity is the same as it is in the coating furnace - i.e., the lower half-cell is the side facing away from the tin source during coating.

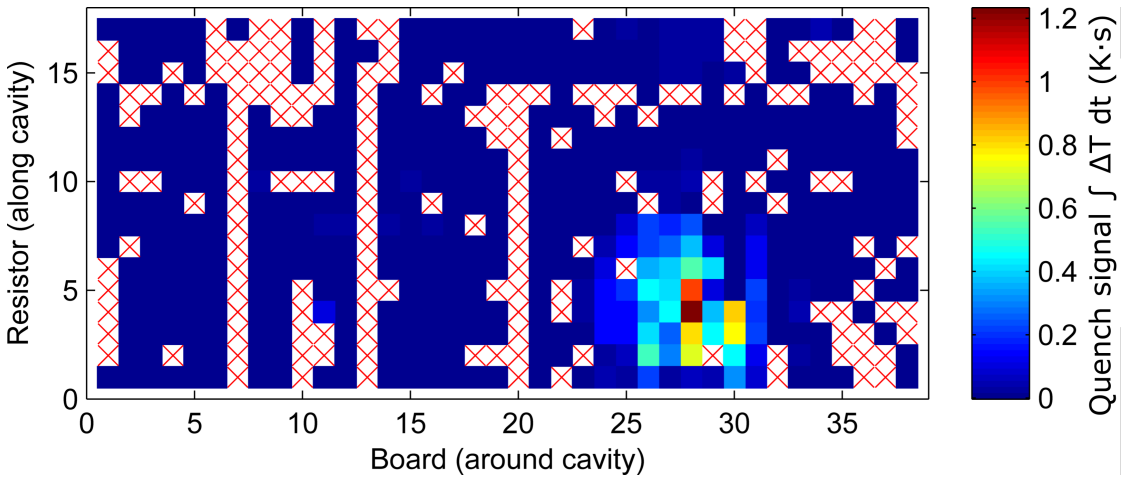

Figure 6.9: Quench map of LTE1-7, taken at a bath temperature of 2.0 K. The colorbar is a time integral of the heating at each sensor beginning immediately after quench. The longer the sensor stays hot, the greater the value. The quench origin is found to be at board 28, resistor 4, on the lower half of the cavity.

by a quench originating at this location, which, due to thermal currents generated due to the bimetallic interface during the heating above the transition temperature, resulted in significant amounts of magnetic flux being trapped. The increase in trapped flux at this location results in increased losses and the heating seen at this location. This location was confirmed as the origin of the quench by the a quench map, shown in Figure 6.9.

An example of a single-scan measurement is shown in Figure 6.10 (left). Two Y-axes are given – one for the temperature difference between the chosen sensor and the bath, and one for the accelerating gradient in the cavity. Shortly after triggering the measurement, the signal generator is turned on, which allows the cavity to fill with power. Although the drive signal is a pulse, the gradient in the cavity increases in a $1 - e^x$ fashion as determined by the quality factor of the resonator and the coupling strength between the drive antenna and the cavity, β. After a pre-determined period, the drive signal is turned off, and the

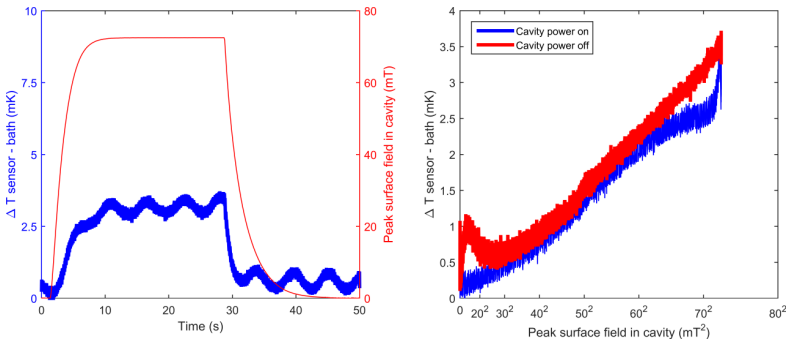

Figure 6.10: Left, an example of a "single-scan" measurement taken at the quench origin at a bath temperature of 2.0 K. After acquisition on a chosen sensor is triggered, the field in the cavity (red) is altered, while being measured using a pickup probe. Simultaneously, the temperature at the sensor (blue) is also acquired. In this trace, RF power was turned on at the 2 second mark and off at 30 seconds. The cavity did not quench during this trace. The temperature oscillations are due to the opening and closing of the cryostat pumping valve that maintains the bath temperature of 2.0 K. On the right, the value of the peak surface field (squared) is plotted against the ΔT at that time, with the blue line corresponding to the time the cavity is filling ($t = 2 - 30$ s in the left plot) and red to the time after the RF power is turned off. The linear shape indicates that the temperature rise is due to Ohmic heating.

cavity rings down in a fashion similar to the filling. During this time, both the gradient in the cavity and the local heating are measured, allowing them to be plotted against each other. This is done so in Figure 6.10 (right), where the local temperature difference from the bath ΔT is plotted against the square of the peak surface magnetic field in the cavity, H_{pk}^2. In such a plot the Ohmic dissipation from the surface resistance R_s is described by $\Delta T \propto \frac{1}{2} R_s H_{pk}^2$ and so appears as a linear increase.

These three methods have been used to carefully analyse the RF behaviour of the quench origin, both before, during, and after quench.

6.2.2 Sudden heating before quench

After the origin of the cavity quench was determined using quench mapping, the temperature map single-scan mode was used to investigate heating at the quench origin as a function of the RF field in the cavity. This was done by setting the ultimate field to be achieved in the cavity through the power setting on the amplifier, and then allowing the cavity to fill with power at the rate determined by the coupling. Unless the power setting was too high (and with it, the ultimate field that the cavity would converge too), the cavity would not quench, but instead equilibrate at a set field, until the power was turned off and the cavity field allowed to decay naturally.

The cavity was cooled very carefully, trapping as little flux as possible, resulting in very good performance at high fields. While operating at 2.0 K bath temperature, the cavity was taken to increasingly higher fields while taking single-scan traces. At fields nearing the quench field, sudden jumps in the temperature at the quench origin were seen, in the manner shown in the singlescan trace shown in Figure 6.11. These jumps were also seen at 4.2 K; an example of measurements of ΔT against B_{pk}^2 at the quench origin at both 2.0 and 4.2 K is shown in Figure 6.12. At both temperatures, jumps were seen, as well as a hysteresis in the ΔT between the temperature rise (as the cavity fills with power) and the temperature fall (as the cavity rings down).

Despite the sudden increase in temperature, the cavity did not quench, and these traces were found to be highly repeatable, with both the height of each jump and the field at which it occurred being identical to the last within measurement error. The size of the hysteresis was also found to be identical between repeated measurements at the same field and temperature. Eventually,

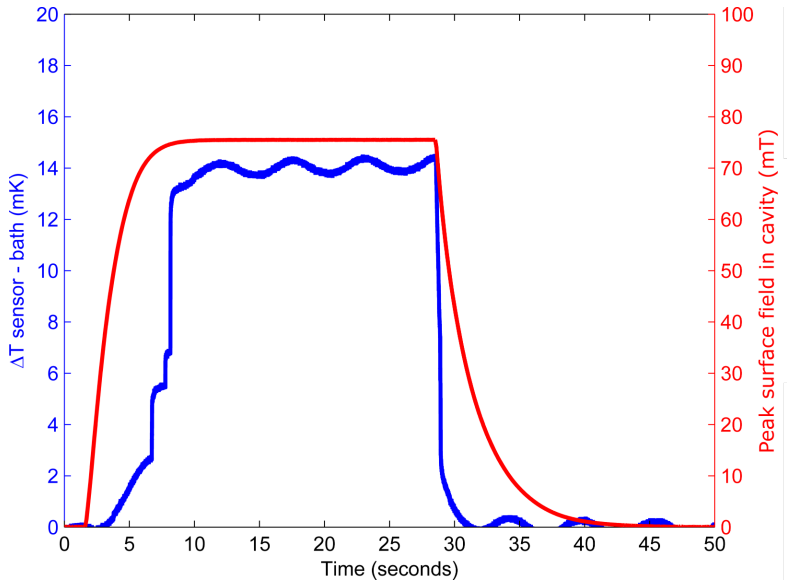

Figure 6.11: A singlescan trace from LTE1-7 taken at 2.0 K at the quench origin, during which the gradient in the cavity is taken very close to (but not allowed to exceed) the quench field of the cavity. At surface fields very close to the quench field, sudden jumps in temperature can be seen on top of the more conventional Ohmic heating.

however, the cavity was brought to a power level that resulted in a quench, changing the quality factor of the cavity dramatically due to an increase in the amount of trapped magnetic flux.

A number of traces were collected that demonstrated these jumps, allowing statistics to be collected regarding the peak field in the cavity at which they occurred and the increase in temperature seen at the quench origin. The experiment at 2.0 K was repeated following a warm-up and re-cool of the cavity to restore the performance of the cavity. The thermal contact of the T-map sensors with the cavity at the quench origin was found to have been degraded, likely due to the thermal cycling. This prevented a comparison of the absolute heights of the temperature jumps from cool-down to cool-down, however, by normalising all the jumps in a cool-down by the mean of the height of the first jump seen, the relative heights can be compared. This is done in Figure 6.13. The

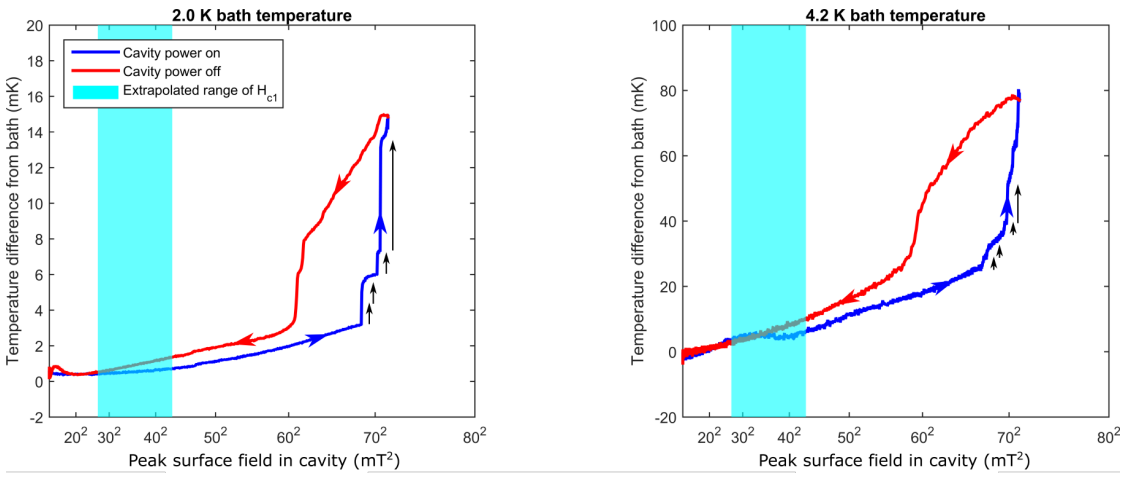

Figure 6.12: A plot of the temperature difference of a sensor (in this case, the quench origin sensor) from the bath, ΔT, against the square of the peak surface magnetic field in the cavity. These example traces were taken at bath temperatures of 2.0 K (left) and 4.2 K (right). The jumps seen during the cavity fill (evident in Figure 6.11) are marked with arrows. At both 2.0 K and 4.2 K, a hysteresis effect is seen in the ΔT during the fill and ring-down portions of the trace.

fields at which the jump occur, and the height of the fourth (the largest) jump, were unchanged to within the systematic error of the measurement.

This jump phenomenon was also found to exist while operating the cavity at 4.2 K. The experiment described so far at 2.0 K was repeated - in a separate cooldown - at 4.2 K, and once again the jumps were seen as the cavity was brought close to the quench field. The jumps were again found to be repeatable, and the field at which the jump occurred and (normalized) jump in temperature have been plotted in a similar fashion to the 2.0 K data in Figure 6.13. The fields at which the jumps occur appear to have reduced slightly compared to those at 2.0 K, although it is again difficult to quantify whether this is significant due to the systematic errors of the measurement.

The most striking feature of the jump phenomenon is that the first three jumps, to within the limits of the measurement, are identical in height. This

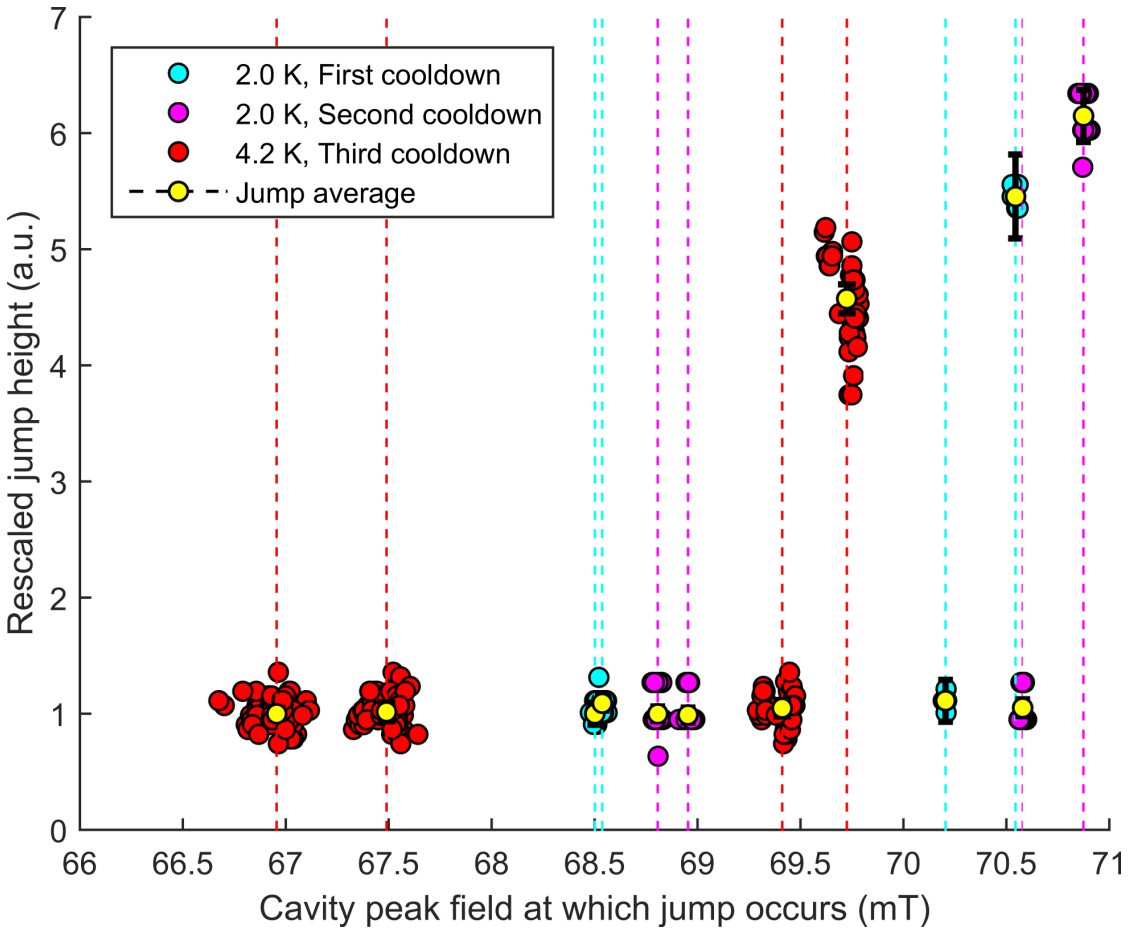

Figure 6.13: Scatter plot of the jumps seen during the three cooldowns (2 at 2.0 K, 1 at 4.2 K). Each set of jumps has been normalised to the mean of the height of the first jump seen in that series.

is true for all three cooldowns, the two at 2.0 K and the one at 4.2 K, and is evident in the scatter plot of Figure 6.13. The pattern in all three cooldowns is the same: three jumps of identical height followed by a larger one. This strongly suggests that the mechanism behind these jumps is quantised in nature.

For the measurement performed at 4.2 K, following data collection before cavity quench, the cavity was brought to quench. After this one single quench, jumps were still visible in singlescan traces, but the heights of the jumps, and the field at which they occurred, had measurably changed. This is demonstrated in Figure 6.14. Seeing as a quench causes significant amounts of magnetic flux gen-

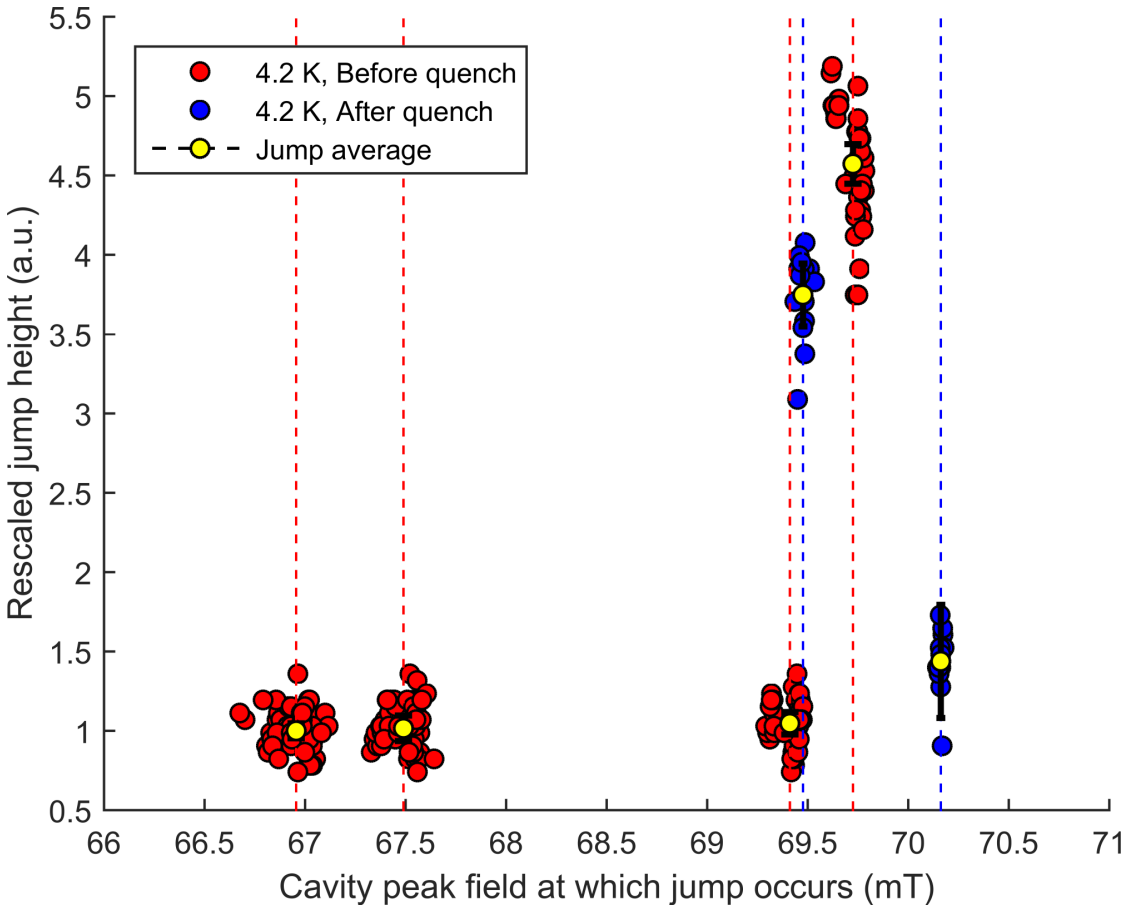

Figure 6.14: Scatter plot of the jumps seen at 4.2 K before and after quench. All jumps have been rescaled such that the first jump has a mean height of 1.

erated by the thermal gradients to be trapped, this would seem to suggest that the mechanism behind the jump phenomenon is affected by the distribution or density of trapped flux at that location. Further work will include temperature mapping measurements investigating this jump phenomenon as a function of different amounts of trapped flux in the cavity (applied using a Helmholtz coil).

Calibrating the temperature map against Q vs E data allows the jumps to be converted from a temperature difference to a power dissipation. At a given accelerating gradient, the dissipated power in the cavity can be related to the total heating across the cavity by[Kno97]

$$P_{diss} = \frac{1}{K_T} \sum_{n=1}^{646} A_n \Delta T_n \,, \tag{6.4}$$

where the sum is made over the 38×17 sensors of the T-Map, each of which accounts for an area A_n (note that this is not actually the area that the sensor physically covers, which is less than A_n). From a given calibration T-Map such as the one in Figure 6.16 a), the calibration constant K_T can be determined. For the first and second cool-downs are 2.0 K, this calibration was found to be 7.3 and 2.4 $\mathrm{Kcm}^2/\mathrm{W}$. Picturing the defect causing the jumps as a point source under the sensor, whose physical area is 3×3 mm in area, this indicates that the height of the first three jumps during the first and second cool-down each correspond to an increase in the dissipated power of (152 ± 23) and (123 ± 19) μW, respectively. By contrast, the power dissipated at the quench origin just before the quench occurs is ≈ 2 mW.

In summary, the most striking result of this measurement is that the sudden heating seen at fields close to the quench field of the cavity appear to be due to a quantised phenomenon, where the smallest unit appears to be an increase in dissipated power of $\approx 120-150$ μW. A physical mechanism to explain this observation will be discussed later in subsection 6.2.6; before this, however, we will continue with presenting results from the temperature mapping test of LTE1-7.

6.2.3 Hard and soft quenches

Accompanying the newer single-scan traces are a number of more conventional temperature maps. Maps taken before a quench reveal, as expected, no regions of significant heating at medium fields. However, following the first quench (of

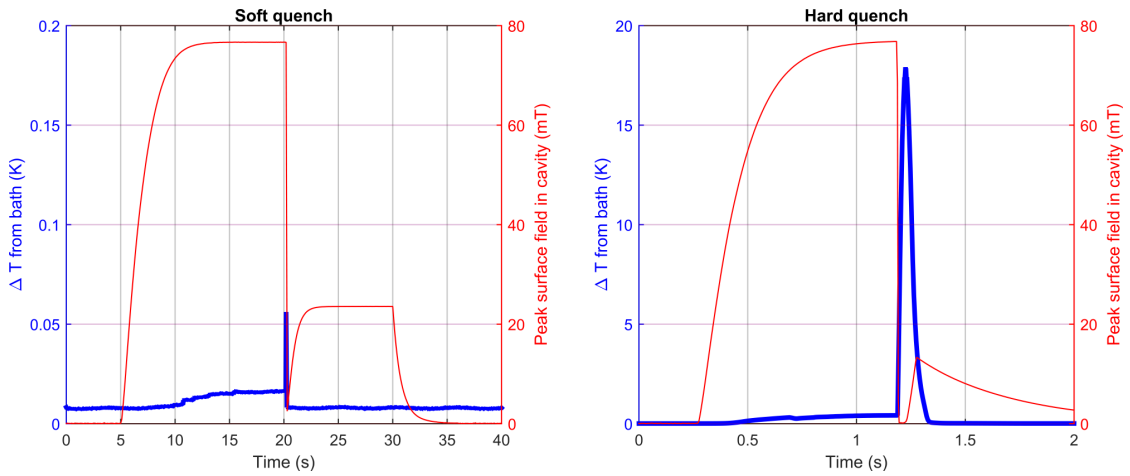

Figure 6.15: Difference between a "soft" quench, in which the field in the cavity only just reaches the quench field, and only a small spike in temperature is seen at the quench origin at the moment of quench; and a "hard" quench, in which the field in the cavity rises fast enough to trigger a large temperature spike that takes the quench origin above the transition temperature of 18 K.

the kind seen in Figure 6.15 a), heating was seen at the equator region of the cavity. Heating of such kind after a quench is common as the transition above T_c during quench results in significant flux trapping, which would indicate that the cavity quenched at the equator location seen in Figure 6.16 a). However, a quench map taken immediately after this T-Map re-stated that the origin of the quench was at the location seen in Figure 6.9. Since a quench map consists of quenching the cavity, usually very quickly, and multiple times, another temperature map was taken after the quench map. This map now showed heating both at the equator (as seen previously) and at the quench origin, as shown in Figure 6.16 b).

Repeating this measurement after a thermal cycle again showed the same behavior: after the first quench, heating was observed at the equator. This time, however, the heating was at a different location on the equator, as shown in Figure 6.16 c). A subsequent quench map agreed with Figure 6.9, and a following

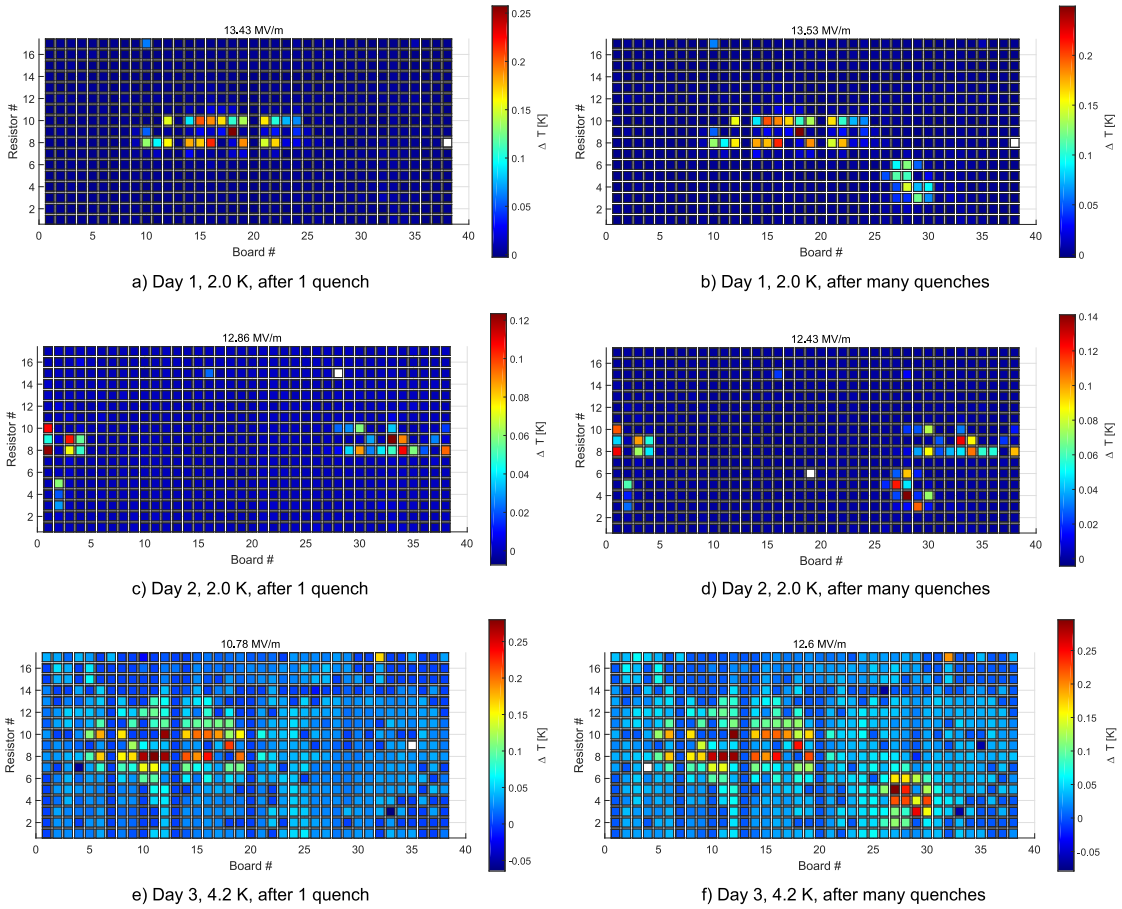

Figure 6.16: Collection of temperature maps taken during the three cooldowns. Maps a), c) and e) were taken after 1 soft quench, in which the cavity was only just brought to the quench field. Maps b), d) and f) were taken after the many hard quenches necessary to construct a quench map such as that seen in Figure 6.9.

T-Map again showed heating at the quench origin, as seen in Figure 6.16 d).

Further investigation of the single-scan traces revealed that the behavior of the trace in which the cavity is first quenched does not match the traces in which the cavity is deliberately taken to quench. In the first, in which the power setting on the amplifier is only just enough to bring the cavity to quench, only a small jump in temperature (not exceeding T_c) is seen at the quench origin - as seen in Figure 6.15 a). However, traces in which the power setting on the amplifier is more than sufficient to bring the cavity to the quench field, temperature jumps

above 18 K are seen, exceeding the transition temperature. This would suggest that for the quench shown in Figure 6.15 a) the quench origin identified by Figure 6.9 did not go above the transition temperature, as suggested by the lack of heating seen at the quench origin in Figure 6.16 a), c) and e). Indeed, the heating from trapped flux seen at the equator following these quenches would seem to confirm that the quench did not originate at the quench origin identified by Figure 6.9, but at a location on the equator – surprisingly, at a different location on the equator for each cooldown. By comparison, when the cavity is brought to quench quickly, the traces such as Figure 6.15 b) confirm that the region shown in Figure 6.9 does go above the transition temperature, and the heating at this region seen in the T-Maps of Figure 6.16 b), d), and f) (taken after many hard quenches) agrees with this location being the quench origin.

This puzzling behaviour implies a difference between quenches in which the field in the cavity is taken to the quench field very slowly (or held for some time at a field just below the quench field), and those in which the field in the cavity is raised to the quench field quickly (with the power from the amplifier being enough to settle at a field in the cavity above the quench field, were the cavity able to sustain it). The fact that Nb_3Sn cavities can be filled quickly enough to outrun local thermal limitations and thus briefly achieve fields above the CW quench field has already been shown in High-Pulsed Power results, in which the cavity can achieve fields up to 25 MV/m (above the CW quench field of $\approx$ 17 MV/m). Following this reasoning it would seem to suggest that the difference in the quench origin between hard and soft quenches could be due to some very slow – order of many 10s of seconds – thermal feedback mechanism, but this is far from sure. This result remains one of the more puzzling results from this experiment, and until further work can be performed to investigate it only

informed speculation can be made as to the mechanism behind this behaviour.

6.2.4 Temperature "slip" phenomenon

Another phenomenon seen in single-scan traces is what can best be described as a temperature slip, in which the temperature at a sensor increases to a slip field before decreasing significantly to a lower temperature, then rising again at a lower rate. This phenomenon is demonstrated, both as a single-scan trace and plotted as ΔT vs B_{pk}^2, in Figure 6.17 a). This phenomenon was first seen in single-scan traces taken at 2.0 K after the cavity was quenched, replacing the presence of the jumps seen before quench. However, unlike the temperature jumps, the field at which the slip occurs is not constant between traces. Instead, for a modestly fixed ultimate field achieved in the cavity, the amount by which the temperature decreases during the slip – referred to as slip ΔT – is a function of the field in the cavity at which the slip begins. This can be seen in Figure 6.17 b).

This temperature slip phenomenon was also seen at 4.2 K, but even before the cavity had quenched, and occurring at much lower fields. In all traces at 4.2 K, the slip field was lower than the field at which jumps occurred. Furthermore, also at 4.2 K, a second, small slip was often seen, although this phenomenon was not found to be consistent between traces. An example of this double-slip phenomenon can be seen compared to a single-slip trace in Figure 6.18.

When taken at a set value of maximum field, we again see a linear relationship between the slip ΔT and the field at which the slip occurs. When altering

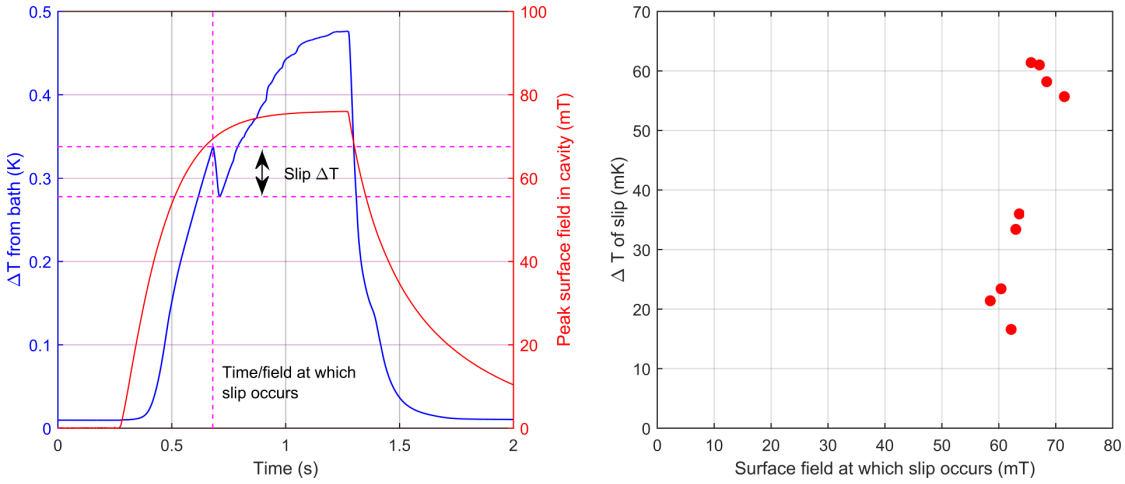

Figure 6.17: a) An example of the "slip" phenomenon, as seen in cavity LTE1-7 while operating at 2.0 K, in this case seen at the quench origin after many quenches. The time at which slip begins to occur is labelled the "slip field", and the temperature difference between the beginning and end of the slip is given to be the "slip ΔT". b) At 2.0 K, after quenching the cavity many times, a measurement of the slip ΔT against the peak surface magnetic field at which the slip occurs.

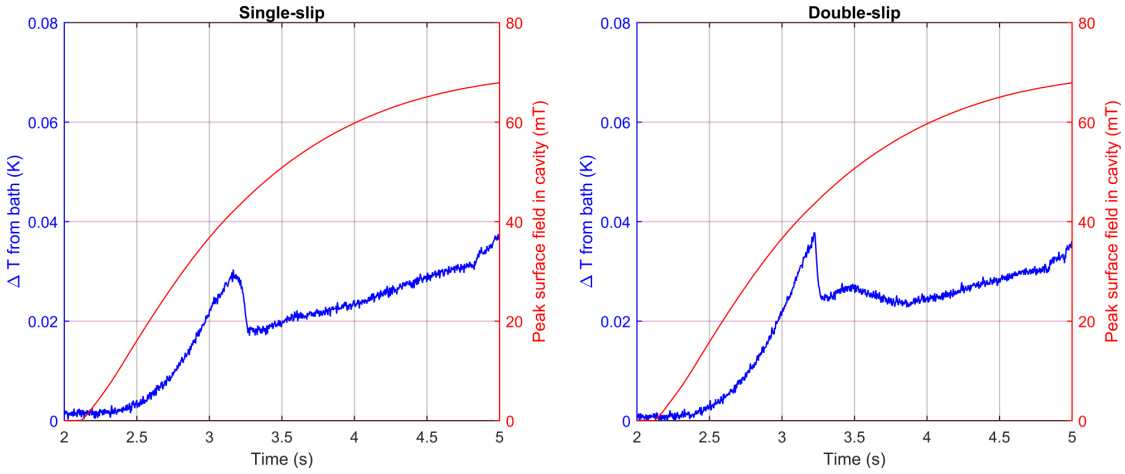

Figure 6.18: A example of the "single slip" and "double slip" features seen in traces taken at 4.2 K after many quenches of cavity LTE1-7. The second slip is always more subtle than the first.

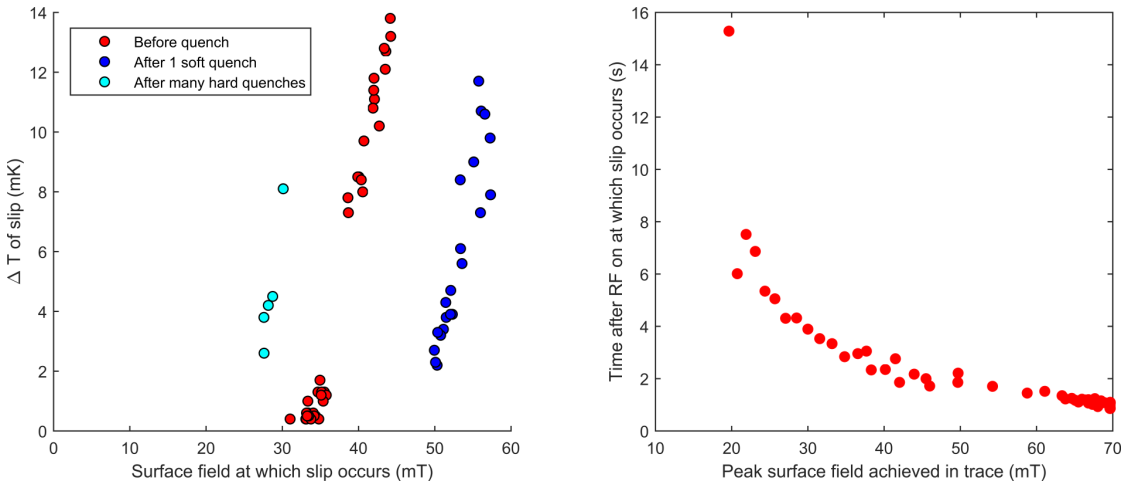

Figure 6.19: a) The ΔT of the slip versus the peak magnetic surface field at which the slip occurs (for reference, see Fig. 6.17 a)) at 4.2 K before quench, after 1 soft quench, and after many hard quenches. b) Changing the fill time of the cavity, the time after RF on at which the slip occurs against the maximum surface magnetic field achieved in the trace.

the value of the maximum field by altering the power output of the amplifier (and with it the rate at which the cavity fills with power), the plot of slip ΔT against slip field appears far messier - instead, we see a relationship between the time between RF on and the slip occurring and the maximum field achieved in the trace. This is shown in Figure 6.19 b). The slip occurs even at very low values of stable accelerating gradient, far below the field at which the jumps occur.

After the first quench of the cavity at 4.2 K, the cavity field was reduced, as described in the section above on the temperature jumps. During this time it was also observed that the relationship between the slip ΔT and the slip field, while still linear, changed noticeably. After quenching the cavity many times, it had changed again, suggesting that, like the jumps in temperature, the mechanics of the temperature slip phenomenon are impacted by the distribution of trapped flux in the region. The changes after one quench and after many can

be seen in Figure 6.19 a).

The jumps in temperature were only found at two other sensors other than that located at the quench origin, and both of these were immediately next to the latter. This suggests that the jump phenomenon, to currently detectable limits, is centred at the quench origin identified by Figure 6.9. The slip phenomenon, however, was seen at a number of different sensors around the cavity. Whereas the jumps occurred at fields just below the quench field, the slip phenomenon occurred at fields significantly below that, and was correlated largely with areas of the cavity being heated by trapped flux following quench. This suggests that the jump and slip phenomena are unrelated, and that the latter is related in some manner to the magnetic flux trapped in the cavity walls. Therefore, further research will investigate the prevalence and nature of these slips in a Nb_3Sn cavity as a function of the amount of flux trapped during cooldown (as applied by a Helmholtz coil mounted on the cavity).

6.2.5 Surface analysis of cavity cut-outs

Following the temperature mapping experiment, the cavity was removed from the testing insert and sealed, whereupon it was moved to the machine shop. Here the quench origin was cut-out, with special care being taken to avoid excessive surface vibration (to prevent cracking) and heating (to prevent any change in chemistry). After the quench origin was removed, three further samples from the ends of the two half cells and the equator were also cut.

Scanning electron microscopy of the three samples revealed no cracking or debris further than 0.1 mm from the edge of the sample, confirming that the

careful cut-out procedure was successful. General chemical analysis of the four samples using EDS showed no significant difference in the surface chemistry of the four regions as expected, since the coating method is known to be uniform to within measurable limits over these scales.

Closer imaging and chemical analysis of the quench region did not show any detectable difference is surface stoichiometry that might reveal the origin of the quench location. However, backscatter imaging did reveal regions of sharp topography, in which the Nb_3Sn layer appeared bent over some substrate feature. Such a feature is seen in the SEM image collection shown in Figure 6.20.

The niobium substrate is known to be re-crystallizing during the coating process, as the temperatures achieved during coating – > 1100°C - are high enough to do so. The Nb_3Sn grains grown during the coating process are on the order of many millimeters in size, three orders of magnitude larger than the average size of the Nb_3Sn grains. The movement of niobium grain boundaries during the Nb_3Sn growth process may induce significant stress in the Nb_3Sn layer, and result in the features seen in Figure 6.20. The presence of strain in Nb_3Sn is known to weaken the superconducting properties of the material [God06], and the sharp edges will lead to field enhancement. These two contributions would combine to make these regions weaker from a flux-entry standpoint than their neighbours, making these a candidate for the quench origin. Further surface analysis is underway to characterize these features, as well as to search for other features in the region of the quench origin.

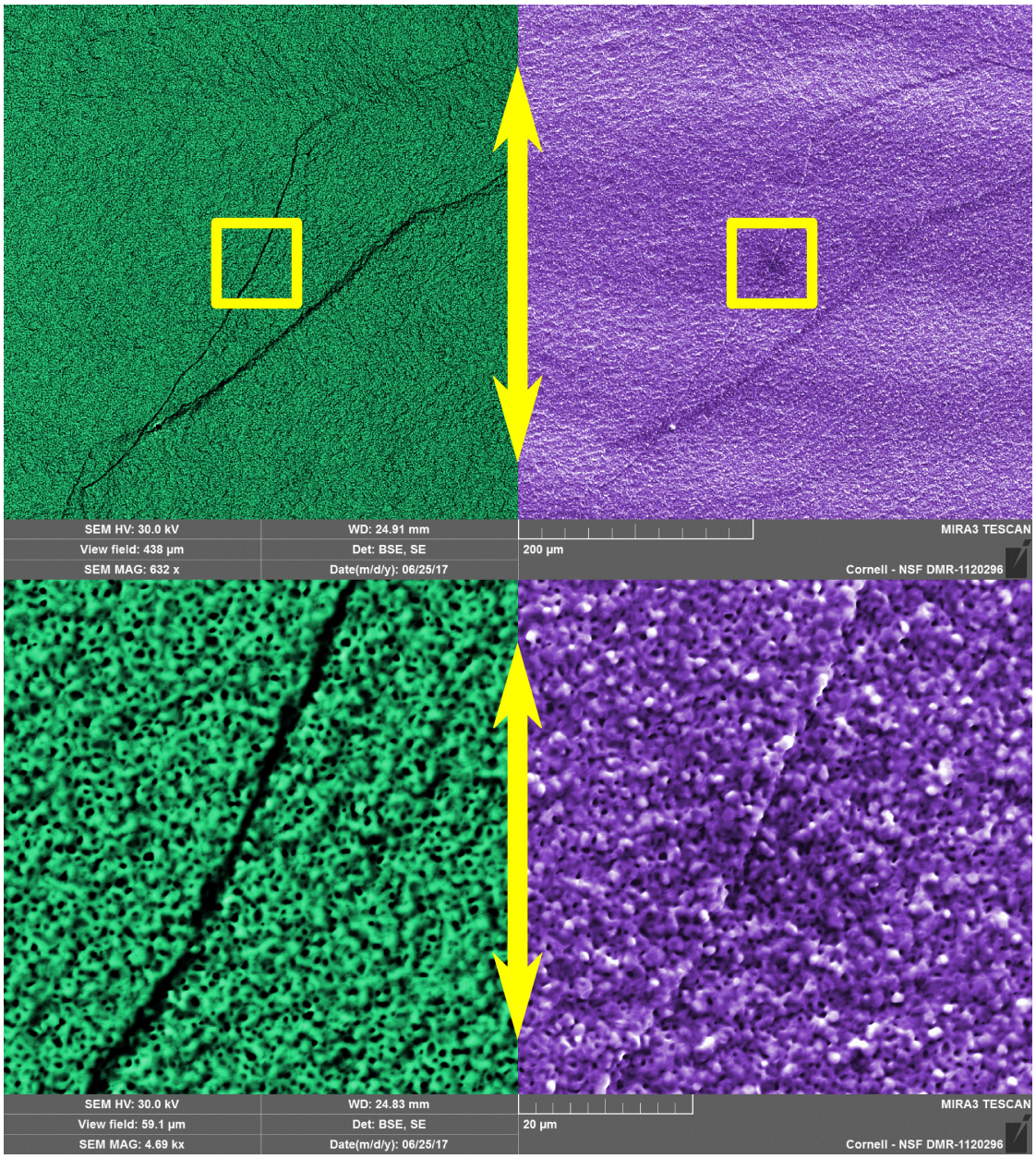

Figure 6.20: Compositional backscatter (left) and chamber secondary electron (right) images of a feature found at the quench origin. A sharp ridge across which the Nb_3Sn layer bends to conform. The upper images are of a wide area - the yellow insets indicate the region in which the lower images were taken. The yellow double-headed arrow indicates the direction of the oscillating surface RF magnetic field.

6.2.6 Theoretical candidates for quench mechanisms

Following from the results presented in subsection 6.2.2, the presence of quantised jumps in temperature at the quench origin at surface fields close to the quench field strongly suggests a quantised phenomenon. The most plausible explanation for this is dissipation due to quantised entry of magnetic vortices into a defect, at fields above B_{c1} but below B_{sh}. However, the question remains what kind of defect would result in this early flux entry.

A primary candidate for such a defect is quantised vortex entry at grain boundaries. In the model described by Alex Gurevich and Ahmad Sheikhzada [SG17, GS17], quantised vortex entry occurs at grain boundaries whose width, on the order of ξ, causes them to act as Josephson junctions. These work to hinder the passage of the supercurrent J induced by the applied RF magnetic field.

At these grain boundaries, modelled as strongly-coupled under-damped Josephson junctions, vortices can begin to enter in a quantised fashion when the surface field exceeds a grain boundary thermodynamic critical field, B_{GB}. Once a vortex enters, it remains in the grain boundary between RF cycles, transitioning from vortex to anti-vortex with the cycle of the RF field. The vortex dissipates energy as it travels the length of the grain boundary and back due to experiencing viscous drag from the superconductor, in a manner not dissimilar to losses from trapped magnetic flux. Vortices continue to penetrate the grain boundary until the RF field is lowered to a field beneath that at which they originally entered, resulting in hysteresis. This is observed in simulations performed by Gurevich and Sheikhzada, such as that reproduced in Figure 6.21. In this figure, the peak normalised supercurrent induced by the RF field $\beta = J_0/J_c$

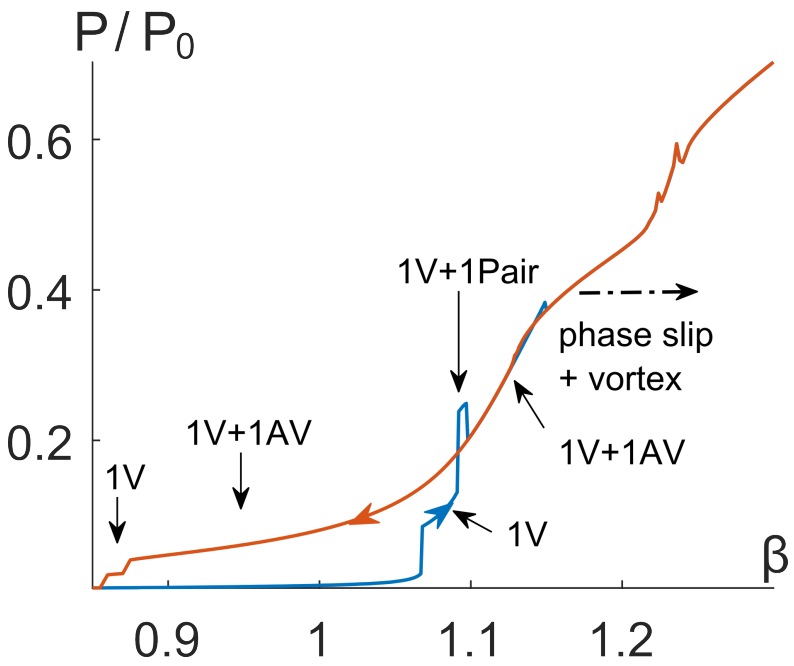

Figure 6.21: Normalised power dissipated in a grain boundary as a function of normalised current through the grain boundary, modelled as an underdamped Josephson junction. The result is plotted as the peak normalised supercurrent through the grain boundary induced by the RF field $\beta = J_0/J_c$ (where $J = J_0 \sin(\omega t)$ is the supercurrent across the grain boundary induced by the surface RF field with angular frequency ω) against the power dissipated in the grain boundary (normalised to the power dissipated when the grain boundary is fully normal conducting). Figure reproduced from [SG17].

(where $J = J_0 \sin(\omega t)$ is the supercurrent across the grain boundary induced by the surface RF field with angular frequency ω) is plotted against the power dissipated in the grain boundary (normalised to the power dissipated when the grain boundary is fully normal conducting). As β exceeds 1, vortices begin to enter in a quantised fashion, until a runaway occurs (a "phase slip") at the end of which the grain boundary is driven into the fully normal conducting state.

Figure 6.21 is analogous in what it presents – a power dissipated against an applied field – to the experimental measurement shown earlier in Figure 6.12. What is interesting is that both demonstrate similar features: sudden, quantised

jumps in power dissipated, and a hysteresis as the field is increased and decreased. It is this observation that makes this model a candidate for explaining the quench seen in LTE1-7. Admittedly, the model used to generate Figure 6.21 was very simple, assuming an ideal grain boundary free of defects. However, further simulations performed by Gurevich and Sheikhzada indicate that more realistic grain boundaries will show more complex behaviour, with multiple jumps, possibly of different heights – which would be in line with the less ideal behaviour demonstrated by Figure 6.12.

This would explain the identical height of the first three jumps observed during the three cooldowns (whose data is presented in Figure 6.13) as being due to the entry of a single vortex, one for each jump. Since the applied RF magnetic field is virtually identical for each jump, differing by at most 4%, the power dissipated by any single vortex will appear identical. As more vortices enter, the behaviour becomes more complicated, and eventually the grain boundary will be driven into the phase slip state and become normal conducting (at which point the power dissipation will likely be so great as to induce a cavity quench).

Once a grain boundary is in the phase slip state, the power dissipated approaches an ohmic dependence (with an offset) of $P \approx R\mu_0^2(B_{pk}^2 - B_{GB}^2)/(2\lambda^2)$ [GS17]. Analogous to Figure 6.21, the grain boundary critical field is expected to lie at the centre of the hysteresis seen in Fig. Figure 6.12, then we can deduce that $B_{GB} \approx 65$ mT. Assuming a grain boundary thickness of 2 nm, a penetration depth of 140 nm, and a normal conducting resistivity of 1 μΩm, then a grain boundary in the phase slip state 1 micron wide by 1 micron deep dissipates $\sim$ 50 μW at the quench field of $\approx$ 75 mT. A larger grain boundary, 3 micron wide and 3 micron deep (extending through the entire thickness of the layer),

would dissipate ~ 400 μW. These surface field values assume no surface field enhancement due to topology, which can be as high as a factor of 2 [PHLM17], which would raise these values to 180 μW - 1.6 mW. Taking into consideration a realistic range of values of the penetration depth, grain boundary size, and field enhancement factor, the expected range for the dissipation at the quench field is 30 μW - 3 mW. These numbers are in qualitative agreement with those obtained by calibrating the temperature map data to dissipated power in subsection 6.2.2, in which the power dissipated at the quench origin just power to quench was observed to be (2.2 ± 0.5) mW. Furthermore, simulations such as those that produced Figure 6.21 suggest that the power dissipated by a single vortex should be on the order of 1/10 of the phase slip value, which would be ~ 100 – 200 μW; this is again qualitatively consistent with the power dissipated by the first three jumps seen in Figure 6.12, which correspond to an increase in dissipated power of (130 ± 30) μW.

A second (albeit less explored) candidate for flux entry is T_c suppression at the surface. Solutions to the Gibbs free energy per unit length of a vortex suggest that a second barrier could form for regions of T_c suppression that are on the order of the λ in depth, as indicated by Figure 6.22. This calculation was motivated by the discovery of small tin-depleted grains on the surface, found in some sample cross-sections. An example of such a grain is shown in Figure 6.23. Although not tin-depleted to the degree seen at regions in the bulk – such as those shown in Figure 3.15 – a depletion on the order of 2-3 at-% Sn is sufficient to reduce the superheating field by up to 75%. The theory is that at fields just beneath the quench field, vortices could break into these small surface grains but still be unable to overcome the barrier that would allow them to travel into the bulk, limiting their destructive potential. However, at slightly higher fields,

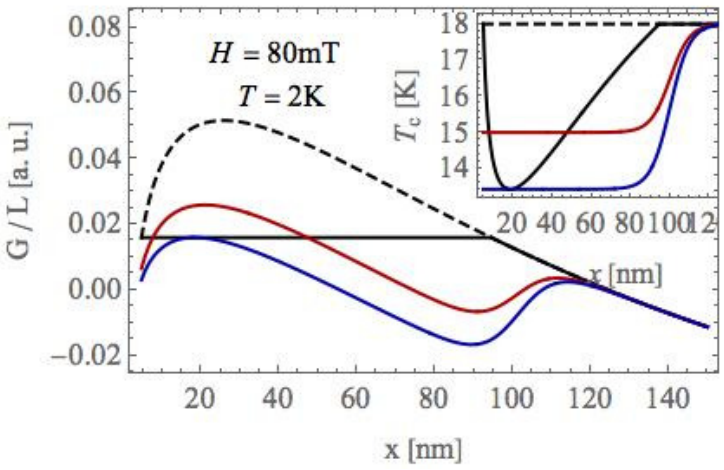

Figure 6.22: Gibbs free energy per unit length of a vortex at a surface field of 80 mT in Nb_3Sn at a bath temperature of 4.2 K, for three different scenarios: no T_c suppression, a specific T_c suppression that removes the energy barrier entirely, and a constant T_c suppression of 3-5 K in which a second, smaller barrier appears to remain. This figure courtesy of Danilo B. Liarte and James P. Sethna, Cornell University.

the pile-up of vortices becomes great enough that they break out of the grain and into the bulk, quenching the cavity. It is however still unclear whether this model would result in the same quantisation and hysteresis seen in Figure 6.12. Exploring this potential limitation requires understanding and controlling the formation of these tin-depleted regions, a task currently being undertaken using ab-initio growth simulation tools such a Joint Density Function Theory [APJ92, SGLW+12, IBA00].

6.3 Conclusions on cavity quench mechanisms

Experimental data presented in this work strongly suggests that the origin of quench in current Nb_3Sn cavities is flux entry at a defect. The data appears consistent with flux entry at grain boundaries, although it is difficult to confirm this

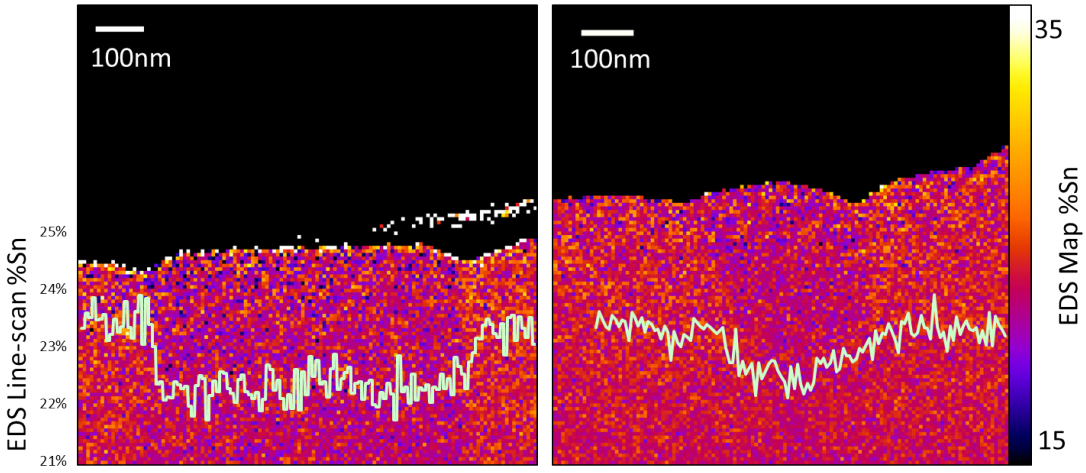

Figure 6.23: Two examples of slightly tin-depleted grains seen at the RF surface in cross-section of samples coated at Cornell. Overlaid on the EDS map is a line EDS; due to the standardless quantification used, the absolute error of the measurement is large, but relative differences are precise to the level of the noise seen in the measurement. This image courtesy of Paul Cueva and David A. Muller, Cornell University.

based on the results of this measurement alone. The next step should be to find a way to alter the mean free path l in Nb_3Sn cavities; such an objective is shared with the next step in the study of the sensitivity to trapped flux. Although it is well established that the mean free path can be reduced using impurity doping [GRS+13, MGL17], developing a method to increase the mean free path may prove more complicated.

CHAPTER 7

CONCLUSION

The results from new experiments carried out to understand the current limitations on the efficiency and achievable gradient in Nb_3Sn cavities have been presented in the previous two chapters, and initial conclusions were drawn. In this chapter we will summarise these conclusions and discuss the next steps to take in the development of Nb_3Sn for SRF cavities. We will conclude with what can currently be achieved with Nb_3Sn cavities, and use this to drive an outlook to the future.

7.1 Considerations for the coating of niobium structures

Studies performed using pre-anodisation of niobium samples revealed that the formation of thin film regions such as those seen in Figure 5.4 can be suppressed using pre-anodisation. The performance of the first cavity coated at Cornell, associated with the presence of thin film regions in this cavity, strongly suggests that the Q-slope seen in both previous cavities at the University of Wuppertal and currently at Jefferson National Laboratory is due to the small but significant presence of these regions.

The conclusion drawn from the sample study presented in section 5.1 is that the formation of these regions is due to an unsuccessful handover from the nucleation stage to the coating stage. Although the presence of a secondary hot-zone for the tin heater assists the process in supplying tin gas sooner during the ramp-up, care must be taken that the gas does not cool excessively during its passage to the niobium surface. In the absence of a ΔT during the ramp-up, the

use of pre-anodisation to ensure uniform coverage is necessary even in smaller furnaces such as that used at Siemens AG.

For small structures, pre-anodisation is not advised since the lowering of the substrate RRR is expected to lead to global thermal feedback (as seen in Figure 5.19). In the case of 2-10 GHz cavities, a single secondary hot-zone is expected to be sufficient to ensure uniform coating provided a nucleation agent is used, without the need for pre-anodisation. However, for larger structures such as 500 MHz cavities, particularly those made from large grain niobium, the presence of a secondary heater will be likely be insufficient (unless the source area and/or ramp-up ΔT are sufficiently large), and pre-anodisation will be required. Fortunately, the lower frequency of these cavities means that global thermal feedback from the lowering of the RRR during coating will not be a significant issue until very high (as yet unachievable) fields.

7.1.1 Impact of trapped magnetic flux

A measurement of the sensitivity to trapped flux in Nb_3Sn cavities is a function of the applied RF field. In the absence of the Q-slope seen in the Wuppertal cavities, a linear Q-slope remains due to this field-dependent sensitivity. The dependence is linear, which allows us to write the contribution to residual resistance from trapped flux as

$$R_{\text{residual}} = R^0_{fl} + R^1_{fl} B_{RF} \ , \tag{7.1}$$

where B_{RF} is the applied RF magnetic field. Using previously published data on

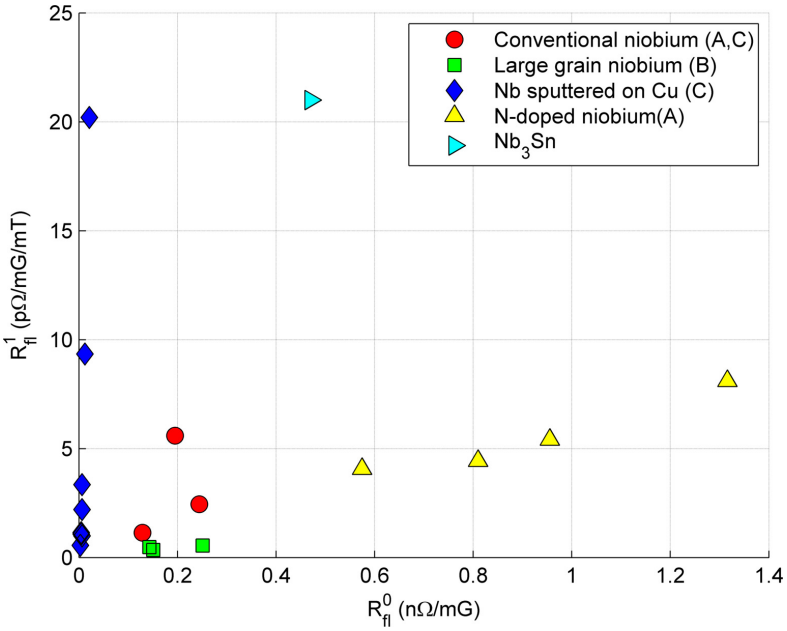

Figure 7.1: Data from literature sources comparing the values of R^0_{fl} and R^1_{fl} for different niobium surfaces against that measured in Nb_3Sn. This data was collected from (A) [MCG+15] (B) [CG07] (C) [BCD+97].

niobium cavities, we can observe how Nb_3Sn compares. The values of R^0_{fl} and R^1_{fl} from a number of published results [MCG+15, CG07, BCD+97] are compared to that of Nb_3Sn in Figure 7.1. As can be seen, the R^0_{fl} of Nb_3Sn is comparable to that of bulk, undoped niobium; however, the R^1_{fl} is much higher than bulk niobium, more similar to some niobium on copper films.

The slope in the sensitivity could prove problematic for efficient operation at high accelerating gradients. To ensure the highest possible Q, the amount of trapped flux must be minimized. In nitrogen-doped cavities, this has been achieved by cooling in a large gradient to expel ambient magnetic flux [PCC+16]. In Nb_3Sn however, the presence of such a large temperature gradient would result in the generation of large thermoelectric currents that will lead to significant amounts of trapped flux, even in spite of the improved expulsion of ambient flux. Because of this, a slow cooldown in a small thermal gradient is

necessary, although this is certain to trap the largest amount of ambient magnetic flux. Because of this, shielding from external magnetic fields is critical.

Current contemporary SRF accelerator designs using niobium, such as that of LCLS-II, demand that the ambient magnetic be less than 5 mG [CGGW17]. The use of active compensation coils for cryomodule degaussing [Cra15] has allowed ambient fields as low as 1 mG to be achieved. From the flux trapping experiment presented in section 5.2, we can determine that for cavity LTE1-7 the contribution to the residual resistance from thermal gradients and ambient trapped flux is

$$R_{\text{res}} = \left(0.47\frac{\text{n}\Omega}{\text{mG}}B_{\text{amb}} + 2.9\frac{\text{n}\Omega}{\text{K/m}}\frac{\Delta T}{\Delta L}\right) + \left(0.02\frac{\text{n}\Omega}{(\text{mG})\,(\text{mT})}B_{\text{amb}} + 0.13\frac{\text{n}\Omega}{\left(\frac{\text{K}}{\text{m}}\right)(\text{mT})}\frac{\Delta T}{\Delta L}\right)B_{RF} \tag{7.2}$$

where B_{amb} is the ambient magnetic field trapped during cooldown, $\Delta T/\Delta L$ is the thermal gradient across the cavity, and B_{RF} is the applied RF surface field. In the vertical test cryostat at Cornell, the best thermal gradients that could be achieved were approximately 200 mK/m, and the ambient field was measured to be 5 mG. Considering a state of the art cryomodule in which the thermal gradient during cooldown was 100 mK/m, and the ambient field 1 mG, the Q of the cavity at 16 MV/m would be improved by a factor of ≈ 2. This is demonstrated in Figure 7.2.

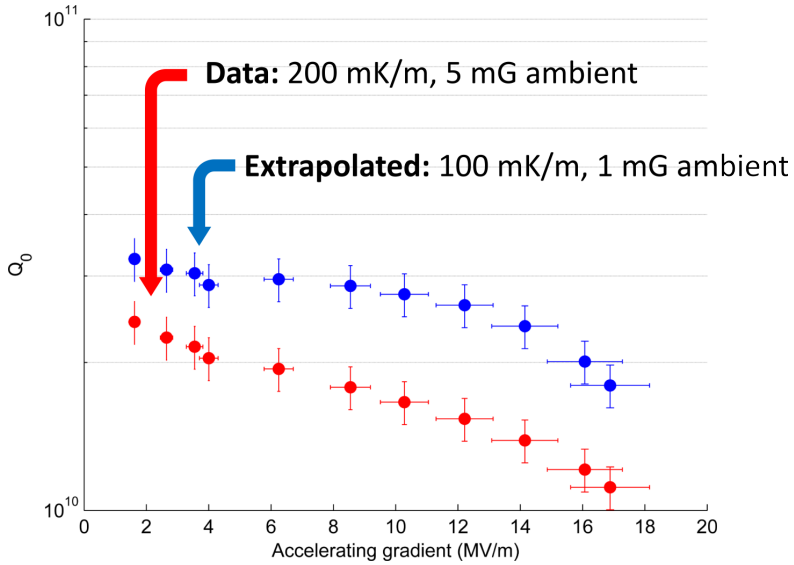

Figure 7.2: A Q vs E obtained at a bath temperature of 4.2 K from cavity LTE1-7 in the Newman vertical test setup. Equation 7.2 has been used to extrapolate the performance for a state-of-the-art cooldown.

7.1.2 Maximum achievable gradient

Results from the experiment investigating the dynamics of the cavity quench, presented in section 6.2, strongly suggest that the origin of the cavity quench is magnetic flux entry at a defect. The behavior seen appears consistent with flux entry at grain boundaries, in a manner described by vortex entry at grain boundaries modelled as under-damped, strongly-coupled Josephson junctions [SG17].

The observations indicate that the thermodynamic critical of the grain boundary is between 60 and 120 mT, depending on the level of field enhancement at the quench origin (which is unknown, but has be surmised to be as high as 2 from simulations of samples). Given a bulk thermodynamic critical field extrapolated to be 490 mT, this gives a ratio of $B_{GB}/B_C = 0.1 - 0.3$, which would indicate a somewhat strongly coupled grain boundary (since $B_{GB}/B_C > 1/\kappa$

[GS17]).

The current-blocking nature of the grain boundaries is most likely due to the dirty nature ($l \leq \xi_0$) of the bulk superconductor reducing the coherence length ξ to be on the order of or less than the width of a grain boundary. Extrapolations from cavity measurements indicate a material coherence length of $\xi = 2 - 3$ nm, while imaging of layer cross-sections such as that seen in Figure 7.3 suggest grain boundaries up to 2 nm thick. Given the dependence of the coherence length on the normal conducting electron mean free path l, as given by Equation 1.7, a lengthening of the mean free path would result in an increase in the coherence length. Seeing as the tunnelling through Josephson junctions is exponentially sensitive to the coherence length of the bulk superconductor, a small change in coherence length could result in a large difference in the behaviour of the boundary.

The difference between a hard and soft quenches, as discussed in Section subsection 6.2.3, appears to indicate that although the quench originates at a defect, said defect is likely only the worst of many. Although high pulsed power experiments indicate that the defect can be outrun to some degree, it is likely that this defect is not that much worse than other regions in the cavity - otherwise, the greater variance in the quench fields seen in Figure 6.1 would be expected. This leads us to conclude that the quench, although not being strictly fundamental to Nb_3Sn itself, originates from a common material feature (such as a grain boundary) whose worst offender is identified as the quench origin.

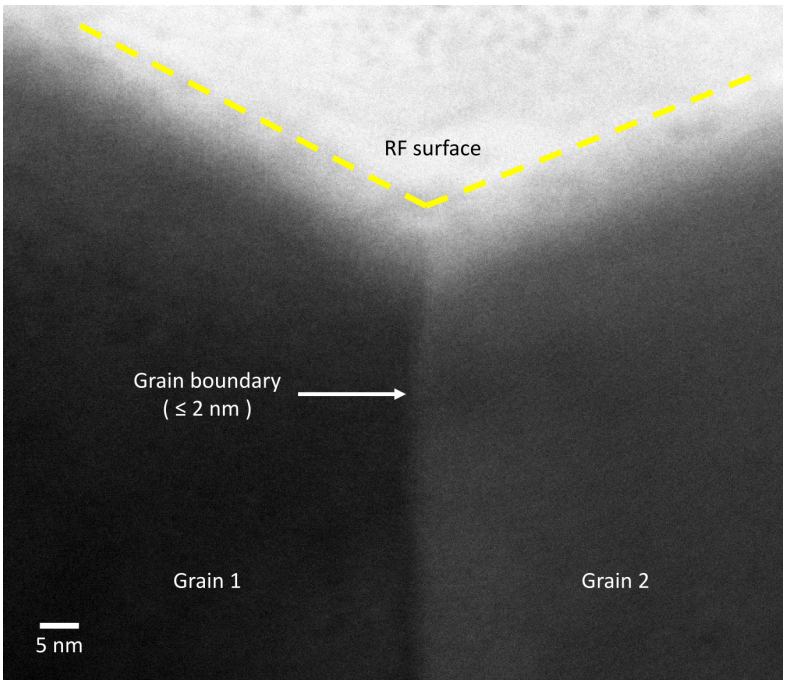

Figure 7.3: A STEM HAADF image of a grain boundary in a Nb_3Sn cross-section. The image indicates a grain boundary thickness of less than 2 nm. Image courtesy of Paul Cueva, Muller Group, Cornell University.

7.2 Outlook

7.2.1 Altering the electron mean free path

It has been mentioned a number of times throughout this work that altering the normal conducting electron mean free path could be critical in investigating how to overcome the current limitations on efficiency and gradient. In this section we will motivate the reasoning for this research direction and describe a proposal for a series of experiments that could be undertaken to achieve this goal.

The Nb_3Sn cavities produced so far have largely been in the dirty limit, with

$l < \xi_0$. To date, there has been little variation seen in the mean free path of Nb_3Sn cavities, with values measured from $l = 1-5$ nm [Pos14], with no cavities known to be in the clean limit $l \gg \xi_0$. As such, no good data exists for Nb_3Sn to determine the manner in which the quench field and residual Q-slope depend on the mean free path when going from the dirty to the clean limit.

Figure 7.1 gives data from niobium on copper cavities. These cavities were part of a study performed at CERN and Jefferson National Lab [BCC+99] to investigate losses from residual resistance in niobium coated on copper using sputtering techniques. The purity of the copper substrate and the coating gas resulted in different values for the superconducting penetration depth λ (which, by extension, implies a different mean free path). The residual Q-slope R^1_{fl} was found to be a function of λ, as seen in Figure 7.4 reproduced from [BCC+99].

The analytical result from the weak collective flux pinning scenario described in subsection 5.2.1 gives an expected dependence of the slope R^1_{fl} on the penetration depth of $R^1_{fl} \propto \lambda^2$. As can be seen in the fit overlaid on Figure 7.4, this dependence is an excellent fit to the high-λ data, which corresponds to the short mean free path or dirty limit. The turn-around in the shorter λ, comparatively cleaner region, is not described by the analytical result since viscous forces dominate here. It is not clear if this reversal of R^1_{fl} is specific to these niobium on copper cavities or if such as feature would also be present in a study on Nb_3Sn cavities.

Given that Nb_3Sn produced by the vapour diffusion method is in the dirty limit, the dependence of $R^1_{fl} \propto \lambda^2$ is expected to hold. Although decreasing the mean free path further would be useful in mapping out this dependence, it is not expected to be useful in decreasing the value of R^1_{fl}. However, whilst the

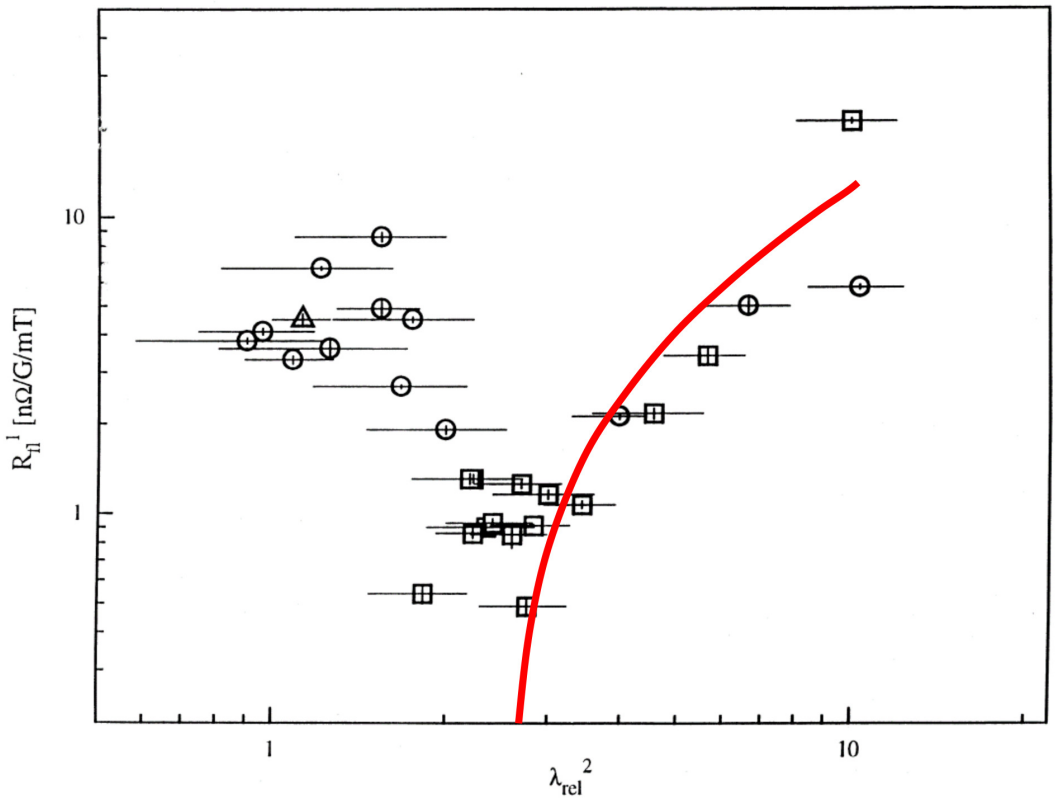

Figure 7.4: A measurement of the residual Q-slope R^1_{fl} against the square of the normalised RF penetration depth. A fit of $A\lambda^2 + B$ has been superposed on the image. This image was adapted from [BCC+99], with the penetration depth $\lambda^2_{\text{rel}} = 1 + (\pi/2)(\xi_0/l)$.

mean free path can be decreased in a controlled manner using impurity doping [GKL16, MGL17], no similar method exists for increasing it. Historically, the RRR of niobium has been increased (and with it, the mean free path) using high temperature bakes using titanium as a getter [Pad85, Kne88], although the temperatures required - $\approx$ 1400°C - are not expected to be ideal for maintaining good layer stoichiometry in the absence of a tin supply. The use of titanium also results in a thin coating of titanium that must be removed using chemical etching. Lower temperature anneals at 400-800°C for extended periods of time, without the use of a getter, could be useful in slowly removing impurities, although this is not assured. Changes to the coating process, such as active pumping during

the coating (although dangerous for the pumps a cold trap would be required) could also reduce the presence of impurities during coating.

Such experimentation is however limited by the fact that measurements of the mean free path using SRF cavities are time consuming and expensive, as they require a cavity to be coated and tested for each data point. An alternative method of measuring the mean free path is to perform a measurement of the upper critical field of a single sample, from which the mean free path can be determined using

$$l = \left[0.619 \frac{2\pi\xi_0 H_{c2}}{\phi_0} - \frac{1.134}{\xi_0} \right]^{-1} , \tag{7.3}$$

which is obtained by combining Equation 1.7 with the low-temperature value of H_{c2} [Tin12],

$$H_{c2} = \frac{\phi_0}{2\pi\mu_0\xi^2} . \tag{7.4}$$

This is not valid in the far clean limit as $l/\xi_0 > 10$ because Equation 1.7 breaks down as $\xi \to 5.172$ nm, but this correspond to a value of l one order of magnitude greater than the currently measured values. Although the systematic uncertainty in the absolute value of the measurement is modestly high, the relative precision between samples is expected to be more than sufficient to observe changes to the mean free path for different coating and post-processing methods. An instrument such as the Quantum Design Physical Property Measurement System (PPMS) in use at the Cornell Center for Materials Research would be very appropriate for such a measurement. The use of samples would significantly reduce the cost and time required to investigate candidates for increasing

the mean free path. Once a method has been identified, it can be applied to a cavity.

A benefit to using a PPMS for such a measurement is that the system is also capable of DC critical current measurements, which could be useful in measuring the impact of the change in mean free path on the current-blocking resistance of grain boundaries predicted by the vortex entry theory. However, the presence of the niobium substrate, which is superconducting below 9.2 K, would make such a measurement somewhat difficult. Furthermore, the behaviour of grain boundaries at DC and low frequency is expected to be different from the behaviour at RF frequencies.

7.2.2 Current state-of-the-art and future projects

The best performance achieved in three of the single-cell cavities in use in the Cornell Nb_3Sn research program is shown in Figure 7.5. Even with the current limitations due to trapped flux and vortex-entry quench, these cavities achieve Qs of greater than 10^{10} at 4.2 K and fields above 16 MV/m. For comparison, the Q specification for LCLS-II, adjusted for 4.2 K to take into account the change in the coefficient of performance of the cryoplant (as extrapolated from Figure 2.1), is also shown. All three of these cavities achieve this specification.

This performance opens up new possibilities for SRF technology. The first, most obvious of these is the operation of 1.3 GHz cavities at 4.2 K, significantly reducing the construction and operational cost of the machine. However, with the lower BCS resistance, the door is also open to operating at higher frequencies, which means comparatively smaller cavities. Although this might require

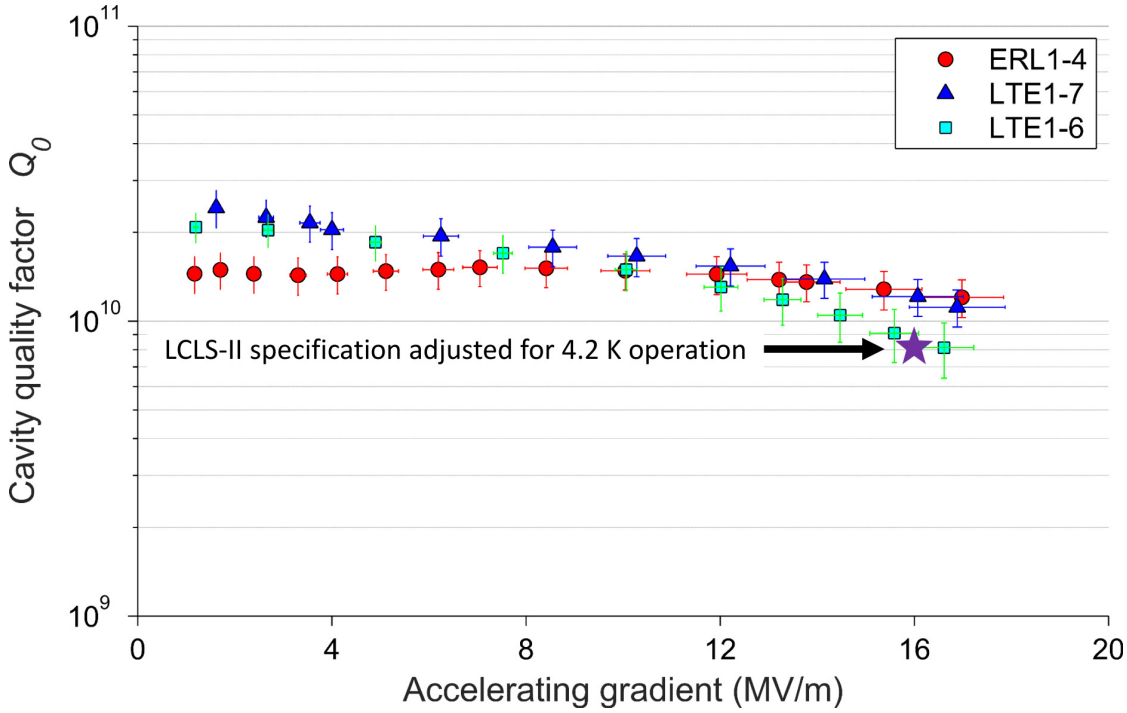

Figure 7.5: The best performance observed in three different 1.3 GHz single-cell cavities that have seen use in the Cornell University Nb_3Sn programme, operating at a bath temperature of 4.2 K. The Q-specification for LCLS-II is shown, adjusted to take into account the improved efficiency of the cryoplant at 4.2 K.

returning to sub-4.2 K operation, the adoption of 3.9 GHz cavities would reduce the size of the cryomodule considerably. To demonstrate this, a 3.9 GHz multi-cell cavity is shown standing next to a single-cell 1.3 GHz cavity in Figure 7.6. Moving to higher frequency would result in reductions of the capital cost of the machine, both in terms of the bill of materials and the physical footprint required.

Another exciting prospect is the operation of a 1.3 GHz cavity using a gaseous helium cryo-cooler at 4.5 K. Modern cryo-coolers exist that are capable of extracting up to 2 W of power at 4.2 K [Cry]. By comparison, a single-cell 1.3 GHz Nb_3Sn cavity operating at 10 MV/m, assuming the performance extrapolated in Figure 7.2 of $Q_0 = 2.7 \times 10^{10}$ at 4.2 K, would dissipate 0.5 W of heat.

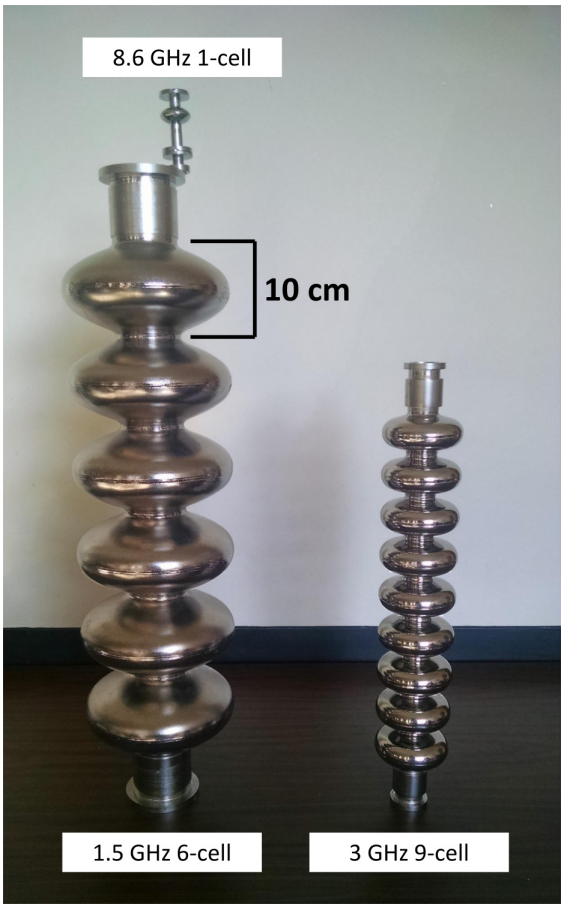

Figure 7.6: A size comparison of a 1.5 GHz 6-cell and a 3 GHz 9-cell cavity. An 8.6 GHz single-cell can be seen perched on the beampipe of the 1.5 GHz 6-cell. A doubling of the frequency results in a significantly smaller cavity in all dimensions.

Using conduction cooling, such a cryomodule would be free of liquid helium. Operating solely on the cryocooler, which is a turn-key system with considerably lower maintenance requirements, this cryomodule would be affordable to smaller institutions such as universities and industry. An sketch of such a cryomodule, alongside some example operating parameters, is shown in Figure 7.7.

These smaller cryomodules would allow Nb_3Sn to fulfill demands beyond those of large installations such as particle colliders and hard X-ray light

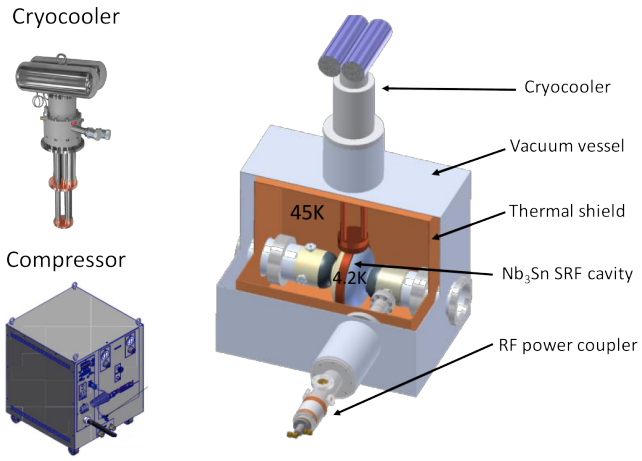

Parameter	Value
$E_{acc,max}$	10 MV/m
$\Delta E_{beam,max}$	few MeV
$I_{beam,max}$	>100 mA CW
Number of cavity cells	1 - 4
Cavity frequency	1300 MHz
T_{cavity}	4.2 K
Cavity Q_0	2.7×10^{10}

Figure 7.7: An example of what a cryocooler-equipped module would look like. Using a cryocooler power from a compressor unit, a single-cell or small multi-cell Nb_3Sn cavity powered by a solid state amplifier (not shown) can be operated at 4.2 K. Some example specifications for such a machine are shown in the table on the right.

sources. A small, low-emittance accelerator could provide a beam capable of generating an intense beam of soft X-rays for diffraction experiments or extreme UV for photolithography. A high current electron beam, disregarding emittance, is would also be useful for applications such as high intensity X-ray generation (for use in cargo scanning) and electron beam processing for high through-put polymer cross-linking.

The current state-of-the-art performance is a promising indicator that Nb_3Sn stands not just to slash the capital and operational costs of future large-scale projects, but also to enable a new breed of SRF accelerators. These new machines will be the first of their kind to be accessible to smaller institutions and industrial applications, and will herald a new chapter in the story of particle accelerators and their impact upon society.

BIBLIOGRAPHY

[ABHT83] L Allen, M Beasley, R Hammond, and J Turneaure. RF surface resistance of high-Tc superconducting A15 thin films. *IEEE Transactions on Magnetics*, 19(3):1003–1006, may 1983.

[AMC86] G Arnolds-Mayer and E Chiaveri. On a 500 MHz single cell cavity with Nb3Sn surface. In *Proceedings of The Third Workshop on RF Superconductivity*, Chicago, 1986.

[APJ92] Tomas A. Arias, M C Payne, and J D Joannopoulos. Ab initio molecular dynamics: Analytically continued energy functionals and insights into iterative solutions. *Phys. Rev. Lett.*, 69(7):1077–1080, aug 1992.

[BBF+13] Ties Behnke, James E Brau, Brian Foster, Juan Fuster, Mike Harrison, James McEwan Paterson, Michael Peskin, Marcel Stanitzki, Nicholas Walker, and Hitoshi Yamamoto. The International Linear Collider Technical Design Report - Volume 1: Executive Summary. 2013.

[BBR+16] E Barzi, M Bestetti, F Reginato, D Turrioni, and S Franz. Synthesis of superconducting Nb 3 Sn coatings on Nb substrates. *Superconductor Science and Technology*, 29(1):15009, 2016.

[BCC+99] Cristoforo Benvenuti, S Calatroni, I E Campisi, P Darriulat, M A Peck, R Russo, and A-M Valente. Study of the surface resistance of superconducting niobium films at 1.5 GHz. *Physica C: Superconductivity*, 316(3):153–188, 1999.

[BCC+15] P Bishop, M. Checchin, Holly Conklin, A. Crawford, E. Daly, K. Davis, M. Drury, Ralf Georg Eichhorn, J. Fischer, Fumio Furuta, Mingqi Ge, Daniel Gonnella, Anna Grassellino, C. Grimm, Terri Gruber, Daniel Leslie Hall, A. Hocker, Georg Hoffstaetter, John Julian Kaufman, G. Kulina, Matthias Liepe, James Maniscalco, M. Martinello, O. Melnychuk, Tim O'Connell, J. Ozelis, A. Palczewski, Peter Quigley, C.E. Reece, Alex Romanenko, M. Ross, A. Rowe, D. Sabol, James Sears, D. Sergatskov, W. Soyars, R. Stanek, Vadim Veshcherevich, R. Wang, and G. Wu. LCLS-II SRF Cavity Processing Protocol Development and Baseline Cavity Performance Demonstration. In *Proceedings of SRF 2015*, page MOPB033, Whistler, BC, sep 2015.

[BCD+97] Cristoforo Benvenuti, I E Campisi, Pierre Darriulat, C Durand, M A Peck, Sergio Calatroni, R Russo, and A M Valente. Magnetic flux trapping in superconducting niobium. Technical report, 1997.

[BCD+01] C Benvenuti, S Calatroni, P Darriulat, M A Peck, and A-M Valente. Fluxon pinning in niobium films. *Physica C: Superconductivity*, 351(4):429–437, 2001.

[BKM+97] P Boccard, P Kneisel, G Müller, J Pouryamout, and H Piel. Results from some temperature mapping experiments on Nb3Sn RF cavities. In *Proceedings of the Eighth Workshop on RF Superconductivity*, Padova, 1997.

[BPG+15] Chaoyue Becker, Sam Posen, Nickolas Groll, Russell Cook, Christian M. Schlepütz, Daniel Leslie Hall, Matthias Liepe, Michael Pellin, John Zasadzinski, and Thomas Proslier. Analysis of Nb3Sn surface layers for superconducting radio frequency cavity applications. *Applied Physics Letters*, 106(8):082602, feb 2015.

[BS65] John Bardeen and M J Stephen. Theory of the Motion of Vortices in Superconductors. *Phys. Rev.*, 140(4A):A1197—-A1207, nov 1965.

[Cam85] I E Campisi. High field RF superconductivity: To pulse or not to pulse? *IEEE Transactions on Magnetics*, 21(2):134–141, mar 1985.

[CC64] G D CODY and R W COHEN. Thermal Conductivity of Nb3Sn. *Rev. Mod. Phys.*, 36(1):121–123, jan 1964.

[CCJ+08] S P Chockalingam, Madhavi Chand, John Jesudasan, Vikram Tripathi, and Pratap Raychaudhuri. Superconducting properties and Hall effect of epitaxial NbN thin films. *Phys. Rev. B*, 77(21):214503, jun 2008.

[CF84] I E Campisi and Z D Farkas. Pulsed rf superconductivity program at SLAC. In *Proceedings of the Second Workshop on RF Superconductivity*, Geneva, aug 1984.

[CG07] G Ciovati and A Gurevich. Measurement of RF losses due to trapped flux in a large grain niobium cavity. *Proceedings of the 2007 Workshop on RF Superconductivity*, TUP13:132–136, 2007.

[CGGW17] Saravan Kumar Chandrasekaran, Anna Grassellino, Chuck Grimm,

and Genfa Wu. Magnetic Field Management in LCLS-II 1.3 GHz Cryomodules. In *28th Linear Accelerator Conf.(LINAC'16), East Lansing, MI, USA, 25-30 September 2016*, pages 527–530. JACOW, Geneva, Switzerland, 2017.

[CGM+15] Mattia Checchin, Anna Grassellino, Martina Martinello, Alexander Romanenko, and John Zasadzinski. Mean Free Path Dependence of the Trapped Flux Surface Resistance. In *17th International Conference on RF Superconductivity (SRF2015), Whistler, BC, Canada, Sept. 13-18, 2015*, pages 129–134. JACOW, Geneva, Switzerland, 2015.

[Cha66] J P Charlesworth. The superconducting transition temperatures of Nb6Sn5 and NbSn2. *Physics Letters*, 21(5):501–502, 1966.

[Cha95] Jonathan S. Chapman. Superheating Field of Type-II Superconductors. *SIAM J. Appl. Math.*, 55:1233–1258, 1995.

[Cio04] Gianluigi Ciovati. Effect of low-temperature baking on the radio-frequency properties of niobium superconducting cavities for particle accelerators. *Journal of Applied Physics*, 96(3):1591–1600, 2004.

[CMM70] J P Charlesworth, I Macphall, and P E Madsen. Experimental work on the niobium-tin constitution diagram and related studies. *Journal of Materials Science*, 5(7):580–603, jul 1970.

[Cra14] Anthony C Crawford. A study of thermocurrent induced magnetic fields in ILC Cavities. *arXiv preprint arXiv:1403.7996*, 2014.

[Cra15] Anthony C Crawford. In Situ Cryomodule Demagnetization. 2015.

[Cry] Cryomech. PT420 Two-Stage Pulsed Tube cryocooler.

[CRZ+06] G. Carta, G. Rossetto, P. Zanella, L. Crociani, Vincenzo Palmieri, and F. Todescato. Attempts to deposit Nb3Sn by MO-CVD. In *Proceedings of the international workshop on thin films and new ideas for pushing the limits of RF superconductivity*, Padua, 2006.

[CSB+11] C Cooper, K Sato, B Bullock, S Joshi, and A Palczewski. Centrifugal barrel polishing of cavities worldwide. In *Proceedings of SRF*, pages 571–575, 2011.

[dHHR+78] deceased Hans Martens, M Harald, M Rainer, M Hans-Wolfgang,

M Gunter, M Sigrid, M Hannelore, and M Helmut. Method for the manufacture of a superconductive Nb3 Sn layer on a niobium surface for high frequency applications, 1978.

[DHL17] J Ding, Daniel Leslie Hall, and Matthias Liepe. Simulations of RF field-induced feedback in niobium and Nb3Sn cavities. In *Proceedings of SRF 2017*, Lanzhou, jul 2017.

[Die78] H Diepers. Method for the anodic polishing of surfaces of intermetallic niobium compounds and niobium alloys. *US Patent 4,072,588*, pages 1–5, 1978.

[DJD+81] H Devantay, J L Jorda, M Decroux, J Muller, and R Flükiger. The physical and structural properties of superconducting A15-type Nb-Sn alloys. *Journal of Materials Science*, 16(8):2145–2153, aug 1981.

[DKR+06] Silvia M. Deambrosis, G Keppel, Vincenzo Ramazzo, C Roncolato, R.G. Sharma, and Vincenzo Palmieri. {A15} superconductors: An alternative to niobium for {RF} cavities. *Physica C: Superconductivity*, 441(12):108–113, 2006.

[DMP+89] D Dasbach, G Müller, M Peiniger, H Piel, R W W Roth, and Fachbereich Physik. Nb3Sn coating of high purity Nb cavities. *IEEE Transactions on Magnetics*, 25(2):1862–1864, mar 1989.

[Dor03] R C Dorf. *CRC Handbook of Engineering Tables*. Electrical Engineering Handbook. CRC Press, 2003.

[DR84] B David and H Rogalla. Determination of Optimum Preparation Parameters for Thin High-Tc Nb3Ge Films. In A F Clark and R P Reed, editors, *Advances in Cryogenic Engineering Materials : Volume 30*, pages 631–638. Springer US, Boston, MA, 1984.

[DRR+09] Silvia M. Deambrosis, Vincenzo Ramazzo, A.A. Rossi, V. Rupp, R.G. Sharma, S. Stark, F. Stivanello, and Vincenzo Palmieri. A15 Superconductors by Thermal Diffusion in 6 GHz Cavities. In *Proceedings of SRF 2009*, Berlin, 2009.

[DSMS71] H Diepers, O Schmidt, H Martens, and F S Sun. A new method of electropolishing niobium. *Physics Letters A*, 37(2):139–140, 1971.

[Edw95] D A Edwards (ed.). TESLA Test Facility (TTF) Linac Conceptual Design Report. Technical Report Ch. 4, 1995.

[EKR+15] G.V. Eremeev, M.J. Kelley, C.E. Reece, U. Pudasaini, and J. Tuggle. Progress with Multi-Cell Nb3Sn Cavity Development Linked with Sample Materials Charaterization. In *Proceedings of SRF 2015*, Whistler, 2015.

[FPB79] P. Feschotte, A. Polikar, and G. Burri. Equilibres de phases dans les systemes binaries Nb-Ge et Nb-Sn. *C. R. Seances Acad. Sci., Ser. C*, 1979.

[GC13] A Gurevich and G Ciovati. Effect of vortex hotspots on the radio-frequency surface resistance of superconductors. *Phys. Rev. B*, 87(5):54502, feb 2013.

[GEF+14] Daniel Gonnella, Ralf Georg Eichhorn, Fumio Furuta, Mingqi Ge, Daniel Leslie Hall, Y. He, Georg Hoffstaetter, Matthias Liepe, Tim O'Connell, Sam Posen, Peter Quigley, James Sears, Vadim Veshcherevich, Anna Grassellino, and Alex Romanenko. NITROGEN-DOPED 9-CELL CAVITY PERFORMANCE IN THE CORNELL HORIZONTAL TEST CRYOMODULE. In *Proceedings of LINAC 2014*, Geneva, aug 2014.

[GFG+16] Mingqi Ge, Fumio Furuta, Daniel Gonnella, Daniel Leslie Hall, Georg Hoffstaetter, Matthias Liepe, Tim O'Connell, and James Sears. SURFACE TOPOGRAPHY TECHNIQUES AT CORNELL UNIVERSITY: OPTICAL INSPECTION AND SURFACE REPLICA. In *Proceedings of IPAC 2016*, Busan, may 2016.

[GKL16] Dan Gonnella, John Kaufman, and Matthias Liepe. Impact of nitrogen doping of niobium superconducting cavities on the sensitivity of surface resistance to trapped magnetic flux. *Journal of Applied Physics*, 119(7):73904, 2016.

[GL09] V L Ginzburg and L D Landau. On the Theory of Superconductivity. In *On Superconductivity and Superfluidity: A Scientific Autobiography*, pages 113–137. Springer Berlin Heidelberg, Berlin, Heidelberg, 2009.

[God06] A Godeke. A review of the properties of Nb3Sn and their variation with A15 composition, morphology and strain state. *Superconductor Science and Technology*, 19(8):R68—-R80, aug 2006.

[GPSS05] R.L. Geng, Hasan Padamsee, A Seaman, and V. Shemelin. World Record Accelerating Gradient Achieved in a Superconducting RF Cavity. In *Proceedings of PAC 2005*, Knoxville, Tennessee, 2005.

[GRS+13] Anna Grassellino, Alex Romanenko, D. Sergatskov, O. Melnychuk, Y. Trenikhina, A. Crawford, A. Rowe, M. Wong, T. Khabiboulline, and F. Barkov. Nitrogen and argon doping of niobium for superconducting radio frequency cavities: a pathway to highly efficient accelerating structures. *Superconductor Science and Technology*, 26(10):102001, 2013.

[GS17] Alexander Gurevich and Ahmad Sheikhzada. Current-blocking grain boundaries in SRF cavities and RF dissipation due to nonlinear dynamics of Josephson vortices under strong RF fields. In *Proceedings of SRF 2017*, Lanzhou, jul 2017.

[Gur14] Alexander Gurevich. Reduction of dissipative nonlinear conductivity of superconductors by static and microwave magnetic fields. *Physical review letters*, 113(8):87001, 2014.

[Hak88] M Hakimi. TMS Symposium on Niobium and Niobium Alloys in Superconducting Applications Bronze-processed Nb3Sn for r.f. applications. *Journal of the Less Common Metals*, 139(1):159–165, 1988.

[Hal70] J Halbritter. Comparison between measured and calculated RF losses in the superconducting state. *Zeitschrift für Physik*, 238(5):466–476, 1970.

[Hal90] J Halbritter. RF residual losses, surface impedance, and granularity in superconducting cuprates. *Journal of Applied Physics*, 68(12):6315–6326, 1990.

[Ham75] R Hammond. Electron beam evaporation synthesis of A15 superconducting compounds: Accomplishments and prospects. *IEEE Transactions on Magnetics*, 11(2):201–207, mar 1975.

[Hay14] William M Haynes. *CRC handbook of chemistry and physics*. CRC press, 2014.

[Hei99] M A Hein. *High-Temperature-Superconductor Thin Films at Microwave Frequencies*. Springer Tracts in Modern Physics. Springer Berlin Heidelberg, 1999.

[HGK+15] Daniel Leslie Hall, Terri Gruber, John Julian Kaufman, Matthias Liepe, James Maniscalco, Sam Posen, Byeonghee Yu, and Thomas Proslier. Nb3Sn Cavities: Material Characterisation and Coating Process Optimisation. In *Proceedings of SRF 2015*, Whistler, sep 2015.

[HGM+84] H Heinrichs, T Grundey, N Minatti, Gunter Muller, M Peiniger, H Piel, G Unterborsch, and H P Vogel. Activities on RF-Superconductivity at Wuppertal. In *Proceedings of the Second Workshop on RF Superconductivity*, Geneva, 1984.

[HHO74] J Hasse, W D Hermann, and R Orlich. On the microwave absorption of superconducting Nb3Sn. *Zeitschrift f{ü}r Physik*, 271(3):265–268, 1974.

[Hil76] B Hillenbrand. Superconducting Nb3Sn cavities with high quality factors and high critical flux densities. *Journal of Applied Physics*, 47(9):4151, 1976.

[Hil80] B Hillenbrand. The Preparation of Superconducting Nb3Sn Surfaces for RF applications. In *Proceedings of the First Workshop on RF Superconductivity*, Karlsruhe, 1980.

[HKP+81] B Hillenbrand, N Krause, H Pfister, K Schnitzke, and Y Uzel. Supraleitende Nb3Sn Resonatoren. Technical report, Siemens AG, 1981.

[HLM16] Daniel Leslie Hall, Matthias Liepe, and James Maniscalco. RF Measurements on High Performance Nb3Sn Cavities. In *Proceedings of IPAC 2016*, Busan, may 2016.

[HMP+75] B Hillenbrand, H Martens, H Pfister, K Schnitzke, and G Ziegler. Superconducting Nb3Sn cavities. *IEEE Transactions on Magnetics*, 11(2):420–422, mar 1975.

[HMP+77] B Hillenbrand, H Martens, H Pfister, K Schnitzke, and Y Uzel. Superconducting Nb3Sn cavities with high microwave qualities. *IEEE Transactions on Magnetics*, 13(1):491–495, jan 1977.

[HMS92] E Haebel, A Mosnier, and J Sekutowicz. Cavity shape optimization for a superconducting linear collider. In *Proceedings of the Fifteenth Conference on High energy accelerators*, volume 2, pages 957–959, Hamburg, 1992.

[HP97] Tom Hays and Hasan Padamsee. Measuring the RF Critical Field of Pb, Nb, and Nb3Sn. In *Proceedings of the Eighth Workshop on RF Superconductivity*, pages 789–794, Padova, 1997.

[HSY+01] T Higuchi, K Saito, Y Yamazaki, T Ikeda, and S Ohgushi. Centrifugal barrel polishing of L-band niobium cavities. In *Proceedings of the 10th Workshop on RF Superconductivity*, pages 431–432, 2001.

[HUS80] B Hillenbrand, Y Uzel, and K Schnitzke. On the preparation of Nb3Sn-layers on monocrystalline Nb-substrates. *Applied Physics*, 23(3):237–240, nov 1980.

[IBA00] Sohrab Ismail-Beigi and Tomas A. Arias. New algebraic formulation of density functional calculation. *Computer Physics Communications*, 128(1):1–45, 2000.

[JAA+17] T Junginger, S H Abidi, R Astley, T Buck, M Dehn, S Gheidi, R Kiefl, P Kolb, D Storey, E Thoeng, and Others. Field of first flux entry and pinning strength of superconductors for RF application measured with muon spin rotation. *arXiv preprint arXiv:1705.05480*, 2017.

[JCC+91] J F Julião, J W R Chagas, H L Cesar, N L Dias, Franco Decker, and U U Gomes. Anodic niobium pentoxide films: growth and thickness determination by in situ optoelectrochemical measurements. *Electrochimica Acta*, 36(8):1297–1300, 1991.

[KAK+85] P Kneisel, J Amato, J Kirchgessner, K Nakajima, H Padamsee, H Phillips, C Reece, R Sundelin, and M Tigner. Performance of superconducting storage ring cavities at 1500 MHz. *IEEE Transactions on Magnetics*, 21(2):1000–1003, mar 1985.

[KB96] F Koechlin and B Bonin. Parametrization of the niobium thermal conductivity in the superconducting state. *Superconductor Science and Technology*, 9(6):453, 1996.

[KBH+07] J W Kooi, J J A Baselmans, M Hajenius, J R Gao, T M Klapwijk, P Dieleman, A Baryshev, and G de Lange. IF impedance and mixer gain of NbN hot electron bolometers. *Journal of Applied Physics*, 101(4):44511, 2007.

[KHL16] Adam Kline, Daniel Leslie Hall, and Matthias Liepe. Study of Sn Vapor Diffusion in the Synthesis of Nb3Sn Films. Technical report, Cornell University, 2016.

[KHPU81] N Krause, B Hillenbrand, H Pfister, and Y Uzel. Nb and Nb3Sn cavities produced by sheet material. *IEEE Transactions on Magnetics*, 17(1):927–930, jan 1981.

[KL95] Peter Kneisel and B Lewis. Advanced surface cleaning methods: three years of experience with high pressure ultrapure water rinsing of superconducting cavaties. Technical report, Continuous Electron Beam Accelerator Facility, Newport News, VA (United States), 1995.

[KM00] Alfred Koethe and Jens Ingolf Moench. Preparation of ultra high purity niobium. *Materials Transactions, JIM*, 41(1):7–16, 2000.

[Kne88] P Kneisel. Use of the titanium solid state gettering process for the improvement of the performance of superconducting rf cavities. *Journal of the Less Common Metals*, 139(1):179–188, 1988.

[Kno97] Jens Knobloch. *Advanced Thermometry Studies of Superconducting Radio-Frequency Cavities*. Phd, Cornell University, 1997.

[Kri12] Mahadevan Krishnan. Niobium coatings for SRF cavities produced by high power impulse magnetron sputtering. In *Proceedings of the fifth international workshop on thin films and new ideas for pushing the limits of RF superconductivity*, Newport News, 2012.

[KTO05] Norikiyo Koizumi, Takao Takeuchi, and Kiyoshi Okuno. Development of advanced Nb 3 Al superconductors for a fusion demo plant. *Nuclear Fusion*, 45(6):431, 2005.

[LAH+17] Danilo B Liarte, Tomas Arias, Daniel L Hall, Matthias Liepe, James P Sethna, Nathan Sitaraman, Alden Pack, and Mark K Transtrum. SRF Theory Developments from the Center for Bright Beams. 2017.

[LDGL09] Mei Li, Zhenmin Du, Cuiping Guo, and Changrong Li. Thermodynamic optimization of the Cu–Sn and Cu–Nb–Sn systems. *Journal of Alloys and Compounds*, 477(1):104–117, 2009.

[Loe04] L B Loeb. *The Kinetic Theory of Gases*. Dover phoenix editions. Dover Publications, 2004.

[LP13] Matthias Liepe and Sam Posen. Nb3Sn for SRF Application. In *Proceedings of SRF 2013*, Paris, sep 2013.

[MCG+15] M Martinello, M Checchin, A Grassellino, O Melnychuk, S Posen, A Romanenko, D Sergatskov, and J F Zasadzinski. Trapped flux surface resistance for different surface treatments. *Proceedings of the Seventeenth International Conference on RF Superconductivity*, MOPB015, 2015.

[MDF+17] F. Marhauser, E.F. Daly, J.A. Fitzpatrick, A. Palczewski, J. Preble, and K.M. Wilson. Status of the LCLS-II Accelerating Cavity Production. In *Proceedings of IPAC 2017*, Copenhagen, 2017.

[Meu58] G Meurant. *Advances in Chemical Engineering*. Number v. 2 in Advances in Chemical Engineering. Elsevier Science, 1958.

[MGGC54] B T Matthias, T H Geballe, S Geller, and E Corenzwit. Superconductivity of Nb3Sn. *Phys. Rev.*, 95(6):1435, sep 1954.

[MGL17] J T Maniscalco, D Gonnella, and M Liepe. The importance of the electron mean free path for superconducting radio-frequency cavities. *Journal of Applied Physics*, 121(4):43910, 2017.

[Mit10] Shinji Mitsunobu. Status of KEK studies on MgB2. In *Proceedings of the fourth international workshop on thin films and new ideas for pushing the limits of RF superconductivity*, Padua, 2010.

[MKM96] G Müller, P Kneisel, and D Mansen. Nb3Sn layers on high-purity Nb cavities with very high quality factors and accelerating gradients. In *Proceedings of the Fifth European Particle Accelerator Conference*, Sitges, 1996.

[MO87] S A Mucklejohn and N W O'Brien. The vapour pressure of tin(II) chloride and the standard molar Gibbs free energy change for formation of SnCl2(g) from Sn(g) and Cl2(g). *The Journal of Chemical Thermodynamics*, 19(10):1079–1085, 1987.

[MSJ67] J. Matricon and D. Saint-James. Superheating Fields in Superconductors. *Physics Letters A*, 24(5):241–242, 1967.

[MZRB79] D F Moore, R B Zubeck, J M Rowell, and M R Beasley. Energy gaps

of the A15 superconductors Nb3Sn, V3Si, and Nb3Ge measured by tunneling. *Phys. Rev. B*, 20(7):2721–2738, oct 1979.

[Oka90] H. Okamoto. Nb-Sn (Niobium-Tin). *Binary Alloy Phase Diagrams, II Ed., Ed. T.B. Massalski*, 1990.

[Oka03] H Okamoto. Nb-Sn (Niobium-Tin). *Journal of Phase Equilibria*, 24(4):380, jul 2003.

[OMFB79] T P Orlando, E J McNiff, S Foner, and M R Beasley. Critical fields, Pauli paramagnetic limiting, and material parameters of Nb3Sn and V3Si. *Phys. Rev. B*, 19(9):4545–4561, may 1979.

[ONSA04] Sachiko Ono, Takumi Nagasaka, Hiroki Shimazaki, and Hidetaka Asoh. Fabrication of porous niobia by anodizing of niobium. *Proc. Electrochem. Soc*, 19(2006):123, 2004.

[Pad85] H Padamsee. A new purification technique for improving the thermal conductivity of superconducting Nb microwave cavities. *IEEE Transactions on Magnetics*, 21(2):1007–1010, 1985.

[PCC+16] S Posen, M Checchin, A C Crawford, A Grassellino, M Martinello, O S Melnychuk, A Romanenko, D A Sergatskov, and Y Trenikhina. Efficient expulsion of magnetic flux in superconducting radiofrequency cavities for high Q0 applications. *Journal of Applied Physics*, 119(21):213903, 2016.

[PCH+99] Markus Perpeet, A Cassinese, M A Hein, T Kaiser, Gunter Muller, H Piel, and J Pouryamout. Nb3Sn films on sapphire. A promising alternative for superconductive microwave technology. *IEEE Transactions on Applied Superconductivity*, 9(2):2496–2499, jun 1999.

[PDK+93] D Proch, B Dwersteg, G Kreps, A Matheisen, W D Moller, D Renken, J Sekutowicz, and W Singer. Laboratory Report DESY. *Proc. SRF93*, 1993.

[Pei83] M Peiniger. *Herstellung Und Test Eines S-Band Resonators Mit Nb3Sn Oberflache*. PhD thesis, Universitat Gesamthochschule Wuppertal, 1983.

[PEK+17] U Pudasaini, G V Eremeev, M J Kelley, C E Reece, and J Tuggle. {E}xamination of {C}utouts {I}nner {S}urfaces from {N}b3{S}n

{C}oated {C}avity. In *Proc. of Linear Accelerator Conference (LINAC'16), East Lansing, MI, USA, 25-30 September 2016*, number 28 in Linear Accelerator Conference, pages 189–192, Geneva, Switzerland, may 2017. JACoW.

[PFH+17] Ryan Porter, Fumio Furuta, Daniel Hall, Matthias Liepe, and James Maniscalco. Effectiveness of Chemical Treatments for Reducing the Surface Roughness of Nb3Sn. In *8th Int. Particle Accelerator Conf.(IPAC'17), Copenhagen, Denmark, 14â 19 May, 2017*, pages 1145–1148. JACOW, Geneva, Switzerland, 2017.

[PHK+88] M Peiniger, M A Hein, N Klein, G Mueller, H Piel, and P Thuenus. Work on Nb3Sn cavities at Wuppertal. In *Proceedings of The Third Workshop on RF Superconductivity*, Lemont, Illinois, sep 1988.

[PHLM17] Ryan Porter, Daniel Leslie Hall, Matthias Liepe, and James Maniscalco. Surface Roughness Effect on the Performance of Nb3Sn Cavities. In *28th Linear Accelerator Conf.(LINAC'16), East Lansing, MI, USA, 25-30 September 2016*, pages 129–132. JACOW, Geneva, Switzerland, 2017.

[PHLX12] Sam Posen, Georg Hoffstaetter, Matthias Liepe, and Yi Xie. Recent Developments in the Cornell Nb3Sn Initiative. In *Proceedings of IPAC 2012*, New Orleans, Louisiana, may 2012.

[PKH98] Hasan Padamsee, Jens Knobloch, and Tom Hays. *RF Superconductivity for Accelerators*. Wiley Series in Beam Physics and Accelerator Technology. Wiley, 1st edition, 1998.

[PL11] Sam Posen and Matthias Liepe. Stoichiometric Nb3Sn in First Samples coated at Cornell. In *Proceedings of SRF 2011*, Chicago, Illinois, jul 2011.

[PL13] Sam Posen and Matthias Liepe. RF Test Results of the First Nb3Sn Cavities Coated at Cornell. In *Proceedings of SRF 2013*, Paris, sep 2013.

[PLX11] Sam Posen, Matthias Liepe, and Yi Xie. Cornell SRF New Materials Program. In *Proceedings of IPAC 2011*, San Sebastian, sep 2011.

[PMR+15] Sam Posen, O. Melnychuk, Alex Romanenko, D. Sergatskov, Daniel Leslie Hall, Matthias Liepe, Y. Trenikhina, Daniel Leslie Hall,

and Matthias Liepe. Cutout Study of a Nb3Sn Cavity. In *Proceedings of SRF 2015*, Whistler, sep 2015.

[PMRT15] Sam Posen, M. Merio, Alex Romanenko, and Y. Trenikhina. Fermilab Nb3Sn R&D Program. In *Proceedings of SRF 2015*, Whistler, dec 2015.

[Pos14] Sam Posen. *Understanding and Overcoming Limitation Mechanisms in Nb3Sn Superconducting RF Cavities*. PhD thesis, Cornell University, 2014.

[PS08] A Piróth and J Sólyom. *Fundamentals of the Physics of Solids: Volume II: Electronic Properties*. Fundamentals of the Physics of Solids. Springer Berlin Heidelberg, 2008.

[PVL15] Sam Posen, Nicholas Valles, and Matthias Liepe. Radio Frequency Magnetic Field Limits of Nb and Nb3Sn. *Phys. Rev. Lett.*, 115(4):47001, jul 2015.

[RDS+09] A.A. Rossi, Silvia M. Deambrosis, S. Stark, Vincenzo Ramazzo, V. Rupp, R.G. Sharma, F. Stivanello, and Vincenzo Palmieri. Nb3Sn films by Multilayer Sputtering. In *Proceedings of SRF 2009*, Berlin, 2009.

[RKM+92] R W Roth, H G Kurschner, Gunter Muller, H Piel, and D Reschke. Thermal Stability of Superconducting Nb Cavities at 3 GHz. In *Proceedings of the 1992 European Particle Accelerator Conference*, Berlin, mar 1992.

[RSI+16] Guillaume Rosaz, Alban Sublet, Katsyarina Ilyina, Sergio Calatroni, Mauro Taborelli, Sarah Aull, Akira Myasaki, Walter Venturini-Delsolaro, Karl Schirm, Mikko Karppinen, Nikolai Schwerg, Matthieu Therasse, Floriane Leaux, Anite Fontenla, and Josep Busom Descarrega. Production and R&D thin films activities at CERN for SRF applications. In *Proceedings of TESLA Technology Workshop*, Paris, 2016.

[Sch81] Klaus K Schulze. Preparation and characterization of ultra-high-purity niobium. *JOM*, 33(5):33–41, 1981.

[SG17] Ahmad Sheikhzada and Alex Gurevich. Dynamic transition of vortices into phase slips and generation of vortex-antivortex pairs in

thin film Josephson junctions under dc and ac currents. *Phys. Rev. B*, 95(21):214507, jun 2017.

[SGLW+12] R. Sundararaman, D. Gunceler, K. Letchworth-Weaver, K. Schwarz, and Tomas A. Arias. JDFTx, 2012.

[SSW+06] W Singer, X Singer, H Wen, A Ermakov, D Proch, A Brinkmann, J Iversen, G Kreps, D Reschke, A Matheisen, A Schmidt, M Spiwek, Peter Kneisel, K Kowalski, A Bernasik, A Dangwal, G Mueller, K R Baldner, J Van Santen, and H G Brokmeier. Large Grain/Single Crystal R&D at DESY. In *Single Crystal Nb Technology Workshop, CBMM*, oct 2006.

[Sti78] J B Stimmell. *Microwave superconductivity of Nb3Sn*. PhD thesis, Cornell University, 1978.

[STS73] Y M Shy, L E Toth, and R Somasundaram. Superconducting properties, electrical resistivities, and structure of NbN thin films. *Journal of Applied Physics*, 44(12):5539–5545, 1973.

[SW62] E Saur and J Wurm. Preparation und Supraleitungseigenschaften von Niobdrahtproben mit Nb3Sn-Uberzug. *Die Naturwissenschaften*, 49(6):127–128, 1962.

[SWPF65] H.A. Schwettman, P.B. Wilson, J.P. Pierce, and W.M. Fairbank. The Application of Superconductivity to Electron Linear Accelerators. *International Advances in Cryogenic Engineering*, 10, 1965.

[TCRK08] Hui Tian, Sean G Corcoran, Charles E Reece, and Michael J Kelley. The mechanism of electropolishing of niobium in hydrofluoric–sulfuric acid electrolyte. *Journal of the Electrochemical Society*, 155(9):D563—-D568, 2008.

[TCS11] Mark K. Transtrum, Gianluigi Catelani, and James P. Sethna. Superheating field of superconductors within Ginzburg-Landau theory. *Physical Review B*, 83(9):094505, mar 2011.

[Tin12] M Tinkham. *Introduction to Superconductivity*. Dover Books on Physics Series. Dover Publications, Incorporated, 2nd edition, 2012.

[TRK+06] Hui Tian, Charles E Reece, Michael J Kelley, Shancai Wang, Lukasz Plucinski, Kevin E Smith, and Matthew M Nowell. Surface stud-

ies of niobium chemically polished under conditions for superconducting radio frequency (SRF) cavity production. *Applied Surface Science*, 253(3):1236–1242, 2006.

[TSGS02] C Toffolon, C Servant, J. C. Gachon, and B Sundman. Reassessment of the Nb-Sn system. *Journal of Phase Equilibria*, 23(2):134–139, mar 2002.

[Tsu02] Tajima Tsuyoshi. Possibility of MgB2 Application to Superconducting Cavities. In *Proceedings of EPAC 2002*, Paris, 2002.

[TW68] J P Turneaure and Ira Weissman. Microwave Surface Resistance of Superconducting Niobium. *Journal of Applied Physics*, 39(9):4417–4427, 1968.

[Val13] Nicholas Valles. *Pushing the Frontiers of Superconducting Radio Frequency Science: From the Temperature Dependence of the Superheating Field of Niobium to Higher-Order Mode Damping in Very High Quality Factor Accelerating Structures*. PhD thesis, Cornell University, 2013.

[VL11] Nicholas Valles and Matthias Liepe. The Superheating Field of Niobium: Theory and Experiment. In *Proceedings of SRF 2011*, pages 293 – 301, Chicago, Illinois, jul 2011.

[VLF+14] N Valles, M Liepe, F Furuta, M Gi, D Gonnella, Y He, K Ho, G Hoffstaetter, D S Klein, T O'Connell, S Posen, P Quigley, J Sears, G Q Stedman, M Tigner, and V Veshcherevich. The main linac cavity for Cornell's energy recovery linac: Cavity design through horizontal cryomodule prototype test. *Nuclear Instruments and Methods in Physics Research Section A: Accelerators, Spectrometers, Detectors and Associated Equipment*, 734:23–31, jan 2014.

[Wei09] H Weise. The European XFEL based on superconducting technology. In *SRF*, volume 9, page 6, 2009.

[WPJ01] Yuxing Wang, Tomasz Plackowski, and Alain Junod. Specific heat in the superconducting and normal state (2-300 K, 0-16 T), and magnetic susceptibility of the 38 K superconductor MgB2: evidence for a multicomponent gap. *Physica C: Superconductivity*, 355(3-4):179–193, jun 2001.

[WPW+15] F.˜S. Wells, A.˜V. Pan, X.˜R. Wang, S.˜A. Fedoseev, and

H Hilgenkamp. Analysis of low-field isotropic vortex glass containing vortex groups in YBa$_{2}$Cu$_{3}$O$_{7-x}$ thin films visualized by scanning SQUID microscopy. *Scientific Reports*, 5:8677, mar 2015.

[WW57] G K White and S B Woods. Low Temperature Resistivity of Transition Elements: Vanadium, Niobium, and Hafnium. *Canadian Journal of Physics*, 35(8):892–900, 1957.

[XRK13] B P Xiao, C E Reece, and M J Kelley. Superconducting surface impedance under radiofrequency field. *Physica C: Superconductivity*, 490(Supplement C):26–31, 2013.

[Xu17] Xingchen Xu. A review and prospects for Nb3Sn superconductor development. *Superconductor Science and Technology*, 30(9):093001, 2017.

[YSBS15] Mingyun Yuan, Vibhor Singh, Yaroslav M Blanter, and Gary A Steele. Large cooperativity and microkelvin cooling with a three-dimensional optomechanical cavity. *Nature communications*, 6, 2015.